Synthesis, Organization and Characterization of Nanoscale Inorganic Materials

Mei Li

A dissertation submitted to the University of Bristol in accordance with the requirements of the degree of **PhD** in the Faculty of Science, Department of Chemistry

November 2000

Word count: 40,045

Abstract

Nanomaterials such as nanofilaments and nanoparticles of barium chromate, barium sulfate and Prussian blue have been synthesized by using AOT [*bis(2-ethylhexyl) sulfosuccinate*] microemulsions as templates. Nanoparticles with cubic, prismatic, spherical, hollow-shell morphologies have been organized into higher ordered chain structures, superlattices, or disordered aggregates by self-assembly processes involving hydrophobic interactions, biotin-streptavidin bioconnectors or organic-inorganic thin films. The nanoparticles and their aggregates have been characterized by TEM, SAED, EDXA, SEM, XRD, SAXS, DLS, TGA, FTIR, UV-VIS, MS, SDS-PAGE.

Synthesis of barium chromate and barium sulfate nanocrystals in the presence of anionic surfactant AOT water-in-oil reverse micelles or microemulsion droplets at $w \approx 5 - 20$ was undertaken. The morphology of barium chromate and barium sulfate nanoparticles was controlled by changing the $[Ba^{2+}]$:$[SO_4^{2-}]$ or $[Ba^{2+}]$:$[CrO_4^{2-}]$ molar ratio in the AOT microreactors. Prismatic nanocrystals and self-assembled linear chains and rectangular superlattices were formed specifically at molar equivalence. Under identical conditions, but with an excess of Ba^{2+}, high aspect ratio filaments were formed; with a molar excess of SO_4^{2-} or CrO_4^{2-}, spherical colloidal nanocrystals were observed. The size of the prismatic nanoparticles was controlled by the water content of the AOT reverse microemulsions. The chains and superlattices consisted of ordered arrays of prismatic $BaCrO_4$ and $BaSO_4$ nanoparticles held together by the interdigitation of surfactant molecules on specific crystal faces.

Synthesis in AOT reverse microemulsions was also applied to the molecular-based magnet Prussian blue. Hydrophobic cubic nanoparticles with narrow size distributions were obtained and the nanoparticles self-assembled into a well defined square superlattice. The size of Prussian blue nanoparticles increased with increasing w value from 10 to 20, and with decreasing concentration of reactant inside the microemulsion droplets.

Mixing two functionalised micellar surfactants of barium bis(2-ethylhexyl) sulfosuccinate $Ba(AOT)_2$ and hexadecyltrimethylammonium sulphate $(CTA)_2SO_4$ with opposite charge and curvature at molar ratio of $Ba(AOT)_2/(CTA)_2SO_4$ = 1:1~1:4 produced hollow spherical nanoshells of $BaSO_4$ via asymmetric interfacial delivery. The nanoshells were 9.6 nm in size with a 3.4 nm diameter hollow centre and 3.1 nm thick wall.

The well-known specific binding of streptavidin to biotin was exploited in the reversible assembly of disordered networks of inorganic nanoparticles. The iron storage protein ferritin was modified by biotin (*sodium sulfosuccinimidyl-6-biotinamido hexanoate*) ligands and then aggregated by streptavidin to produce iron oxide nanoparticle networks. The rate and degree of molecular cross-linking were dependent on the molar ratio of ferritin to streptavidin and the best results were obtained at a molar ratio of 1:6.

Organic-inorganic thin films were prepared at a substrate surface by self-assembly of AOT surfactant molecules in combination with the inorganic compound uranyl acetate $[UO_2(CH_3COO)_3]$. The UO_2-AOT thin films formed as regular patterns on the substrates, which can be used for the organization of inorganic nanomaterials.

Acknowledgements

Firstly I would like to express my gratitude to my supervisor Professor Stephen Mann for giving me the opportunity to work in this research group and for his encouragement, supervision, help and interest throughout my PhD years.

I am greatly indebted to Dr. Sébastien Vaucher for his collaboration on the Prussian blue project and the barium sulfate nanoshells project, for his support and his friendship, for correcting some of chapters of this thesis, for everything.

I am also indebted to Dr. Heimo Schnablegger (Max-Planck-Institut of Colloids and Interfaces, Germany) for small-angle X-ray scattering and dynamic light scattering measurements in my *Nature* paper and his collaboration on that project.

I am grateful to Dr. Kim K. W. Wang and Dr. Dominic Walsh for their involvement on my training on electron microscopes, for many help in the beginning of my study, and for their friendship.

I would also like to thank Dr. Sean A. Davis for valuable discussions on crystallography and for the technical support on electron microscopes. Many thanks go to Pippa for the technical support on electron microscopes.

I would also like to thank all of my colleagues in the group, past and present, who are Simon, Wayne, Chris, Bao, Nicky, Katja, Deepa, Lala, Erik, Eric, Benedicte, Harish, Wataru, Masa, Fumi, Chiya, Karen, for their friendship and help. I had great time in this group during my PhD.

I am grateful to the University of Bristol for financial support.

My special thanks must go to my husband He Ping and my daughter Dian Dian for their love and support, for everything.

Author's Declaration

I declare that the work in this dissertation was carried out in accordance with the Regulations of the University of Bristol. The work is original except where indicated by special reference in the text and no part of the dissertation has been submitted for any other degree.

Any views expressed in the dissertation are those of the author and in no way represent those of the University of Bristol.

The dissertation has not been presented to any other University for examination either in the United Kingdom or overseas.

Signed: _____ Date: 30th Nov. 2000

Contents

Chapter 1

Introduction

1.1 Controlled synthesis of nanoparticles in microemulsions

Synthesis of nanoparticles is a new emerging field in solid state chemistry.[1,2] Due to their small size, these crystallites exhibit unique catalytic behaviour[3] and show size quantization effects,[4] nonlinear properties[5] and unusual luminescence.[6] Synthesis of ultrafine particles using reactions in microemulsions was first reported by Boutonnet *et al.* in 1982 when they obtained monodispersed metal particles (in the size range 3-5 nm) of Pt, Pd, Rh and Ir by reducing corresponding salts in water pools of water-in-oil microemulsions with hydrazine or hydrogen gas.[7] Since then, a large number of nanosize materials have been synthesized by using microemulsions, such as silica,[8,9] silver,[10-12] copper,[13-17] copper sulfide,[18,19] silver sulfide,[20-22] barium sulfate,[23] cobalt,[24] silver chloride,[25] semiconductor clusters $Cd_{1-y}Mn_yS$[26] and $Cd_yZn_{1-y}S$,[27] platinum,[28-30] gold colloids.[31] calcium sulfate.[32] Many examples of semiconductors,[19,33,34,35] magnetic,[36] or metallic particles[37] were synthesized in AOT reverse micelles or microemulsions.

AOT water-in-oil reverse micelles or microemulsions play an important role in the synthesis of nanoscale materials. One way to perform reduction or (co)precipitation reactions is by mixing two microemulsions of the same composition but with a different dispersed phase, for example one containing a metal salt and the other containing a reactant agent in the water pools of the microemulsion droplets. Metal ions can be introduced to the microemulsion via

the aqueous phase or as surfactant counterions in the case of anionic surfactants; for example copper bis(2-ethyl-hexyl)sulfosuccinate ($Cu(AOT)_2$) can be used as a surfactant for copper incorporation.

Preparation of ultrafine AgCl particles has been reported using AOT/alkane microemulsions as microreactors.[38] Mixing of the microemulsions containing $AgNO_3$ and NaCl led to the precipitation of AgCl and the progress of the reaction was monitored by stopped-flow spectrophotometry using K_2CrO_4 as an indicator. Photometric measurements showed that the formation of AgCl was complete within 60 minutes. An increase in the alkane chain length stabilized the microparticulate dispersion and decreased the growth rate.

An interesting development in this field was the use of a supercritical reverse micellar system for producing $Al(OH)_3$ particles.[39] The advantage of using this system arises from the large increase of water solubilization with applied pressure by the microemulsion, AOT/$Al(NO_3)_3$ under supercritical conditions at 110 °C and 200 bar pressure. Precipitation was initiated by injecting dry ammonia gas into the reaction chamber. Depending on the concentration of $Al(NO_3)_3$, particles with a mean size between 100 and 500 nm could be prepared. The particle size was found to be considerably larger than the micellar diameter. This has been attributed to particle coalescence of precipitated nuclei due to rapid exchange of the electrolytes in the micellar core.

Lianos and Thomas[33] have studied the formation of colloidal CdS in a water-in-oil microemulsion containing AOT, hexane and water. The size of the CdS particles was found to increase with *w* (the molar ratio of water to surfactant) in the range of 5 to 32 nm at constant Cd^{2+} concentration. An increase in Cd^{2+} concentration led to a decrease in particle size. This result was interpreted[40] in terms of enhanced nucleation and less secondary growth at high salt concentration. However, Motte *et al.*[41] have observed that when Na-Cd AOT reverse micelles were used, increases in the water pool concentration and amount of Cd^{2+} ions induced an increase in the size and polydispersity of CdS particles.

The formation of CdS and ZnS nanoparticles in AOT reverse micelles was followed by UV spectrophotometry.[42] Particle formation by nucleation and growth was complete within 0.02s followed by particle coagulation. In the beginning the rate of particle coagulation was dependent on the intermicellar exchange rate. However, when the particle diameter approached the H_2O core diameter, coagulation depended on micellar size.

Kitahara and his group were the first to use surfactant-containing organic media to produce and disperse magnetic particles. Initially they attempted to prepare a stable colloidal solution of magnetic oxide and other particles in cyclohexane using AOT as surfactant.[43,44] They suggested that the dispersion stability of the solid particles in colloidal media was due to adsorption of AOT molecules on the particles. Later on they used water-in-oil microemulsions

(AOT/cyclohexane/$FeCl_3$) as a medium for the preparation of colloidal magnetite.[45] The preparation was accomplished by mixing the above system with NH_4OH or bubbling in NH_3 gas; $FeCl_2$ was added to achieve the desired Fe(II)/Fe(III) ratio. The size distribution of the colloidal suspension (measured by electron microscopy) was consistent with a log-normal curve. The magnetic interaction between colloidal particles was found to be negligible. The authors explained that the size distribution function becomes log-normal due to the reverse micellar droplets which form during the crystal growth of magnetite. Unfortunately, they did not draw any conclusion regarding the parameters responsible for controlling the size of the particles.

Ultrafine nanoparticles of cobalt were prepared by borohydride reduction of a cobalt salt in an AOT/isooctane microemulsion.[46] The particles were found to be extremely small and super-paramagnetic; the particle sizes calculated were ~5.4 Å. Pileni *et al.* [47,48] have shown that metallic copper particles can be synthesised in AOT microemulsions where the particles are either surrounded or not surrounded by an oxide layer.

Silica nanoparticles have been prepared in AOT/decane/ammonium hydroxide microemulsions via base catalysed hydrolysis of tetraethoxysilane.[49] More monodisperse particles were formed on addition of benzyl alcohol, an additive known to act as a cosurfactant. The size distribution has been attributed to the inhibition of nucleation by fast rearrangement of hydrolysed tetraethoxysilane.

Ultrafine SiO_2 particles were also prepared in water/AOT/isooctane microemulsions by hydrolysis of tetraethoxysilane.[50] The processes of drying and calcination were found to influence the purity of the final product. The particles had an increased number of micropores in them compared with powders prepared by other methods.

Fe_3O_4 nanoparticles were also prepared using water/AOT/cyclohexane microemulsions.[51] Nanosize TiO_2 semiconductor particles have been prepared in AOT reverse microemulsions by hydrolysis of titanium tetrabutoxide.[52] The particle formation process was followed by changes in the UV-vis absorption spectra. A mechanism for formation of titanium dioxide ultrafine particles based on the number of micelles was proposed.

Nanosize silver crystallites have been synthesised in AOT reverse micelles.[11] The study described the dependence of various parameters such as micellar structure and nature of the reducing agent or solvent, to control the nanosize of the silver particles.

Since Boutonnet *et al.* successfully synthesized nanoparticles using microemulsions in 1982, a large number of investigations have focused on the synthesis of various nanosize materials and methods for controlling the particle size and quantum size effects. In most studies, however, the nanoparticles synthesized in microemulsions were approximately spherical.[53] There has been

less systematic work performed on what actually controls the size, shape and stability of the particles formed and a valid theory is still not available. In recent years interest has shifted from making monodisperse nanoparticles of different materials with mostly a spherical shape to controlling particle morphology (anisotropic and high-axial-ratio particles), introducing crystallinity and oriented growth[54-56] and ordering nanoparticles into 2D or 3D structured arrays and superlattices.[57-59]

Pileni and co-workers obtained cylindrical copper particles in pure $Cu(AOT)_2$/isooctane/water microemulsions using hydrazine as a reducing agent under an N_2 atmosphere. A series of papers[16,17,60] focused on the influence of the microstructure of the microemulsion phase in which the reduction took place, as well as the shape and homogeneity of the copper particles. The cylindrical shape of the copper particles was attributed to the shape transition in the microemulsions from spheres to cylinders with increasing water content (w).

Further growth and aggregation of the initially formed nanoparticles results in the formation of higher-order structures such as $BaSO_4$ filaments.[24] A non-compact fibre, consisting of 2-20 μm long multiple filaments, and single highly ordered crystalline barite filaments 1-100 μm long and 20-200 nm wide were obtained in AOT/isooctane/water microemulsion at w values between 10 and 29 by Hopwood in our group in 1997. All filaments formed at w = 12-29 were found to be single crystals and elongated predominantly along the (010) crystallographic axis

displaying an uniform thickness and aspect ratios of 1000, and in some instances, consisted of coaligned nanofilaments, 20-50 nm in width. Based on the extremely high aspect ratio, Hopwood suggest that fusion processes, which are irreversible, unidirectional and possibly autocatalytic, are responsible for the final morphology. A mechanism of unidirectional exchange and coalescence in microemulsion droplets followed by crystallization of an amorphous filamentous $BaSO_4$/surfactant phase was proposed. Similar structures for $CaSO_4$[61] and $BaCO_3$[62] nanowires were also obtained.

1.2 Organisation of nanoparticles into superlattices

Nanoparticles and the physical and chemical functional specificity and selectivity they possess, naturally suggest them as ideal building blocks for two- and three-dimensional cluster self-assembled superlattice structures, in which the particles behave like well-defined molecular matter, arranged with long-range translational and even orientational order.[63] Well-defined ordered solids prepared from tailored nanocrystalline building blocks provide new opportunities to optimize and enhance the properties and performance of materials. This is a new initiative in research on cluster engineered materials. Usually external forces are used to organize the nanoparticles, techniques such as biomolecular crosslinking,[64-66] bacteria templates,[67] size selected,[13][20] molecular linking,[68] colloidal crystallization[25,69] have been applied to organize nanocrystals into superlattices.

Transferring DNA, protein and bacteria from the biological to the material world is a new and exciting area. Single-strand DNA oligonucleotides of defined length and sequence have been attached to individual nanocrystals, and these assemble into dimers and trimers on addition of a complementary single-stranded DNA template.[64,65] This method allows the controlled and reversible assembly of gold nanoparticles into supermolecular structures. Oligonucleotides offer several advantages over non-biological linker molecules. For example, discrete sequences of controlled length and with the appropriate surface binding functionality may be prepared in an automated fashion with a DNA synthesizer. In this way, the molecular recognition properties of oligonucleotides may be used to trigger the colloidal self-assembly process. The interparticle distances and stabilities of the supermolecular structures generated by this method can be controlled through the choice of oligonucleotide sequence and length, solvent, temperature and supporting electrolyte concentration.

The highly specific recognition properties of antibodies and antigens make them excellent candidates for ligand-induced assembly of preformed nanoparticles in solution.[70] This method has been applied in the aggregation of gold nanoparticles.[71] The use of bacterial or protein architectures for the template-directed assembly of inorganic nanoparticles has been reported. For example, self-assembled bacterial S-layer was used for synthesis of CdS superlattices[67] and organization of gold nanoparticles.[72]

Self-organization of nanoparticles is a new route for the synthesis of superlattice materials. Recently, spontaneous arrangement or self-assembly with semiconductors such as Ag_2S,[20,22,21] CdS[67] and CdSe[73] or metallic particles such as Au[65,66,68] or Ag[10,24,74] have been reported. Most of this research was based on a size-selection method to self-assemble spherical nanoparticles into superlattices on a solid substrate by solvent evaporation. For example, silver particles were extracted from AOT micelles by adding dodecanethiol. The application of this size-selected precipitation technique narrowed the Ag particle size distribution from 43% to 12.5%, which favors the organization of silver particles in 2D and 3D superlattices.[10]

1.3 The aims of this thesis

Based on previous research, this thesis attempted to

- understand what actually controls the size, shape and stability of the nanoparticles formed in reverse micelles or microemulsions,

- organize nanoparicles into 2D or 3D superlattices by (i) self-assembly in solution; (ii) bioconnectors; (iii) organic-inorganic thin films.

- synthesize novel nanoscale materials by using AOT reverse micelles or microemulsions as microreactors,

- understand the general mechanism of formation of nanofilaments synthesized in microemulsions,

- develop new methods of synthesis of nanoparticles by using a mixture of anionic and cationic surfactants with opposite aggregation curvature.

1.4 Microemulsions

1.4.1 General information about microemulsions

The ancient concept that water and oil do not mix, has undergone modification. Addition of a third component may either increase or decrease the mutual solubility of two partially miscible liquids. If the third component is a surfactant, it reduces the interfacial tension between the pair of immiscible liquids, enabling them to be dispersed between each other. Depending on the proportion of the components, either water-in-oil (w/o) or oil-in-water (o/w) dispersions are produced (Figure 1-1). These microdispersions (called emulsions having diameter of 0.2 – 10 μm) are turbid and may remain stable for a considerable length of time; they are thermodynamically unstable but kinetically stable.[75]

Hoar and Schulman[76,77] described microemulsions for the first time. In the presence of short chain alkanols (e.g butanol, pentanol, hexanol, etc), the emulsions (formed by surfactant/water/oil) transform into solutions having particles of much smaller diameter (~10 nm) called microemulsions, which do not in principle require any mechanical work for their formation. Such preparations are homogeneous, optically isotropic, or low viscosity and thermodynamically stable dispersions of either oil-in-water or water-in-oil (Figure 1-2).[75] The short chain alkanols are so called cosurfactants. The cosurfactants may not be always

an essential requirement, for example, the surfactant Aerosol OT (AOT) may form microemulsion in the absence of a cosurfactant.[78]

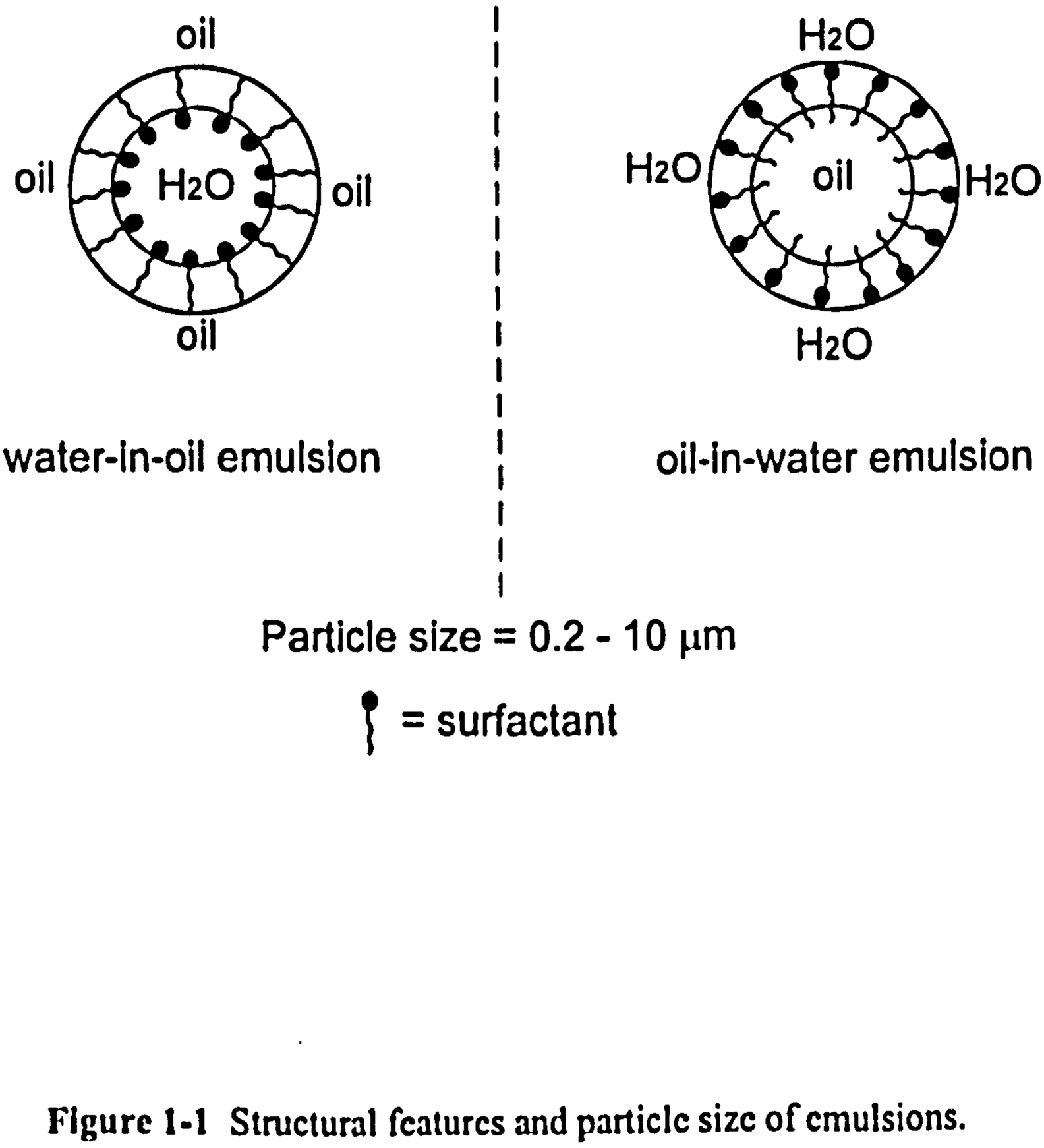

Figure 1-1 Structural features and particle size of emulsions.

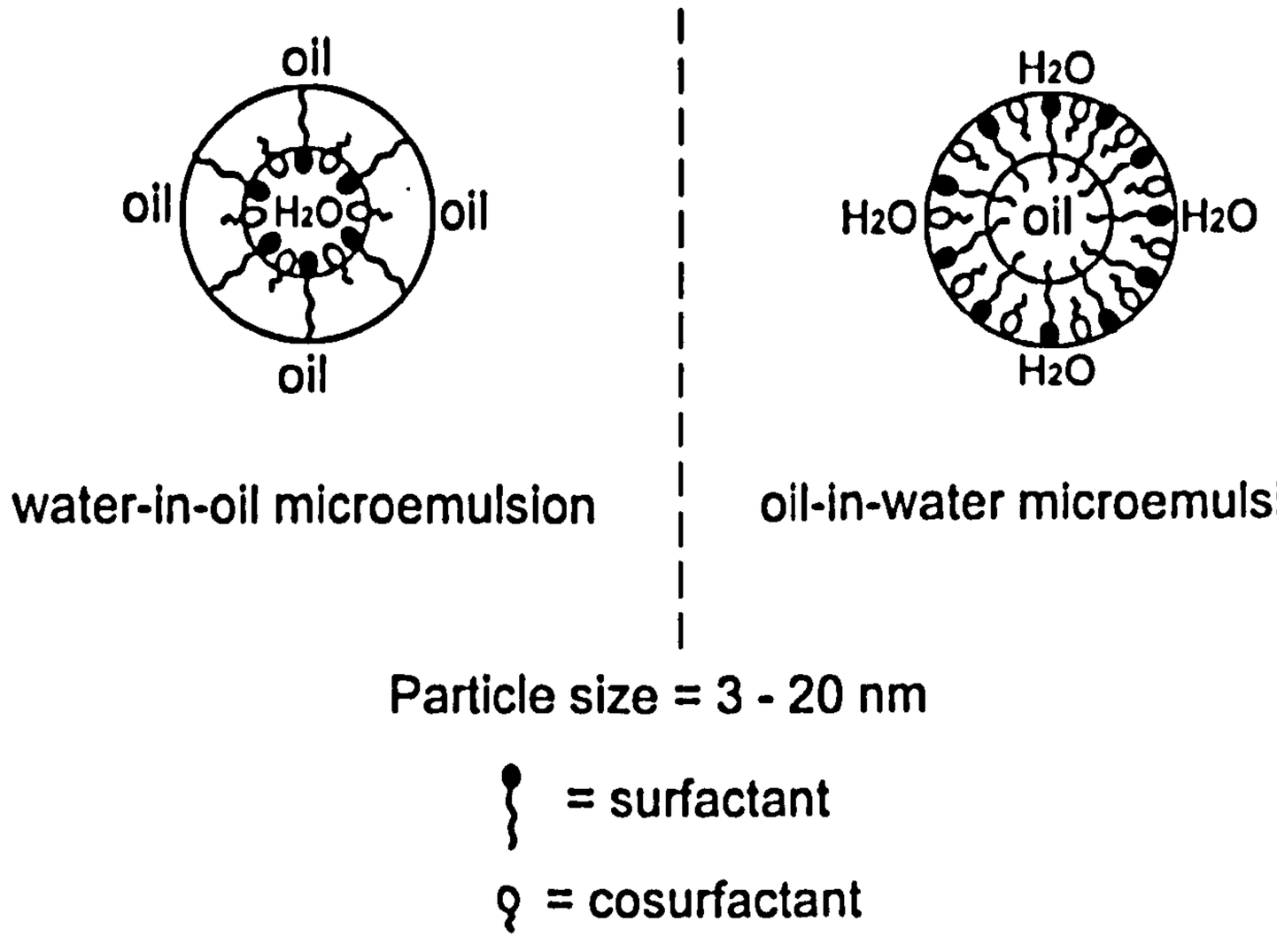

Figure 1-2 Structural features and particle size of microemulsion.

Depending on surfactant concentration, there are four types of aggregates: micelle, microemulsion, liquid crystal and gel phases. Depending on the proportion of water, oil and the surfactant, there are three main types of aggregate structures: normal structure, in which the headgroups form the external surface; reverse structure, in which the hydrocarbon tails form the external surface; bicontinuous structures, in which both the hydrocarbon tails and the headgroups form the internal and external surface and lamellar phases (Figure 1-3).[79] Each

type of aggregate can accommodate various amounts of polar or non-polar solvent and therefore they can act as microreactors.

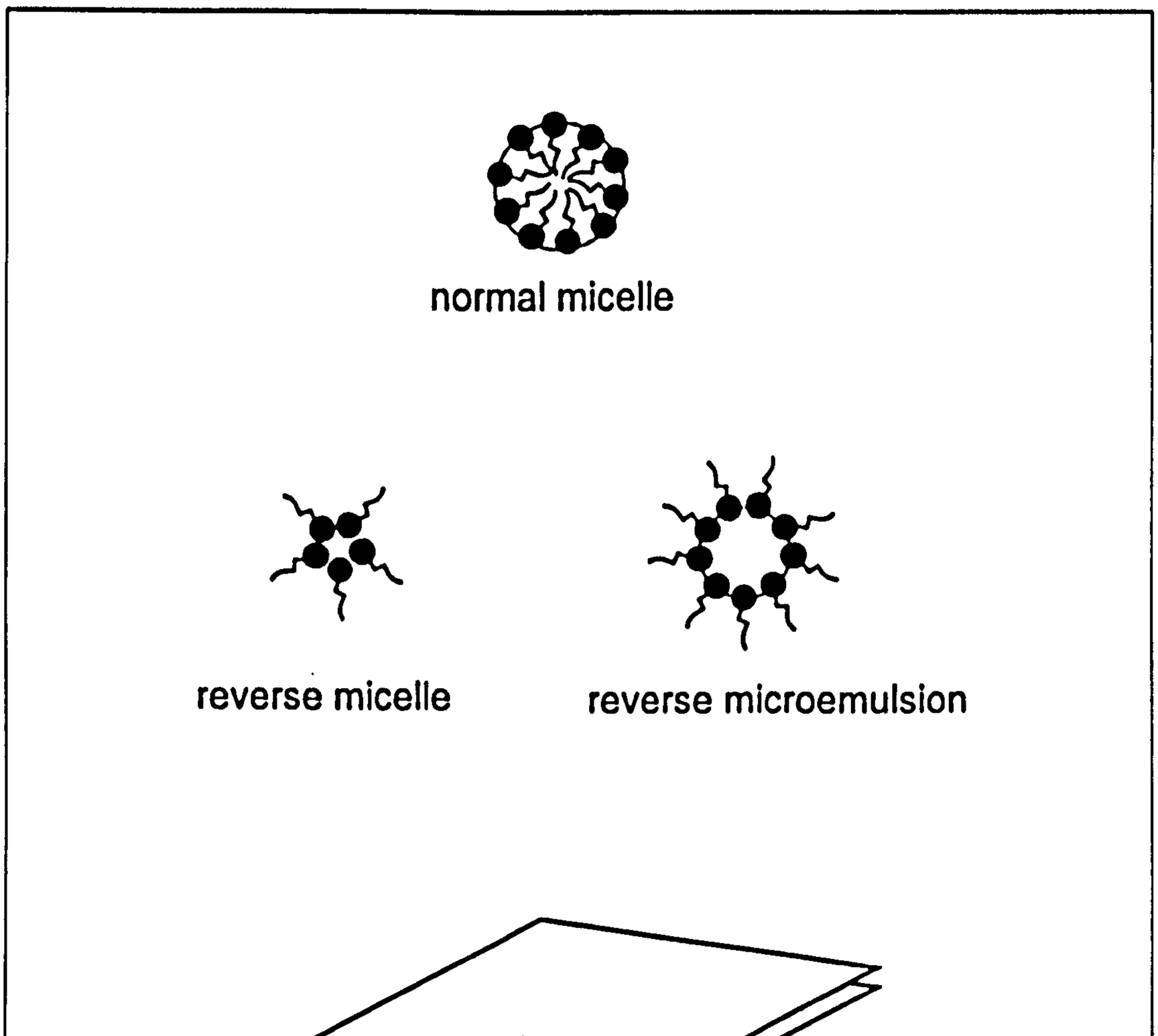

Figure 1-3 Normal, reverse and lamellar structures.

1.4.2 Reverse micelles and microemulsions

Cerrain surfactants, dissolved in organic solvents, may form small aggregates called reverse micelles, which can be formed both in the presence and absence of solubilized water. However, if the medium is completely free of water, the aggregates are very small and polydisperse. The presence of water is necessary to form a large surfactant aggregates called reverse microemulsion or water droplets. Water is readily solubilied in the polar core, forming a so called 'water pool', characterized by w, the water-surfactant molar ratio (w = [H_2O]/[Surfactant]). The water pool radius (R_w) is found to be linearly dependent on the water content. This can be explained by a geometrical model[80] assuming that the water droplets are monodisperse spheres: the volume and the surface of the sphere are respectively attributed to the volume of water molecules, V, and the surface occupied by the surfactant at the oil-water interface, $\sum$. This is supported by the fact that the area per surfactant molecule is constant and the all surfactant molecules are assumed to participate to the interface. From this model, the relationship found is:

$$R_w = \frac{3V}{\sum}$$

The volume of a water molecule (V_{aq}) is about 30 Å^3.

It can be deduced:

$$V = N \cdot V_{aq} \cdot [H_2O]$$

where N is the Avogadro number.

1.4.3 AOT reverse micelles and microemulsions

More than fifty years ago, Aerosol OT [sodium Bis(2–ethylhexyl)sulfosuccinate or as sodium dioctyl sulfosuccinate] (AOT) was recognized as forming reverse micelles in hydrocarbon oils. There aggregates take up considerable amounts of water without using any cosurfactants.[82] In general, microemulsions can exhibit different type of structures such as discrete spherical water droplets, interconnected bicontinuous water channels, interacting rods, etc. The simplest microstructure of water-AOT-oil is that of spherical water droplets of colloidal dimensions possessing a small degree of polydispersity. The droplet size can be accurately controlled by water content *w*. For the NaAOT-water-isooctane system, the water-pool radius follows the relation:

$$R_w = 1.5\ w\ (Å)^{[81]}$$

So as the size of the droplets increases, the concentration of discrete micelles decrease while the water content (*w*) increases. The maximum w value is ~60 for the NaAOT-water-isooctane system.[83] The water droplet concentration [RM] is the ratio of the AOT concentration over the aggregation number and, at a given water content *w*, is given by the following relation:

$$[RM] = 3\times10^3\ \phi_w / 4\ N\ \pi\ R_w^3$$

where N is the Avogadro number and ϕ_w is the polar volume fraction, that is the ratio of the volume of water over the total volume.

The molecular weight of sodium AOT is 444.5 and the linear length of the molecule is about 11 Å. The minimum cross-sectional area of the di-alkyl chain is 0.6 nm^2 and the area per sulphonate headgroup is 0.5 nm^2.[84,85] The AOT molecule has three chiral carbons: C1 adjacent to the head group, C4 and C4' (Figure 1-4). This implies the existence of eight optical isomers. Aggregation numbers of AOT typically range from 12 to 30 in apolar solvents.[2] The aggregation of 'dry' AOT has a large dependence on the hydrocarbon solvent used.[86] The mean aggregation numbers of AOT in isooctane is 15.[2] Dijk *et al.* have measured the low-frequency permittivity of AOT/water/isooctane microemulsion at the temperature range of 10° – 45°C and as a function of the concentration of water droplets. The results indicate that the droplet shapes are temperature independent.[87]

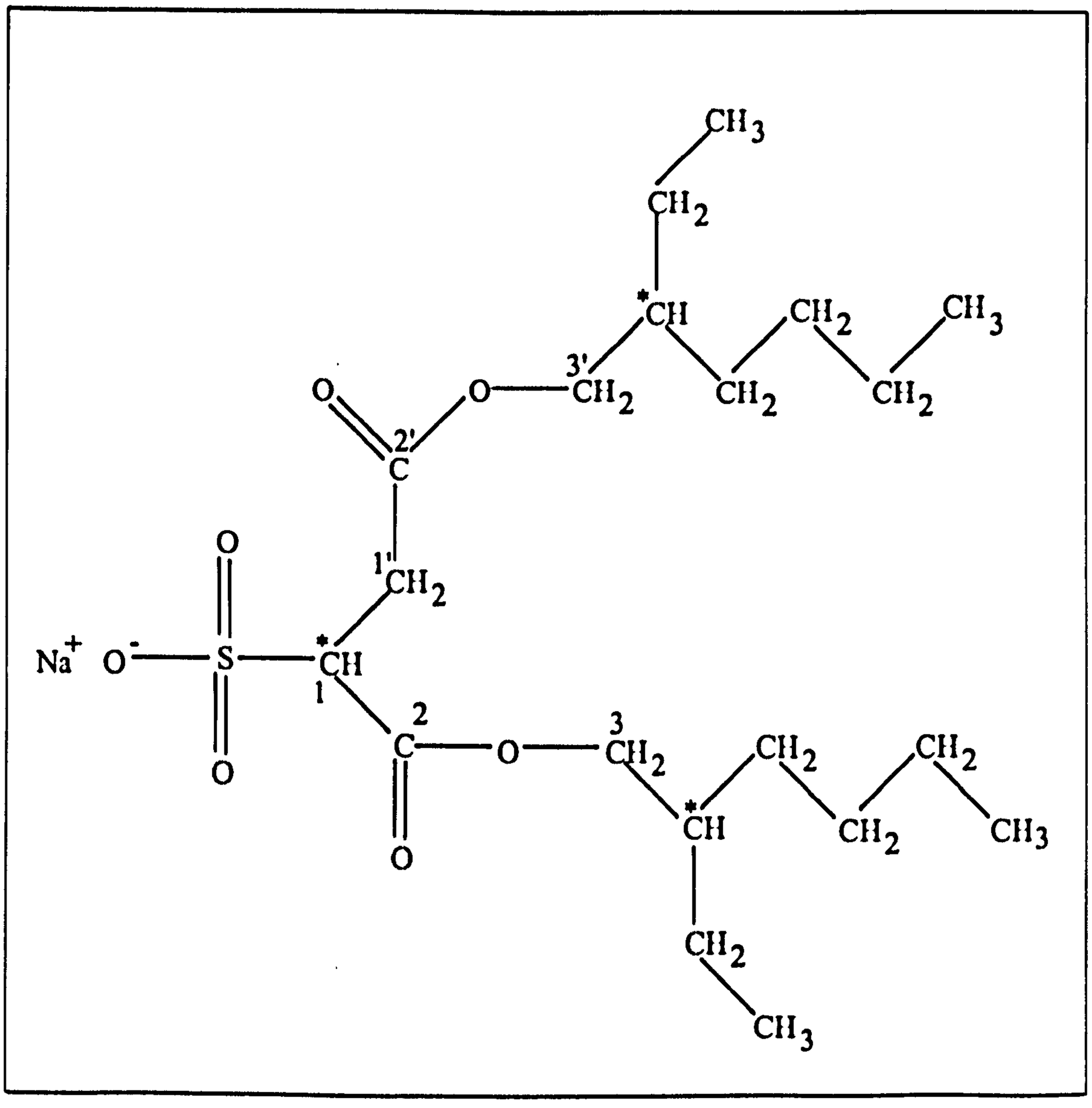

Figure 1-4 Chemical structure of sodium AOT. Symbols * show three chiral carbons.

A typical phase diagram for the water, NaAOT, isooctane (2,2,4-trimethylpentane) system is shown in Figure 1-5.[83,88] In this system the affinity of the surfactant for oil is greater than the affinity for water and reverse structures are preferred. The essential features are (i) that the reverse micelle and microemulsion region extends from the oil-rich corner, (ii) that the normal micelle region extends from the water-rich corner and (iii) that the liquid crystalline and gel region extends from the surfactant-rich corner. Where ternary phase diagrams differ is in the extent of the three phases and their degree of overlap. If all three phases overlap then a three phases region is formed. Since there are only three components, the maximum number of phases at any one composition is three at constant temperature and pressure.

In the diagram, a large two phase region is present, consisting of the normal micelle phase together with either the reverse microemulsion or liquid crystalline phase. The tie line AB is called a critical tie line, along which all the three phase occur. The AOT system, with its preference for reverse structures, is an example of a Winsor II system.[89] A Winsor I system is one in which the affinity of the surfactant for oil is less than the affinity for water and normal structures are preferred. A Winsor III system is one in which the affinity of the surfactant for oil is similar to the affinity for water and there is an almost equal preference for normal, reverse and bicontinuous structures.

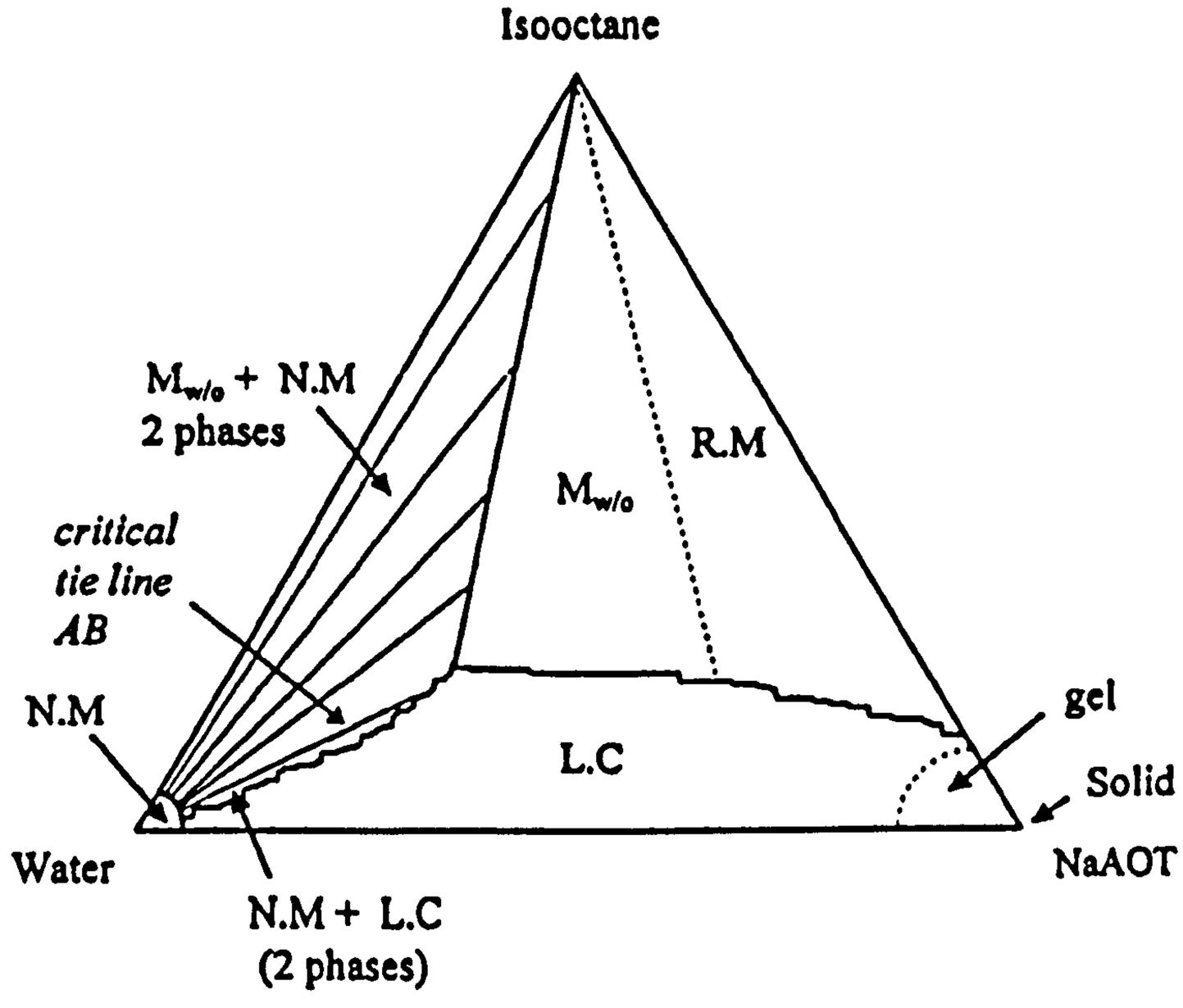

Figure 1-5 The ternary phase diagram for NaAOT-water-isooctane system at 20 C. $M_{w/o}$: water in oil microemulsion, R.M: reverse micelle, N.M: normal micelle, L.C: liquid crystal.

Changes in the nature of the counterions of the AOT reverse micelles perturb strongly the phase diagram of the system.[90] It is well known that below $w = 60$, NaAOT-water-isooctane form monodispersed water spherical droplets. Above this water content, a lamellar system is obtained. Using bimetallic derivatives, such as $Cu(AOT)_2$, $Co(AOT)_2$, $Cd(AOT)_2$ $Ca(AOT)_2$, and $Ba(AOT)_2$, the limit in

water solubilization drastically decreases, depending on the counterion and never reaches a value up to $w = 8$. Strong structural change was observed by increasing the water content. At low water content spherical droplets are observed. By increasing the water content, cylinder aggregates are formed.[90] At higher water content a phase transition is observed with two isotropic phases, with the lower phase containing mainly surfactant. By using mixed bimetallic AOT and NaAOT, finite aggregates are obtained, but the shapes of the reverse micelles are considerably deformed especially at low water content, the limit of the w value increases and spherical droplets are formed at high water content. Figure 1-6 shows the $Ba(AOT)_2$-water-isooctane system phase diagram.[79]

AOT has been used in a number of syntheses of inorganic nanosize materials such as silica,[9] silver,[10] copper,[16,91] platinum,[30] barium sulphate,[24] cobalt,[25] *et al.* The principal reason for using AOT reverse micelles and microemulsion droplets in the preparation of ultrafine particles is that this method is powerful for controlling particle size and the corresponding size distribution, although the principle is not yet clear.

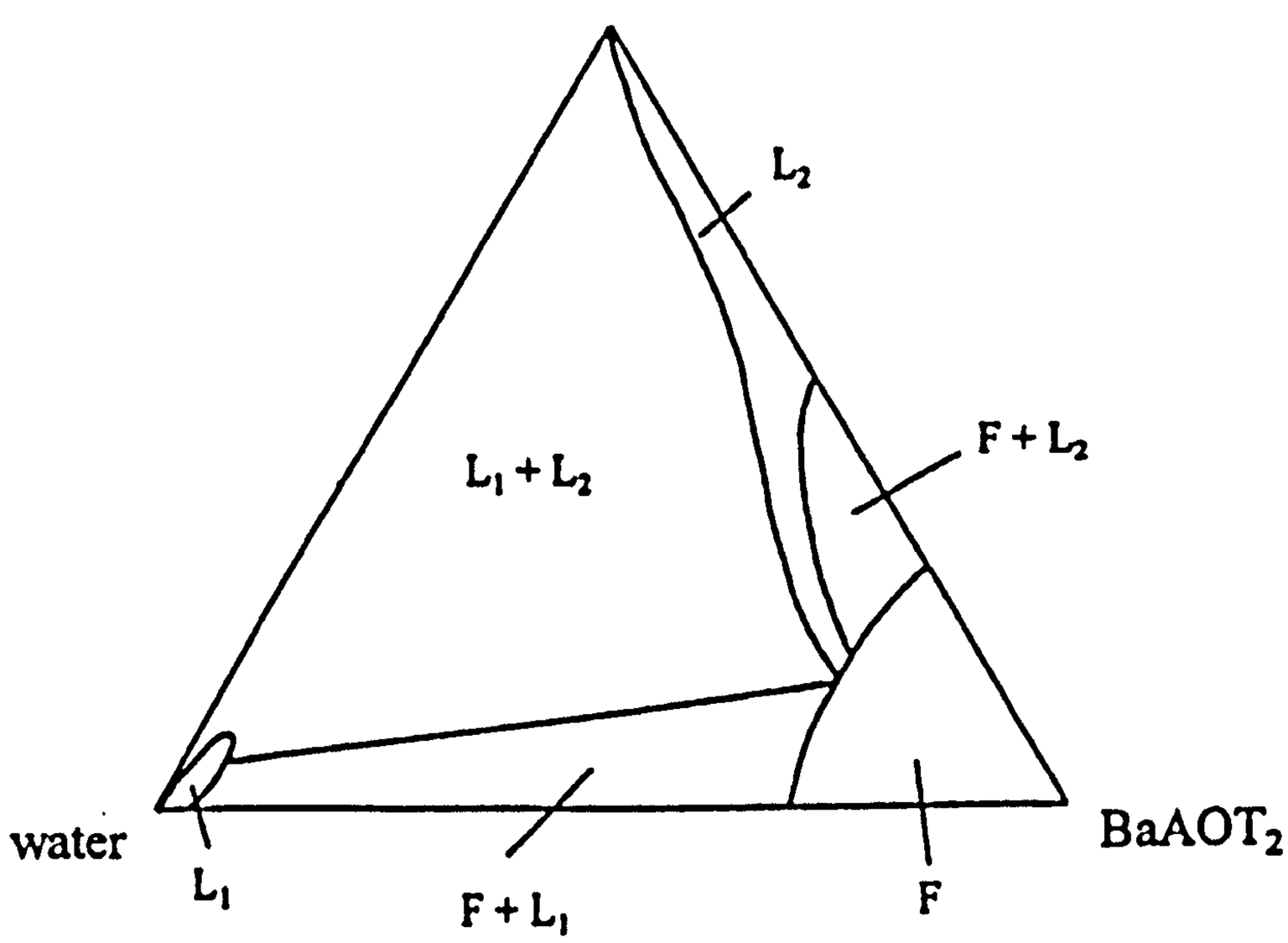

Figure 1-6 The ternary phase diagram for $BaAOT_2$-water-isooctane system. F: reverse hexagonal liquid crystal phase; L_1: transparent phase as being pre- or dilute micellar; L_2: reverse micelle phase.

1.5 Kinetics of the formation of nanoparticles in reverse micelles and microemulsions

Microemulsions are used as microreactors because they can exchange the content of their water pools by a collision process. The rate of communication between droplets is very fast,[92] and it is assumed that this exchange can only take place following an energetic collision between two droplets, forming a 'transient droplet dimer'.[93] This process is energetically unfavourable because it implies a change in the curvature of the surfactant film.[93] Therefore, the rate constant of this process is not diffusion-controlled, and only a very small fraction of the total collisions (1 in 1000 for AOT surfactant films) between droplets leads to reactant exchange.[92] In most cases droplet communication is the rate-determining step in particle formation.[94]

It is generally accepted that material exchange between droplets, which leads to particle formation takes place via the formation of intermediate dimeric droplet aggregates. Dimers, which allow free passage of the solubilised species, were proposed for the first time by Fletcher et al.[95] For AOT-stabilised water-in-oil microemulsions exchange of solubilisate between the water pools of the microemulsion droplets occurs with a second order rate constant of 10^6-10^8 $dm^3mol^{-1}s^{-1}$, in other words two to four orders of magnitude slower than the droplet encounter rate as predicted by simple diffusion theory; this indicates that

successful fusion events take place only in 0.01-1% of binary droplet collisions.[95,96] Collision between two droplets results in the formation of short-lived droplet clusters that dissociate in two isolated droplets (Figure 1-7).

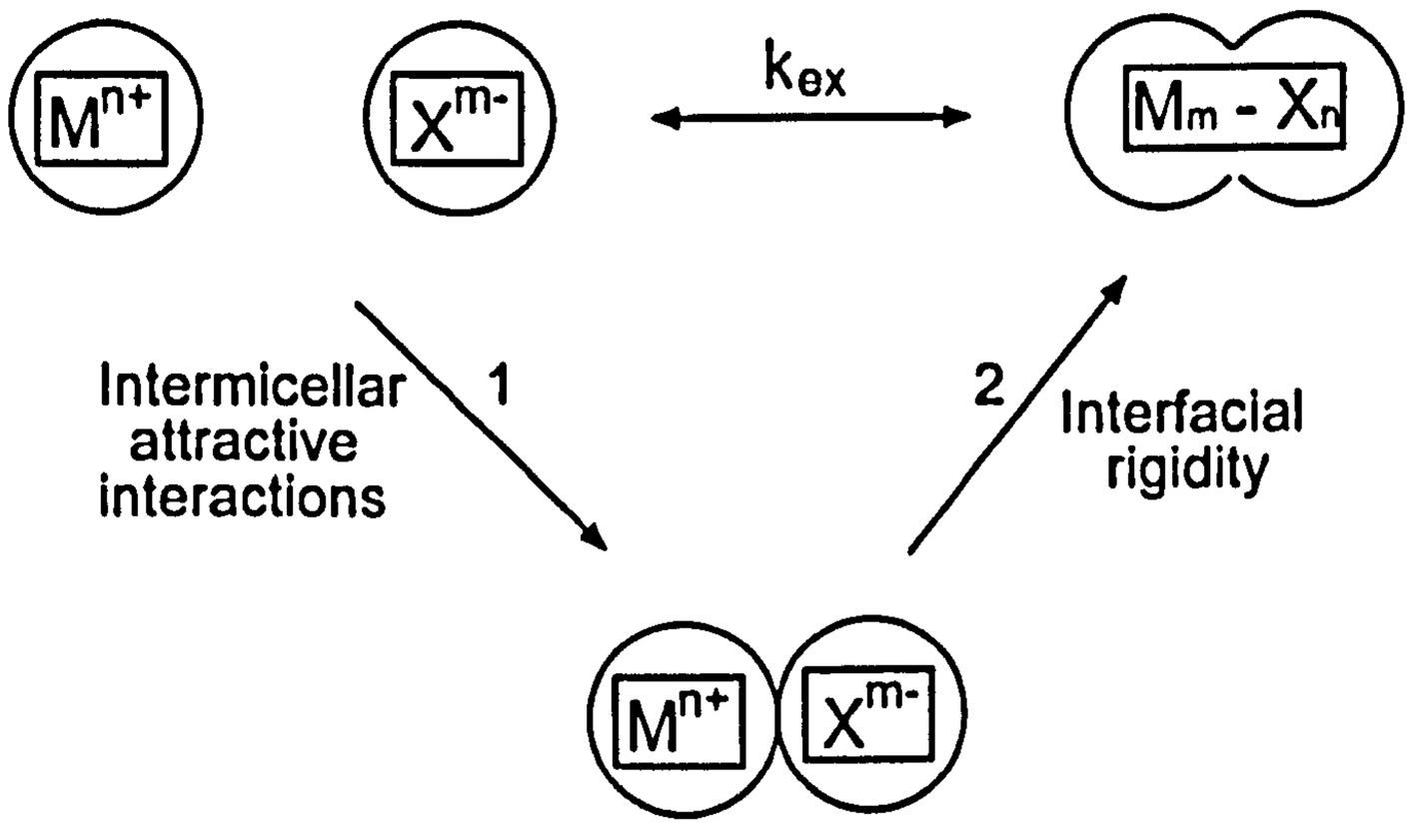

Figure 1-7 Schematic representation of the intermicellar exchange process. 1, collision between reverse micelles; 2, opening of the interfacial layer.

The intermicellar exchange process can be expressed as the sum of two equilibria: (i) the formation of a dimer made of two micelles in contact; (ii) the water pool micellar exchange. The first equilibrium is related to the attractive interactions between droplets whereas the second one is associated to the interface rigidity. The intermicellar exchange rate constant k_{ex} can be expressed as

$$k_{ex} = C_0 k_1 k_2$$

Where the k_1 and k_2 are the probabilities if collision of two micelles and of the interface opening when two micelles are in contact, respectively. The constant C_0 includes all the other processes (in particular, the details of the kinetic processes). The rate constant k_1 is related to the intermicellar structure, and k_2 is related to the dynamical properties of the water-surfactant-oil interface that are related to the bending elastic modulus of the interface. The intermicellar exchange rate constant decreases with water volume fraction. This effect is linked to the variation of the intermicellar interaction potential. The attractive interactions govern the decrease of the exchange process with the increase in the number of droplets. The interfacial rigidity decreases with increasing water volume fraction. Furthermore, surfactant monolayer rigidity decreases with increasing the number of droplets.

Tojo *et al.*[97] have studied the kinetics of the formation of nanoparticles in microemulsions by Monte Carlo computer simulation. It is observed that nanoparticle formation in microemulsions occurs in three different steps (nucleation, growth by autocatalysis and growth by ripening), which can or cannot overlap depending mainly on concentration. The compartmentalization of the reactants induces a separation of the nucleation and growth processes, which can be clearly observed when the concentration of reactants is relatively high, the growth by ripening and growth by autocatalysis over an existing nucleus appear

on different time scales at high concentrations. On the contrary, the time scale of both growth processes overlap when the concentration is low. The surfactant film flexibility affects the kinetics of the reaction as rigid films can be associated with a slow interdroplet communication rate, when the interdroplet communication is the rate-determining step in particle formation in microemulsions.

1.6 References

[1] Brus, L.E., *J. Phys. Chem.*, **90**, 2555 (1986).

[2] De, T.K., Maitra, A., *Adv. Colloid Interface Sci.*, **59**, 95 (1995).

[3] Fox, M.A., *Top. Curr. Chem.*, **142**, 72 (1989).

[4] Brus, L.E., *J. Chem. Phys.*, **80**, 4403 (1984).

[5] Wang, Y., *Acc. Chem. Res.*, **26**, 133 (1991).

[6] Serpone, N., Sharmr, D.K., Jamieson, M.A., Gratzel, M., Ramsden, J.J., *Chem. Phys. Lett.*, **115**, 473 (1985).

[7] Boutonnet, M., Kizling, J., Stenius, P., Maire, G., *Colloids Surf.*, **5**, 209 (1982).

[8] Arriagada, F.J., Osseo-Asare, K., *J. Colloid Interface Sci.*, **211**, 210 (1999).

[9] Arriagada, F.J., Osseo-Asare, K., *J. Colloid Interface Sci.*, **170**, 8 (1995).

[10] Taleb, A., Petit, C., Pileni, M.P., *Chem. Mater.*, **9**, 950 (1997).

[11] Petit, C., Lixon, P., Pileni, M.P., *J. Phys. Chem.*, **97**, 12974 (1993).

[12] Taleb, A., Petit, C., Pileni, M.P., *J. Phys. Chem. B*, **102**, 2214 (1998).

[13] Lisiecki, I., Pileni, M.P., *J. Phys. Chem.*, **99**, 5077 (1995).

[14] Tanori, J., Pileni, M.P., *Adv. Mater.*, **7**, 862 (1995).

[15] Pileni, M.P., Gulik-Krzywicki, T., Tanori, J., Filankembo, A., Dedieu, J.C., *Langmuir*, **14**, 7359 (1998).

[16] Tanori, J., Pileni, M.P., *Langmuir*, **13**, 639 (1997).

[17] Pileni, M.P., Tanori, J., Filankembo, A., *Colloid and Surfaces A*, **123**, 561 (1997).

[18] Haram, S.K., Mahadeshwar, A.R., Dixit, S. G., *J. Phys. Chem.*, **100**, 5868 (1996).

[19] Petit,C., Pileni, M.P., *J. Phys. Chem.*, **92**, 2282 (1988).

[20] Motte, L., Billoudet, F., Lacaze, E., Pileni, M.P., *Adv. Mater.*, **8**, 1018 (1996).

[21] Motte, L., Billoudet, F., Pileni, M.P., *J. Phys. Chem.*, **99**, 16425 (1995).

[22] Motte, L., Billoudet, F., Lacaze, E., Douin, J., Pileni, M.P., *J. Phys. Chem. B*, **101**, 138 (1997).

[23] Li, M., Schnablegger, H., Mann, S., *Nature*, **402**, 393 (1999).

[24] Hopwood, J., Mann, S., *Chem. Mater.*, **9**, 1819 (1997).

[25] Petit, C., Taleb, A., Pileni, M.P., *Adv. Mater.*, **10**, 259 (1998).

[26] Bagwe, R.P., Khilar, K.C., *Langmuir*, **13**, 6432 (1997).

[27] Levy, L., Hochepied, J.F., Pileni, M.P., *J. Phys. Chem.*, **100**, 18322 (1996).

[28] Cizeron,J., Pileni, M.P., *J. Phys. Chem.*, **99**, 17410 (1995).

[29] Ahmadi, T.S., Wang, Z.L., Henglein, A., Ei-Sayed, M.A., *Chem. Mater.*, **8**, 1161 (1996).

[30] Ahmadi, T.S., Wang, Z.L., Green, T.C., Henglein, A., Ei-Sayed, M.A., *Science*, **272**, 1924 (1996).

[31] Badia, A., Gao, W., Singh, S., Demers, L., Cuccia, L., Reven, L., *Langmuir*, **12**, 1262 (1996).

[32] Rees, G. D., Evans-Gowing, R., Hammond, S. J., Robinson, B. H., *Langmuir*, **15**, 1993 (1999).

[33] Lianos, P., Thomas, J.K., *Chem. Phys. Lett.*, **125**, 299 (1986).

[34] Petit, C., Lixon, P., Pileni, M.P., *J. Phys. Chem.*, 94, 4734 (1990).

[35] Petit, C., Lixon, P., Pileni, M.P., *J. Phys. Chem.*, 94, 1598 (1990).

[36] Globe,M., Kanino, K., Kandori, K., Kitahara, A., *J. Colloid Interface Sci.*, **93**, 293 (1983).

[37] Lisiecki, I., Pileni, M.P., *J. Am. Chem. Soc.*, **115**, 3887 (1993).

[38] Hou, M.J., Shah, D.O., *Interfacial Phenomena Biotechnology and Material Processing*, 443 (1988).

[39] Steigerwald, M.L., Alivisatos, A.P., Gibson, J.M., Harris, T.D., Kortan, R., Muller, A.J., Thayen, A.M., Duncan, T.M., Doughlass, D.C., Brus, L.E., *J. Amer. Chem. Soc.*, **110**, 3046 (1988).

[40] Lianos, P., Thomas, J.K., *J. Colloid Interface Sci.*, **117**, 505 (1987).

[41] Motte, L., Lebrun, A., Pileni, M.P., *Prog. Colloid Interface Sci.*, 89, 99 (1992).

[42] Hirai, T., Sato, H., Komasawa, I., *Ind. Eng. Chem. Res.*, 33(12), 3262 (1994).

[43] Kandori, K., Kazama, A., Kon-no, K., Kitahara, A., *Bull. Chem. Soc. Jpn.*, **57**, 1797 (1984).

[44] Kandori, K., Kon-no, K., Kitahara, A., *Bull. Chem. Soc. Jpn.*, **57**, 3419 (1984).

[45] Bandow, S., Kimura, K., Kon-no, K., Kitahara, A., *Jpn. J. Appl. Phys.*, **26**, 713 (1987).

[46] Chen, J.P., Lee, K.M., Sorensen, C.M., Klabunde, K.J., Hadjipanayas, G.C., *J. Appl. Phys.*, **75**, 5876 (1994).

[47] Pileni, M.P., Lisiecki, I., *Colloids Surf. A.*, 80(1), 63 (1993).

[48] Lisiecki, I., Boulanger, L., Lixon, P., Pileni, M.P., *Prog. Colloid Polym. Sci.*, **89**, 103 (1992).

[49] Arriagada, F.J., Osseo-Asare, K., *J. Disper. Sci. Tecchnol.*, **15**(1), 59 (1994).

[50] Cho, S.H., Ko, M.H., Doh, J.B., Won, C.H., Kang, Y., Chun, B.S., *Taehen Kumsok Hakhoechi*, **32**(1), 7 (1994).

[51] Shin, K.S., Cho, S.H., Kang, Y., Won, C.H., Chun, B.S., *Taehen Kumsok Hakhoechi*, **31**(11), 1367 (1993).

[52] Hirai, T., Sato, H., Komasawa, I., *J. Am. Chem. Soc.*, **32**, 3014 (1993).

[53] Sager W.F.C., *Current Opinion in Colloid & Interface Science*, **3**, 276 (1998).

[54] Walsh, D., Mann, S., *Nature*, **377**, 320 (1995).

[55] Leff, D.V., Ohara, P.C., Heath, J.R., Gelbart, W.M., *Curr. Opinion Colloid Interface Sci.*, **2**, 177 (1997).

[56] Lopez, Perez J.A., Lopez, Quintela M.A., Mira, J., Rivas, J., Charles, S.W., *J. Phys. Chem. B*, **101**, 8045 (1997).

[57] Hostetler, M.J., Murray, R.W., *Curr. Opinion Colloid Interface Sci.*, **2**, 42 (1997).

[58] Fendler, J.H., *Curr. Opinion Colloid Interface Sci.*, **2**, 365-369 (1997).

[59] Pileni, M.P., Motte, L., Billoudet, F., Mahrt, J., Willig, F., *Mater. Lett.*, **31**, 255 (1997).

[60] Tanori, J., Gulik-Krzywicki, T., Pileni, M.P., *Langmuir*, **13**, 632 (1997).

[61] Rees, G.D.; Evans-Gowing, R.; Hammond, S.J.; Robinson, B.H., *Langmuir*, **15**, 1993 (1999).

[62] Qi, L.; Ma, J.; Cheng, H.; Zhao, Z., *J. Phys. Chem. B*, 1997, **101**, 3460.

[63] Whetten, R.L., Khoury, J.T., Alvarez, M.M., Murthy, S., Vezmar, I., Wang, Z.L., Cleveland, C.C., Luedtke, W.D., Landman, U., *Adv. Mater.*, 8, 428 (1996).

[64] Mirkin C.A., Letsinger R.L., Mucic R.C., Storhoff J.J., *Nature*, **382**, 607 (1996).

[65] Alivisatos A.P., Johnsson K.P., Peng X., Wilson T.E., Loweth C.J., Bruchez Jr M.P., Schultz P.G., *Nature*, **382**, 609 (1996).

[66] Elghanian, R., Storhoff, J.J., Mucic, R.C., Letsinger, R.L., Mirkin, C.A., *Science*, **277**, 1078 (1997).

[67] Shenton W., Pum D., Sleylr U.B., Mann S., *Nature*, **389**, 585 (1997).

[68] Andres R.P., Bielefeld J.D., Henderson J.I., Janes D.B., Kolagunta V.R., Kubiak C.P., Mahoney W.J., Osifchin R.G., *Science*, **273**, 1690 (1996).

[69] Korgel B.A., Fitzmaurice D., *Adv. Mater.*, **10**, 661 (1998).

[70] Mann, S., Davis, S.A., Hall, S.R., Li, M., Rhodes, K.H., Shenton, W., Vaucher, S., Zhang, B., *J. Chem. Soc., Dalton Trans*, 3753 (2000).

[71] Shenton, W., Davis, S.A., Mann, S., *Adv. Mater.*, **11**, 449 (1999).

[72] Hall, S.R., Shenton, W., Engelhardt, H., Mann, S., *Angew. Chem.*, 2001, in press.

[73] Murray, C.B., Kagan, C.R., Bawendi, M.G., *Science*, **270**, 1335 (1995).

[74] Hhrfenist S.A., Wang Z.L., Alvarez M.M., Vezmar I., Whetten R.L., *Adv. Mater.*, **9**, 817 (1997).

[75] Paul, B.K., Moulik, S.P., *J. Dispersion Science and Technology*, **18(4)**, 301 (1997).

[76] Hoar, T.P., Schulman, J.H., *Nature*, **152**, 102 (1943).

[77] Cooke, C.E., Schulman, J.H., *Surface Chemistry*, Munksgaard, Copenhagen, p231 (1965).

[78] Mitchell, D.J., Ninham, B.W., *J. Chem. Soc. Farad T.*, **77**, 601 (1981).

[79] Hopwood, J. D. Barium Sulfate Crystallisation in Synthetic and Biological systems, *University of Bath*, Ph.D. Thesis, 1996.

[80] Pileni, M.P., Zemb, T., Petit, C., *Chem. Phys. Lett.*, **118**, 414 (1985).

[81] Pileni, M.P., *Advances in Colloid and Interface Science*, **46**, 139 (1993).

[82] Matton, R.W., Mathews, M.B., *J. Chem. Phys.*, **17**, 496 (1949).

[83] Tamamushi, B., Watanabe, N., *Colloid and Polymer Science*, **258**, 174 (1980).

[84] Tamamushi, B., Watanabe, N., *Colloid and Polymer Science*, **258**, 174 (1980).

[85] Oakenfull, D., *Journal of the Chemical Society, Faraday Transactions I*, **76**, 1875 (1980).

[86] Eicke, H.F., *Top. Curr. Chem.*, **87**, 85 (1980).

[87] Dijk, M.A.V., Joosten, J.G.H., Levine, Y.K., Bedeaux, D., *J. Phys. Chem.*, 93, 2506 (1989).

[88] Eicke, H.F., Rehak, J., *Helvetica Chimica Acta*, 59, 2883 (1976).

[89] Robinson, B.H., *Chemistry in Britain*, 26, 342 (1990).

[90] Petit, C., Lixon, P., Pileni, M.P., *Langmuir*, 7, 2620 (1991).

[91] Lisiecki I., Björling M., Motte L., Ninham B., Pileni M.P., *Langmiur*, 11, 2385 (1995)

[92] Fletcher, P.D.I., Robinson, B.H., Bermejo-Barrera, F., Oakenfull, D.G., In *Microemulsions*; Robb, I.D., Ed.; Plenum Press: New York, p221 (1982).

[93] Zana,R., Lang, J., In *Microemulsions; Structure and Dynamics*; Frieberg, S.E., Bothorel, P., Eds.; CRC Press: Boca Raton, FL, p153 (1987).

[94] Towey, T.F., Khan-Lodhi, A., Robinson, B.H., *J. Chem. Soc., Faraday Trans*, 86, 3757 (1990).

[95] Fletcher, P.D.I., Howe, A.M., Robinson, B.H., *J. Chem. Soc. Faraday Trans*, 83(1), 985 (1987).

[96] Jain, T.K., Casin, G., Badiali, J.P., Pileni, M.P., *Langmuir*, 12, 2408 (1996).

[97] Tojo, C., Blanco, M.C., Rivadulla, F., Lopez-Quintela, M.A., *Langmuir*, 13, 1970 (1997).

Chapter 2

Experimental methods

2.1 Materials

The chemicals used in all experiments were analytical grade and were used without further purification. The lists will be given in the experimental sections of each chapter.

2.2 Chemical methods

The chemical methods will be given in the sections of each chapter; methods for preparation of the samples were different in each chapter.

2.3 Physical methods

Only general information about the physical methods used throughout the thesis is given in this chapter.

2.3.1 Transmission Electron Microscopy (TEM)

Transmission electron microscopy (TEM) analysis was performed in bright field mode using either a JEOL 2000 FX high-resolution electron microscope operating at 200 keV or a JEOL 1200 EX electron microscope operating at 120 keV.

Standard tungsten filaments were used. Images were recorded on KODAK Electron Image Film SO-163 producing very high resolution negatives and processed using a recommended KODAK solution. Samples for transmission electron microscopy (TEM) were deposited onto Formvar-coated, carbon-reinforced, 3 mm diameter, copper electron microscope grids. After air drying, the grids were washed with either pure solvent or water dependent on the samples.

2.3.2 Selected Area Electron Diffraction (SAED)

Selected area electron diffraction (SAED) was used to determine whether the materials synthesized were crystalline, polycrystalline or amorphous, and to identify the crystallographic system and orientation of the crystal with respect to the electron beam.

The d-spacing was measured from the diffraction pattern for each spot or rings using the formula:

$$d = \frac{2\lambda L_{mm}}{D_{mm}}$$

where λ is the relativistic wavelength of the electron beam, equal to 0.0251 Å at 200 keV and 0.0334 Å at 120 keV, respectively, L_{mm} is the camera length in

millimetres and D_{mm} is the distance in millimetres between reflections on opposite sides of the central spot or the diameter of diffraction rings.

2.3.3 Energy Dispersive X-ray Analysis (EDXA)

Energy Dispersive X-ray Analysis provided a qualitative and semi-quantitative elemental analysis of materials being imaged on the TEM screen. Analysis was carried out using either a JEOL 2000FX transmission electron microscope equipped with a Link lithium-drifted silicon-type EDXA detector, or a JEOL 1200EX linked with an OXFORD INSTRUMENTS-X-Ray Analysis ISIS300 system equipped with a silicon detector and a beryllium window, allowing for semi-quantitative analysis of elements of atomic number greater than sodium.

2.3.4 Scanning electron microscopy (SEM)

SEM was carried out with a JEOL JSM 5600LV high vacuum and partial vacuum (10 Pa-10^{-4} Pa) scanning electron microscope with secondary electron detector based on the scintillator-photomultiplier design of Everhard and Thornley (1960). Also fitted was a solid state backscattered electron detector for compositional and topographical information. This was operated at accelerating voltages between 1 – 30 keV. Images were stored digitally or on film.

Samples for SEM were mounted onto circular carbon adhesive pads attached to aluminum stubs. Samples were air-dried and gold-coated with an Edwards S150B sputter-coater or left uncoated.

2.3.5 X-ray diffraction (XRD)

Powder X-ray diffraction measurements were performed using a Philips PW 1710 diffractometer with Cu Kα radiation. Scan angle (2θ) was over a range of 4 to 60 degrees. X-rays were produced with a 4KW generator on a 2KW copper anode target tube. Two wavelengths were produced α_1 = 1.54060 Å and α_2 = 1.54439 Å. The intensity of α_1 was twice that of α_2. The interplanar d-spacings corresponding to each peak were calculated using the Bragg equation:

$$d = \frac{n\lambda}{2\sin\theta}$$

where n is the diffraction order (equal to 1), λ is the Cu Kα wavelength in Å (equal to half of the scan angle).

2.3.6 Small-angle X-ray scattering (SAXS)

Small-angle X-ray scattering measurements were carried out at the Max-Planck-Institut of Colloids and Interfaces (Germany). The data were obtained from a

Kratky compact camera system that was equipped with a stepping motor and a counting tube with an impulse-height discriminator. The light source was a conventional X-ray tube with fixed copper target operating at 40 mA and 30 kV. Small-angle X-ray scattering analysis was also performed using an Enraf Nonius X-ray generator.

2.3.7 Dynamic light-scattering (DLS)

A. Dynamic light-scattering measurements were carried out at the Max-Planck-Institut of Colloids and Interfaces (Germany). The experiments were performed using either a laboratory-built goniometer with temperature control (±0.05K), an attached single-photon detector ALV/SO-SIPD and a multiple-tau digital correlator ALV5000/FAST from the company ALV in Langen/Germany. The light source was an INNOVA 300 argon-ion laser operated at 488.0 nm wavelength in single-frequency mode and powered at approximately 500 mW, or an ALV-5000 multiple-tau correlator (ALV-Laser GmbH, Langen) that allows for simultaneous dynamic (time-dependent) and static (angle-dependent) acquisition of light intensities. The light source was a continuous-wave frequency doubled Nd-YAG laser (coherent-Adlas) operating at 532 nm wavelength.

The sample cell was temperature controlled (±0.05K) (Hellma, MÜllheim/Germany) and charged with 1 ml of solution. The samples were centrifuged for 5 min at 5000 rpm before measurement and put into the

thermostated sample holder. The correlation functions were recorded immediately afterwards in periods of 120 seconds.

B. Another series of experiments were carried out in the University of Bristol with a Malvern Autosizer 4700 operating at 532 nm and 90° detector angle. Particle sizes were reported in diameter contribution. Prior to measurement all samples were filtered through a 0.2 μm membrane.

2.3.8 Thermogravimetric analysis (TGA)

Thermogravimetric analysis was performed with Simultaneous Thermal Analysis STA409EP. The experiments were typically run on powdered samples at 20 - 800°C at 5°C/min under flowing nitrogen.

2.3.9 Fourier Transform Infrared spectroscopy (FTIR)

Fourier Transform Infrared analysis was performed with a BRUKER IFS25, PERKIN ELMER Spectrum One or a Perkin Elmer Spectrum RX spectrophotometers. The spectra were recorded from 4000-200 cm^{-1} using KBr discs or liquid cells.

2.3.10 Ultraviolet and visible spectroscopy (UV-vis)

UV-vis measurements were carried out with a PERKIN ELMER Lambda II UV-VIS spectrometer equipped with Perkin Elmer UV Winlab (Version 1.1) computer software. The spectra were recorded from 200-800 nm.

UV-vis was also used to measure the turbidity (τ) of the solutions. The turbidity as a function of time was determined by monitoring the change of the optical transmission ($T = I / I_o$) with time at 600 nm. The turbidity was calculated from

$$\tau = \frac{-\ln(T)}{l}$$

where l was the cell length (equal to 1.0 cm).

UV-vis was also used for quantitative analysis of protein concentrations at 562 nm.

2.3.11 Mass spectrometry (MS)

The measurements were run by Service staff in the University of Bristol. The experiments were carried out with a MICROMASS AUTOSPEC mass spectrometer operating at 30 keV. The Fast Atom Bombardment (FAB+ and FAB–) ionization technique was used for high molecular weight compounds.

2.3.12 Sodium dodecylsulfate – polyacrylamide gel electrophoresis (SDS-PAGE)

Sodium dodecyl sulfate (SDS)-polyacrylamide gel electrophoresis was undertaken on protein solutions containing 0.125M Tris buffer (pH 6.8), 4% SDS, 20% glycerol, 10% 2-mercaptoethanol and 0.0004% bromophenol blue. The samples were loaded onto a 3% stacking gel (3% acrylamide, 0.125M Tris pH 6.8, 0.1% TEMED [N,N,N',N'-tetramethylethylenediamine], 0.05% ammonium persulphate) with a 7.5% separating gel (7.5% acrylamide/bisacrylamide, 0.375 M Tris pH 8.8, 0.1% SDS, 0.1% TEMED, 0.05% ammonium persulphate) and run at 120V for 4 hours with conventional cathode to anode polarity. The gel was stained with Coomassie brilliant blue R250 (0.25% in water/methanol/glacial acetic acid = 5:5:1 v/v) for 30 minutes and then destained with a mixture of water/methanol/glacial acetic acid at 6.5:2.5:1 (v/v) for 12 hours.

Chapter 3

Synthesis and self-assembly of nanoparticle chains, superlattices and filaments in complex fluids

(Published in *Nature*, 402, 393-395, 1999)

3.1 Introduction

Research has successfully fabricated self- assembled nanocrystal superlattices or nanocrystal arrays of metal, semiconductor and inorganic particles. There are new forms of material of fundamental interest and technological importance. There are four key steps to developing these materials: (i) controlled preparation of size and shape selected nanoparticles, (ii) control of the self-assembly process to produce large well-ordered nanocrystal superlattices, (iii) structural characterization, and (iv) modeling the dynamic behavior of the system.[1] Size controlled preparation of nanoparticles has been achieved by many methods such as water content of reverse micelles,[2] size selectivity.[3-5] However, the shape-controlled preparation of nanoparticles is general more difficult. Most nanoparticles have been synthesised in spherical shape and only a few examples were successfully controlled in a different shape. One example was reported by Ahmadi *et al* [6] who successfully controlled platinum nanoparticles in tetrahedral, cubic, irregular-prismatic, icosahedral and cubo-octahedral shapes by changing the ratio of the concentration of the capping polymer material to the concentration of the platinum. Another one used electrochemical methods to prepare Au nanorods.[7]

Self-assembled arrays involve self-organization of size selected nanoclusters encapsulated in protective compact organic coating into monolayers, thin films, and superlattices. A key step in this process is the fabrication of size and shape

controlled nanocrystal arrays that have the potential to grow large enough for technological applications. Colloidal chemistry, or soft chemistry, has played a powerful role in this process. Self-organization of nanoparticles is a new route to the synthesis of superlattice materials–solid, periodic arrays built using nanocrystals as building blocks, achieved by preparing size and shape–selected nanocrystals using colloid chemistry and then using self-assembly as a means of joining them together. Methods for assembling nanoparticle superstructures generally rely on preformed spherical nanoparticles and external processing, such as solvent evaporation,[8-9] molecular cross-linking,[10-15] or template-patterning.[16-19] The dynamical behavior of complex fluids suggests that these superstructures might be directly accessible through instability thresholds induced by *in situ* chemical reactions.

Reverse micelles and microemulsions have been used extensively as confined media for the preparation of discrete inorganic nanoparticles.[20-22] Because these reactions are spatially constrained but interfacially active, it should be possible to synergistically couple nanoparticle synthesis and self-assembly over a range of length scales to produce materials with complex organization.

Here we demonstrate shape- and size-controlled synthesis of barium chromate nanocrystals in the presence of anionic surfactant AOT water-in-oil reverse micelles or microemulsion droplets and organization of the nanoparticles into unusual linear aggregated structures in solution-phase and subsequently

spontaneous self-assembly into two-dimensional superlattices in one step. The morphology of barium chromate nanoparticles synthesized in AOT reverse micelles or microemulsion droplets was controlled by changing the molar ratio of two reactants (Ba^{2+}/CrO_4^{2-}) in the microreactor of AOT water-in-oil microemulsions under the conditions investigated. Prismatic, long filament and spherical shapes of $BaCrO_4$ nanoparticles can be controlled by reaction stoichiometry. $BaCrO_4$ prismatic nanoparticles and self-assembled chains and rectangular superlattices were formed specifically at molar equivalence ($1 : 1.4 \leq [Ba^{2+}] : [CrO_4^{2-}] \leq 1.4 : 1$). Under identical conditions, but with an excess of Ba^{2+} ($2.7 : 1 \leq [Ba^{2+}] : [CrO_4^{2-}] \leq 5.5 : 1$), $BaCrO_4$ high aspect ratio filaments were formed. With a molar excess of CrO_4^{2-} ($1 : 4.6 \leq [Ba^{2+}] : [CrO_4^{2-}] \leq 1 : 2.7$), the colloidal suspension consisted of cuboidal and spherical $BaCrO_4$ nanocrystals. The size of the prismatic nanoparticles can be controlled by the water content of the AOT reverse microemulsions. The chains and superlattices consist of ordered arrays of prismatic $BaCrO_4$ nanoparticles held together by the interdigitation of bilayer surfactant molecules on specific crystal faces. Our results indicate that chemical control of reactions in complex fluids can have a profound influence on the emergence of self-assembled nanostructures.

3.2 Materials and Experiments

3.2.1 Materials

3.2.1.1 Chemical list

All the materials were of analytical grade and used without further purification.

Table 3-1 Chemicals used in this chapter

Common name	Chemical name	Formula	Molecular weight	Supplier
	sodium chromate	Na_2CrO_4	162.0	Aldrich
	barium chloride	$BaCl_2$	208.2	Aldrich
NaAOT	sodium bis(2-ethylhexyl) sulphosuccinate	$C_{20}H_{37}O_4SO_3Na$	444.5	BDH
isooctane	2,2,4-trimethyl pentane	C_8H_{18}	114.0	Aldrich

3.2.1.2 Synthesis of Barium bis(2-ethylhexyl) sulfosuccinate [$Ba(AOT)_2$]

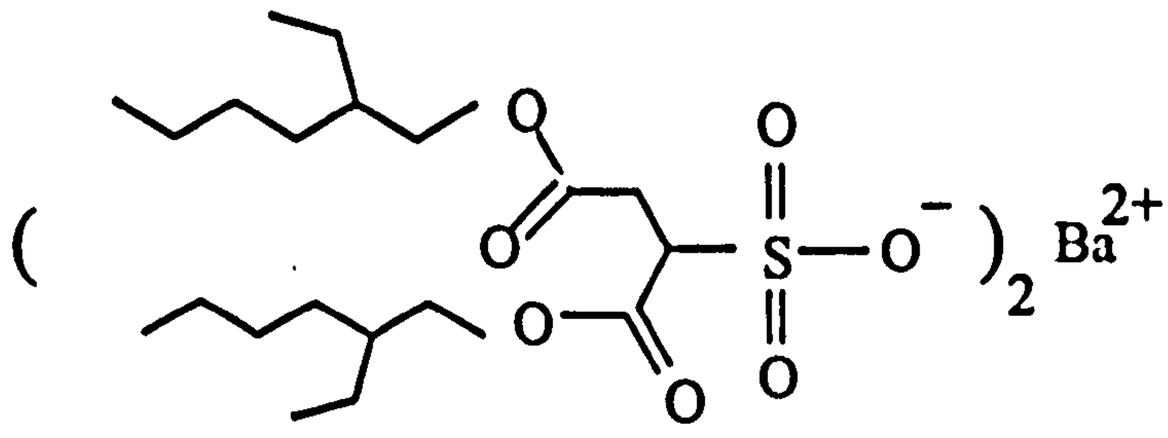

$Ba(AOT)_2$ (MW = 980) was prepared by direct reaction of sodium AOT and barium chloride in water.[23] 50 mM of aqueous solution of sodium AOT was mixed with 25 mM of barium chloride aqueous solution. The barium AOT product (a white precipitate) was centrifuged, washed with water and then dried under vacuum. Dried Barium AOT was then dissolved in isooctane (at a weight ratio of 1:6), and filtered through a 0.2 μm solvent-resistant membrane. The solvent was removed with a rotary evaporator and the compound was dried under high vacuum and stored in a dessicator. Characterisation by flame emission and elemental analysis showed the surfactant to be pure barium AOT. Negative FAB– Mass spectrometry showed the formation of clusters $[A + nM]^-$ ($A = [AOT]^-$, M = $BaAOT_2$, n = 0 and 1) negative analogues of $[C + nM]^+$ ($C = [NR_4]^+$, $M = NR_4X$, X = halogens), in the case of quaternary ammonium salts [24] for M.S. FAB (-) m/z : 1400, 40% $[BaAOT_3]^-$; 421, 100% $[AOT]^-$.

3.2.2 Experimental methods

3.2.2.1 Preparation of $BaCrO_4$ nanoparticles

Typically, 0.18 mL of aqueous Na_2CrO_4 solution (0.02 to 0.50 M, pH ≈ 9) were added with shaking to 10 mL of a solution of NaAOT dissolved in isooctane (0.1 M) to give yellow suspensions of microemulsion droplets with water to surfactant molar ratios (w =$[H_2O]/[NaAOT]$ = 5 – 20). To introduce Ba^{2+} into the reaction, a small amount of $Ba(AOT)_2$ dissolved in isooctane (0.395 mL, 0.05 M, w<1) was added to 10 mL of the chromate-containing microemulsion to give a final NaAOT

: $Ba(AOT)_2$ molar ratio of 50 : 1. Using these conditions, the $[Ba^{2+}]$: $[CrO_4^{2-}]$ molar ratio was systematically changed between values of 5.5 : 1 to 1 : 4.6 by modifying the concentration of Na_2CrO_4 in the microemulsion water droplets. The reactions took place at room temperature and the samples were analysed from one hour to one week.

3.2.2.2 Transmission electron microscopy (TEM)

Samples for TEM were collected within one week directly from the microemulsion fluid as well as the precipitated material, and deposited onto Formvar-coated carbon-reinforced, 3mm diameter, copper electron microscope grids. The samples were air–dried and washed with pure isooctane.

TEM analysis was performed in bright field mode using either a JEOL 2000FX high –resolution electron microscope operating at 200keV or a JEOL 1200EX electron microscope operating at 120keV (section **2.3.1**). The imaged particles were characterized by energy-dispersive X-ray analysis (EDXA) (section **2.3.3**) and selected area electron diffraction (SAED) (section **2.3.2**). The diffraction patterns were indexed with references to the data given in table 3-2.

Table 3-2 X-ray diffraction data for barium chromate.

D (Å)	{hkl}	Int
4.55	200	7
4.428	011	13
3.978	111	25
3.871	201	8
3.669	002	60
3.516	210	100
3.403	102	35
3.171	211	80
2.901	112	35
2.805	301	10
2.770	020	40
2.542	212	14
2.495	121	5
2.253	221	20
2.211	022	5
2.175	401,113	60
2.157	203,312	30
2.150	122	45
2.106	410	10
1.972	321	5
1.905	303	15
1.835	004	10
1.799	104,123	10
1.711	230,114	30
1.702	204,223	5

The data are from JCPDS-ICDD (c) 1995 PDF-2 Sets 1-45 database.

$A = 9.112$ Å $b = 5.541$ Å $c = 7.343$ Å

$\alpha = \beta = \gamma = 90°$

3.2.2.3 Small-angle X-ray scattering (SAXS)

Samples for SAXS were prepared as in section **3.2.2.1**. These included NaAOT water-in-oil microemulsion droplets and $Ba(AOT)_2$ micelles in isooctane.

Small-angle X-ray scattering measurements were carried out at the Max-Planck-Institut of Colloids and Interfaces (Germany). The data were obtained from a Kratky compact camera system that was equipped with a stepping motor and a counting tube with an impulse-height discriminator. The light source was a conventional X-ray tube with fixed copper target operating at 40 mA and 30 kV (section **2.3.6**).

3.2.2.4 Dynamic light–scattering (DLS)

Samples for dynamic light-scattering measurements were prepared as in section **3.2.2.1**. The results were recorded as follows: 1) the hydrodynamic radii of particle populations as a function of time; 2) the number of particle populations as a function of time. The time axis started from the moment of mixing $Ba(AOT)_2$ micelles and sodium chromate containing NaAOT microemulsions.

Dynamic light-scattering measurements were carried out at the Max-Planck-Institut of Colloids and Interfaces (Germany) (section **2.3.7**).

3.2.2.5 Mass spectrometry (MS)

Samples for mass spectrometric analysis were pure synthesized $Ba(AOT)_2$ submitted as dry powder. The measurements were run by Service staff with a MICROMASS AUTOSPEC mass spectrometer operating at an energy of 30 keV (section **2.3.1.1**). Negative Fast Atom Bombardment (FAB–) ionization techniques were used for this measurement.

3.2.2.6 Fourier Transform Infrared spectroscopy (FTIR)

Samples for Fourier Transform Infrared (FTIR) analysis were taken from the sedimented materials and washed for three times with isooctane to remove free AOT molecules and air-dried. The spectra were recorded from 4000-200 cm^{-1} using KBr discs. Fourier Transform Infrared analysis was performed with a PERKIN ELMER Spectrum One spectrophotometer (section **2.3.9**).

3.2.2.7 Thermogravimetric analysis (TGA)

Samples for thermogravimetric analysis were taken from the sedimented materials, washed with isooctane for three times to remove free AOT molecules, and then air-dried. Thermogravimetric analysis was performed with a Simultaneous Thermal Analysis STA409EP. The experiments were typically run

on powdered samples from 20 – 800°C with a temperature ramp of 5°C/min under flowing nitrogen (section **2.3.8**).

3.3 Results and Discussion

3.3.1 Description of $BaCrO_4$ nanoparticle chains and superlattices

Barium bis(2-ethylhexyl) sulphosuccinate ($Ba(AOT)_2$) reverse micelles were added to sodium chromate (Na_2CrO_4)-containing NaAOT microemulsion droplets, to give a final molar ratio of $[Ba^{2+}] : [CrO_4^{2-}] \approx 1$ and water content $w = [H_2O] : [NaAOT] = 10$. This produced a yellow precipitate *ca.* 3 hours after mixing of the reactants at 25°C. Transmission electron microscopy (TEM) images of samples taken directly from the liquid phase of the microemulsion showed remarkable chain-like arrays containing up to 60 nanoparticles (Figure 3-1). The colloidal chain structures were 50 to 500 nm in length and consisted of rectangular-shaped particles that were uniform in length (mean = 16.0 ± 1.5 nm) and width (mean = 6.0 ± 0.4 nm) (Figure 3-2), and preferentially aligned so that the long axis of each particle was perpendicular to the chain direction. Each crystal along the length of the chain was separated by a regular spacing of 2 nm. Corresponding TEM studies on the sedimentary material showed thin flake-like aggregates of a 2-D superlattice constructed from a pseudo-rectangular ($90° \leq 0 \leq 100°$) array of uniform-sized $BaCrO_4$ nanoparticles that were separated by an interparticle spacing of 2 nm (Figure 3-3).

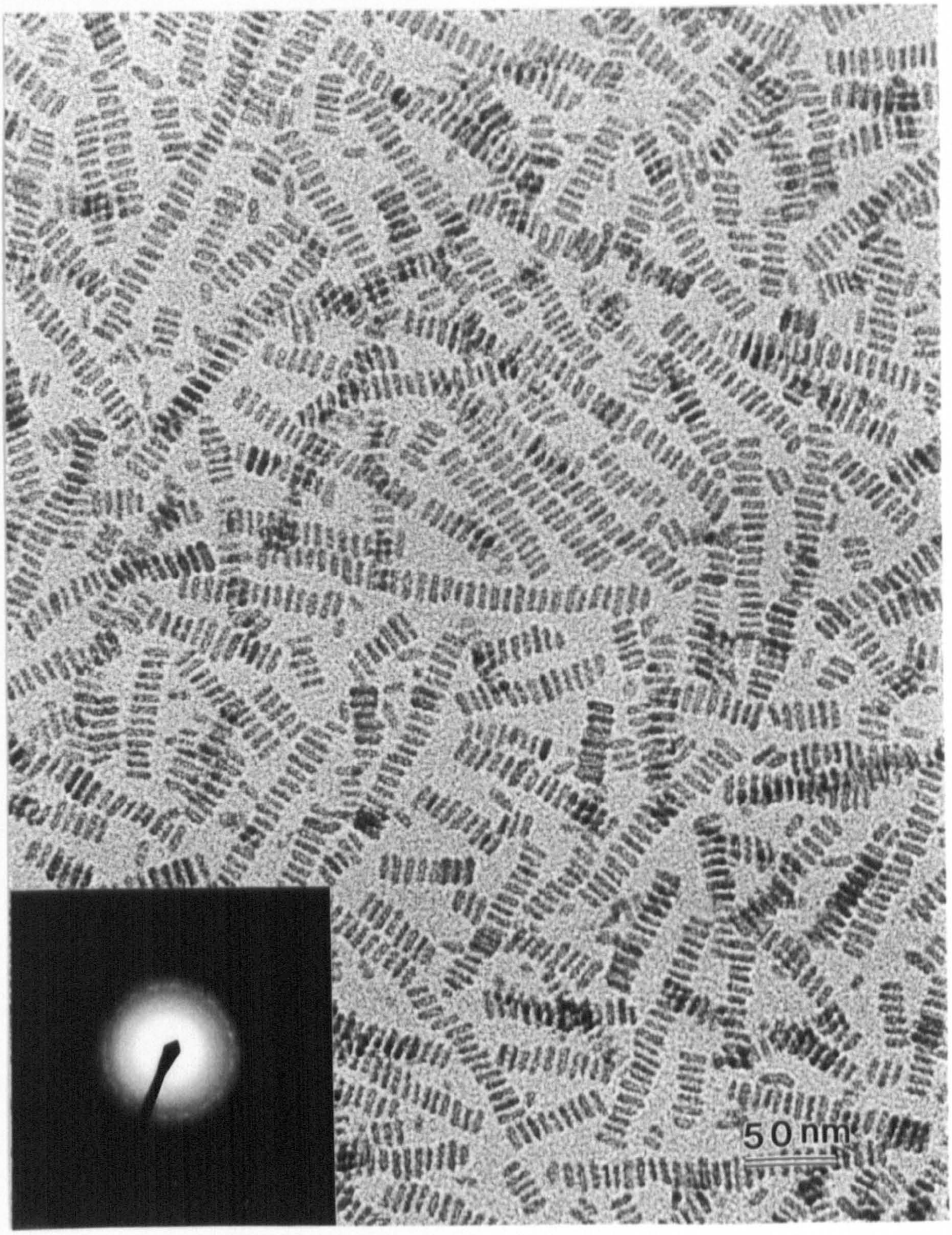

Figure 3-1 TEM image showing ordered chains of prismatic $BaCrO_4$ nanoparticles prepared in AOT reverse microemulsions at $[Ba^{2+}]$: $[CrO_4^{2-}]$ molar ratio ≈ 1 and $w = 10$ (section **3.2.2.1**). Scale bar = 50 nm, and associated electron diffraction pattern (insert).

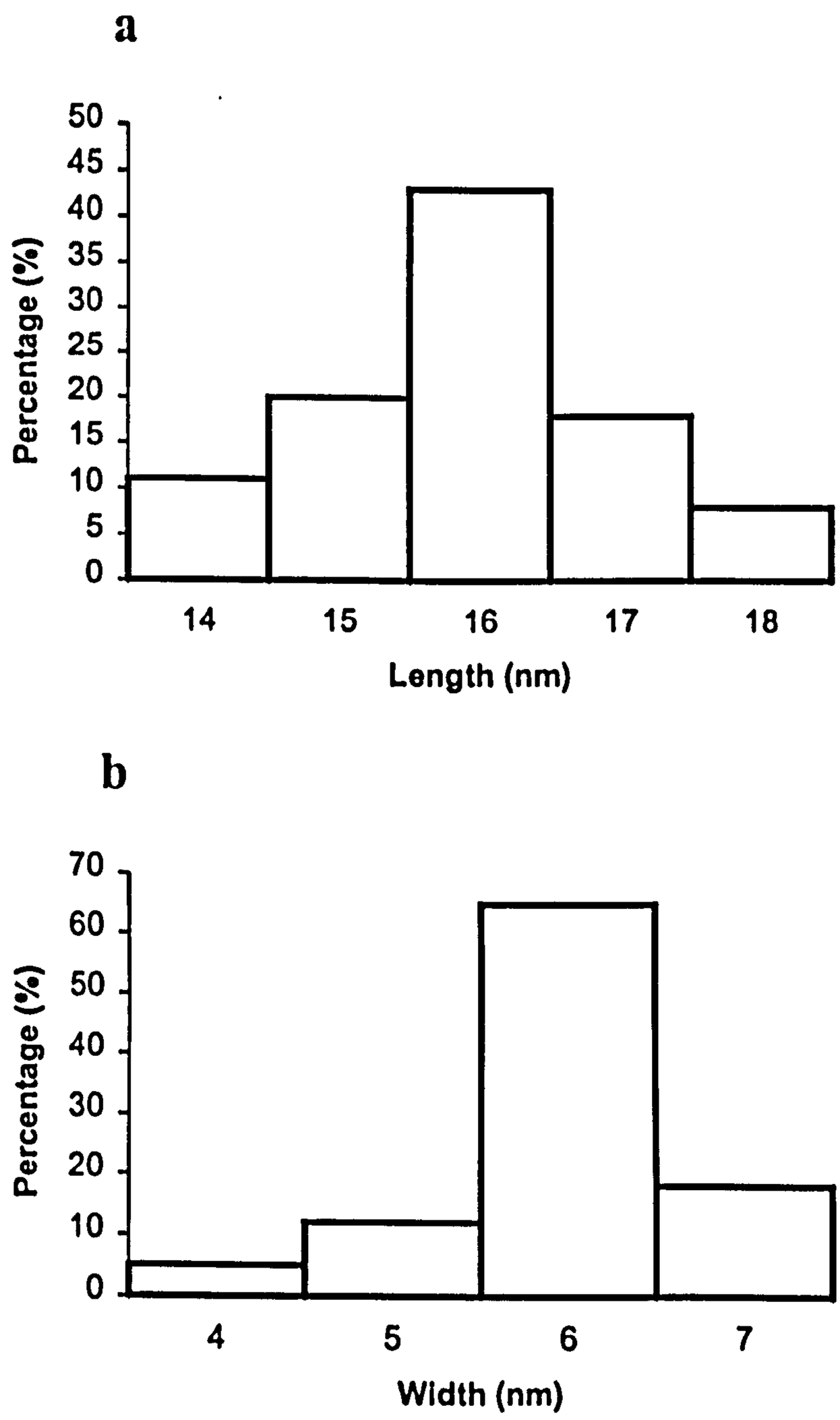

Figure 3-2 Histograms of the size distribution of $BaCrO_4$ rectangular nanoparticles in chain structures prepared at $[Ba^{2+}] : [CrO_4^{2-}] = 1 : 1$ and $w = 10$, corresponding to Figure 3-1. (a) the distribution of the length, (b) the distribution of the width.

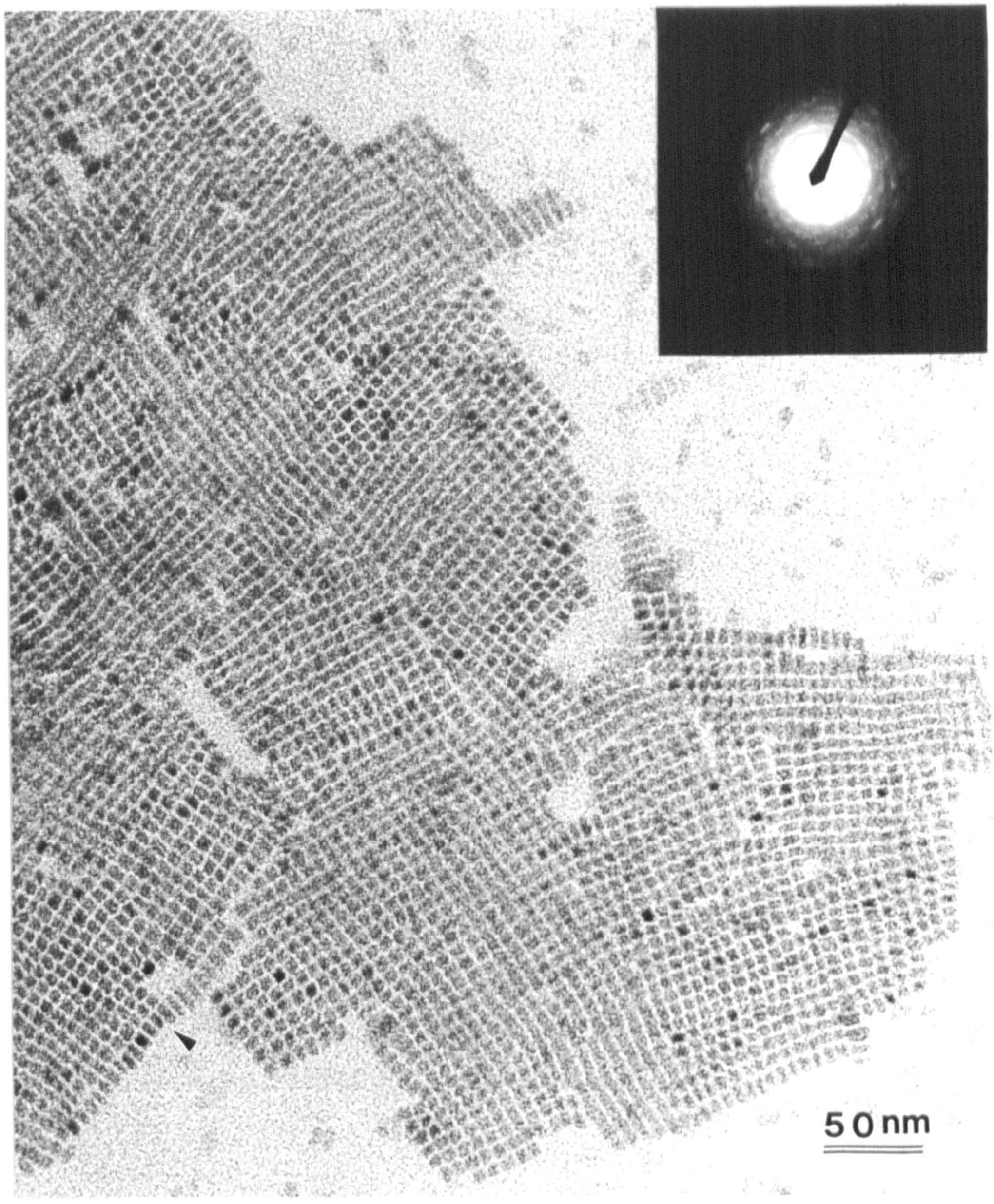

Figure 3-3 Rectangular superlattice of $BaCrO_4$ nanoparticles. These were formed by two-dimensional aggregation of nanoparticle chains prepared in AOT reverse microemulsions at $[Ba^{2+}]$:$[CrO_4^{2-}]$ molar ratio $\approx$ 1 and w = 10 (section **3.2.2.1**). Arrow shows dislodged particles revealing the prismatic morphology of individual crystallites. Scale bar = 50 nm. Insert, the electron diffraction pattern gives the superimposition of reflections from zone axes approximately parallel to the [100] direction.

a

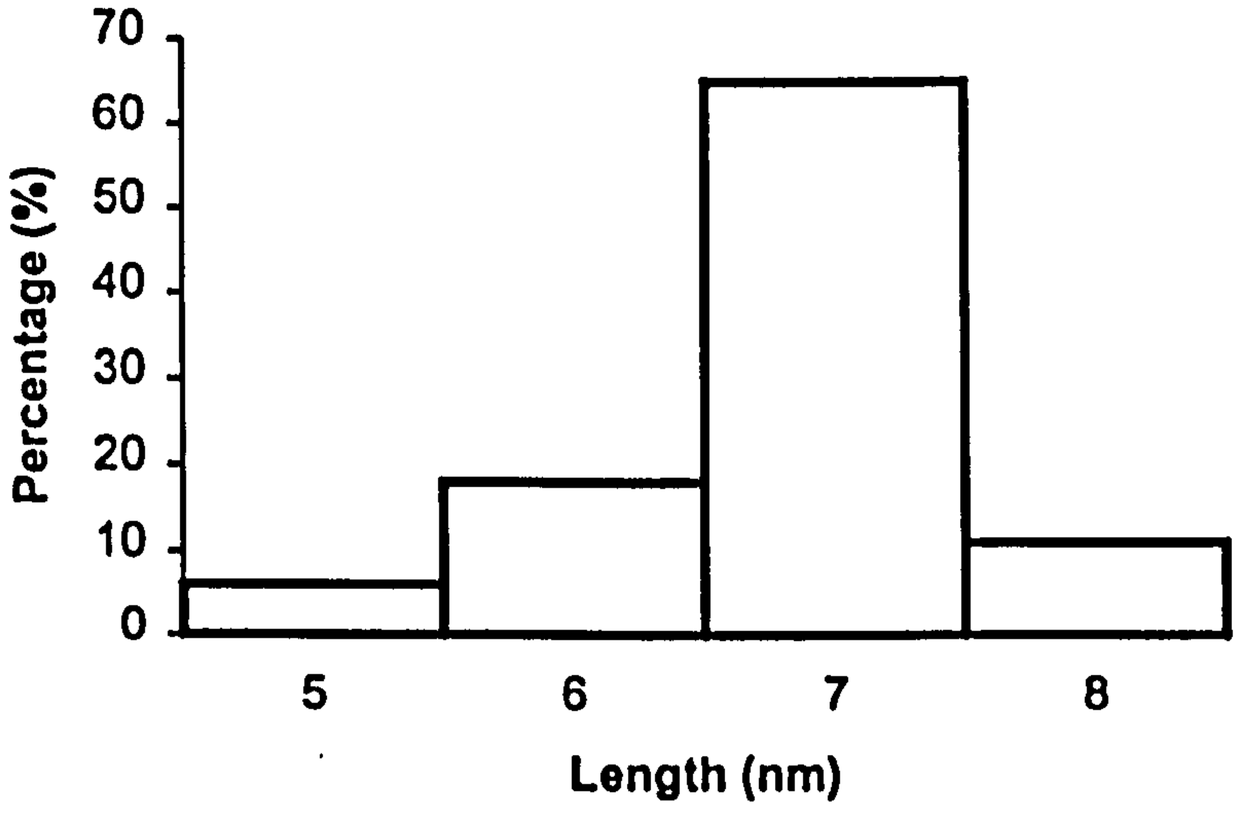

b

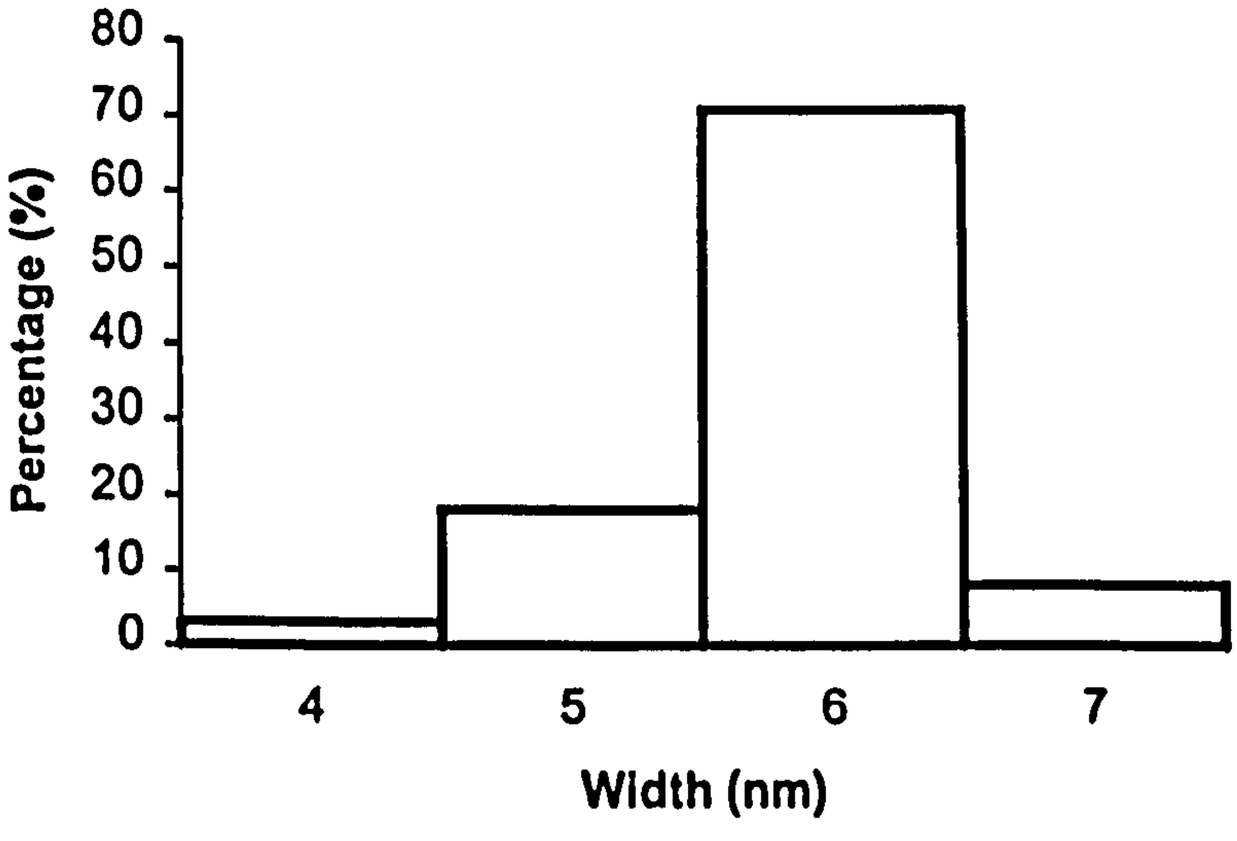

Figure 3-4 Histograms of the size distribution of $BaCrO_4$ rectangular nanoparticles in superlattice structures prepared at $[Ba^{2+}] : [CrO_4^{2-}] = 1 : 1$ and $w = 10$, corresponding to Figure 3-3. (a) the distribution of the length, (b) the distribution of the width.

Images of tilted lattices indicated that the particles were prismatic and identical to those present in the chain motif, and aligned with their long axis perpendicular to the plane of the superlattice. Viewed in-plane, the nanoparticles were rectangular in shape with mean dimensions of 6.8 ± 0.6 nm and 5.9 ± 0.5 nm (Figure 3-4), indicating two different types of side face.

3.3.2 Identification of nanoparticle chains and superlattices

TEM imaged nanoparticle chains and superlattices were characterized by energy-dispersive X-ray analysis (EDXA) and selected area electron diffraction (SAED) respectively. The EDXA spectra indicated same presence of Ba (4.4, 4.8, 5.1 keV), Cr (5.4, 5.9 keV), S (2.3, 2.6 keV) and O (0.5 keV) either in chain structures or in superlattices (Figure 3-5). Imaged nanoparticle chains and superlattices were also characterized by selected area electron diffraction (SAED). Typical barium chromate d-spacings 4.56 Å (200), 3.98 Å (111), 3.17 Å (211), 2.89 Å (112) and 2.17 Å (401,113) indexed according to **Table 3-2** were obtained in chain structures by measuring the powder electron diffraction rings (Figure 3-1 insert). Selected area electron diffraction pattern of imaged superlattices showed d-spacings of 3.66 Å (002), 3.18 Å (211), 2.78 Å (020), 2.26 Å (221), 2.14 Å (122) and 1.80 Å (104,123) (Figure 3-3 insert). The results indicating that the nanoparticle chains and superlattices were crystalline barium chromate.

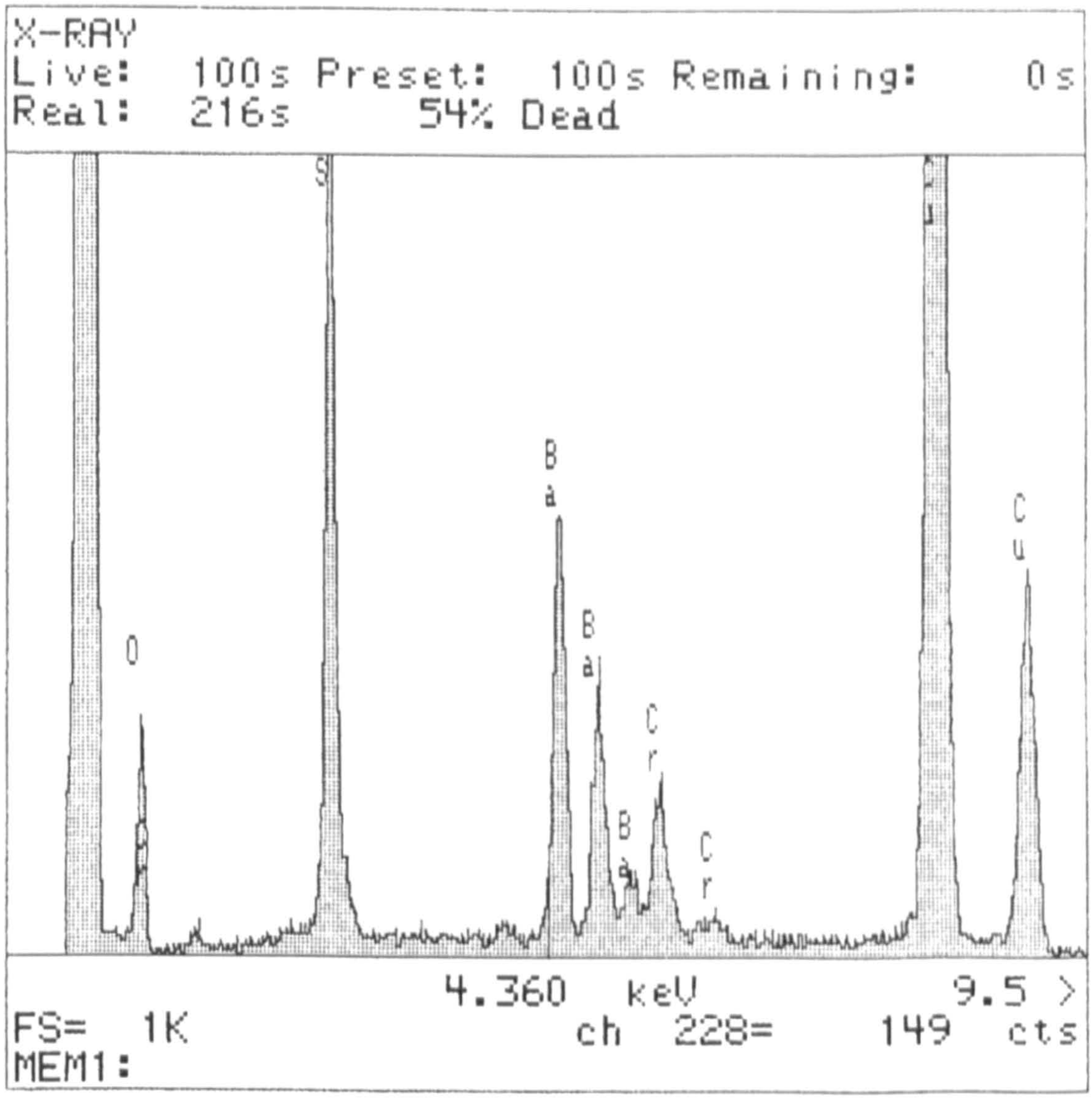

Figure 3-5 Energy-dispersive X-ray analysis (EDXA) spectrum recorded from $BaCrO_4$ nanoparticle chains or superlattices prepared in AOT reverse microemulsions at $[Ba^{2+}]$:$[CrO_4^{2-}]$ molar ratio $\approx$ 1 and w = 10 corresponding to Figure 3-1 or Figure 3-3.

3.3.3 Investigation of the molar ratio of two reactants Ba^{2+}/CrO_4^{2-}

The molar ratio of $[Ba^{2+}]$ to $[CrO_4^{2-}]$ was systematically changed between values of 5.5 : 1 to 1 : 4.6 by modifying the concentration of Na_2CrO_4 in the microemulsion water droplets (Table 3-3).

Table 3-3 concentrations of Na_2CrO_4 and the molar ratio of Ba^{2+}/CrO_4^{2-}

No.	$[Na_2CrO_4]$ (M)	molar ratio of Ba^{2+}/CrO_4^{2-}	molar ratio of NaAOT/Na_2CrO_4
1	0.02	5.5:1	278
2	0.04	2.7:1	139
3	0.08	1.4:1	69
4	0.11	1:1	51
5	0.15	1:1.4	37
6	0.30	1:2.7	19
7	0.50	1:4.6	11

The systematically change in concentrations of Na_2CrO_4 and the molar ratio of Ba^{2+}/CrO_4^{2-} at the constants of [NaAOT] = 0.1 M, $[Ba(AOT)_2]$ = 0.05 M , the molar ratio of NaAOT / $Ba(AOT)_2$ = 50 and $w = H_2O$ / NaAOT = 10.

The $BaCrO_4$ nanoparticle chains (Figure 3-1) and superlattices (Figure 3-3) were formed specifically at molar equivalence ($1 : 1.4 \leq [Ba^{2+}] : [CrO_4^{2-}] \leq 1.4 : 1$) (No.3~5 in Table 3-3). Under identical conditions, but with an excess of Ba^{2+}, ($2.7 : 1 \leq [Ba^{2+}] : [CrO_4^{2-}] \leq 5.5 : 1$) (No. 1~2 in Table 3-3), $BaCrO_4$ filaments with lengths up to 50 μm were deposited in the form of single threads or bundles of loosely aggregated fibres with highly uniform widths, straight edges and well-defined flattened ends (Figure 3-6).

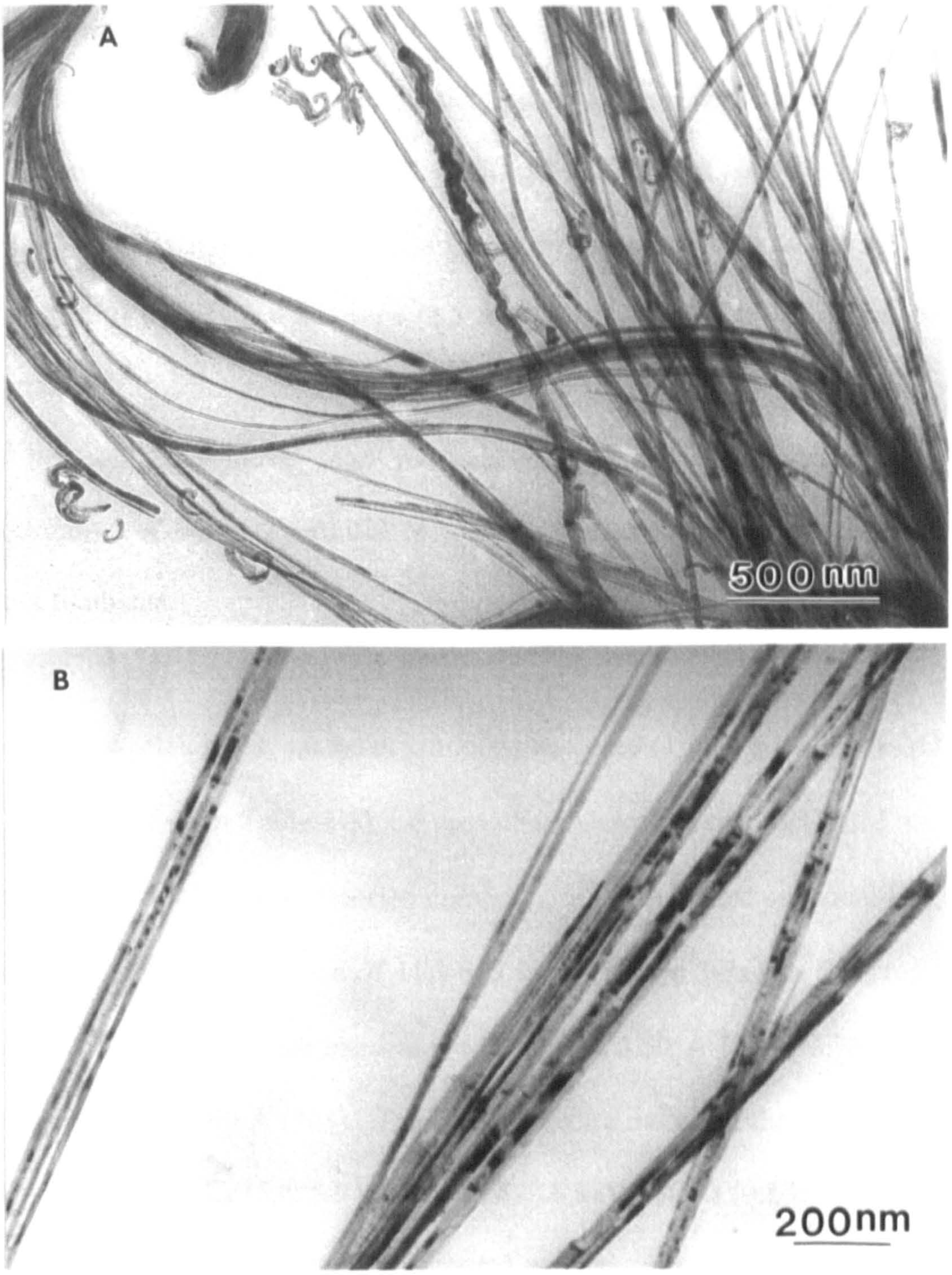

Figure 3-6 (**a**) TEM image of bundles of $BaCrO_4$ nanofilaments prepared in AOT reverse microemulsions at $[Ba^{2+}]:[CrO_4^{2-}] \approx 5 : 1$ and $w = 10$, scale bar = 500 nm; (**b**) higher magnification image of single filaments, scale bar = 200 nm.

The filaments were 20 to 500 nm in width, with an aspect ratio of approximately1000. Electron diffraction patterns were consistent with single crystal $BaCrO_4$ filaments preferentially oriented along the crystallographic *a* axis (Figure 3-7a,c). High resolution TEM image (Figure 3-7b) showed lattice fringes correspond to the (210) d-spacings (3.5 Å). However, if the experiments were undertaken at this low concentration of chromate (0.04M, same as No.2 in Table 3-3) but with the molar ratio re-established at 1 : 1 by decreasing the concentration of $Ba(AOT)_2$ (0.018 M), low yield chain structures were obtained, but not filaments.

In contrast, when a molar excess of chromate was used ($1 : 4.6 \leq [Ba^{2+}] : [CrO_4^{2-}] \leq 1 : 2.7$) (No.6~7 in Table 3-3), no precipitate was observed, and TEM studies showed that the colloidal suspension consisting of cuboidal and spherical $BaCrO_4$ nanocrystals with a mean size of 11.1 ± 2.5 nm (Figure 3-8a,b). Selected area electron diffraction patterns showed d-spacings of 3.50 Å (210), 2.76 Å (020), 2.21 Å (022) and 1.90 Å (303). The EDXA spectra indicated the presence of Ba (4.4, 4.8, 5.1 keV), Cr (5.4, 5.9 keV), S (2.3, 2.6 keV) and O (0.5 keV) (Figure 3-9). The results indicated that the spherical nanoparticles were $BaCrO_4$ cyrstals. However, when experiments were undertaken at these increased chromate concentrations (0.3 M, same as No. 6 in Table 3-3) but with the molar ratio re-established at 1 : 1 by increasing the $Ba(AOT)_2$ concentration (0.135 M), chains and superlattices, and not discrete spherical nanoparticles, were specifically deposited.

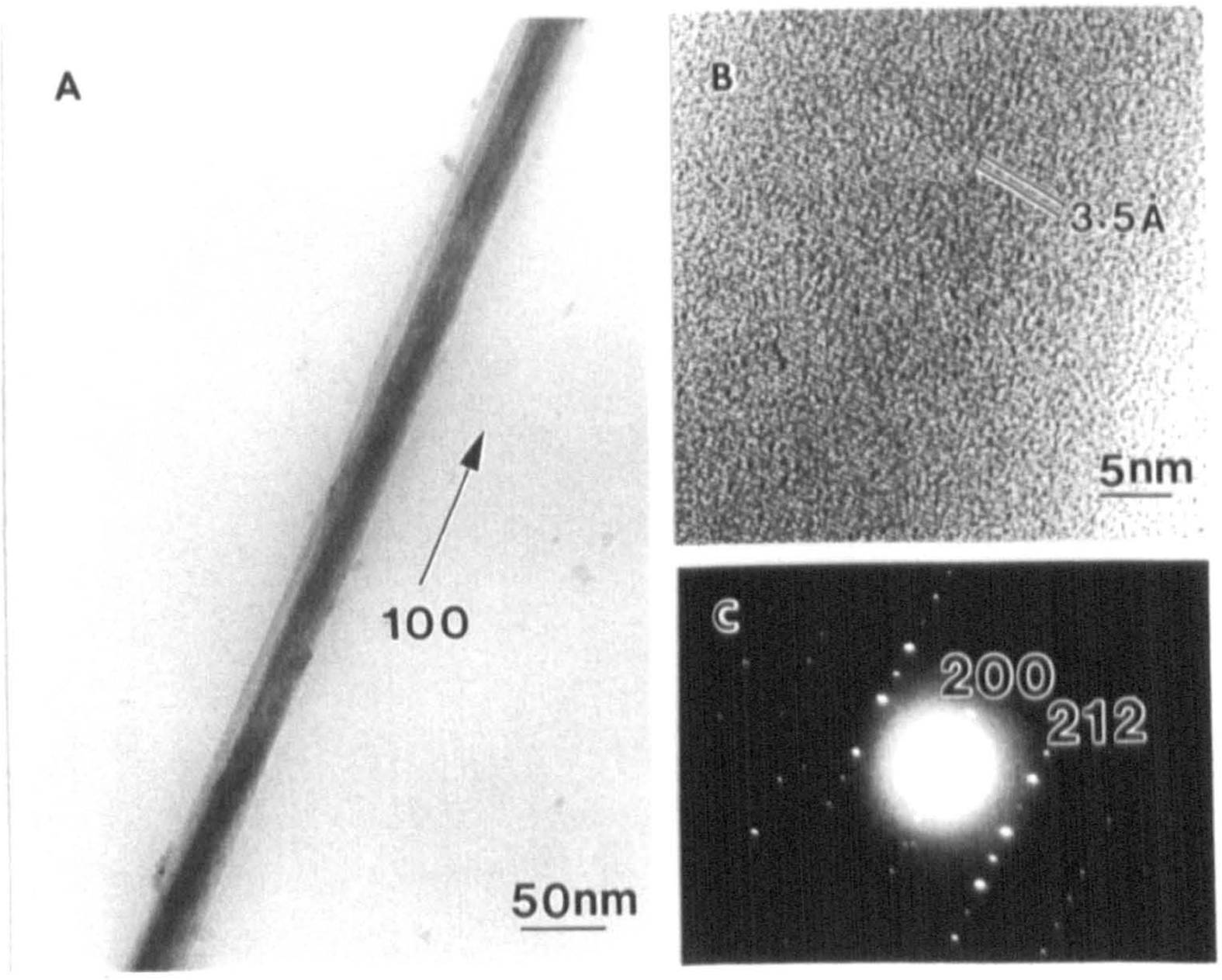

Figure 3-7 (**a**) single $BaCrO_4$ nanofilaments elongated along the crystallographic *a* axis, scale bar = 50 nm; (**b**) high-resolution TEM image shows $BaCrO_4$ lattice fringes correspond to (210) d-spacings (3.5 Å); (**c**) shows [0-21] zone electron diffraction pattern recorded from an individual fibre.

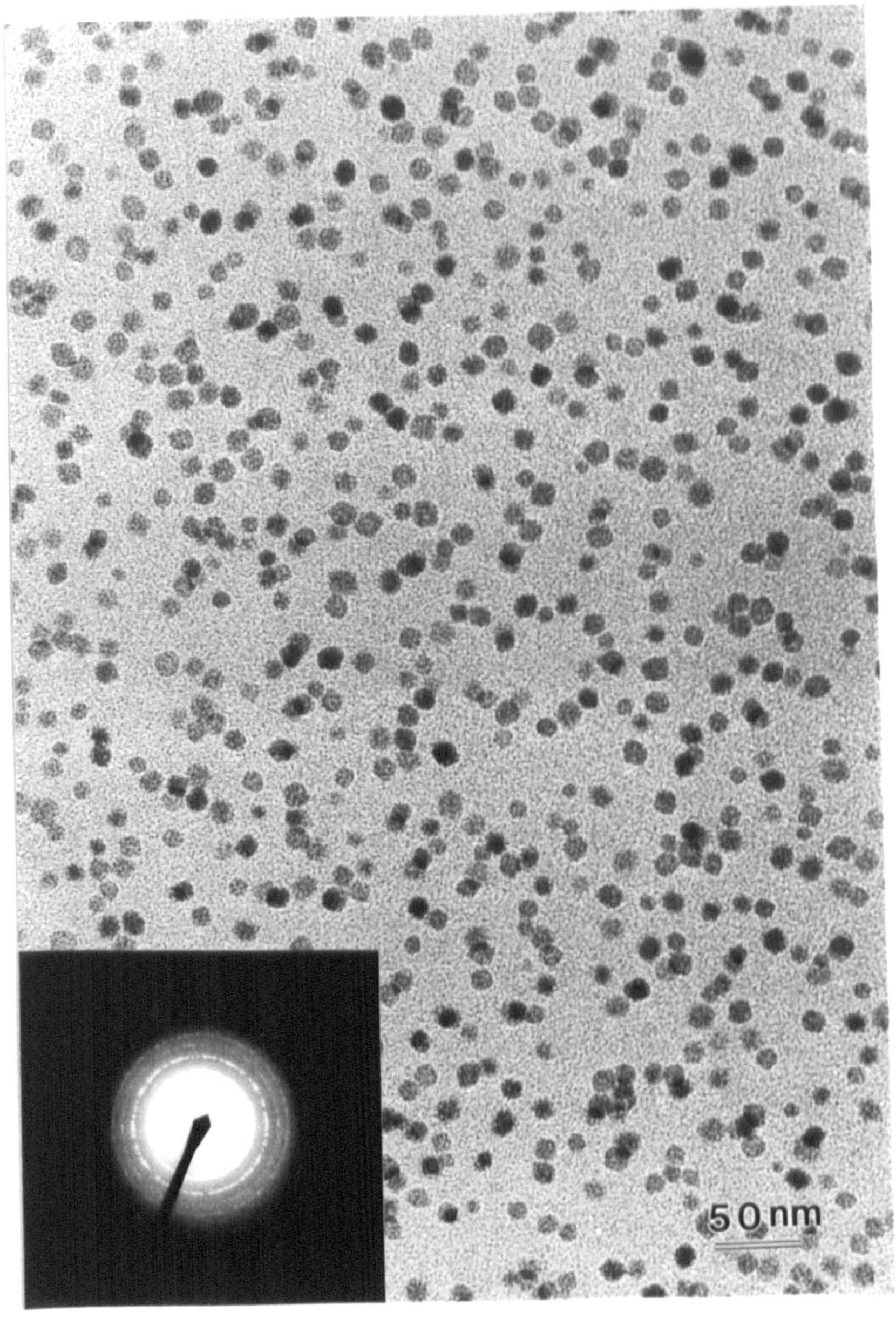

Figure 3-8a TEM image of spherical $BaCrO_4$ nanoparticles prepared at $[Ba^{2+}]:[CrO_4^{2-}] \approx 1 : 5$ and $w = 10$; scale bar = 50 nm, and associated electron diffraction patern (insert).

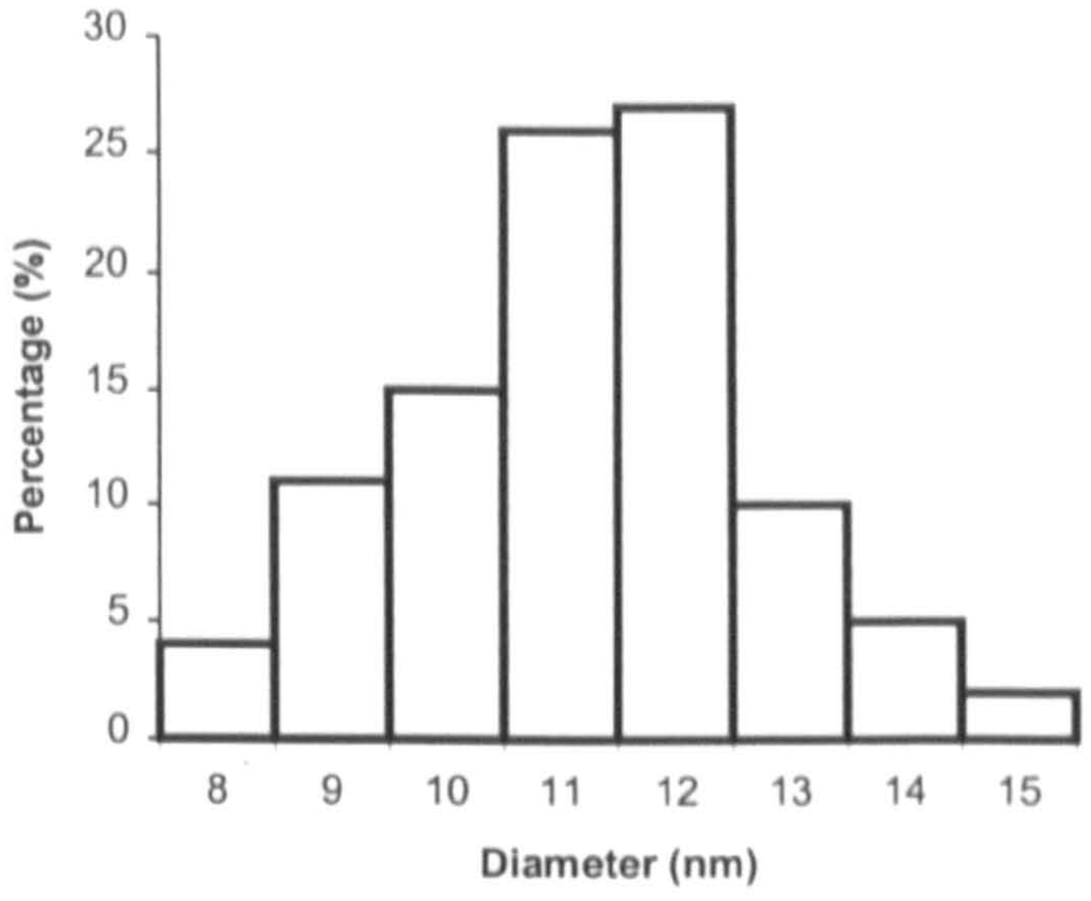

Figure 3-8b Histogram of size distribution of $BaCrO_4$ spherical nanoparticles prepared at $[Ba^{2+}] : [CrO_4^{2-}] = 1 : 5$ and $w = 10$, corresponding to Figure 3-8a.

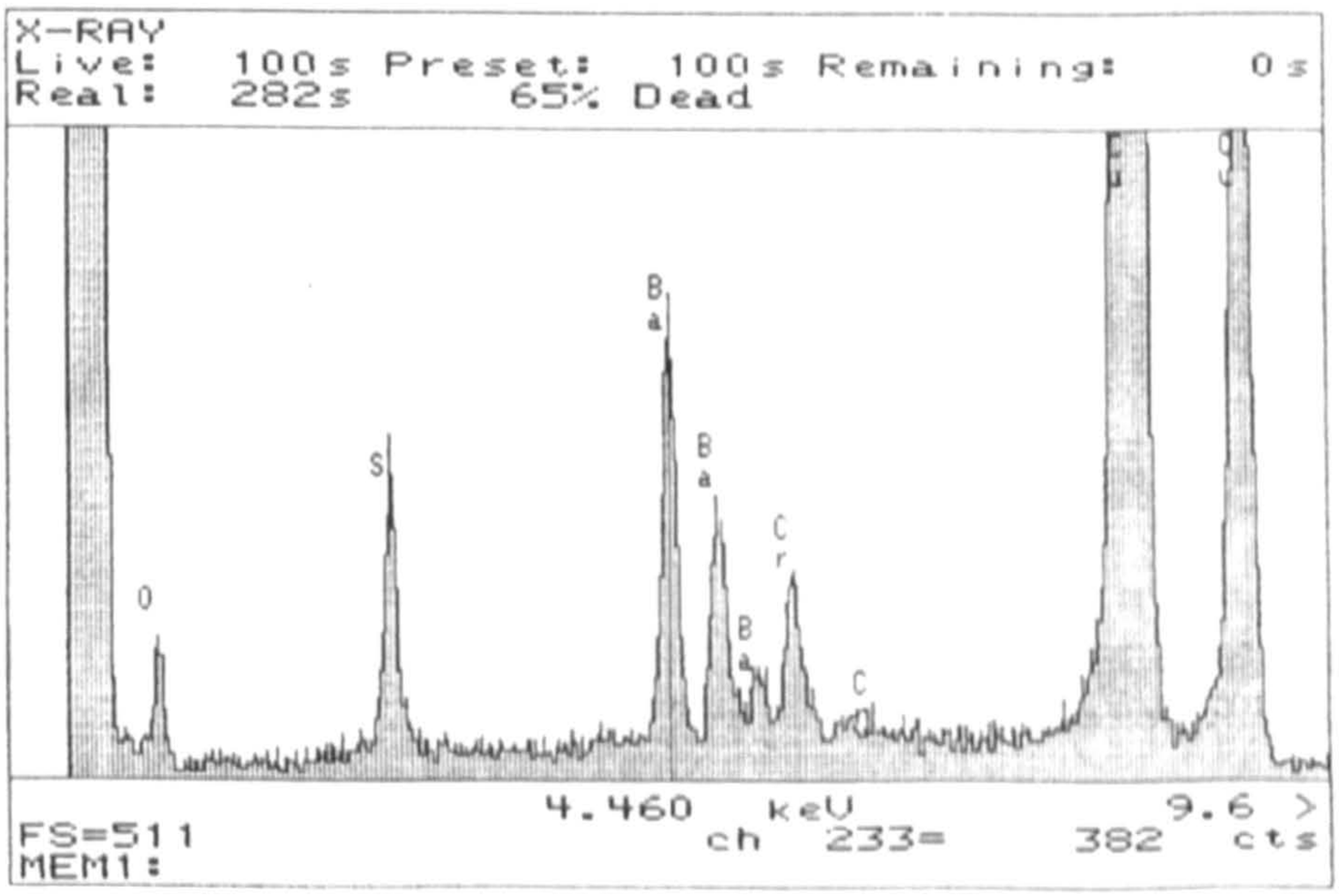

Figure 3-9 Energy-dispersive X-ray analysis (EDXA) spectrum recorded from $BaCrO_4$ spherical nanoparticles prepared at $[Ba^{2+}]:[CrO_4^{2-}] \approx 1 : 5$ and $w = 10$ corresponding to Figure 3-8a.

3.3.4 Investigation of water content in the microemusions (*w* value)

Systematic changes in the water content ($5 \leq w \leq 20$), and hence the diameter of the microemulsion droplets, was used to control the size of the nanoparticles present in both the chain and superlattice structures. For constant values of $[Ba^{2+}]$: $[CrO_4^{2-}] \approx 1$, increases in *w* gave increased mean particle sizes that were correlated in the chain and superlattice nanostructures (Table 3-4 and Figure 3-10).

Table 3-4 Mean dimensions for individual prismatic $BaCrO_4$ nanoparticles

w value (H_2O/NaAOT)	chain-like stacks (nm)	superlattices (nm)	microemulsion radius (nm)
5	14.5±1.2×5.6±0.4	6.4±0.6×5.3±0.5	1.5±0.5
10	16.0±1.5×6.0±0.4	6.8±0.6×5.9±0.5	2.2±0.6
15	17.5±1.4×6.3±0.4	7.4±0.7×6.1±0.6	–
20	18.3±1.5×8.4±0.8	10.0±1.1×8.1±0.7	3.2±0.6

The particles were viewed side-on (chains) and end-on (superlattice) by electron microscopy. The nanostructures were synthesized in AOT/water/isooctane reverse microemulsions at $[Ba^{2+}] : [CrO_4^{2-}] \approx 1 : 1$, $[NaAOT] : [Ba(AOT)_2] = 50$, and various water content *w* values. Sizes of the corresponding microemulsion water droplets were determined by small angle X-ray scattering. $\sigma < 10\%$ for all data.

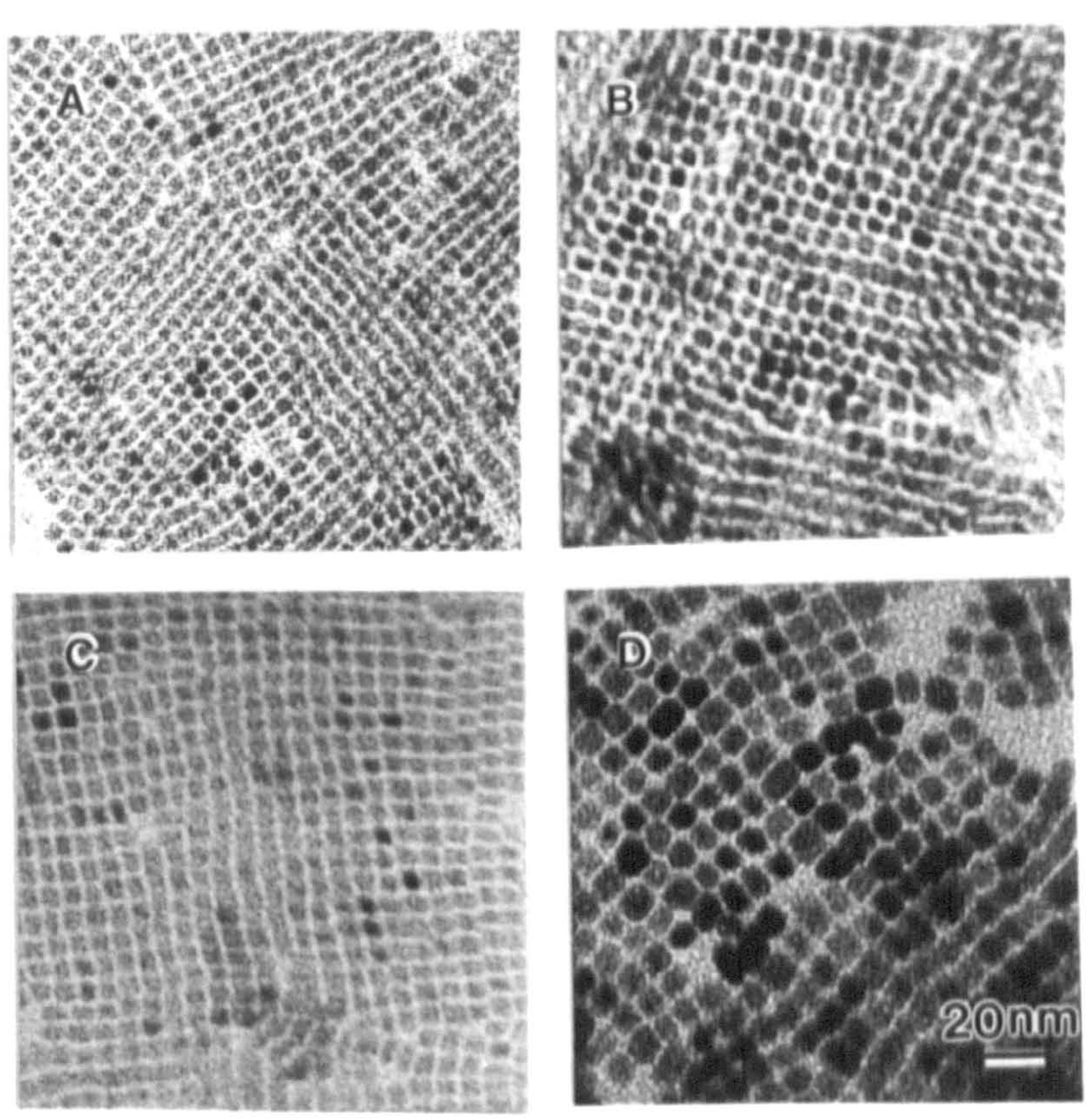

Figure 3-10 TEM images of $BaCrO_4$ nanoparticle superlattices prepared in AOT reverse microemulsions at $[Ba^{2+}]$:$[CrO_4^{2-}]$ molar ratio $\approx$ 1 and various w value. (**a**) $w = 5$; (**b**) $w = 10$; (**c**) $w = 15$; (**d**) $w = 20$. Scale bars a = b = c = d = 20 nm.

The sizes of the microemulsion droplets were measured using small-angle X-ray scattering (SAXS). The droplets were prepared by the same method as section **3.2.2.1** but without reactant (Na_2CrO_4) in the water phase. Figure3-11 clearly showed that the microemulsion sizes increased as the *w* value increased, indicating that the particle sizes increased as the droplet size increased. However, comparing the final size of the particles with the size of microemulsion droplets in which they formed showed that both sizes were not commensurate. The nanoparticles synthesized were significantly larger than the microemulsion droplets under the conditions investigated. The mechanism of formation of nanoparticles in AOT reverse microemulsions is not clear so far.

3.3.5 Dynamic study of the formation of chain and superlattice structures

The formation of $BaCrO_4$ nanoparticle chains and superlattices as a function of time was studied by transmission electron microscopy (TEM) and dynamic light scattering (DLS). Samples for TEM were prepared as in section **3.2.2.1** at $w = 10$ and taken from 1 hour after mixing of $Ba(AOT)_2$ micelles with an Na_2CrO_4-containing NaAOT microemulsion. TEM images of the early stages (1 hour) of chain assembly showed low contrast structures with striped patterns (Figure 3-12a), rather than isolated nanoparticles with prismatic morphology. TEM images corresponding to samples taken at 3 hours still showed low contrast but developing chains were clearly apparent (Figure 3-12b). After 6 hours, nanoparticle chain arrays with long order were observed in solution (Figure 3-12c).

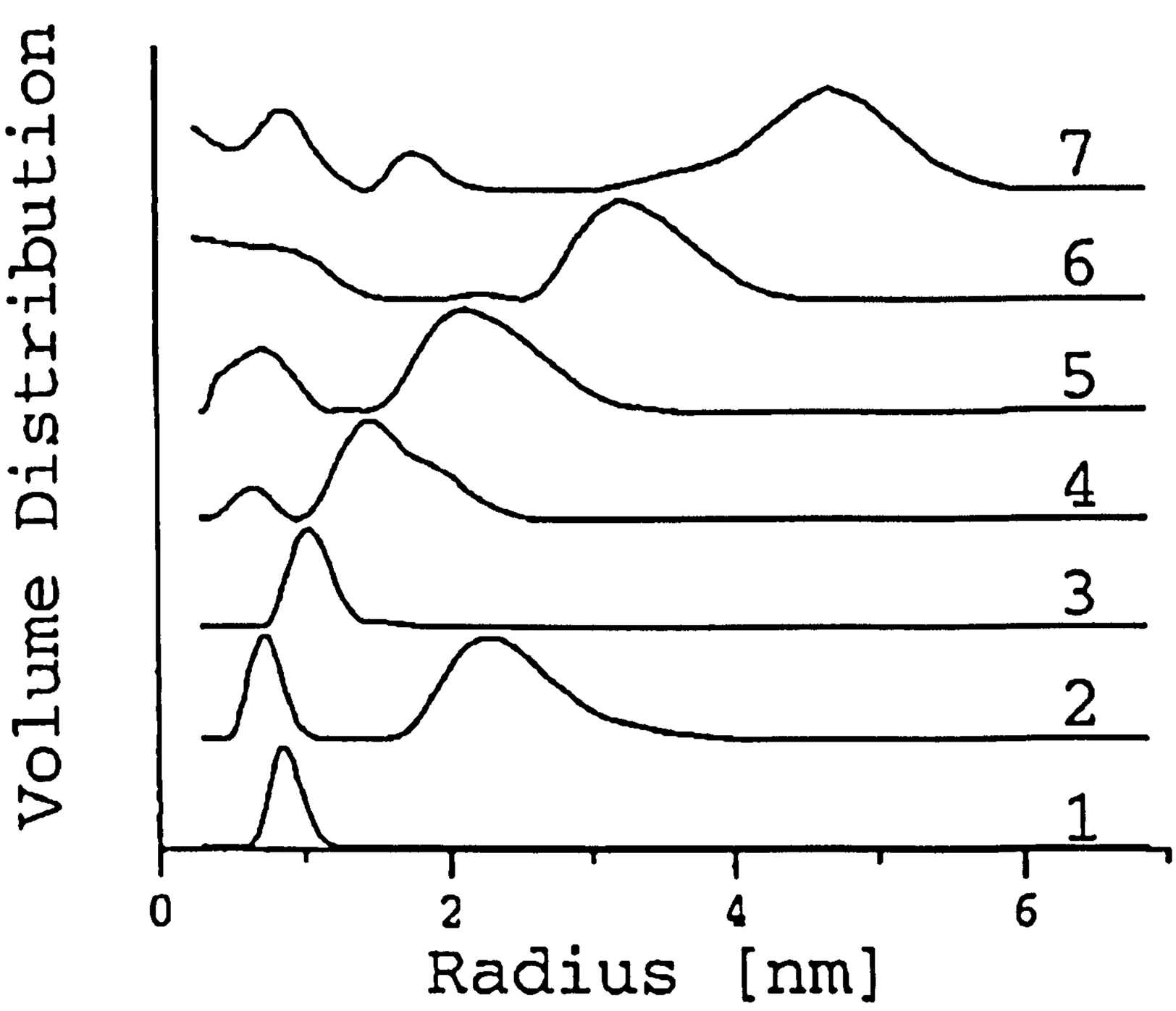

Figure 3-11 Size distributions of AOT micelles and microemulsions measured by small-angle X-ray scattering. (1) $Ba(AOT)_2$ micelles (0.05M in isooctane, $w <$ 1); (2) NaAOT microemulsions (0.1 M in isooctane + H_2O, $w = 10$); (3) NaAOT (0.1 M in isooctane) + H_2O ($w = 1$) + $Ba(AOT)_2$ 0.05 M in isooctane ([NaAOT]:[$Ba(AOT)_2$] = 50:1); (4) same as (3) but $w = 5$; (5) same as (3) but $w =$ 10; (6) same as (3) but $w = 20$; (7) same as (3) but $w = 30$. (figure supplied by Dr. Heimo Schnablegger, Max-Planck-Institut of Colloids and Interfaces, Germany)

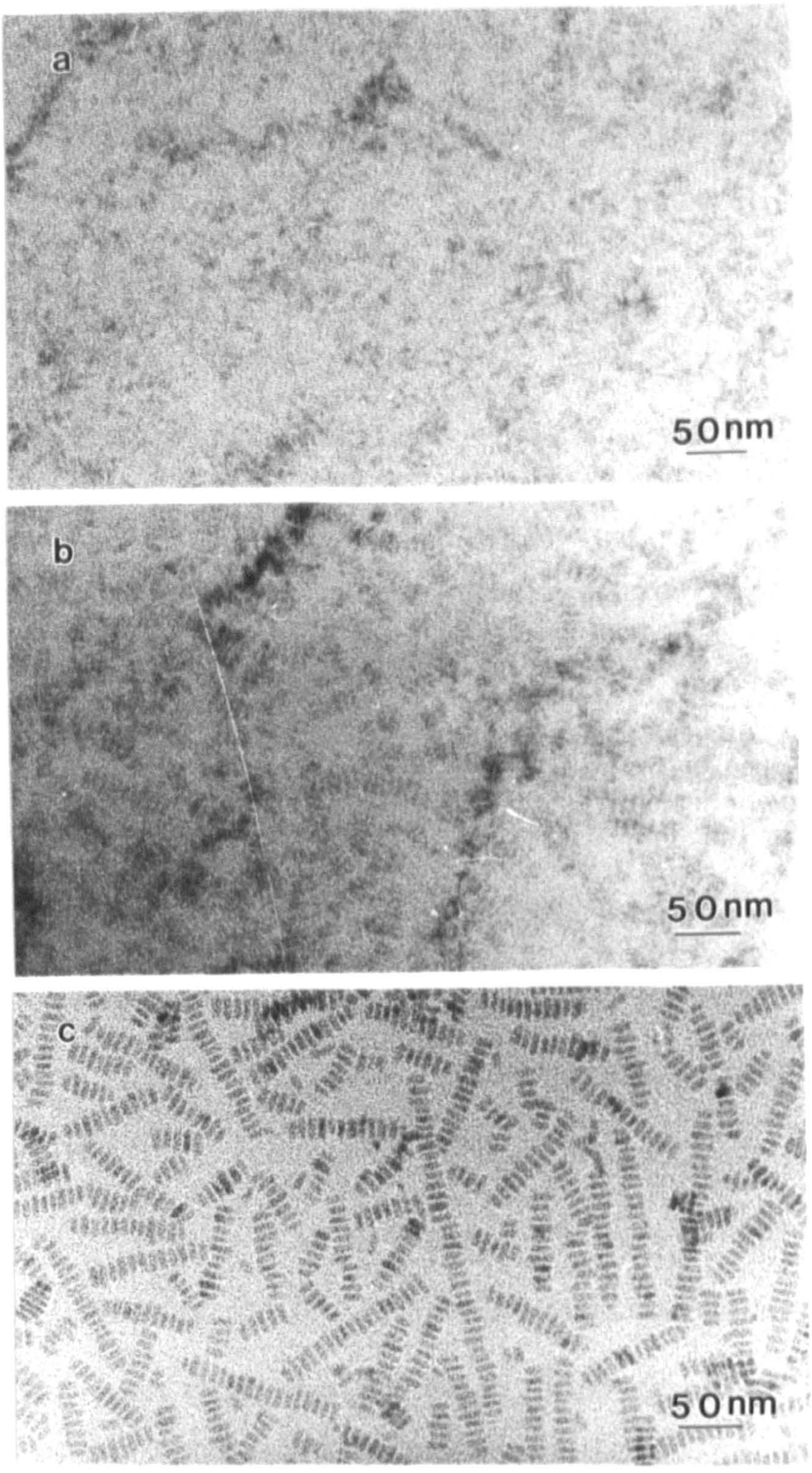

Figure 3-12 TEM images of $BaCrO_4$ developing chain structures. Samples were prepared at $[Ba^{2+}] : [CrO_4^{2-}]$ molar ratio ≈ 1 and $w = 10$ and taken after (**a**) 1 hour; (**b**) 3 hours; (**c**) 6 hours. Scale bars a = b = c = 50 nm.

The results suggest that $BaCrO_4$ growth occurs in association and concurrent with the self-organization of stacked micellar aggregates and not through sequential attachment of individual nanoparticles. This was confirmed by dynamic light scattering (DLS).

Dynamic light scattering of unstirred reaction mixtures, prepared as in section **3.2.2.1** at $w = 10$, suggested the presence of microemulsion water droplets with a constant hydrodynamic radius of 5.8 ± 0.5 nm throughout the time course of the experiments (Figure 3-13 curves 1 in a and b). Similar observations were made using small angle X-ray scattering (SAXS), which detected significant numbers of Ba^{2+}-containing spherical water droplets in the reaction mixtures, even after 25 hours at 25 °C. DLS also suggested the appearance of a second component within 3 hours at 25°C (18 hours at 20°C), which progressively increased in scattering intensity over 6 hours at 25°C, until the experiment was terminated due to bulk precipitation (Figure 3-13 curves 2 in a and b). Formation of the aggregate was coincident with a decrease in the number of microemulsion droplets (Figure 3-14). Although the complexity of the system prevents a conclusive analysis of the DLS data, the results suggest that the second component is associated with the formation of aggregates in the microemulsion fluid. Supporting this interpretation are the results of a TEM analysis of corresponding samples, which show the appearance of the second component in the DLS studies to be concurrent with the appearance of nanoparticle chains.

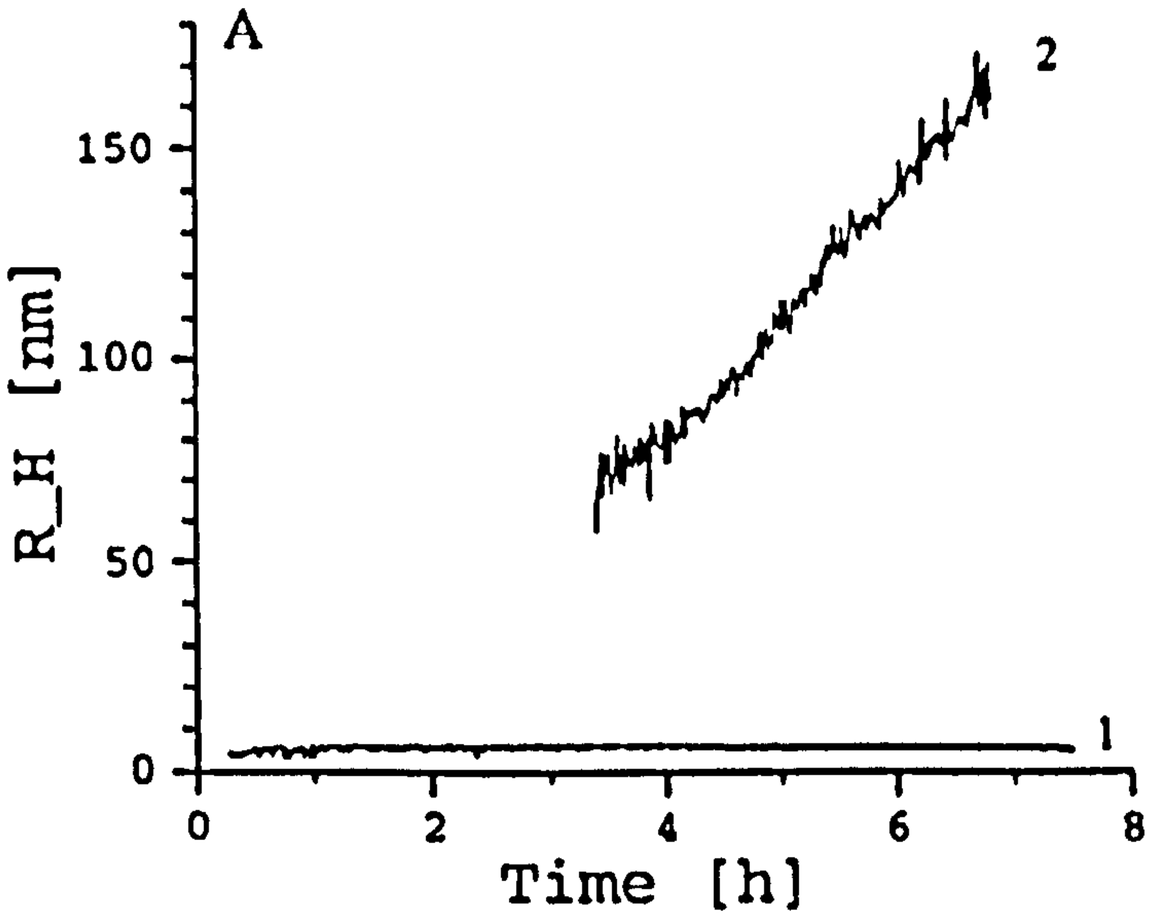

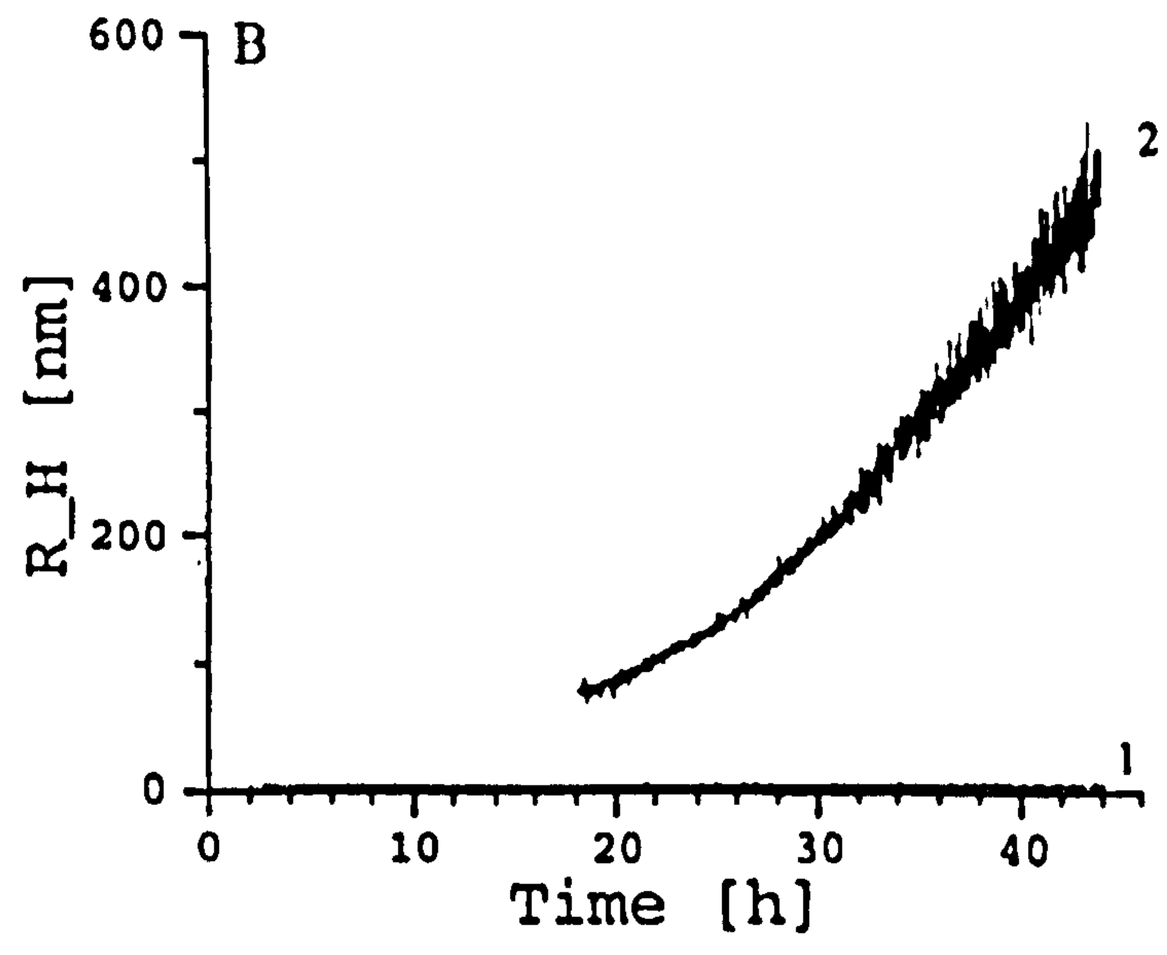

Figure 3-13 Hydrodynamic radii of two kinds of particle populations as function of time at (a) 25°C (b) 20°C measured by dynamic light-scattering. Samples were prepared in AOT reverse microemulsion at $[Ba^{2+}]$:$[CrO_4^{2-}]$ molar ratio ≈ 1 and w = 10 (section **3.2.2.1**). (figure supplied by Dr. Heimo Schnablegger, Max-Planck-Institut of Colloids and Interfaces, Germany)

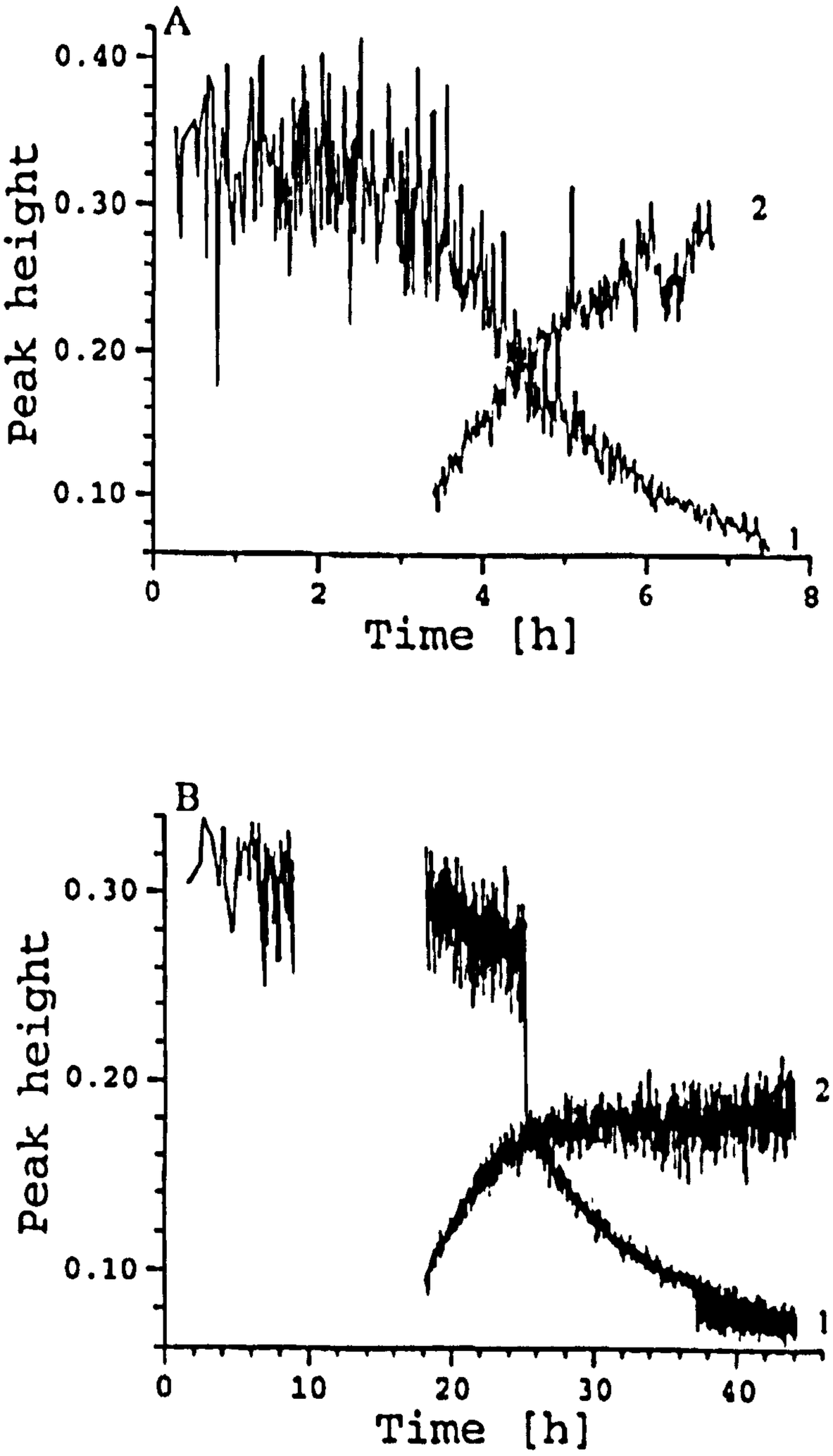

Figure 3-14 Peak heights of two particle populations as function of time measured by dynamic light scattering at (a) 25 °C and (b) 20 °C. The peak height is proportional to the squared volume of the respective particles. Curves 1 are corresponding to the small particles and curves 2 are corresponding to the big particles in figure 3-13. (figure supplied by Dr. Heimo Schnablegger, Max-Planck-Institut of Colloids and Interfaces, Germany)

3.4 General discussion

3.4.1 Molar ratios

Using the molar ratio of two reactants to control the morphology of nanoparticles synthesized in reverse microemulsions is reported for the first time by this work. The $BaCrO_4$ nanoparticle chains and superlattices were formed specifically at molar equivalence ($1 : 1.4 \leq [Ba^{2+}] : [CrO_4^{2-}] \leq 1.4 : 1$). Under identical conditions, but with an excess of Ba^{2+} by decreasing the concentrations of chromate ($2.7 : 1 \leq [Ba^{2+}] : [CrO_4^{2-}] \leq 5.5 : 1$), $BaCrO_4$ filaments were formed, or with a molar excess of CrO_4^{2-} by increasing the concentrations of chromate ($1 : 4.6 \leq [Ba^{2+}] : [CrO_4^{2-}] \leq 1 : 2.7$), the colloidal suspension consisted of cuboidal and spherical $BaCrO_4$ nanocrystals. However, if the experiments were undertaken at low (0.04M) or high (0.3 M) concentrations of chromate, but with the molar ratio re-established at 1 : 1 by modifying the concentration of $Ba(AOT)_2$, chains and superlattices structures were obtained, and not the filaments or spherical nanoparticles (section **3.3.3**). This indicated that the molar ratio, rather than the absolute concentrations, was responsible for the organized structures.

The same results were observed in the synthesis of $BaSO_4$ under the same conditions. $BaSO_4$ nanoparticle chain structures were synthesized at molar equivalence ($[Ba^{2+}] : [SO_4^{2-}] = 1 : 1$ and $w = 10$) (Figure 3-15) and $BaSO_4$

nanofilaments were formed at the molar ratio of $[Ba^{2+}] : [SO_4^{2-}] = 5 : 1$ (Chapter 4).

We propose the following model to account for the remarkable influence of reaction stoichiometry on the shape, size and self-assembly of higher-order $BaCrO_4$ structures in complex fluids. On mixing, transfer of water molecules from the chromate-containing microemulsions to the "dry" $Ba(AOT)_2$ reverse micelles acts as a strong driving force for the exchange of ions, which results in an increase in intramicellar supersaturation, and nucleation and growth of surfactant-encapsulated $BaCrO_4$ crystals. At molar equivalence, there is no net charge at the crystal surfaces with the consequence that the particles develop regular faces and a prismatic morphology in accordance with the unit cell symmetry, and aggregate into ordered chains by the mechanism proposed in Scheme 3-1. In contrast, a molar excess of CrO_4^{2-} offsets the growth anisotropy due to excess negative surface charge to produce spherical nanoparticles. The AOT molecules are also negatively charged, so there is negligible interaction (adsorption) of the surfactant onto the particle surface and therefore no additional driving force for surfactant-induced aggregation into longer range structures. An excess of Ba^{2+} ions, on the other hand, results in positively charged clusters that interact with the AOT headgroups to such an extent that further growth into regularly shaped nanoparticles is inhibited. Instead, large unstructured micellar aggregates are formed which precipitate from solution and slowly transform over a period of days and weeks into the filamentous structures (see Chapter 4).

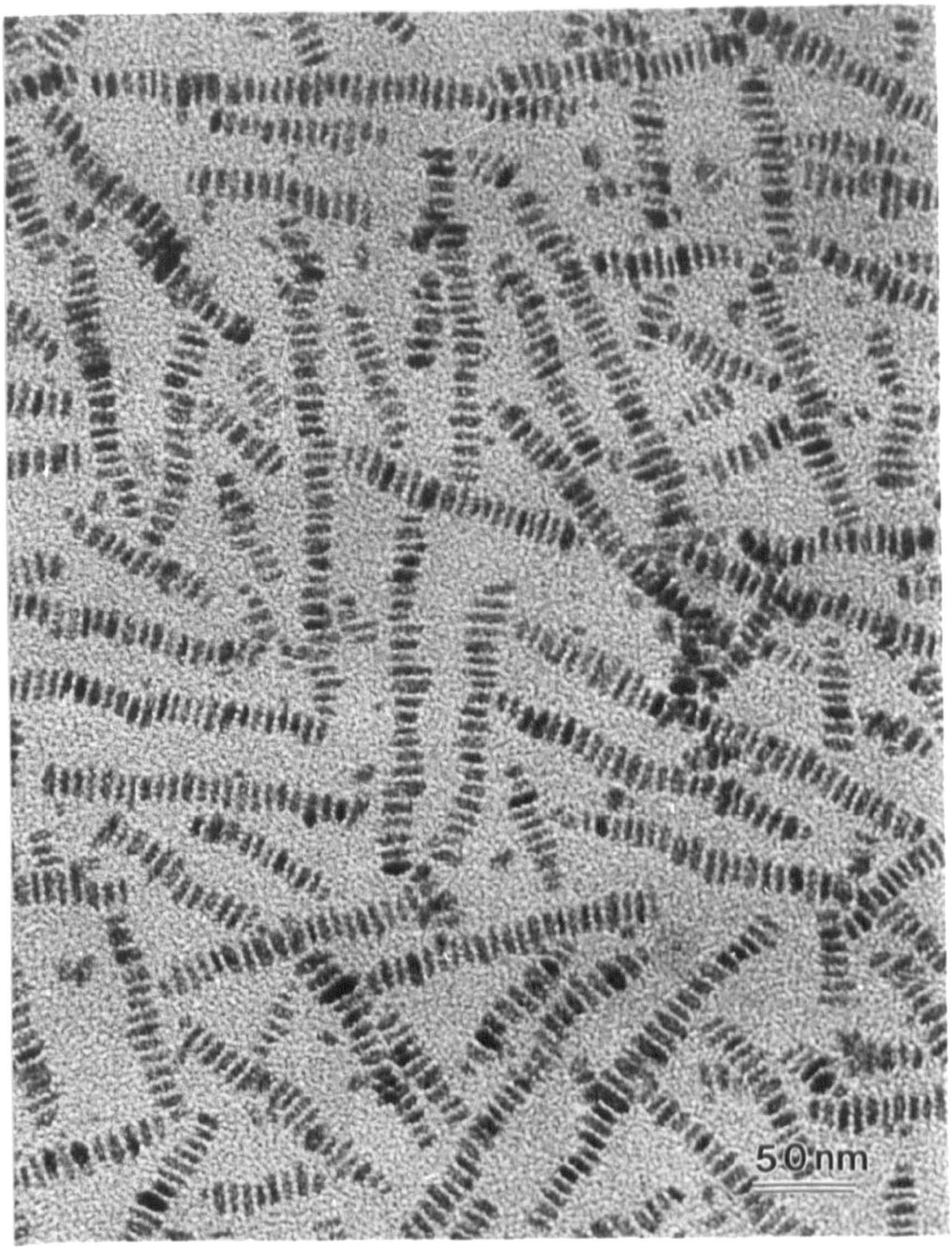

Figure 3-15 TEM image showing ordered chains of prismatic $BaSO_4$ nanoparticles prepared in AOT reverse microemulsion at $[Ba^{2+}]$: $[SO_4^{2-}]$ molar ratio ≈ 1 and $w = 10$. Scale bar = 50 nm

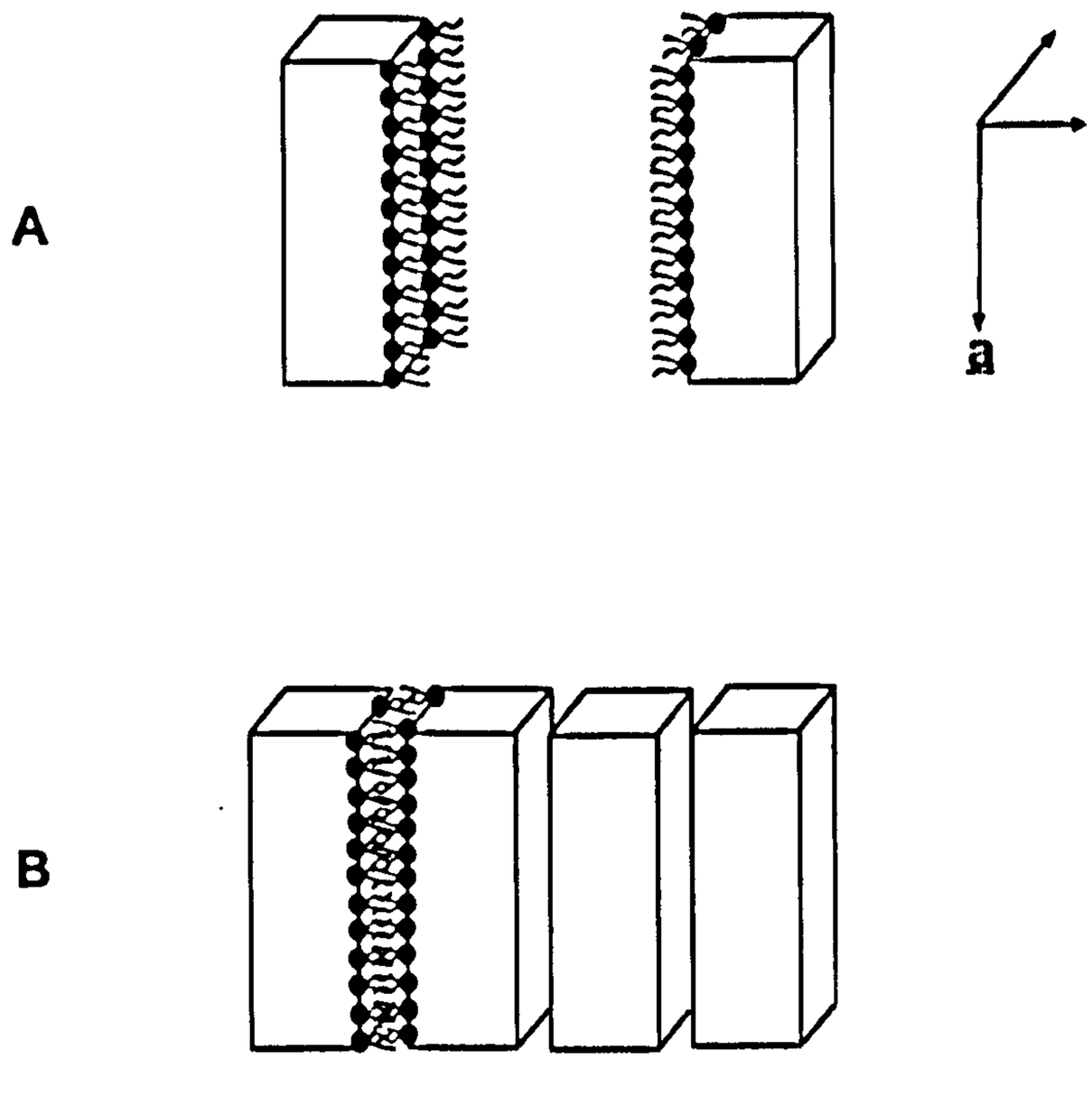

Scheme 3-1: Proposed model for the surfactant-induced self-assembly of nanoparticle chains and superlattices. (a) surfactant-coated prismatic $BaCrO_4$ nanoparticles are synthesized by controlled crystallization in microemulsion water droplets. For clarity, only one face is shown with associated surfactant molecules. (b) interdigitation of the surfactant monolayers is induced as the crystal faces develop in shape and size, resulting in preferential aggregation normal to both the prism long axis (crystallographic *a* axis) and largest side face. (c) aggregation in 2-D proceeds as the chains develop in length and number.

3.4.2 Chain structures formed in complex fluids

Most self-assembly nanostructures were obtained by a drying process on the TEM grids. In our case, we believe that the nanochain structures were formed in the complex fluid. This was confirmed by dynamic light scattering (DLS) analysis.

DLS data showed the appearance of two kinds of particles in the reaction solutions. The first one was microemulsion water droplets with a constant hydrodynamic radius of 5.8 ± 0.5 nm throughout the time course of the experiments. The second component, starting from ~70 nm in radius, appeared within 3 hours at 25°C (18 hours at 20°C), and progressively increased in scattering intensity over 6 hours at 25°C (section **3.3.5**). TEM results corresponding to the samples taken after 3 hours showed developing chain structures, suggesting that the second component was self-assembly of chain structures developing in the solution. DLS data also showed that the formation of the aggregates was coincident with a decrease in the number of microemulsion droplets (section **3.3.5**). Although the complexity of the system must prevent a conclusive analysis of the DLS data, they do suggest that the second component is associated with the formation of aggregates in the microemulsion fluid.

TEM images of the early stages of chain assembly showed low contrast structures with striped patterns, rather than isolated nanoparticles with prismatic morphology, suggesting that $BaCrO_4$ growth occurs in association and concurrent

with the self-organization of stacked micellar aggregates and not through sequential attachment of individual nanoparticles. One possibility is that the linear arrays spontaneously self-assemble in the microemulsion fluid from interactions between the hydrophobic tails of AOT molecules adsorbed onto the flat side faces of developing $BaCrO_4$ prismatic crystallites (Scheme 3-1). Taken together, the data suggest that spontaneous self- assembly of $BaCrO_4$ linear arrays occurs in the microemulsion fluid.

3.4.3 Relationship between chains and superlattices

Electron diffraction patterns recorded from superlattice structures showed d-spacings of 3.66 Å (002) and 2.78 Å (020) (section 3.3.2), indicating that the superlattice structures were indexed according to a superimposition of directions close to the [100] zone axis. This suggested that the prismatic crystals were single-domain particles elongated along the crystallographic *a* axis. Electron diffraction patterns recorded from chain structures showed a d-spacing of 4.56 Å (200), suggesting that the superlattices presented in chain motif and aligned with their long axis perpendicular to the plane of the superlattice. This was consistent with a morphology based on a set of {100} end faces with {010} and {001} side faces. The particles are showed in scheme 3-2.

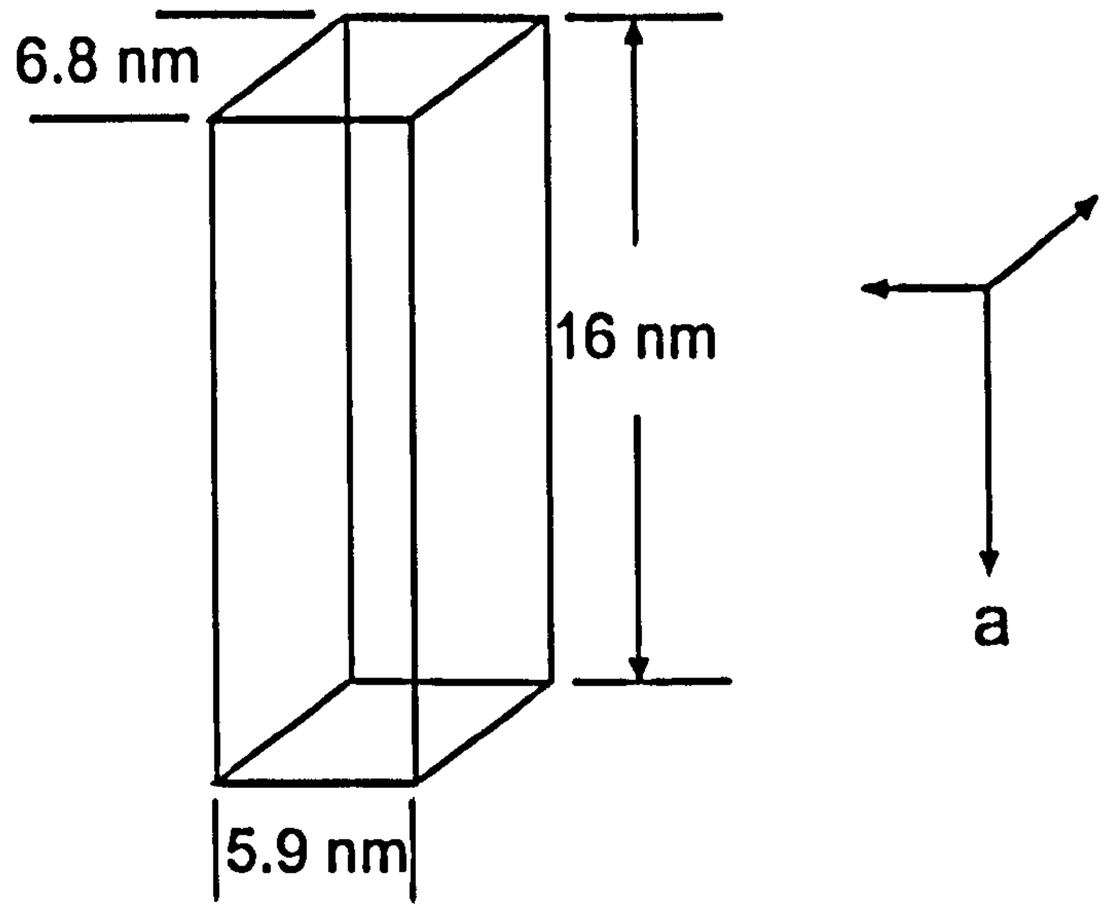

Scheme 3-2. Sketch of individual $BaCrO_4$ prismatic nanoparicles.

Electron diffraction patterns recorded from superlattice structures indicated two different types of side face, but failed to identify unequivocally the crystallographic nature of the side faces because of multiple arcing of the reflections arising from long-range disorder in the air-dried structures. Interestingly, a difference of only *ca.* 14 nm^2 (16×6.8 – 16×5.9 nm^2) in the surface areas of the two sets of side faces appears to be sufficient to stabilize the chain motif prior to superlattice formation, even though the latter has an increased number of particle-particle connections. Significantly, the particle width measured for crystals in the individual chains was commensurate with the shorter in-plane dimension of the superlattice particles, suggesting that the larger side faces were preferentially juxtaposed in the stacked linear array (Scheme 3-3).

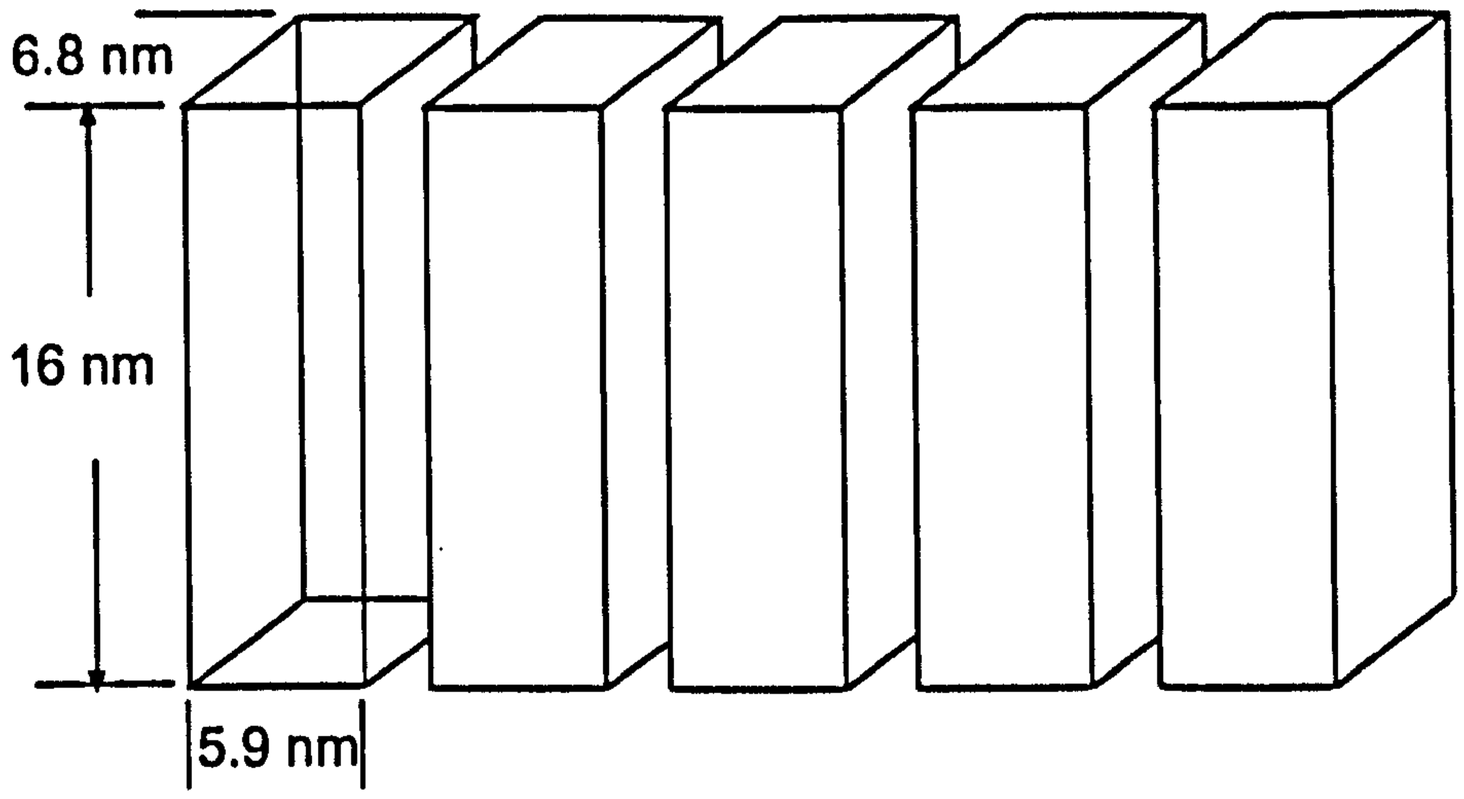

Scheme 3-3. Sketch of chain structure.

3.4.4 Existence of AOT between the particles

TEM images showed that the particles either in chain or superlattice structures were separated by a regular spacing of 2 nm, consistent with the presence of an bilayer of AOT molecules. Energy-dispersive X-ray analysis (EDXA) (section 3.3.2) recorded either from chain or superlattice structures also showed the existence of sulphur (Figure 3-5) along with Ba and Cr. Fourier Transform Infrared (FTIR) spectrum recorded from sedimentary materials (section 3.2.2.6) showed the existence of the ester group carbonyl ($\nu_{(C=O)}$, 1729 cm^{-1}) and the alkyl bands (2860, 2872, 2930, 2959 cm^{-1}), from the headgroups and the alkyl chains of

AOT molecules (Figure 3-16). Taken together, the data suggested the existence of AOT molecules associated with $BaCrO_4$ nanoparticles. This was confirmed by Thermogravimetric analysis (TGA) (section **3.2.2.7**), which showed a weight loss of 15% between 120 and 500°C, corresponding to removal of AOT from the inorganic materials. Loss of surfactant occurred principally around a temperature of 256°C which was 18°C lower than that determined for pure $Ba(AOT)_2$ (274°C).

Obviously, the AOT molecules adsorbed on the surfaces of $BaCrO_4$ nanoparicles with the headgroups and the hydrophobic tails formed a bilayer structure between the particles to reduce the free energy (Scheme 3-1). The prismatic shape and the uniform size of the particles, and large area of the side faces coated with AOT molecules induced self-assembly nanocrystal chain structures, suggesting the shape and the size distribution are the key controls of self-assembly nanostructures.

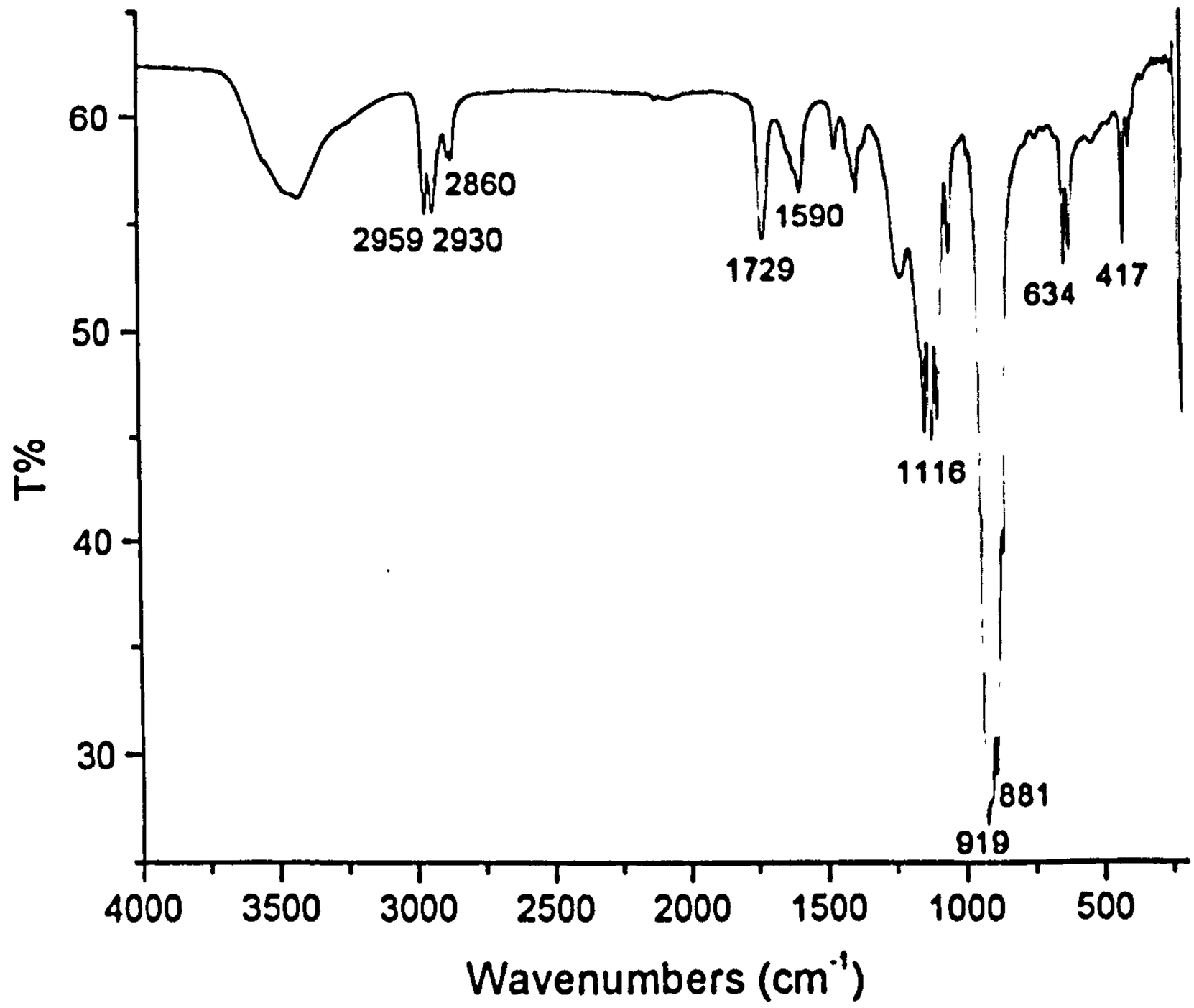

Figure 3-16 Fourier Transform Infrared (FTIR) spectrum of $BaCrO_4$ prepared in AOT reverse microemulsion at $[Ba^{2+}]$: $[CrO_4^{2-}]$ molar ratio ≈ 1 and w = 10 (section **3.2.2.1**). Sample was taken from the sedimented materials.

3.5 Conclusion

With this work we demonstrate that the morphology of barium chromate nanoparticles synthesized in AOT reverse microemulsion droplets at $w = 5 - 20$ can be controlled by the molar ratio of the reactants. When the molar ratio of reactants (Ba^{2+}/CrO_4^{2-}) was around chemical equivalence ($1.4:1 \leq [Ba^{2+}]:[CrO_4^{2-}] \leq 1:1.4$), prismatic shape nanoparticles were synthesized, and self-assembly into unusual linear structures in the complex liquid occurred. These subsequently formed two-dimensional superlattice structures that sedimented as a precipitate. At molar ratios of $2.7 : 1 \leq [Ba^{2+}] : [CrO_4^{2-}] \leq 5.5 : 1$, i.e with an excess of Ba^{2+}, nanofilaments were obtained, whereas spherical nanoparticles were formed at molar ratios of $1 : 4.6 \leq [Ba^{2+}] : [CrO_4^{2-}] \leq 1 : 2.7$, i.e with a molar excess of chromate. If the molar ratio of reactants was kept at 1:1, the prismatic shape nanoparticles can be synthesized over a wide range of w values ($w = [H_2O]/[NaAOT]$) from 5 to 20 and the particle sizes increased from 14.5×6.4×5.3 nm^3 to 18.3×10.0×8.1 nm^3 (Table 3-4), as the water content increased.

Previous research suggested that self-organization of lyophobic nanocrystals at high particle volume fractions into periodic arrays requires only a sufficiently narrow size distribution and the nanocrystal shape and sufficient stabilization provided by adsorbed capping ligands.[17, 20] Our work was in good agreement with that. These $BaCrO_4$ nanoparticles synthesized in AOT reverse micelles or

microemulsion droplets have a narrow enough size distribution (σ < 10%) and were capped by surfactant AOT. The prismatic shape assists in formation of close-packed nanocrystal arrays because a large area of AOT lamellar phase can be formed between two faces of prismatic shape particles. Most self-assembled superlattice structures were obtained by drying capped spherical nanoparticles on the TEM grids. However, in this case, self-assembly occurred in the solution phase, implying that the shape and the size of capped nanoparticles are very important factors in nanoparticle self-assembly.

3.6 References

[1] Wang Z.L., *Adv. Mater.*, 10, 13 (1998).

[2] Motte, L., Billoudet, F., Pileni, M.P., *J. Phys. Chem.*, 99, 16425 (1995).

[3] Bain, C.D., Troughton, E.B., Tao, Y.T., Evall, J., Whitesides, G.M., Nuzzo, R.G., *J. Am. Chem. Soc.*, 111, 7155 (1989).

[4] Bain, C.D., Whitesides, G.M., *J. Am. Chem. Soc.*, 111, 7164 (1989).

[5] Motte, L., Billoudet, F., Lacaze, E., Pileni, M.P., *Ade. Mater.*, 8, 1018 (1996).

[6] Ahmadi, T.S., Wang, Z.L., Green, T.C., Henglein, A., Ei-Sayed, M.A., *Science*, 272, 1924, (1996).

[7] Chang, S.S., Shih, C.W., Chen, C.D., Lai W.C., Wang, C.R.C., *Langmuir*, 15, 701 (1999).

[8] Murray, C.B., Kagan, C.R. Bawendi, M.G., *Science*, 270, 1335 (1995).

[9] Vossmeyer, T. Reck, G., Katsikas, L., Haupt, E.T.K., Schulz, B., Weller, H., *Science*, 267, 1476 (1995).

[10] Andres, R.P., Bielefeld J.D., Henderson, J.I., Janes, D.B., Kolagunta, V.R., Kubiak, C.P., Mahoney, W.J., Osifchin, R.G., *Science*, 273, 1690 (1996).

[11] Brust, M., Bethell, D., Schiffrin, D. J., Kiely, C. J., *Adv. Mat.*, 7, 795 (1995).

[12] Mirkin, C.A., Letsinger, R.L., Mucic, R.C. & Storhoff, J.J., *Nature*, 382, 607 (1996).

[13] Alivisatos, A.P., Johnsson, K.P., Peng, X.G., Wilson, T.E., Loweth, C.J., Bruchez, M.P., Schultz, P.G., *Nature* **382**, 609 (1996).

[14] Li, M., Wong, K.K.W., Mann S., *Chem. Mater.*, **11**, 23 (1999).

[15] Shenton, W., Davis, S. A., Mann, S., *Adv. Mater.*, **11**, 449 (1999).

[16] Shenton, W., Pum, D., Sleytr, U.B., Mann, S., *Nature*, **389**, 585 (1998).

[17] Dieluweit, S., Pum, D., Sleytr, U.B., *Supramol. Sci.*, **5**, 15 (1998).

[18] Davis, S.A., Burkett, S.L., Mendelson, N.H., Mann, S., *Nature*, **385**, 420 (1997).

[19] Davis, S.A., Patel, H.M., Mayes E.L., Mendelson, N.H., Franco, G., Mann S., *Chem. Mater.*, **10**, 2516 (1998).

[20] Petit, C., Taleb, A., Pileni, M.P., *Adv. Mater.*, **10**, 259 (1998).

[21] Taleb, A., Petit, C., Pileni, M. P., *Chem.Mater.*, **9**, 950 (1997).

[22] Sager, W.F.C., *Current Opinion in Colloid & Interface Science*, **3**, 276 (1998).

[23] Hopwood, J., Mann, S., *Chem. Mater.*, **9**, 1819 (1997).

[24] Veith, H. J., *Organic Mass Spectrometry*, **11**, 629 (1976)

Chapter 4

Emergence of Morphological Complexity in Barium Sulfate Fibres Synthesized in AOT Microemulsions.

(Published in *Langmuir*, 16, 7088-7094, 2000)

4.1 Introduction

Reverse micelles and microemulsions formulated with the anionic surfactant sodium bis(2-ethylhexyl) sulfosuccinate (Aerosol OT, AOT) have been extensively used for the synthesis of inorganic nanoparticles of barium chromate,[1] barium sulfate,[2] calcium sulfate,[3] silica,[4] silver,[5,6] and copper.[7, 8] The principal reason for using microemulsions is that particle sizes and corresponding size distributions can be readily controlled by reaction confinement. However, in some studies aggregation of the primarily formed nanoparticles led to uncontrolled formation of micro- or even millimeter-sized clusters. In recent years interest has shifted from making monodisperse nanoparticles of different materials with mostly a spherical shape to controlling particle morphology (anisotropic and high-axial-ratio particles), introducing crystallinity and oriented growth. Further growth and aggregation of the initially formed nanoparticles results in the formation of higher-order structures such as $BaCrO_4$ chains and filaments,[1] $BaSO_4$ filaments[2] and cones,[9] $CaSO_4$[3] and $BaCO_3$[10] nanowires. These studies suggest that complex fluids can be used not only to control the size and shape of inorganic nanoparticles but as dynamical systems for the spontaneous organization of inorganic materials beyond the mesoscopic length scale. This principle has also been exemplified through a number of studies involving inorganic precipitation in bicontinuous microemulsions,[11,12] lyotropic hexagonal mesophases,[13,14] and block copolymer

micelles.[15] In each case, synergistic interactions at the surfactant - inorganic interface result in new instability thresholds and the subsequent emergence of complex forms that represent compromises between competing force fields, such as membrane curvature and lattice energy.

In the past a few years, a large number of investigations focused on the optical, electrical and magnetic properties of the nanoparticles synthesized and on the study of quantum size effects. Less attention has been paid to the progress obtained in recent years on what actually controls the size and shape of the particles formed in microemulsion system, as well as the effects of surfactant and oil chain length and salt concentration. A generally valid theory is still not available.[16]

In this chapter, we describe the processes that give rise to the synthesis of unusual $BaSO_4$-surfactant filamentous structures by reaction of $Ba(AOT)_2$ reverse micelles with NaAOT microemulsion droplets containing Na_2SO_4 at $w = 10$ and $[Ba^{2+}] : [SO_4^{2-}]$ molar ratio $\approx 5 : 1$. The structures originate within loosely associated aggregates of discrete surfactant-encapsulated $BaSO_4$ nanoparticles that internally reorganize into an array of co-aligned crystalline filaments. We use TEM to follow the early stages of growth, which involves the formation of spiral-shaped bundles that subsequently grow uni-directionally to produce the complex mature architectures. Our results indicate that morphological complexity is a

consequence of surfactant-inorganic interactions operating across a range of length scales.

This study, together with previous work,[3,10] suggests that the evolution of these micrometre-scale structures from nanoscale reaction environments occurs through similar mechanisms, and that the elucidation of these generic processes will lead to novel developments in the synthesis of inorganic materials with complex form.[17]

4.2 Materials and Methods

4.2.1 Materials

All materials were of analytical grade (purity >98%) and used without further purification.

Table 4-1 Chemicals used in this chapter

Common name	Chemical name	Formula	Molecular weight	Supplier
	sodium sulphate	Na_2SO_4	142.0	Aldrich
	sodium chromate	Na_2CrO_4	162.0	Aldrich
	phosphotungstic acid	$H_3PW_{12}O_{40}$	2880.2	AGAR
	barium chloride	$BaCl_2$	208.2	Aldrich
NaAOT	sodium bis(2-ethylhexyl) sulphosuccinate	$C_{20}H_{37}O_4SO_3Na$	444.6	BDH
isooctane	2,2,4-trimethyl pentane	C_8H_{18}	114.0	Aldrich

4.2.2 Methods

4.2.2.1 Synthesis of barium bis(2-ethylhexyl) sulfosuccinate [$Ba(AOT)_2$]

$Ba(AOT)_2$ (MW = 980.47) was prepared by direct reaction of sodium AOT [sodium bis(2-ethylhexyl) sulfosuccinate] and barium chloride in water (Section **3.2.1.2**).

4.2.2.2 Preparation of barium sulfate nanofilaments in AOT water-in-oil reverse microemulsion

Synthesis of $BaSO_4$ in AOT water-in-oil microemulsion was undertaken as follows. Typically, 1.8 mL of aqueous Na_2SO_4 solution (20 to 80 mM) were added with shaking to 100 mL of a 100 mM solution of NaAOT dissolved in isooctane to give a suspension of microemulsion droplets with water to surfactant molar ratio $w = [H_2O]/[NaAOT] = 10$. To introduce Ba^{2+} into the reaction, a small amount of $Ba(AOT)_2$ reverse micelles, dissolved in isooctane (4.0 mL, 50 mM, $w < 1$), was added to 100 mL of the sulfate-containing microemulsion to give final molar ratios NaAOT : $Ba(AOT)_2$ = 50 : 1, and $[Ba^{2+}] : [SO_4^{2-}] = 5.5 : 1$ to 1.4 : 1. The mixture was then incubated at 4 to 40°C and samples removed from 1 hour to 35 days.

4.2.2.3 Preparation of barium chromate nanofilaments in AOT water-in-oil reverse microemulsion

Similar to section 4.2.2.2, 1.8 mL of aqueous Na_2CrO_4 solution (20 to 40 mM) were added with shaking to 100 mL of a 100 mM solution of NaAOT dissolved in isooctane to give a suspension of microemulsion droplets with water to surfactant molar ratio $w = [H_2O]/[NaAOT] = 10$. $Ba(AOT)_2$ reverse micelles, dissolved in isooctane (4.0 mL, 50 mM, $w < 1$), was then added to 100 mL of the chromate-

containing microemulsion to give final molar ratios NaAOT : $Ba(AOT)_2$ = 50 : 1, and $[Ba^{2+}]$: $[CrO_4^{2-}]$ = 5.5 : 1 to 2.7 : 1.

4.2.2.4 Preparation of barium phosphotungstate nanofilaments in AOT water-in-oil reverse microemulsion

Similar experiments as section **4.2.2.2** were undertaken with mixture of $Ba(AOT)_2$ reverse micelles (50 mM in isooctane, w < 1) and NaAOT microemulsion containing aqueous phosphotungstic acid ($H_3PW_{12}O_{40}$, 7 mM in water, w = 10) to give final molar ratios NaAOT : $Ba(AOT)_2$ = 50 : 1, and $[Ba^{2+}]$: $[PW_{12}O_{40}^{3-}]$ = 15 : 1.

4.2.2.5 Transmission electron microscopy (TEM)

Samples for transmission electron microscopy (TEM) were collected separately using a glass pipette from both the transparent liquid phase and precipitated materials, and deposited onto formvar-coated, carbon-reinforced, 3 mm diameter, copper electron microscope grids, which were washed with pure isooctane after air-dried.

TEM analysis was performed in bright field mode using either a JEOL 2000FX high –resolution electron microscopy operating at 200keV or a JEOL 1200EX electron microscopy operating at 120keV (section **2.3.1**). Selected area electron

diffraction (SAED) (section **2.3.2**) and energy-dispersive X-ray analysis (EDXA) (section **2.3.3**) were also used to characterize the samples imaged by TEM.

4.2.2.6 Powder X-ray diffraction (PXRD)

Samples for powder X-ray diffraction (PXRD) analysis were taken from precipitated materials and deposited directly on the sample holder, air-dried. The data were collected for 2θ values from 4 to 60° using a PW1710 diffractometer (section **2.3.5**). The diffraction patterns were then indexed with reference to the unit cell of barium sulfate a, b, c, = 8.909, 5.467, 7.188 Å, according to the Cambridge database given in table 4-2.[9]

Table 4-2 X-ray diffraction data for barium sulfate.

D (Å)	{hkl}	I / I_o	D (Å)	{hkl}	I / I_o
8.909	100		2.5550	021	
7.188	001		2.4901	212	13
5.5942	101		2.4560	121	
5.4670	010		2.4529	311	
4.6596	110		2.3298	220	14
4.4545	200	16	2.3138	103	6
4.3514	011	30	2.2893	302	8
3.9100	111	50	2.2272	400	
3.7864	201	12	2.2163	221	25
3.5940	002	30	2.1945	013	
3.4533	210	100	2.1757	022	
3.3330	102	70	2.1308	113	
3.1127	211	95	2.1275	401	
3.0032	012		2.1136	122	
2.9697	300		2.1116	312	
2.8458	112	50	2.1101	203	
2.7971	202		2.0626	410	19
2.7447	301	15	2.0112	320	
2.7335	020		1.9686	213	
2.6133	120	45	1.9550	222	
2.6095	310		1.9368	321	7

a = 8.909 Å b = 5.467 Å c = 7.188 Å

The d-spacings and unit cell dimensions a, b, c are from Cambridge database, Daresbury, U.K. The intensities are those reported in the JCPDS cards.

4.2.2.7 Thermogravimetric analysis (TGA)

Samples for thermogravimetric analysis were taken from the sedimentary materials and washed with isooctane for three times to remove free AOT molecules, then air-dried. Thermogravimetric analysis was performed with Simultaneous Thermal Analysis STA409EP. The experiments were typically run on powdered samples at 24 – 600°C at 5°C/min under flowing nitrogen (section **2.3.8**).

4.2.2.8 Fourier Transform Infrared spectroscopy (FTIR)

Samples for Fourier Transform Infrared (FTIR) analysis were taken from the sedimentary materials and washed with isooctane for six times to remove AOT molecules, air-dried. The spectra were recorded at 4000-400 cm^{-1} using KBr discs. The Fourier Transform Infrared analysis was performed with a Perkin Elmer Spectrum RX spectrophotometer (section **2.3.9**).

4.2.2.9 Small-angle X-ray scattering (SAXS)

Samples for small angle X-ray scattering (SAXS) were collected from the sedimentary materials and air-dried. The data were obtained using an Enraf Nonius X-ray generator (section **2.3.6**).

4.2.2.10 Ultraviolet and visible spectroscopy (UV-vis)

UV-vis spectroscopy was used to measure the turbidity (τ) of the solutions. Samples for turbidity measurements were reaction solutions of the mixture of $Ba(AOT)_2$ micelles and sulfate-containing NaAOT microemulsions. The turbidity as a function of time was determined by monitoring the change of the optical transmission with time at 600 nm (section **2.3.10**).

4.3 Results and Discussion

4.3.1 Description of nanofilaments

4.3.1.1 Barium sulfate

Isooctane mixtures of sulfate-containing NaAOT reverse microemulsion droplets (w = 10, $[Na_2SO_4]$ = 20 to 80 mM) and $Ba(AOT)_2$ reverse micelles (w < 1) (molar ratio of $[Ba^{2+}] : [SO_4^{2-}]$ = 5.5 : 1 to 1.4 : 1) were initially colorless and transparent solutions but became turbid within 24 hours at pH 7 and room temperature (18 – 22°C), after which a white precipitate was slowly formed. TEM images corresponding to the precipitate showed over 95% of the particles were nanofilaments with high aspect ratio (Figure 4-1). The filaments emanated from one end of the fibre, which was usually coiled, and became more divergent as they increased in length towards the other tip. They often terminated along a well-defined uniform growth edge. At the flattened end, the filaments often dispersed into thin bundles or individual filaments (Figure 4-2). The filaments grew with time up to 20 μm in length and 20 ~ 200 nm in width.

4.3.1.2 Barium chromate

Analogous experiments involving the addition of $Ba(AOT)_2$ reverse micelles (50 mM, w < 1) to Na_2CrO_4 (20 to 40 mM) containing NaAOT microemulsion droplets (100 mM, w = 10) (NaAOT : $Ba(AOT)_2$ = 50 : 1, and $[Ba^{2+}] : [CrO_4^{2-}]$ = 5.5 : 1 to 2.7 : 1) also produced high-aspect-ratio fibrous precipitates of $BaCrO_4$

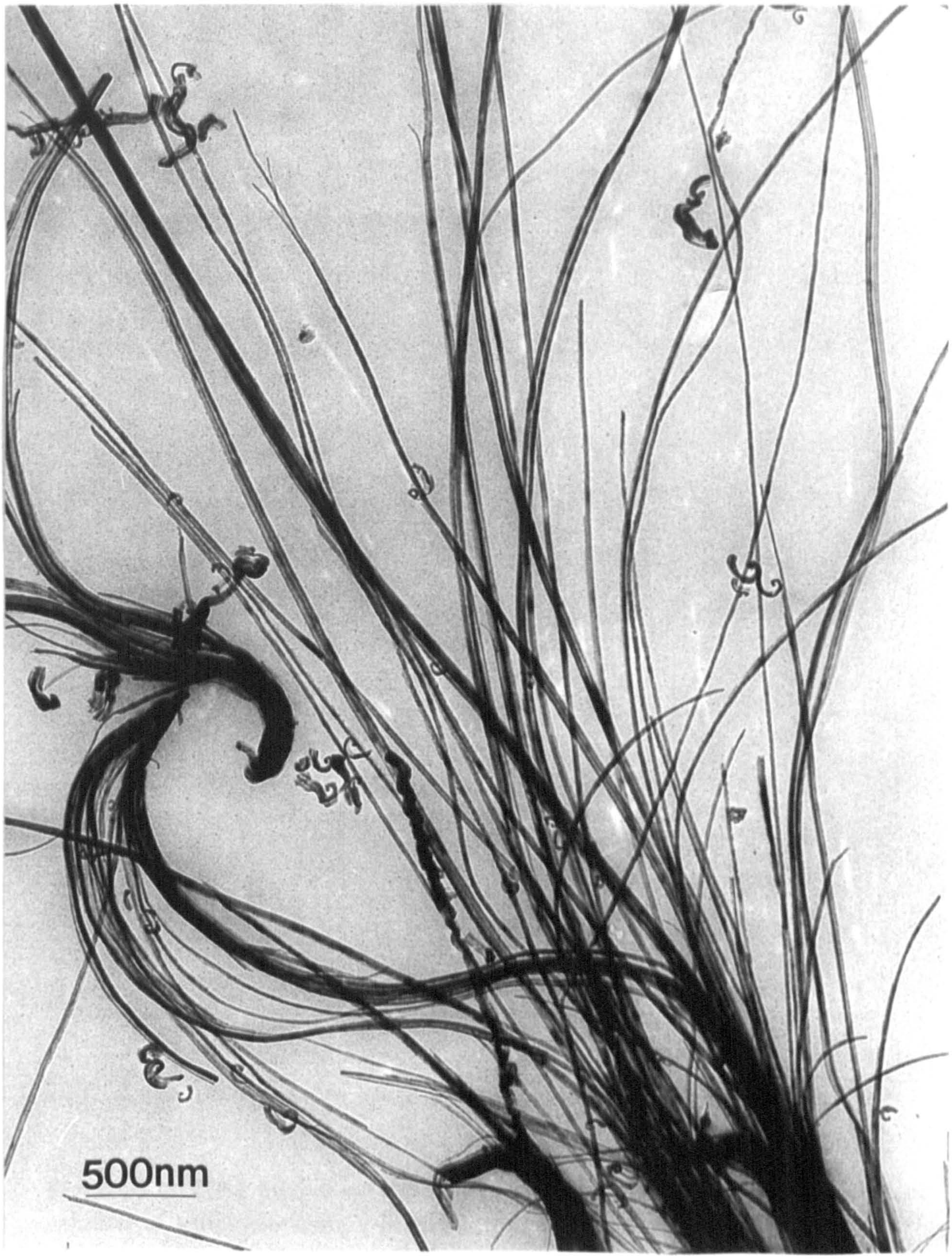

Figure 4-1: TEM image of $BaSO_4$ fibres produced by reaction in the mixture of sulfate-containing NaAOT reverse microemulsion droplets (w=10) and $Ba(AOT)_2$ reverse micelles ($w < 1$) at room temperature, NaAOT : $Ba(AOT)_2$ = 50 : 1, and $[Ba^{2+}] : [SO_4^{2-}]$ = 5.5 : 1 to 1.4 : 1. Scale bar = 500 nm.

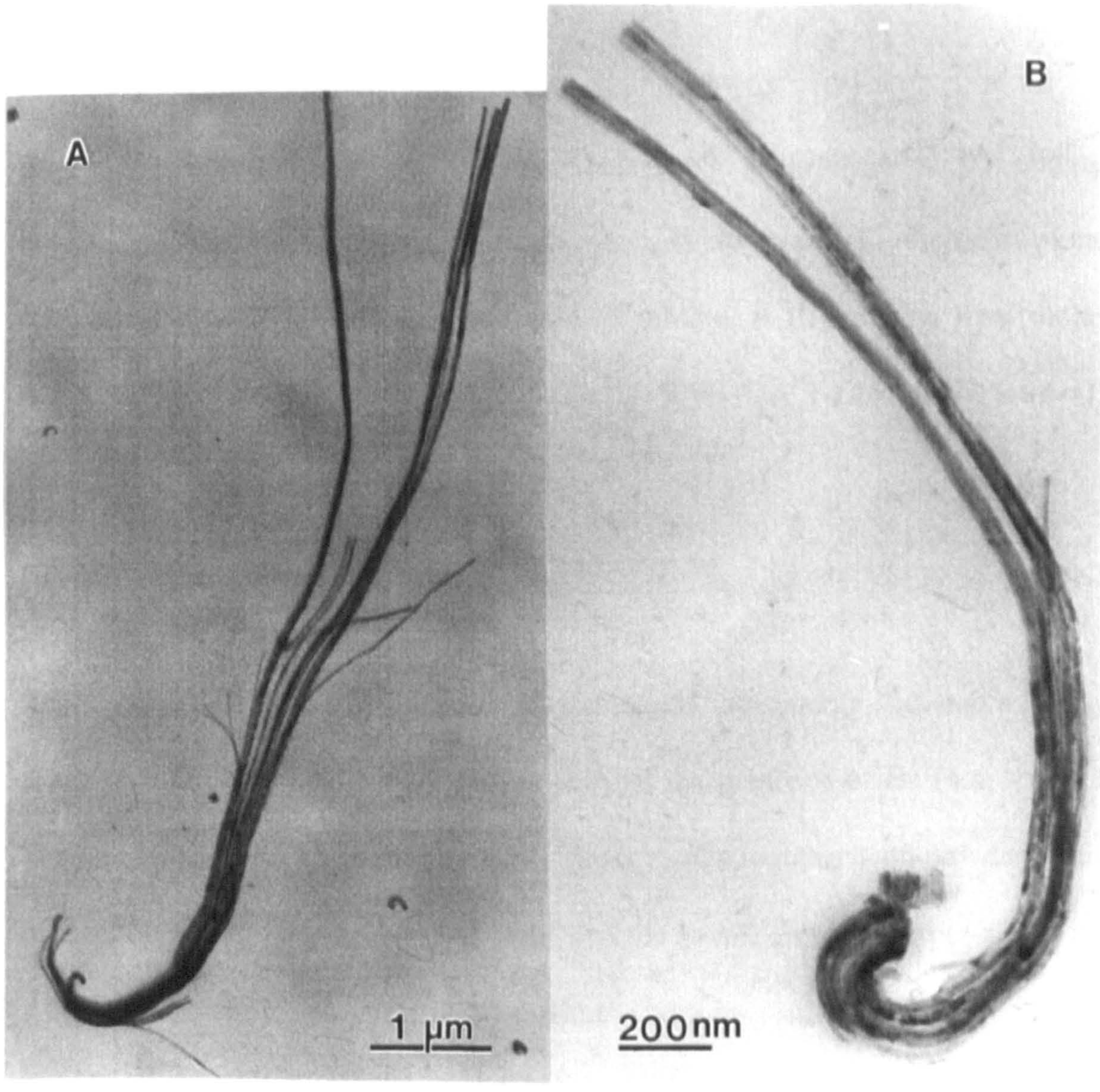

Figure 4-2: TEM images of $BaSO_4$ fibres produced by reactions in isooctane solution of sulfate-containing NaAOT reverse microemulsion droplets (w = 10) and $Ba(AOT)_2$ reverse micelles (w < 1) at room temperature, NaAOT : $Ba(AOT)_2$ = 50 : 1, and $[Ba^{2+}]$: $[SO_4^{2-}]$ = 5.5 : 1 to 1.4 : 1, showing that the filaments emanated from one coiled end, and became more divergent at the other tip, where they terminated often along a well-defined uniform growth edge. Scale bars, **a)** = 1μm, **b)** = 200 nm.

(Figure 4-3) (section 4.2.2.3 and Chapter 3). The $BaCrO_4$ nanofilaments have the same morphologies as the $BaSO_4$ nanofilaments.

4.3.1.3 Barium phosphotungstate

Analogous nanofilaments of $Ba_3[PW_{12}O_{40}]_2$ were also produced by adding $Ba(AOT)_2$ reverse micelles (50 mM, $w < 1$) to NaAOT microemulsions containing aqueous phosphotungstic acid (7 mM, $w = 10$) to give final molar ratios NaAOT : $Ba(AOT)_2$ = 50 : 1, and $[Ba^{2+}] : [PW_{12}O_{40}^{3-}]$ = 15 : 1 (Figure 4-4).

4.3.2 Identification of nanofilaments

TEM imaged nanofilaments were characterized by energy-dispersive X-ray analysis (EDXA). The EDXA spectra showed the presence of Ba (4.4, 4.8, 5.1 keV) and S (2.3, 2.6 keV) (Figure 4-5). These results together with powder X-ray diffraction results (Figure 4-6) indicated that the nanofilaments synthesised in the AOT microemulsions were crystalline barium sulfate. TEM imaged nanofilaments were also characterized by selected area electron diffraction (SAED). The results showed that these structures are barite single crystals elongated along the [010] axis (Figure 4-7a), which is consistent with previous work.[2] Diffraction patterns were indexed according to barite reference data (Cambridge database) given in table 4-2. In addition, high resolution TEM images showed lattice fringes corresponding to $BaSO_4$ (002) d-spacings (3.6 Å) (Figure 4-7b).

Figure 4-3: TEM image of $BaCrO_4$ fibres produced by reaction in isooctane solution of chromate-containing NaAOT reverse microemulsion droplets ($w = 10$) and $Ba(AOT)_2$ reverse micelles ($w < 1$) at room temperature, NaAOT : $Ba(AOT)_2$ = 50 : 1, and $[Ba^{2+}] : [CrO_4^{2-}]$ = 5.5 : 1 to 2.7 : 1. Scale bar = 500 nm.

Figure 4-4: TEM image of $Ba_3[PW_{12}O_{40}]_2$ fibres produced by reaction in isooctane solution of phosphotungstate-containing NaAOT reverse microemulsion droplets (w = 10) and $Ba(AOT)_2$ reverse micelles (w < 1) at room temperature, NaAOT : $Ba(AOT)_2$ = 50 : 1, and $[Ba^{2+}] : [PW_{12}O_{40}^{3-}]$ = 15 : 1. Scale bar = 500 nm.

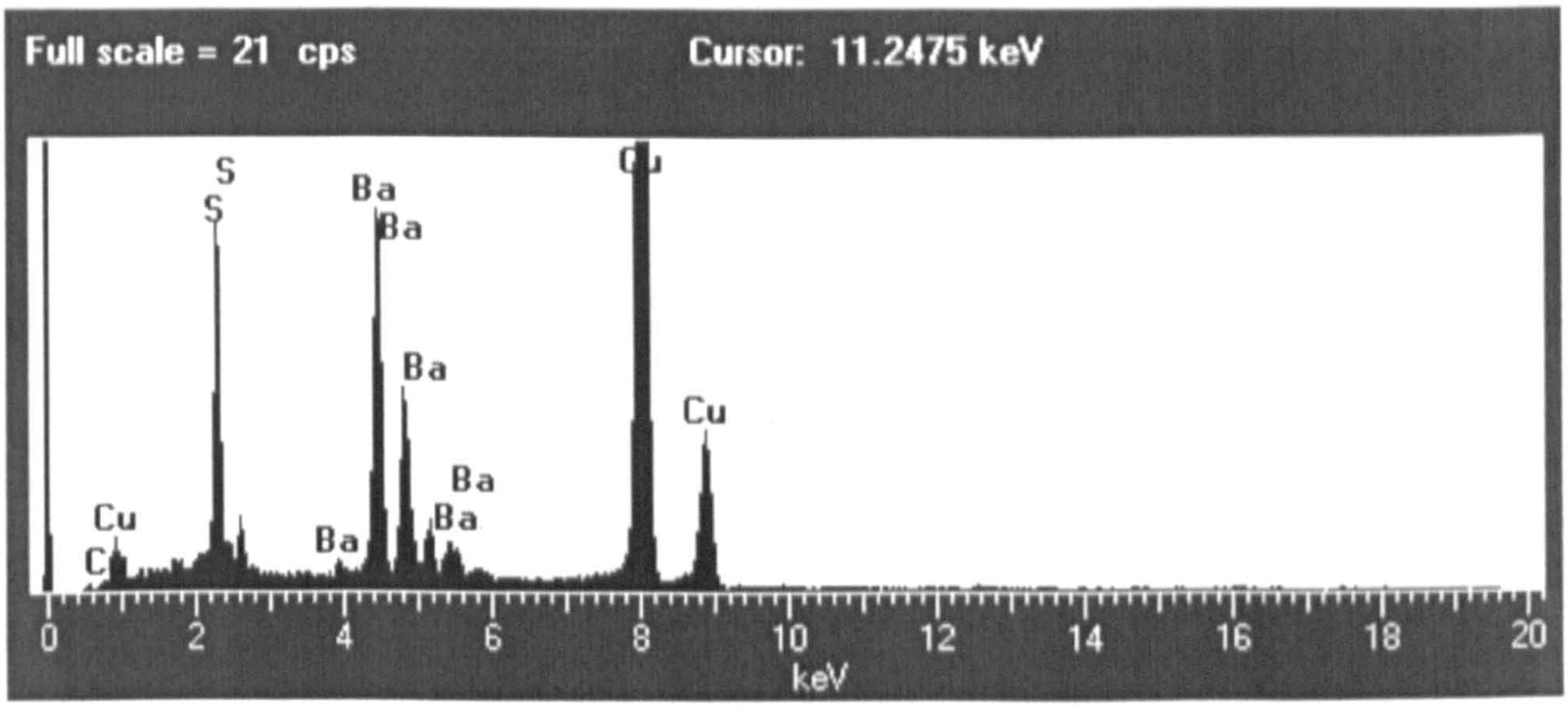

Figure 4-5: Energy-dispersive X-ray analysis (EDXA) spectrum of the filaments showing the presence of barium and sulfur, corresponding to barium sulfate and AOT surfactant. Copper peaks are due to the sample grid.

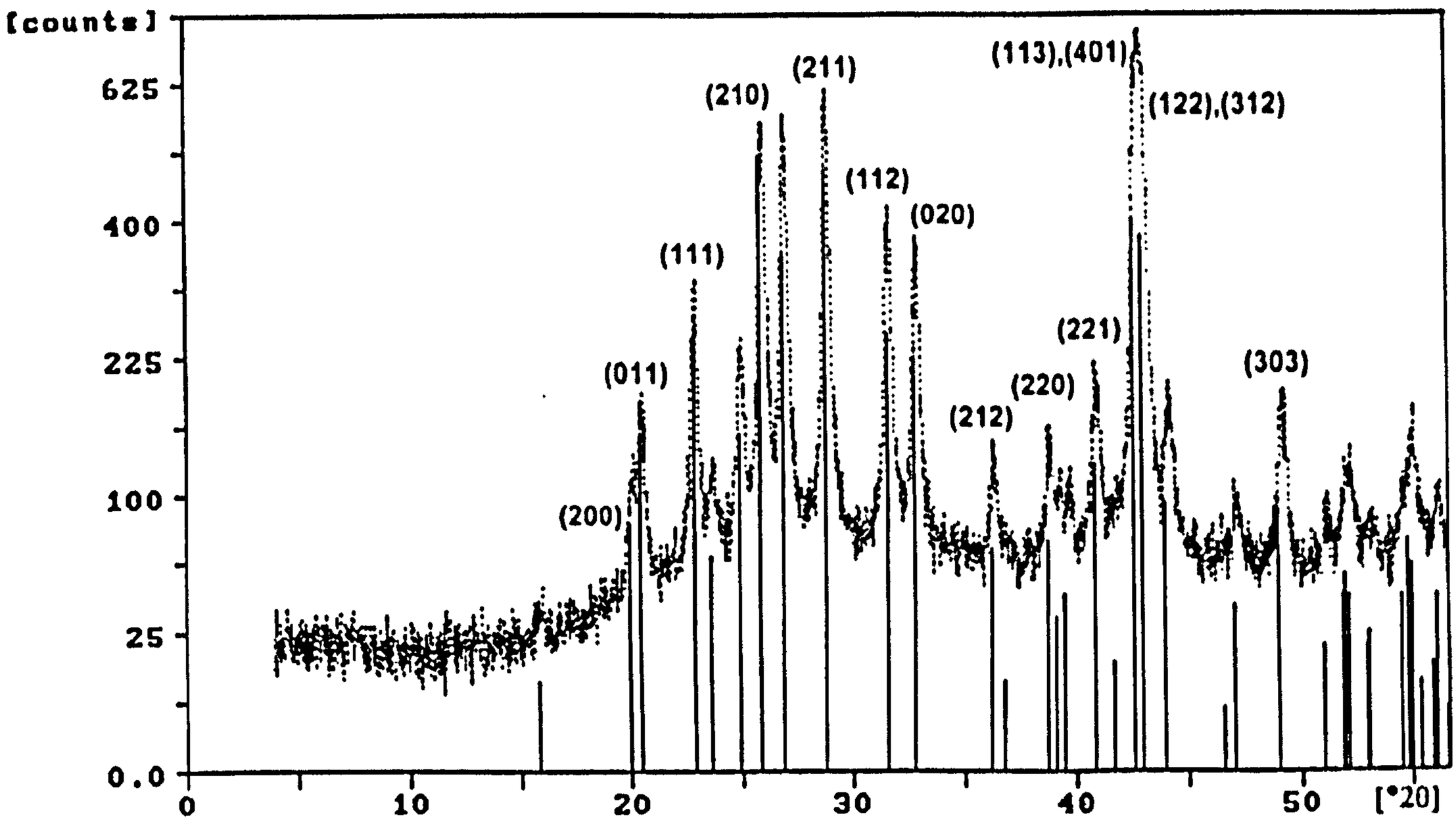

Figure 4-6: Powder X-ray diffraction (PXRD) patterns of $BaSO_4$ filaments synthesized in isooctane mixtures of sulfate-containing NaAOT reverse microemulsion droplets ($w = 10$) and $Ba(AOT)_2$ reverse micelles ($w < 1$) at room temperature, NaAOT : $Ba(AOT)_2$ = 50 : 1, and $[Ba^{2+}] : [SO_4^{2-}]$ = 5.5 : 1 to 1.4 : 1 (·····), standard $BaSO_4$ powder (—).

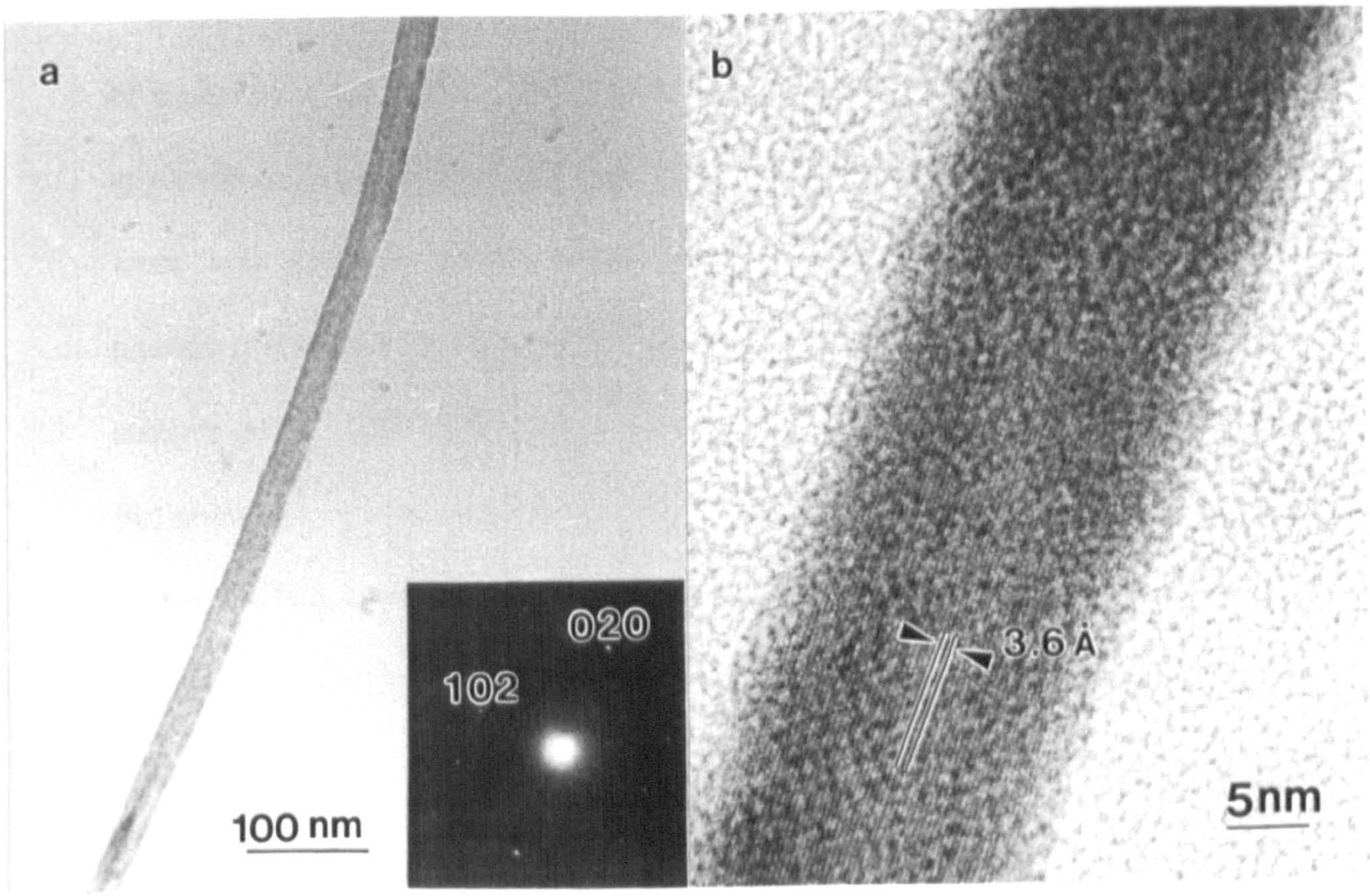

Figure 4-7: TEM images of single $BaSO_4$ fibres produced by reaction in isooctane solution of sulfate-containing NaAOT reverse microemulsion droplets (w = 10) and $Ba(AOT)_2$ reverse micelles (w < 1) at room temperature, NaAOT : $Ba(AOT)_2$ = 50 : 1, and $[Ba^{2+}] : [SO_4^{2-}]$ = 5.5 : 1 to 1.4 : 1. **a)** low magnification image (scale bar = 100 nm) and electron diffraction pattern showed that the filament elongated along the [010] axis; **b)** high resolution TEM image (scale bar = 5 nm) showed lattice fringes correspond to $BaSO_4$ (002) d-spacings (3.6 Å).

4.3.3 The existence of AOT molecules on $BaSO_4$ nanofilaments

High magnification TEM images showed that most of the $BaSO_4$ fibres consisted of a closely packed bundle of 20 to 50 nm-wide filaments that were co-aligned approximately parallel to the fibre axis (Figure 4-8). Presumably, the packing force was AOT molecules. To observe the influence of AOT on $BaSO_4$ nanofilaments, the sedimented materials were washed 6 times with isooctane to remove AOT. The TEM image corresponding to the washed sample (Figure 4-9b) showed larger spacings between the fibres comparing with unwashed sample (Figure 4-9a), implying that AOT molecules may exist between the filaments which can be removed by washing. However, for thick bundles of $BaSO_4$ filaments, AOT molecules buried in the middle of the bundles were difficult to remove and therefore, fourier transform infra-red (FTIR) spectrum recorded on samples washed repeatedly with isooctane still showed the presence of AOT ($\nu_{C=O}$, 1723 cm^{-1}; ν_{C-H} (alkyl), 2961-2900 cm^{-1}; $\nu_{C(O)OC}$(ester), $\nu_{S=O}$, 1181 cm^{-1}) as well as inorganic sulfate and sulfonate moieties (610, 636, 1075, 1122 cm^{-1}) (Figure 4-10), suggesting that the fibres were hybrid composites of closely associated inorganic and organic phases. This was also confirmed by TG analysis, which showed a 11.31% weight loss between 160 and 500°C, corresponding to removal of AOT. Loss of the surfactant occurred principally around a temperature of 256°C which was 18°C lower than that determined for pure $Ba(AOT)_2$ (274°C).

Figure 4-8: TEM image of a bundle of $BaSO_4$ fibres produced by reaction in isooctane solution of sulfate-containing NaAOT reverse microemulsion droplets ($w = 10$) and $Ba(AOT)_2$ reverse micelles ($w < 1$) at room temperature, NaAOT : $Ba(AOT)_2$ = 50 : 1, and $[Ba^{2+}] : [SO_4^{2-}]$ = 5.5 : 1 to 1.4 : 1, showed that the filaments were co-aligned approximately parallel to the fibre axis. Scale bar = 100 nm.

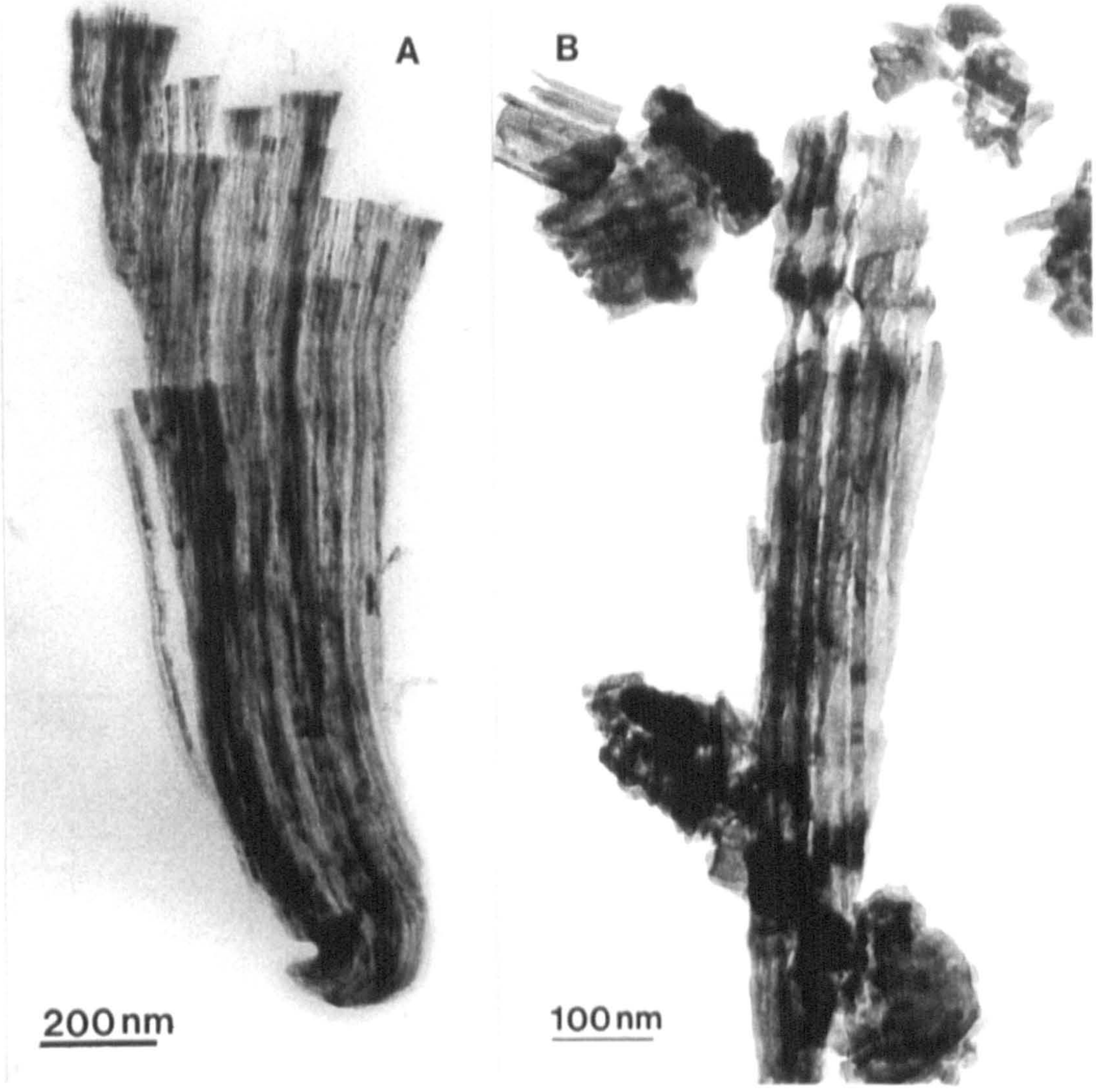

Figure 4-9: TEM images of $BaSO_4$ fibres produced by reactions in isooctane mixtures of sulfate-containing NaAOT reverse microemulsion droplets (w = 10) and $Ba(AOT)_2$ reverse micelles (w < 1) at room temperature, NaAOT : $Ba(AOT)_2$ = 50 : 1, and $[Ba^{2+}]$: $[SO_4^{2-}]$ = 5.5 : 1 to 1.4 : 1. **a)** unwashed sample; **b)** washed with isooctane for 6 times. Scale bars = 200 nm.

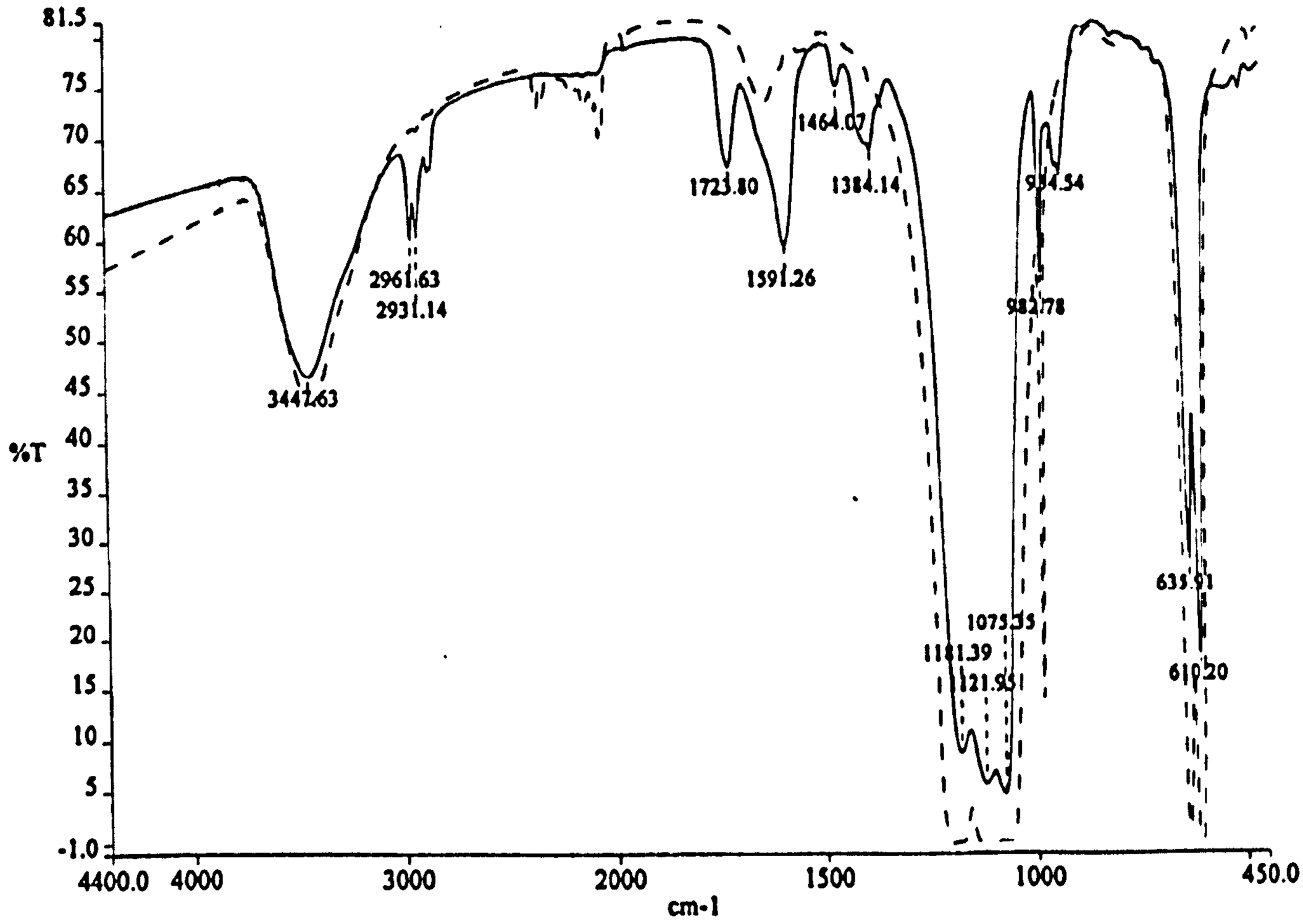

Figure 4-10: Fourier transform infra-red (FTIR) spectra of standard $BaSO_4$ (- - -) and $BaSO_4$ fibres produced by reactions in isooctane mixtures of sulfate-containing NaAOT reverse microemulsion droplets (w = 10) and $Ba(AOT)_2$ reverse micelles (w < 1) at room temperature, NaAOT : $Ba(AOT)_2$ = 50 : 1, and $[Ba^{2+}] : [SO_4^{2-}]$ = 5.5 : 1 to 1.4 : 1 (—), showed the presence of AOT.

No ordered mesostructures were observed for fibres analysed by small-angle XRD. Taken together, the data suggested the existence of AOT molecules associated with $BaSO_4$ nanofilaments.

Interestingly, some single crystalline structures were occasionally twisted and coiled into remarkable helical forms (Figure 4-11). Further work is required to determine whether such structures arise from internal force fields in the surfactant-barite composite (non-axial strain, screw dislocations, rotational and topological defects, for example) or external parameters, such as shear and convection in the complex fluids. We also note that the AOT molecule has eight possible chiral forms, and although we use a mixture of these, we cannot rule out the possibility that the helical structures might be associated with stereoselective recognition of a single chiral conformation during the growth of a barite single crystal.

4.3.4 Temperature dependence

The size, shape and rate of formation of the $BaSO_4$ filaments were dependent on the temperature of the reaction medium. At room temperature (18-22°C), the isooctane mixtures attained a maximum turbidity after 3 days (Figure 4-12). In contrast, only a slight turbidity was observed after 5 days at 4°C, whereas a turbid solution was visible within 4 hours at 30°C. TEM images showed only short, straight filament bundles at 4°C (Figure 4-13), and highly curved fibres and

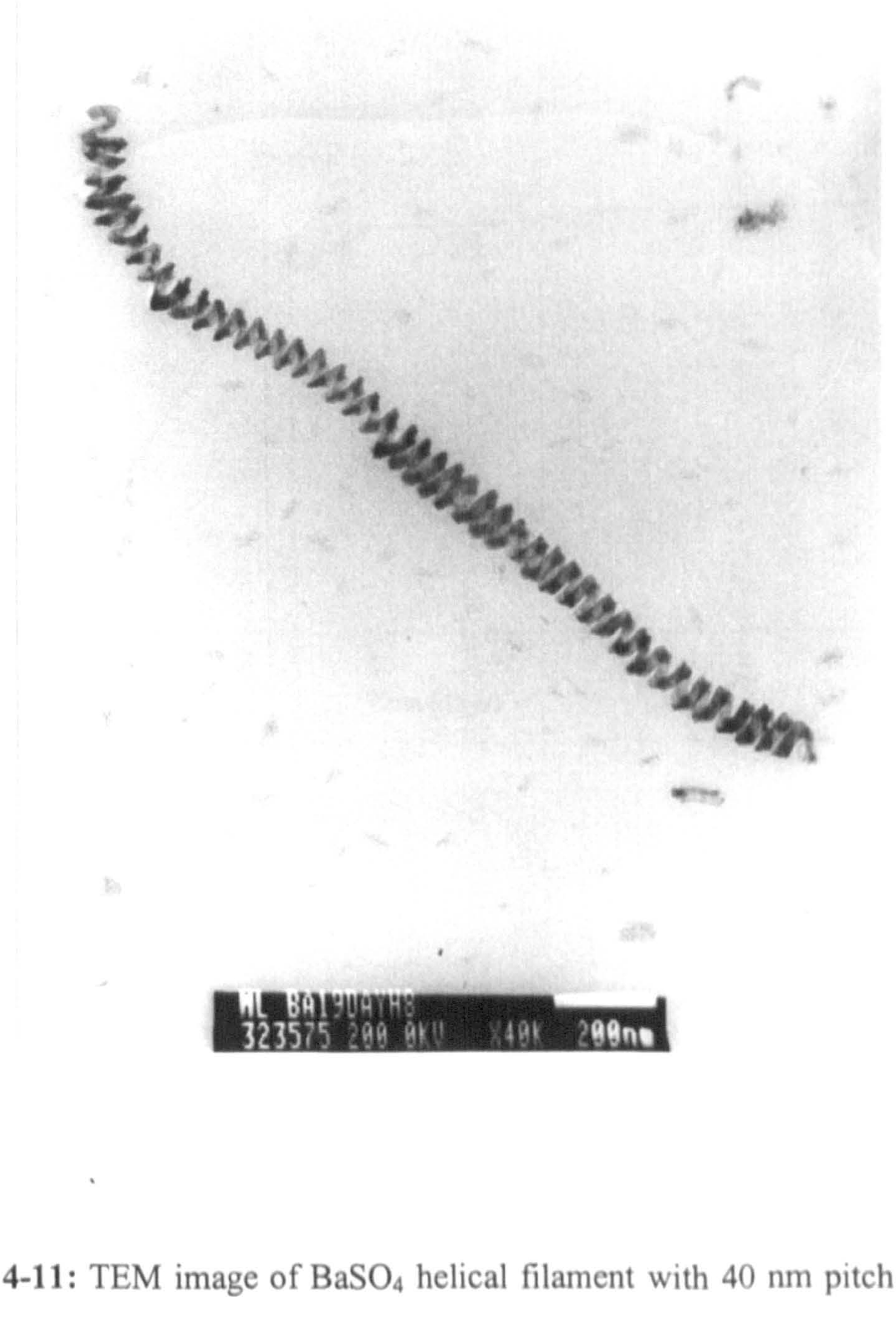

Figure 4-11: TEM image of $BaSO_4$ helical filament with 40 nm pitch produced by reaction in isooctane solution of sulfate-containing NaAOT reverse microemulsion droplets ($w = 10$) and $Ba(AOT)_2$ reverse micelles ($w < 1$) at room temperature, NaAOT : $Ba(AOT)_2$ = 50 : 1, and $[Ba^{2+}] : [SO_4^{2-}] = 5.5 : 1$ to $1.4 : 1$. Scale bars = 200 nm.

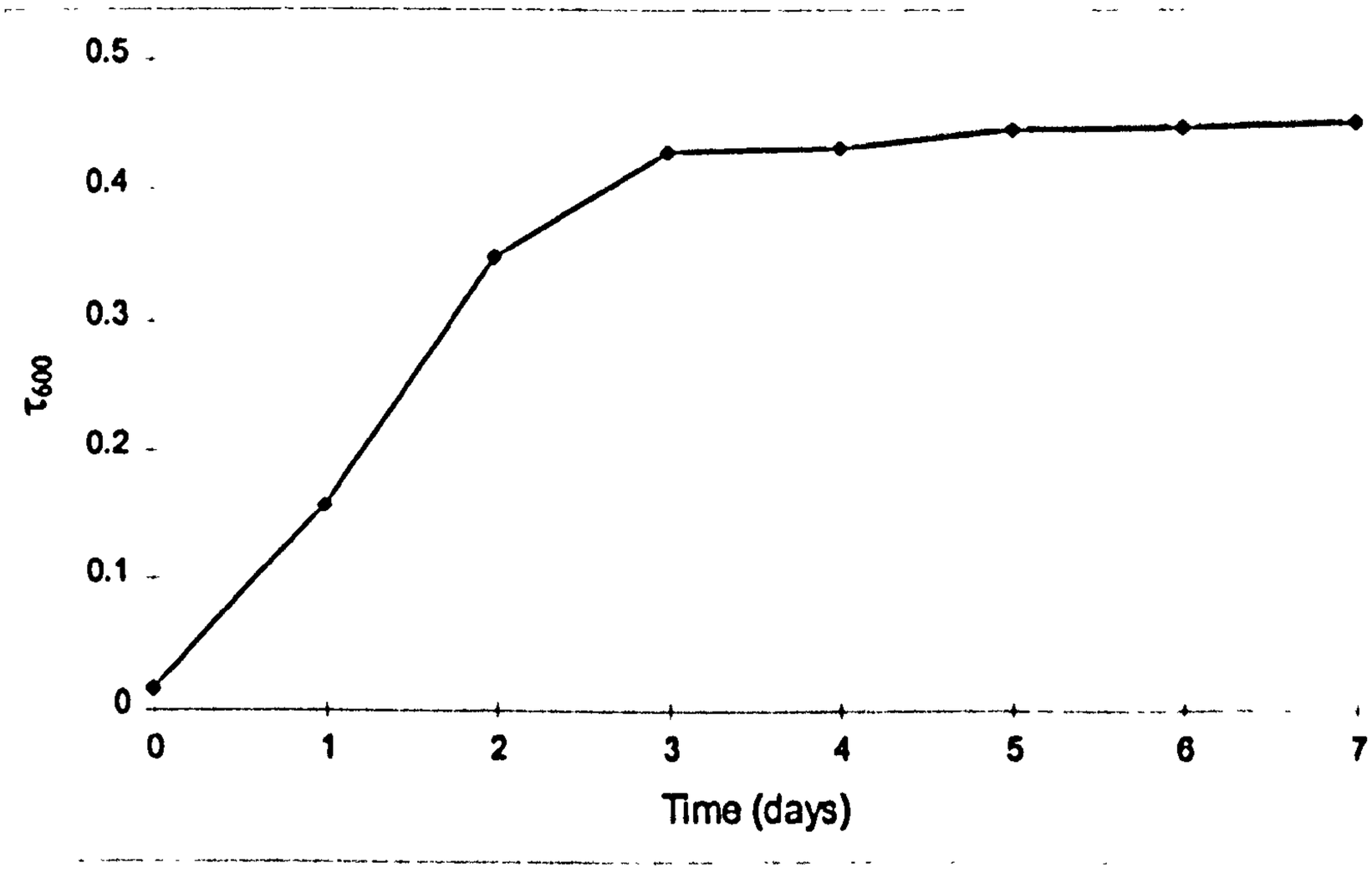

Figure 4-12: Change in turbidity at 600 nm (τ_{600}) with time during $BaSO_4$ nanofilaments growing in isooctane mixtures of sulfate-containing NaAOT reverse microemulsion droplets ($w = 10$) and $Ba(AOT)_2$ reverse micelles ($w < 1$) at room temperature, NaAOT : $Ba(AOT)_2$ = 50 : 1, and $[Ba^{2+}] : [SO_4^{2-}]$ = 5.5 : 1.

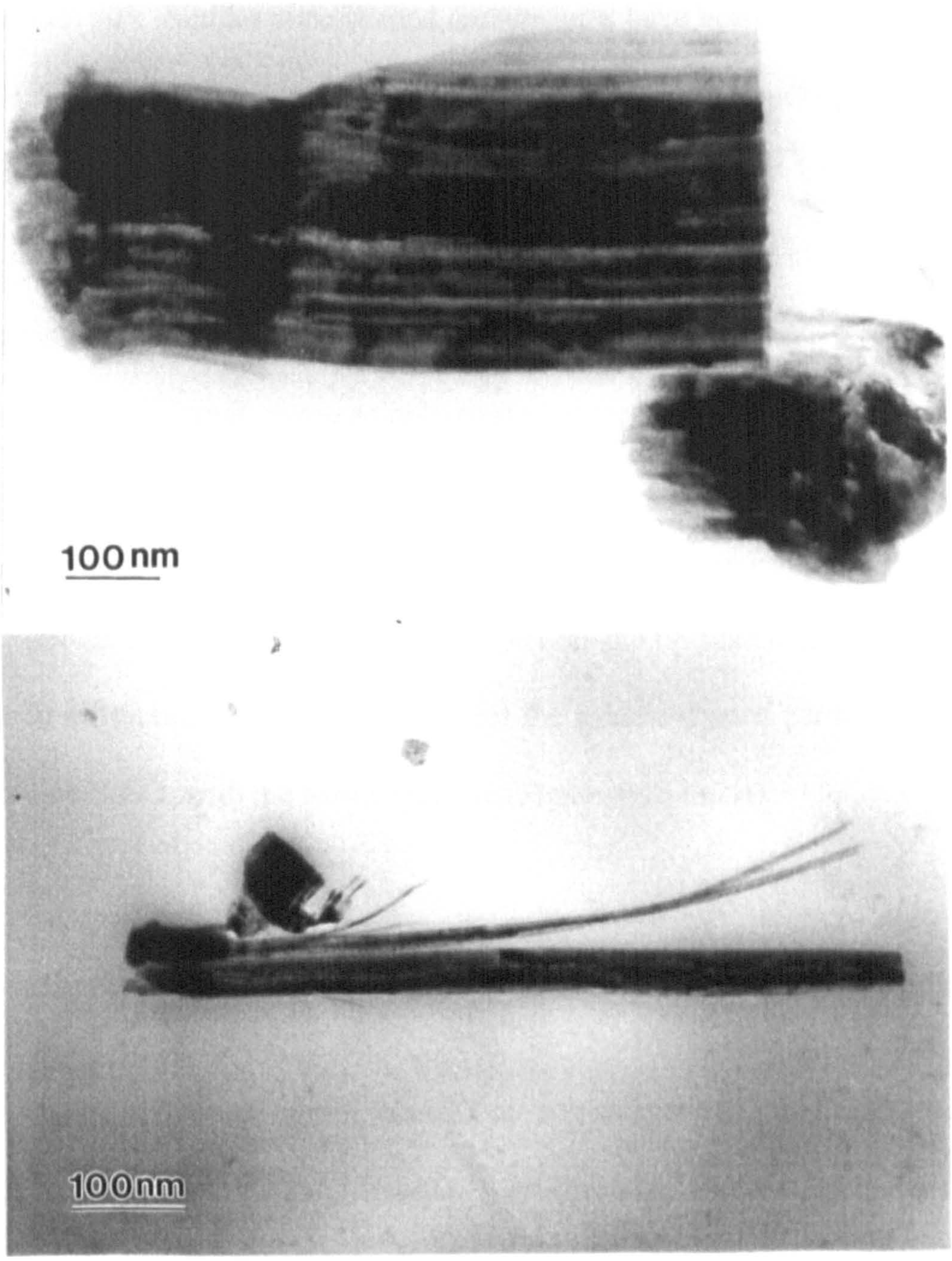

Figure 4-13: TEM images of $BaSO_4$ fibres produced by reactions in isooctane mixtures of sulfate-containing NaAOT reverse microemulsion droplets (w = 10) and $Ba(AOT)_2$ reverse micelles (w < 1) at 4 °C, NaAOT : $Ba(AOT)_2$ = 50 : 1, and $[Ba^{2+}]$: $[SO_4^{2-}]$ = 5.5 : 1, showed short and straight filaments. Scale bars = 100 nm.

cone-shaped structures at 30°C (Figure 4-14). The angles of the nanocones were about 60 – 90°. Similar cone-shaped architectures have been previously reported for $BaSO_4$ crystallization in the presence of anionic polymers such as polyacrylates.[18] In our studies, the cones only appeared at low concentrations of reactant ($[Na_2SO_4]$ = 20 mM, pH ≈ 7) for temperatures between 20 and 30°C. Increasing the temperature to 40°C produced no $BaSO_4$ filaments or cones, but a predominance of larger, dense spindle-shaped aggregates, 100 to 300 nm in length and 60 to 100 nm in width, consisting of disordered 5 – 6 nm nanoparticles which were separated by a distance of 2 – 3 nm (Figure 4-15). These structures remained intact throughout the time course of the reaction and no filaments were observed. Electron diffraction analysis indicated that the spindle-shaped particles contained crystalline $BaSO_4$ with the barite structure (Figure 4-15 insert).

4.3.5 The influence of stirring of the reaction media on $BaSO_4$ morphology

After mixing sulfate-containing NaAOT reverse microemulsion droplets (w = 10, $[Na_2SO_4]$ = 20 to 80 mM) and $Ba(AOT)_2$ reverse micelles (w < 1) (molar ratio of $[Ba^{2+}] : [SO_4^{2-}]$ = 5.5 : 1 to 1.4 : 1), the reaction media were stirred continuously throughout the time course of the experiments at room temperature. The rate of growth of $BaSO_4$ particles was faster compared with that under unstirred conditions, since the reaction medium became cloudy after only 7 hours at room temperature.

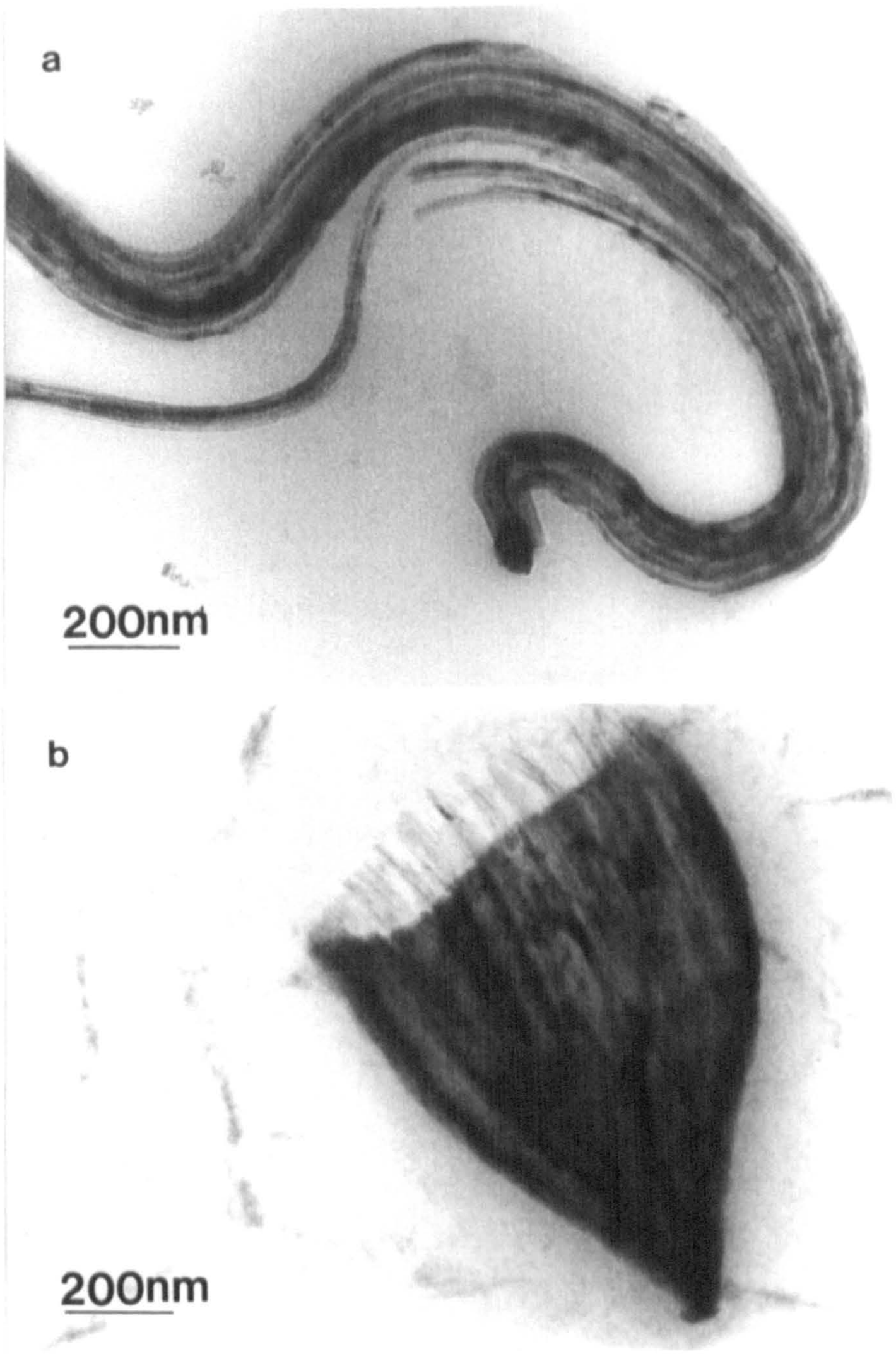

Figure 4-14: TEM images of $BaSO_4$ crystals produced by reactions in isooctane mixtures of sulfate-containing NaAOT reverse microemulsion droplets (w = 10) and $Ba(AOT)_2$ reverse micelles (w < 1) at 30 °C, NaAOT : $Ba(AOT)_2$ = 50 : 1, and $[Ba^{2+}]$: $[SO_4^{2-}]$ = 5.5 : 1, showed **(a)** highly curved fibres and **(b,c)** cone-shaped structures. Scale bars, **a** = **b**= 200 nm, **c** = 400 nm.

Figure 4-14c

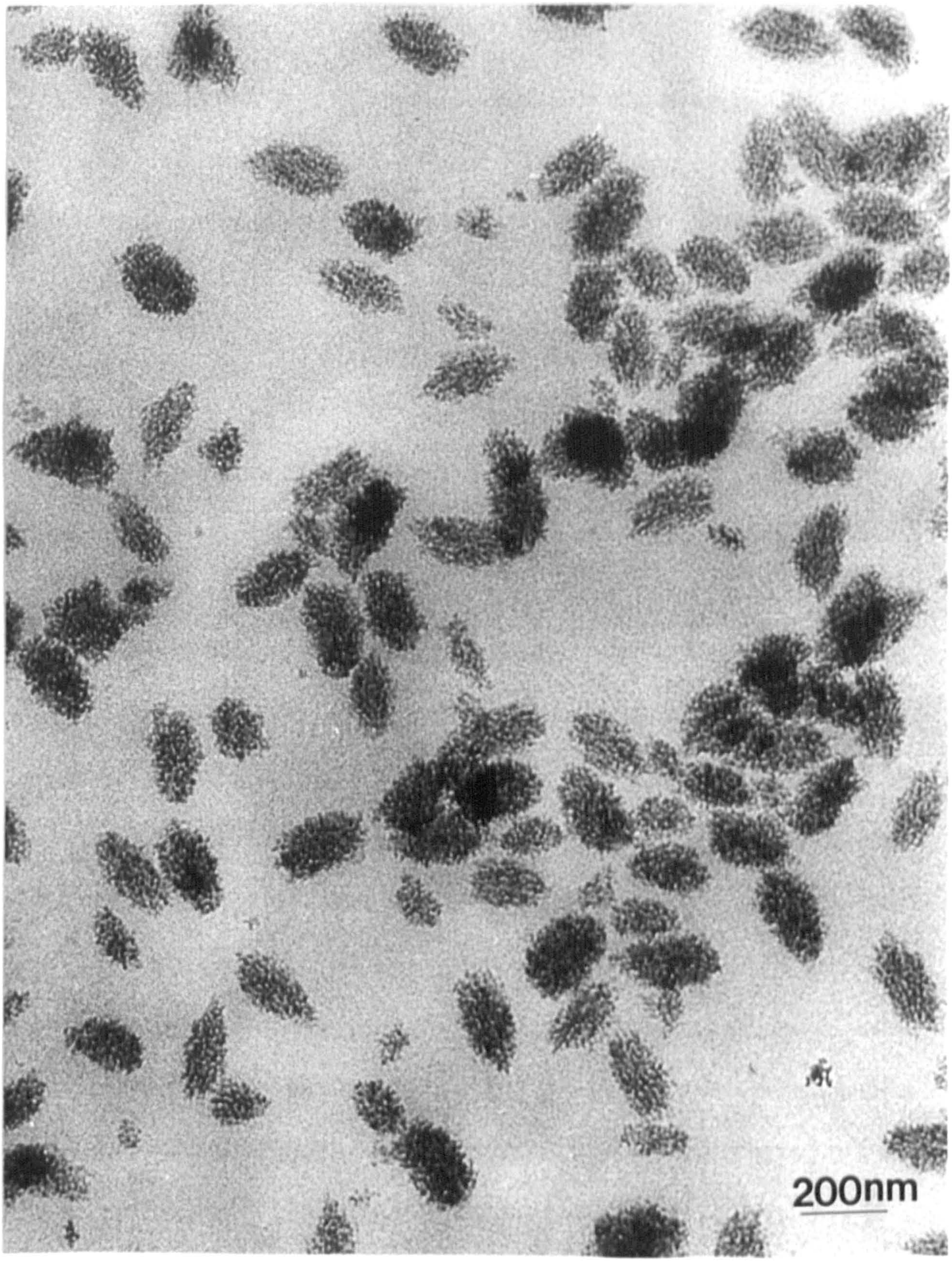

Figure 4-15: TEM image of $BaSO_4$ nanoparticles produced by reaction in isooctane solution of sulfate-containing NaAOT reverse microemulsion droplets ($w = 10$) and $Ba(AOT)_2$ reverse micelles ($w < 1$) at 40 °C, NaAOT : $Ba(AOT)_2$ = 50 : 1, and $[Ba^{2+}] : [SO_4^{2-}] = 5.5 : 1$. Scale bar = 200 nm.

TEM images showed most of $BaSO_4$ nanofilaments were short hair-like crystals (of length<600 nm) and unpacked (figure 4-16). The sizes of the filaments did not increase with time after 2 hours.

4.3.6 Growth with time

The $BaSO_4$-surfactant structures formed at various stages of growth at room temperature were studied using TEM within 5 hours after mixing. Initially, (about 1 hour) small aggregates of randomly packed 4 to 5 nm-sized electron-dense particles were formed prior to the deposition of the filaments (Figure 4-17a). The nanoparticles were approximately spherical in shape and spatially separated within the aggregates. No crystallographic reflections were detected by electron diffraction. The aggregates were generally low in contrast and therefore difficult to image. After 1 hour, many of the aggregates showed the presence of a single electron-dense filament, 3 to 6 nm in width (2-3 hors), closely associated with the nanoparticle-surfactant matrix (Figure 4-17b,c). With time, other nano-filaments were nucleated alongside the first filament, so that filament bundle structures appeared (Figure 4-17d,e). The filaments in the bundles were 3 to 6 nm wide, and remarkably uniform in thickness and density.

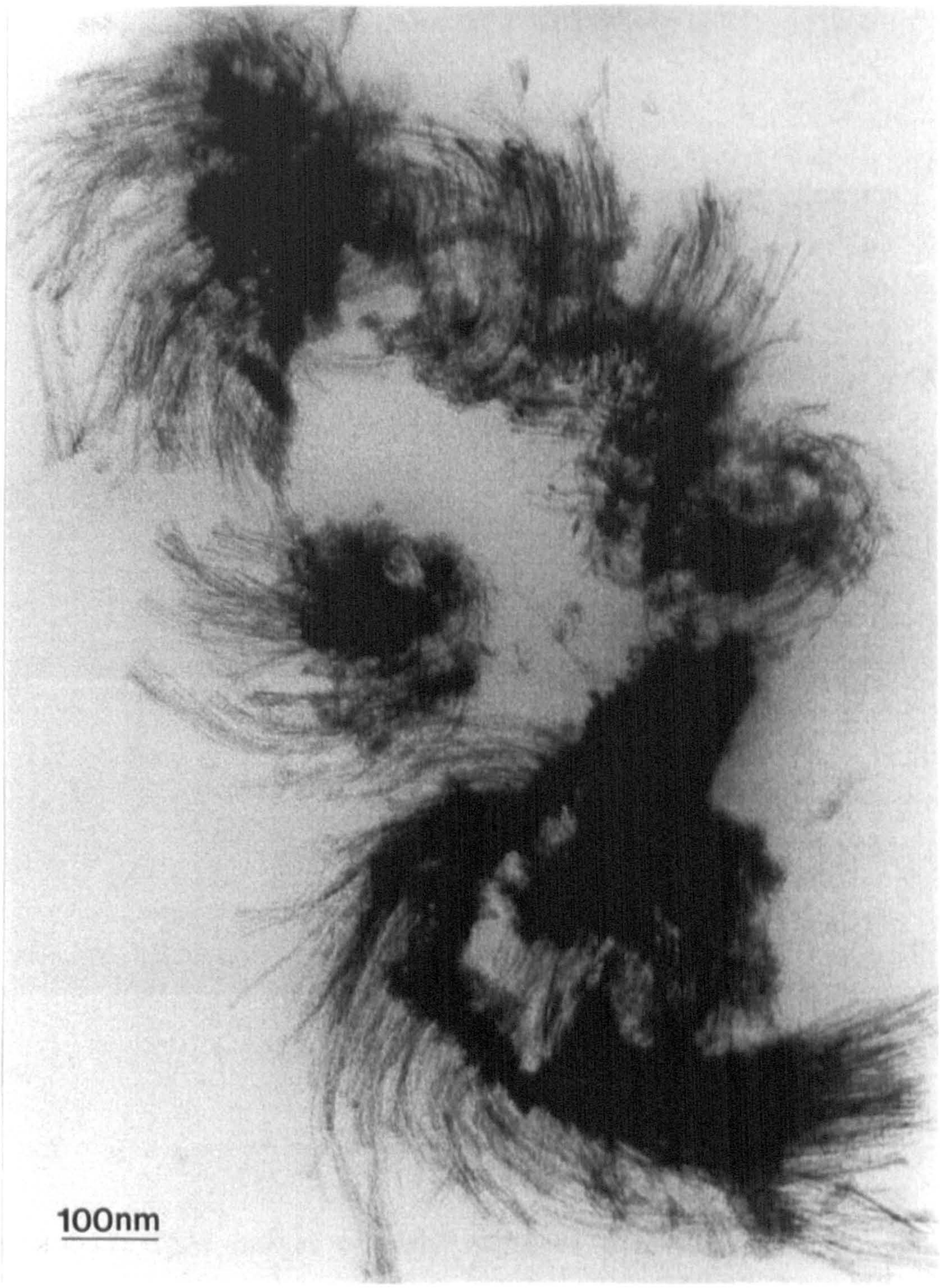

Figure 4-16: TEM image of $BaSO_4$ disconnected bundles of filaments formed in stirred reaction solutions of mixtures of sulfate-containing NaAOT reverse microemulsion droplets ($w = 10$) and $Ba(AOT)_2$ reverse micelles ($w < 1$) at room temperature, NaAOT : $Ba(AOT)_2$ = 50 : 1, and $[Ba^{2+}] : [SO_4^{2-}]$ = 5.5 : 1, scale bar = 100 nm.

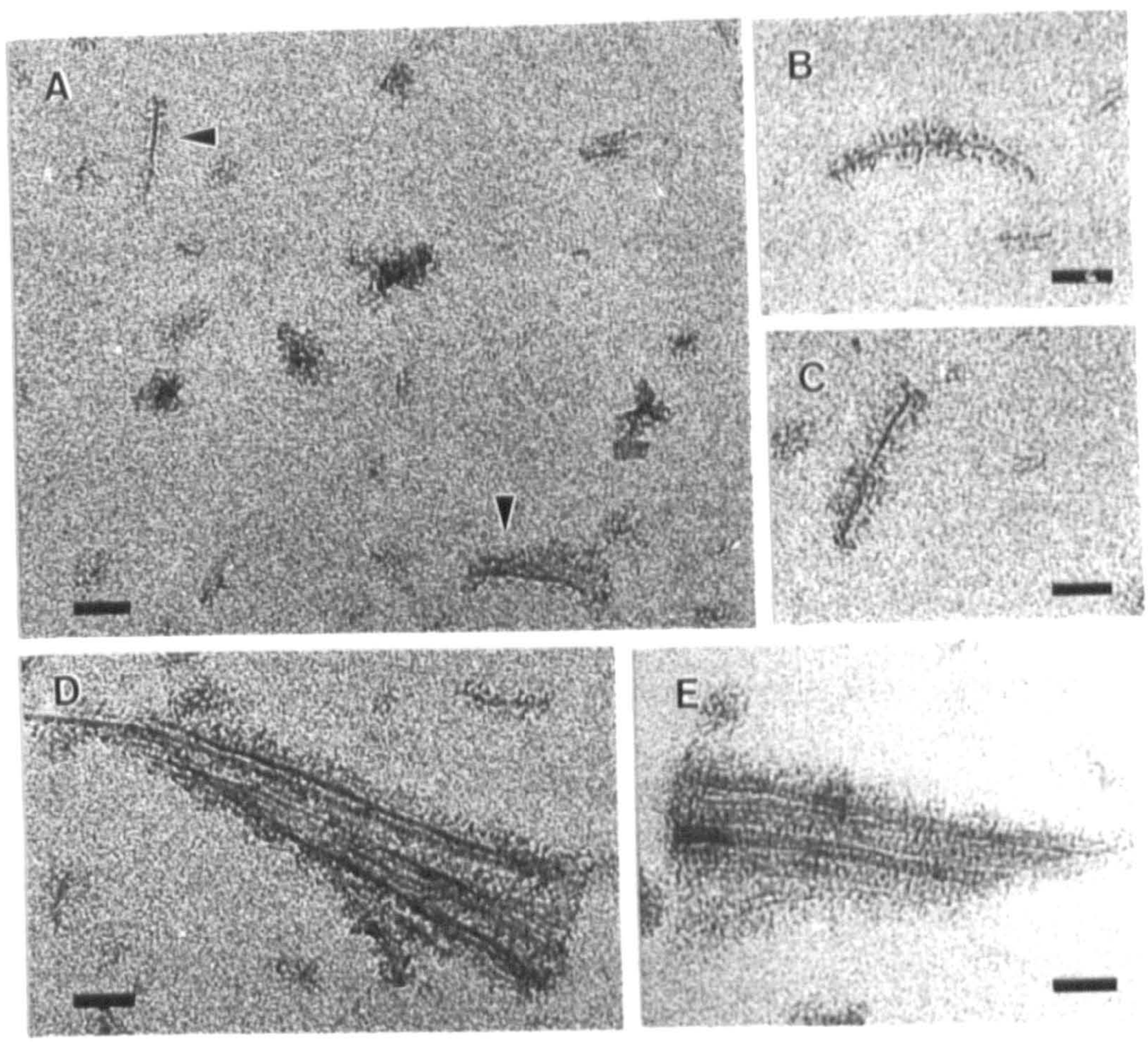

Figure 4-17: TEM images of early stages of fibre formation. **(a)** initially, unstructured aggregates of $BaSO_4$ nanoparticles are produced that undergo reconstruction into individual $BaSO_4$ filaments (arrows); **(b)** and **(c)**, filament nucleation and growth occur within a matrix of electron dense nanoparticles; **(d)** and **(e)**, secondary filaments are nucleated alongside the primary thread to produced co-aligned bundles that constitute the fibre structure. Scale bars = 50 nm in all micrographs.

4.3.7 The influence of the molar ratio of reactants on $BaSO_4$ morphology

$BaSO_4$ nanofilaments were formed specifically at molar ratio of $[Ba^{2+}]:[SO_4^{2-}]$ = 5.5 : 1 to 1.4 : 1 (Figure 4-18a). Under identical conditions but at the molar equivalence ($[Ba^{2+}]:[SO_4^{2-}] \approx 1$) no filamentous structures were observed, instead, unusual higher-order chain structures containing up to 60 nanoparticles were produced (figure 18b). The colloidal chain structures were 50 to 500 nm in length and consisted of rectangular-shaped particles that were uniform in length (mean = 16.0 ± 1.5 nm) and width (mean = 6.0 ± 0.4 nm), and preferentially aligned so that the long axis of each particle was perpendicular to the chain direction. This remarkable coupling of synthesis and self-assembly has been described in detail for $BaCrO_4$ nanoparticles in chapter **3**. In contrast, when a molar excess of sulfate was used ($[Ba^{2+}]:[SO_4^{2-}] \approx 1 : 5$), small single nanoparticles with spherical or elliptical shapes (about 10 nm cross) were obtained (Figure 4-18c).

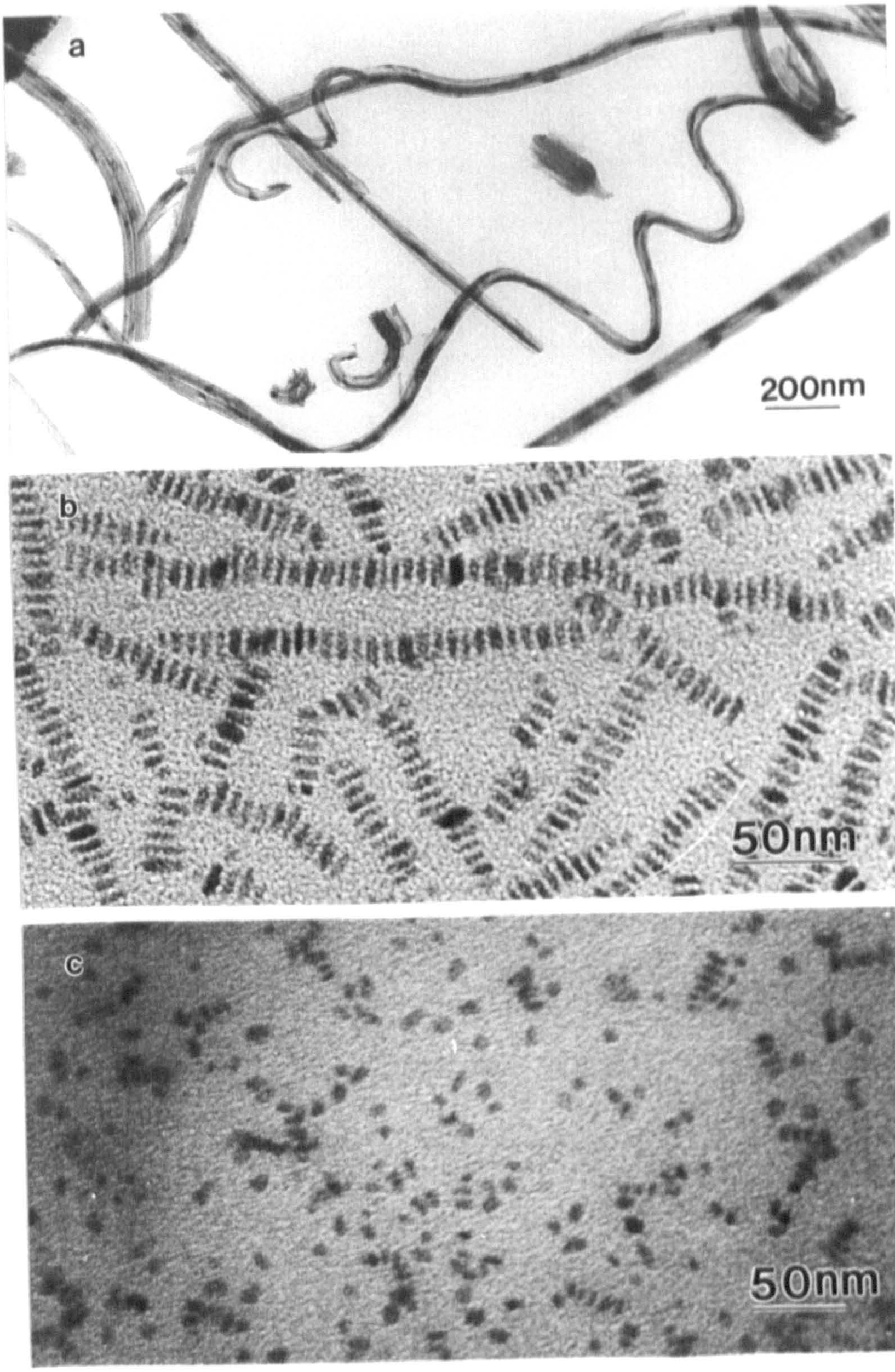

Figure 4-18: $BaSO_4$ products formed from AOT microemulsions at different molar ratios of barium to sulfate; **(a)** $[Ba^{2+}]:[SO_4^{2-}] = 5.5 : 1$, scale bar = 200 nm; **(b)** $[Ba^{2+}]:[SO_4^{2-}] \approx 1 : 1$, scale bar = 50 nm; **(c)** $[Ba^{2+}]:[SO_4^{2-}] \approx 1 : 5$, scale bar = 50 nm.

4.4 General discussion

4.4.1 The activities of AOT on the formation of nanofilaments

The results (section **4.3.3**) clearly showed the existence of AOT molecules associated with $BaSO_4$ nanofilaments. Due to the strong binding interactions between the sulfonate headgroups and inorganic phase, adsorption of the sulfonate headgroups onto the positively charged or structurally matched side faces aligned parallel to the [010] axis occurs once the $BaSO_4$ crystallites are formed. This adsorption inhibited the development of the side faces, also $BaSO_4$ crystal growth was greatest along the [010] direction.[9] Furthermore, high magnification TEM images showed that each filament was separated from its neighbour by a uniform spacing of 3 to 5 nm in width (Figure 4-19). This distance is consistent with the presence of an inter-filament bilayer of AOT molecules that could link adjacent threads and maintain their close proximity within a barite fibrous-surfactant nanocomposite. Because the stirring environment will disturb a bilayer assembly of AOT molecules, interlinking of the filaments was not observed for samples prepared under stirred reaction solutions (Figure 4-16). The results suggest that co-alignment of the nanofilaments within the bundle is facilitated by surfactant-surfactant packing provided that the local environment is unstirred and not subjected to shear and stress fields caused by physical agitation.

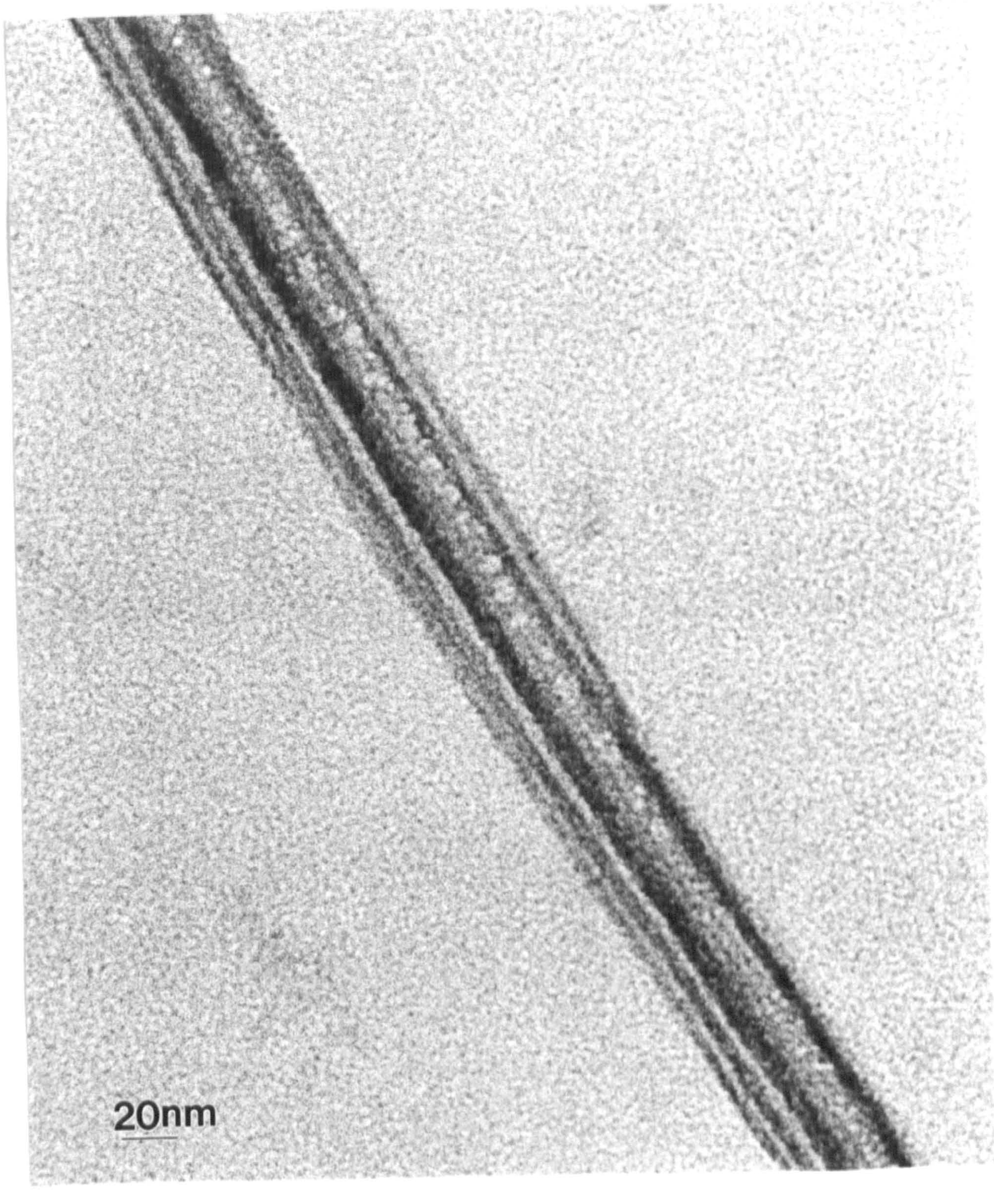

Figure 4-19: TEM image of fibre ultrastructure showing individual electron dense filaments separated by surfactant bilayers (white lines), scale bar = 20 nm.

Clearly, AOT molecules act in two ways in the formation of nanofilaments. Firstly, the sulfonate headgroups adsorbed on positively charged or structural matched faces of either $BaSO_4$, $BaCrO_4$ or $Ba_3[PW_{12}O_{40}]_2$ crystals to inhibit the development of those faces and allow growth of the other faces which were uncoated or less coated by AOT. This might be the driving force for the formation of nanofilaments. Secondly, the hydrophobic tails of AOT adsorbed on the surface of filaments form a lamellar phase that may induce the formation of bundles (Scheme 1).

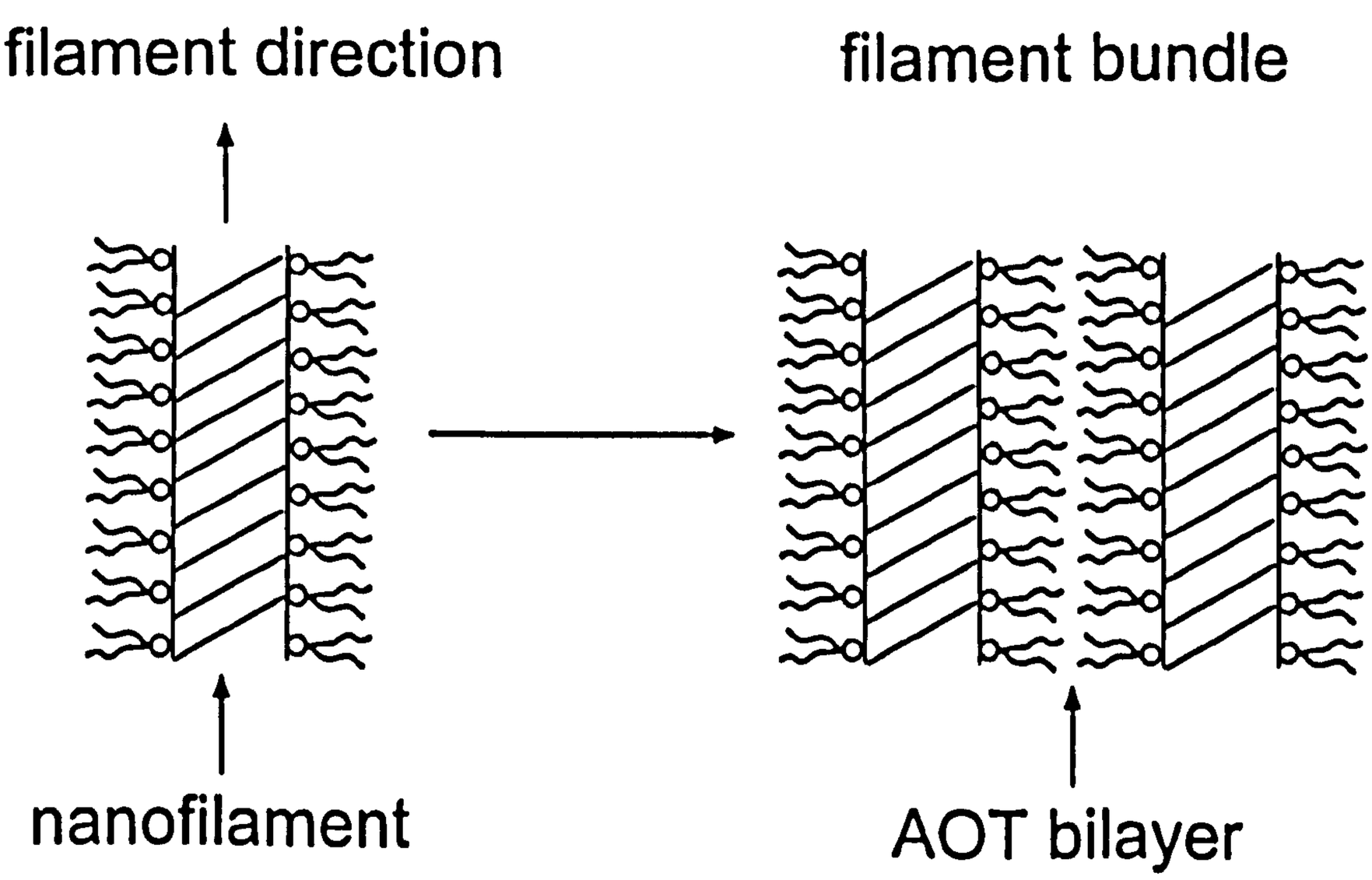

Scheme 4-1: The sketch of $BaSO_4$ nanofilament and the bundles.

4.4.2 Morphological evolution of nanofilaments

The results showed that the morphology of the initial stage of nanofilaments was small aggregates of randomly packed 4 to 5 nm-sized electron-dense particles (section **4.3.6**), which were approximately spherical in shape and spatially separated within the aggregates. These observations suggest that the nucleation and growth of amorphous $BaSO_4$ clusters accompanies fusion and exchange between $Ba(AOT)_2$ reverse micelles and sulfate-containing NaAOT microemulsion droplets. This leads to the inter-micellar aggregation of surfactant-coated nanoparticles to produce larger assemblies. Since the reverse microemulsion droplets contain on average only 0.5 to 2 SO_4^{2-} ions per droplet at $[Na_2SO_4]$ = 20 - 80 mM, w = 10 (radius = 2.2 nm[1]) (see appendix 4.1), many collisions and exchange processes must take place to generate the 5 nm-sized nanoparticles. These collisions and exchange processes are associated with thermal motion of the micelles and the microemulsion droplets, might be influenced by thermodynamic factors, for example, temperature. This was confirmed by performing the experiments at different temperatures. The decrease in reaction rate (turbidity) observed at low temperature (4°C), or the increase in reaction rate (turbidity) observed at high temperature (30°C), are a consequence of the diminished rates or increased rates of nucleation and growth, respectively, associated with these interactive processes.

However, what is the driving force that controls the relatively uniform size of the nanoparticles at an early stage, as well as their spatial separation within the secondary aggregates? One possibility is that growth continues within the water droplets as long as there is a substantial mobility of the AOT and water molecules for further exchange, until all the AOT molecules are irreversibly bound by electrostatic forces to the surface of the incipient inorganic cluster, and water molecules transferred to other microemulsion droplets. This suggests that the primary particles form by controlled micellar processes that are intrinsically self-terminating, which would lead to capping of the inorganic surface and blocking of growth. Only specific particle sizes can therefore be attained before the inorganic cargo becomes kinetically "locked-in" within a shell of partially immobilized AOT molecules. Presumably, a reduction in membrane fluidity could also be responsible for aggregate formation by increasing the free energy and driving force for hydrophobic interactions and interdigitation between colliding core-shell structures. Displacement of intercalated solvent molecules would then drive the process entropically, consistent with the observation that the degree of association and stability of the aggregates was significantly increased at 40 °C.

The further evolution of the filamentous structures occurred in the reconstruction process of the transformation of amorphous $BaSO_4$ to crystals. Once established, the crystals would be unevenly coated by AOT molecules (uncoated or less coated on (010) faces). This unstable factor could be the driving force for further developing the filamentous structures. Moreover, the reconstruction process is

highly anisotropic, and the coalescence and fusion of the $BaSO_4$-surfactant nanoparticles occurs specifically at the ends of the incipient filaments. Many aggregates in the early stage (after 1 hour) showed the presence of a single electron-dense filament (3 to 6 nm in width), which were approximately the same thickness as the diameter of the primary nanoparticles. This implies that the formation of the nanofilaments is associated with the initial nanoparticles. Presumably, the amorphous or primary nanoparticle building blocks aggregate into the linear structure along the (010) direction. In general, linear growth could represent the lowest energy configuration that couples the requirements for particle-particle fusion (reduction in surface free energy and increase in bulk lattice energy) and minimization of membrane curvature (sphere to cylinder transformation). Once established, the linear arrangement would be self-propagating because of persistent differences in the curvature and exchangeability of surfactant molecules located at the ends and sides of the incipient filament.

Clearly, this slow transformation process of amorphous $BaSO_4$ to cryatalline nanofilaments requires a significant degree of mobility in the local environment, which could explain the scarcity of filaments associated with the stabilized spindle-shaped agglomerates produced at 40 °C. Presumably, hydrophobic aggregation occurs concurrently with nucleation, such that the primary nanoparticles are locked into the surfactant network (Scheme 4-2).

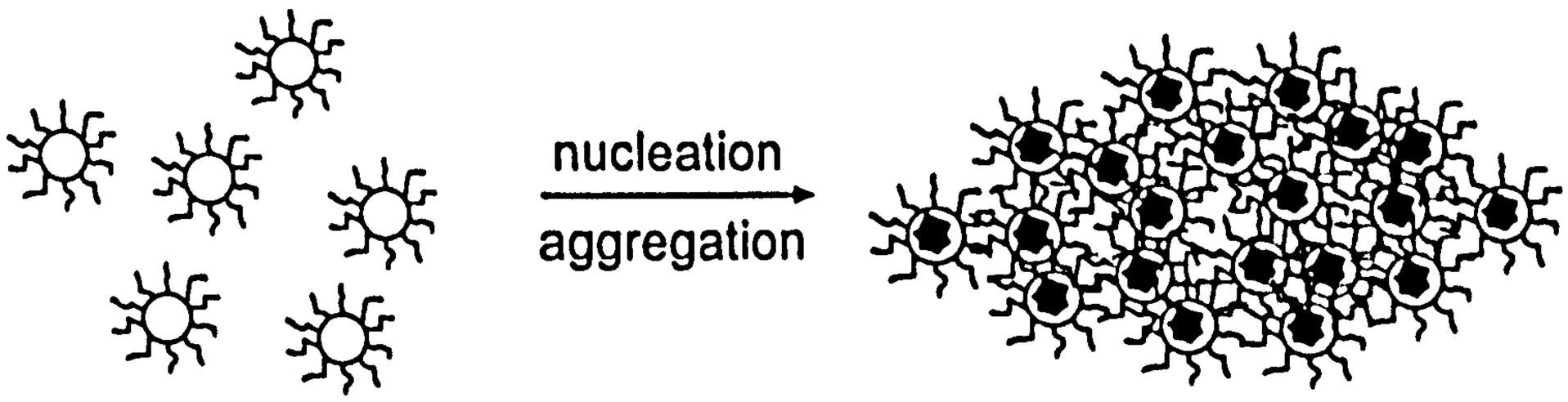

Scheme 4-2 The sketch of the formation of spindle-shape nanoparticles.

However, why did the aggregates form a spindle shape at 40 °C and why was the size of the spindle-shaped particles so regular? The mechanism is not clear yet. Similarly, a high concentration of nuclei (at $[Ba^{2+}]$:$[SO_4^{2-}]$ = 1:1) also induces growth in association and concurrent with the self-organization of stacked micellar aggregates, resulting in linear chain structures. This system was thoroughly discussed in chapter 3.

With the threads extended in length, other nanofilaments might nucleate alongside the first filament by hydrophobic aggregation of the surfactant molecules, such that a bundle of co-aligned threads is constructed within the primary aggregates (Figure 4-17d,e). Further growth occurs along the individual filaments and the filaments remain uniform in thickness, with the threads extending in length. This suggests that the propagation of the unit cell could proceed coherently as the threads extend in length by further attachment of the primary particles, and the

building blocks are amorphous or partially crystalline. Significantly, each filament is an individual unit separated from its neighbour by a bilayer of AOT molecules. This was confirmed by the results observed for the stirred reaction solutions.

Interestingly, the initial growth of filaments adjacent to the primary thread caused the bundles to curve (Figure 4-20a). One possibility is that the locking in of new short filaments by surfactant interdigitation generates a bending force in the non-attached segment of the longer primary thread. This results in the coiling of the bundle into a characteristic spiral-shaped structure (Figure 4-20b) which becomes self-terminating at one end because further addition of the primary nanoparticles is prevented by the spiral-shaped structure. The angle of rotation appeared to be dependent on the number of secondary nucleation events that occurred on the internal edge of the primary filament. For example, turns of 270° and 360° were common; the former was associated with one principal bending event (Figure 4-20b), whereas the latter occurred when a second bending process was induced by nucleation of a new filament on the interior side of an already curved structure (Figure 4-20c). Away from the terminus, the bending energy decreases and the bundle becomes straight as the filaments bunch up and abruptly terminate against a uniform growth edge (Figure 4-20d).

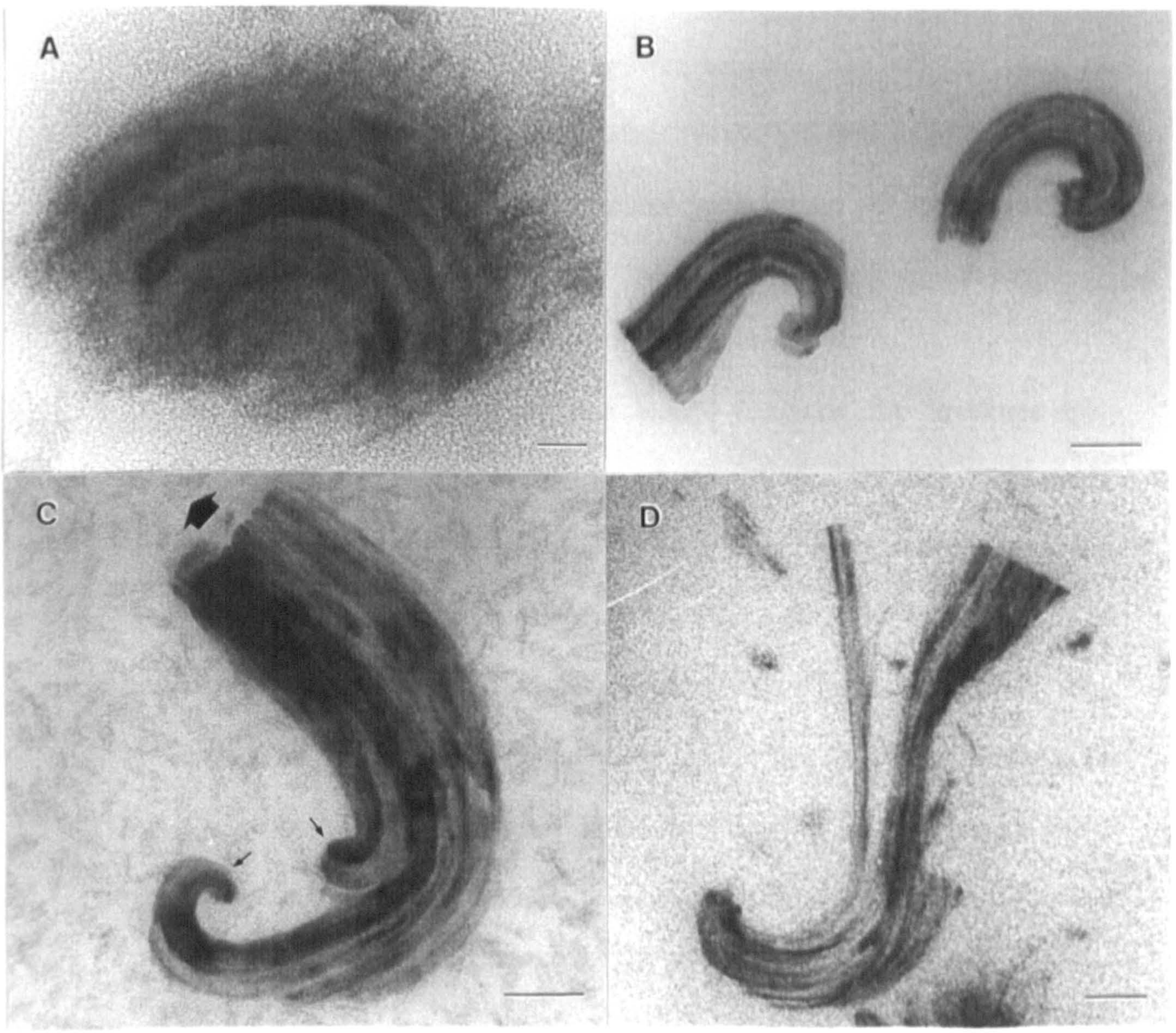

Figure 4-20: TEM images of intermediate stages of fibre formation. **(a)** Curved bundle of $BaSO_4$ filaments within a matrix of aggregated nanoparticles, scale bar = 20 nm; **(b)** uni-directional outgrowth produces spiral-shaped bundles, scale bar = 100 nm; **(c)** composite fibre showing 360° bending due to at least two secondary nucleation events (small arrows), followed by linear outgrowth of a uniform growth front (large arrow), scale bar = 50 nm; **(d)** later stage of growth showing splaying and twisting of filament bundle, scale bar = 100 nm.

The images suggest that the individual $BaSO_4$ threads develop in length until they reach the end of a primary aggregate, which acts as a distinct boundary for the growth of the filament tips. Lateral growth, however, can still take place via secondary nucleation of new filaments along the straight sections of the structure, provided that the surfactant-$BaSO_4$ precursor particles are not depleted, and this can give rise to the specific widening of the bundle towards the growth edge.

As the number of filaments in each bundle increases, the structures splay outwards with the result that many of the bundles develop cone-shaped outgrowths (Figure 4-20d, 4-21a). Dissipation of strain energy arising from lateral packing pressure as well as increases in rigidity in the older coiled end of the structure, for example due to mineral ripening in the interfilament spaces, could be responsible for the development of the axial offset. In some structures, the cone segments appeared to be associated with twisting in the filament bundle (Figure 4-20d), or they could arise from a set of discrete secondary nucleation points on the growth edge (Figure 4-21a), or both. Although the filaments were tightly associated within the cone-like features when formed under unstirring conditions, stirring the reaction medium produced partially unravelled structures that showed individual nanofilaments with continuous bifurcated junctions (Figure 4-21b). These defects, which could contribute to the splayed architecture, possibly arise from a line dislocation at the filament growth tip, where a lateral displacement equal to the radius of a nanoparticle growth unit would produce two sites for further outgrowth.

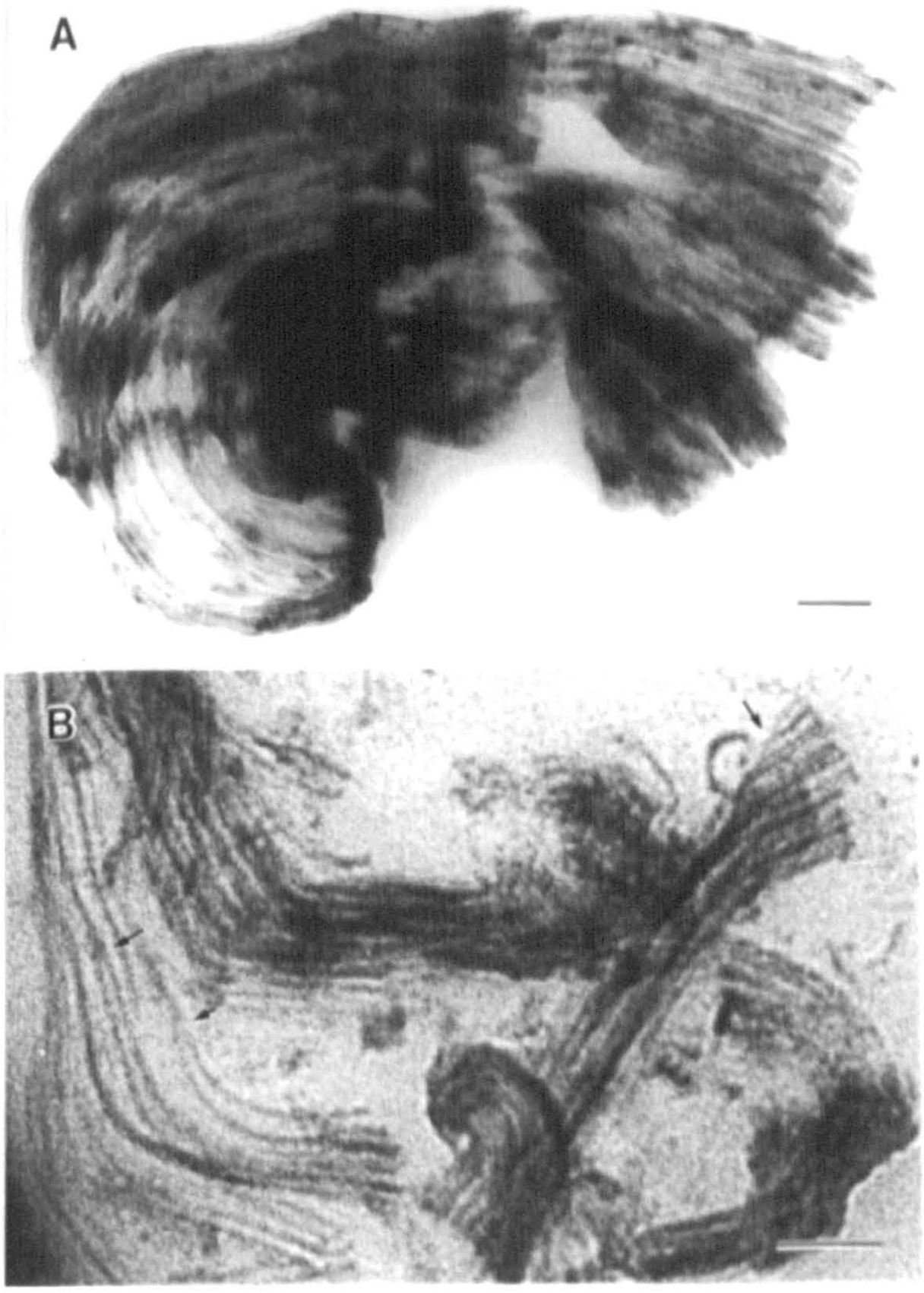

Figure 4-21: TEM images of **(a)** complex filament bundle showing cone-shaped outgrowths and **(b)** disconnected filaments showing bifurcations in individual filaments (arrows). Scale bars = 100 nm. Samples were prepared in microemulsions at room temperature (18 – 22 °C), $w = 10$, NaAOT : $Ba(AOT)_2$ = 50 : 1, and $[Ba^{2+}] : [SO_4^{2-}] = 5.5 : 1$ to $1.4 : 1$, $[SO_4^{2-}] = 20 – 80$ mM, (a) without or (b) with stirring.

4.5 Conclusions

The growth and morphological evolution of crystalline micrometre-long $BaSO_4$ fibres was studied in this chapter. The fibres were synthesised in a mixed solution of $Ba(AOT)_2$ reverse micelles and NaAOT sulfate-containing microemulsions in isooctane at $w = 10$ and $[Ba^{2+}] : [SO_4^{2-}] = 5 : 1 - 1.4 : 1$ under unstirred conditions at room temperature. The fibres consist of bundles of $BaSO_4$ nanofilaments, and grow with time in length up to 20 μm, elongated along their [010] axis. These structures appear to be held together by interdigitated surfactant bilayers at one end and dispersed to thin bundles or individual filaments at the other end. Similar experiments at 4, 30 and 40 °C produced short straight filament bundles, highly curved and cone-shaped structures, and spindle-shaped aggregates, respectively.

The morphological evolution involves nucleation, reconstruction and hydrophobic aggregation of interfilaments. The first stage involves the nucleation of 5 nm size amorphous particles and then reconstruction of a single 5nm-wide $BaSO_4$ crystal filament, followed by further filaments parallel to the primary thread. Co-alignment of the filaments results in coiling of the bundle to give a self-terminating spiral-shaped structure, several hundred nanometres in size. Uni-directional linear outgrowth from the open end eventually gives rise to macroscopic fibres that often become splayed into cone-shaped features.

The formation of complex micrometre-long $BaSO_4$ filamentous structures from organized reaction media confined to the nanoscale represents an emergent process that transcends various length scales. This phenomenon is not limited to the $BaSO_4$ systems; it is also observed for $BaCrO_4$, $Ba_3[PW_{12}O_{40}]_2$, $CaSO_4$[3] and $BaCO_3$[10], suggesting that the evolution of such structures could have a generic basis. Scheme 4-3 summarizes a possible mechanism for the development of morphological complexity based on the results reported in this work. Initially, intramicellar nucleation leads to self-limiting fusion and exchange through reductions in membrane fluidity due to surface adsorption. This controls the size and monodispersity of the surfactant-encapsulated $BaSO_4$ nanoparticles and enhances their inter-micellar association into loosely associated aggregates that slowly transform internally into co-aligned bundles of 5 nm-wide nano-filaments. The filaments grow through the linear coalescence and fusion of the primary nanoparticle building blocks, which results in displacement of AOT molecules and formation of a surfactant bilayer between the $BaSO_4$ threads. The high anisotropy could be driven by strong coupling of lattice and curvature energies specifically for linear association, and propagated by differences in the case of displacement of bound and unbound surfactant molecules along the edges and tips of the developing filament. Furthermore, the early stages of growth of the co-aligned filaments may result in a bending force that produces a spiral-shaped bundle, one end of which is blocked from further development. Growth away from this structure proceeds in an approximately linear fashion and is abruptly terminated at the boundary of the surrounding primary aggregate. Lateral growth

continues via secondary nucleation of new filaments such that the bundle widens principally at the growth edge. The structures then splay outwards with the development of cone-shaped outgrowths, possibly due to lateral packing pressure as well as line defects that give rise to bifurcation at the growth tips of individual filaments.

Finally, it is important to emphasize that the filamentous structures were specifically formed when the $[Ba^{2+}]$: $[SO_4^{2-}]$ molar ratio was greater than 1.0. Under these conditions, there is an excess of barium in the reaction system and the primary $BaSO_4$ nanoparticles are positively charged. This results in a strong electrostatic interaction with the anionic AOT surfactant headgroups to produce the surfactant-nanoparticle aggregates that are the key intermediates for filament formation. In contrast, these interactions are less significant at molar equivalence (neutral surface charge), or for stoichiometries with excess sulfate (negative surface potential), with the result that no nanoparticle aggregates are formed. Consequently, no filamentous structures are observed under these conditions; instead, discrete nanoparticles are formed which under conditions of molar equivalence are self-assembled in solution into unusual higher-order structures such as long linear chains. This remarkable coupling of synthesis and self-assembly has been described in detail for $BaCrO_4$ nanoparticles in chapter 3.

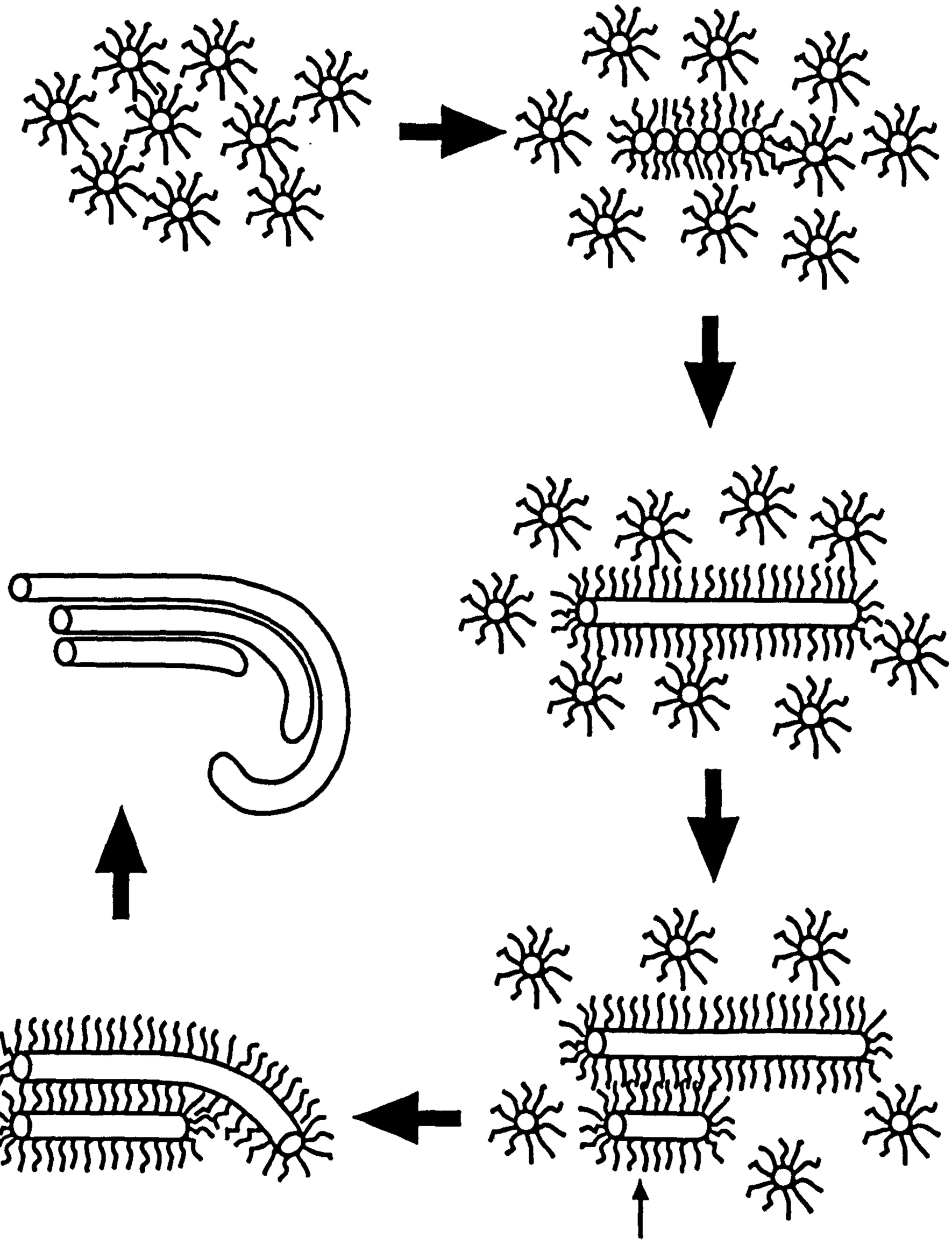

Scheme 4-3: Proposed model for the formation of the $BaSO_4$ nanofilament bundles. See text for details.

4.6 References

[1] Li, M.; Schnablegger, H.; Mann, S., *Nature*, **402**, 393 (1999).

[2] Hopwood, J.D.; Mann, S., *Chem. Mater.*, **9**, 1819 (1997).

[3] Rees, G.D., Evans-Gowing, R., Hammond, S.J., Robinson, B.H., *Langmuir*, **15**, 1993 (1999).

[4] Arriagada, F.J.; Osseo-Asare, K., *J. Colloid and Interface Science*, 170, 8 (1995).

[5] Taleb, A., Petit, C., Pileni, M. P., *Chem. Mater.*, 9, 950 (1997).

[6] Manna, A., Kulkarni, B. D., Bandyopadhyay, K., Vijayamohanan, K., *Chem. Mater.*, 9, 3032 (1997).

[7] Lisiecki, I., Björling, M., Motte, L., Ninham, B., Pileni, M. P., *Langmuir*, 11, 2385 (1995).

[8] Pileni, M.P., Lisiecki, I., *Colloids Surf. A.*, 80(1), 63 (1993).

[9] Hopwood, J.D., Barium Sulfate Crystallisation in Synthetic and Biological systems, *University of Bath*, Ph.D. Thesis, 1996.

[10] Qi, L., Ma, J., Cheng, H., Zhao, Z., *J. Phys. Chem. B*, **101**, 3460 (1997).

[11] Walsh, D., Hopwood, J.D., Mann, S., *Science*, **264**, 1576 (1994).

[12] Walsh, D., Mann, S., *Nature*, **377**, 320 (1995).

[13] Yang, H., Coombs, N., Ozin, G.A., *Nature*, **386**, 692 (1997).

[14] Lin, H.P., Cheng, Y.R., Mou, C.Y., *Chem. Mater.*, **10**, 3772 (1998).

[15] Antonietti, M., Breulmann, M., Goeltner, G. C., Colfen, H., Wong, K.K.W., Walsh, D., Mann, S., *Chem. Eur. J.*, 4, 2491 (1998).

[16] Sager, W.F.C, Controlled Formation of Nanoparticles from Microemulsions, *Current Opinion in Colloid & Interface Science*, 3, 276 (1998).

[17] Mann, S, Ozin, G. A., *Nature*, **382**, 313 (1996).

[18] Benton, W.J., Collins, I.R., Grimsey, I.M., Parkinson, G.M., Rodger, S.A., *Faraday Discuss.*, **95**, 281-297 (1993); Li, M.; Ashley, A.J., Mann, S., unpublished observations.

Appendix 4.1

Calculation of number of reactant molecules in each NaAOT microemulsion droplet

V_m Volume of one microemulsion droplet (nm^3 or L)

R_m Radius of microemulsion droplet (nm)

M_r Molarity of reactants ($mol \cdot L^{-1}$)

N_r Number of reactant molecules (Na_2SO_4 or Na_2CrO_4 or $H_3PW_{12}O_{40}$) in each NaAOT microemulsion droplet

For spherical microemulsion droplet

$$V_m = \frac{4}{3} \cdot \pi \cdot R_m^3 \ (nm^3)$$

$$V_m = \frac{4}{3} \cdot \pi \cdot R_m^3 \times 10^{-24} \ (L)$$

$$N_r = M_r \cdot V_m \times 6.023 \times 10^{23}$$

$$N_r = Mr \cdot \frac{4}{3} \cdot \pi \cdot R_m^3 \times 10^{-24} \times 6.023 \times 10^{23}$$

Chapter 5

Synthesis of Prussian blue nanoparticles and nanocrystal superlattices in reverse microemulsions

(Published in *Angew. Chem. Int. Ed.*, **39**, 1793-1796, 2000)

5.1 Introduction

Prussian blue was first made accidentally in 1704; it was then used for dying fabrics and in a non-silver photographic printing process. Prussian blue is essentially ferric ferrocyanide, but there exists a whole range of such iron blues, having compositions depending on their precise method of preparation. At the molecular level, they all have in common a characteristic cubic structure, but this lattice can accommodate variable amounts of water and metal ions within it, so formulae range from $MFe[Fe(CN)_6]\cdot 5H_2O$ to $Fe_4[Fe(CN)_6]_3\cdot 15H_2O$, (M = Li, Na, K, NH_4).[1] Among known molecular magnets, Prussian blue and related cyanometallates-based coordination polymers offer a range of compounds with unique versatility. The variety of structures and related magnetic properties of this family of compounds have been extensively investigated[2-3] and recently reviewed.[4] Although much work has focused on the relationship between the unit-cell structure and magnetic properties, relatively few attempts have been made towards understanding and controlling the growth mechanism of these magnetic coordination polymers. Periodically banded arrangements (Liesgang bands) have been produced previously for the precipitation of Prussian blue on perfluorinated membranes.[5] Similarly, a dissipative structure has been briefly reported.[6] More recently, incorporation of Prussian Blue in surfactant-containing systems has also been reported, such as Prussian blue inside DODA LB films,[7-8] and Prussian blue formation inside DDAB lamellar vesicles.[9] Herein we coupled synthesis of Prussian blue with reverse microemulsions

prepared from the anionic surfactant sodium bis(2-ethyhexyl)sulfosuccinate (AOT) to produce nanoscale particles. A related material, $[Cu_2\{Fe(CN)_6\}]$, has been recently synthesised in AOT reverse microemulsion media, although the resulting nanoparticles were highly disorganized.[10]

Synthesis of cyanometallate polymers is usually simple. Most methods are based on aqueous chemistry. The synthesis might be direct (mixing of the reactants) or indirect (mixing of one reactant with one precursor which can become the second reactant by oxidising or reducing *in-situ*). Photoformation of Prussian blue is an indirect synthesis which has been thoroughly investigated as an alternative photographic printing process.[1,11]

Organic supermolecular templates and organized reaction media have been recently used for controlling synthesis of traditional inorganic solids, such as silica,[12-14] calcium carbonate,[15-16] barium chromate,[17] and iron oxides.[18-19] These processes allow the control of properties such as particle size, particle shape, surface texture, and organization to be integrated directly into the synthesis method. Such a method could be also applied to molecular-based magnets like Prussian blue.

In this chapter we show that using an organic template confines the synthesis of Prussian blue nanoparticles. Uniform shape and size of Prussian blue nanoparticles can be routinely prepared by injecting the reaction precursor into

nanoscale AOT reverse microemulsion droplets in the oil phase. The growth of the nanoparticles within the restricted reaction field is controlled by multistep processes involving the slow photoreduction of $[Fe(C_2O_4)_3]^{3-}$ to produce Fe^{II} ions that subsequently react with $[Fe(CN)_6]^{3-}$ ions to generate nuclei and clusters of Prussian blue encapsulated within the water droplets. Growth of the molecular magnet occurs by further exchange and fusion between microemulsion droplets to produce Prussian blue nanoparticles. Surfactant AOT molecules adsorbed on the surface of the nanoparticles thereby produce hydrophobic Prussian blue nanoparticles suspended in the oil phase. Moreover, the highly hydrophobic surface properties of Prussian blue nanoparticles enable the facile preparation of self-assembled nanoparticle arrays with 2-D and 3-D superlattice ordering (scheme 5-1).

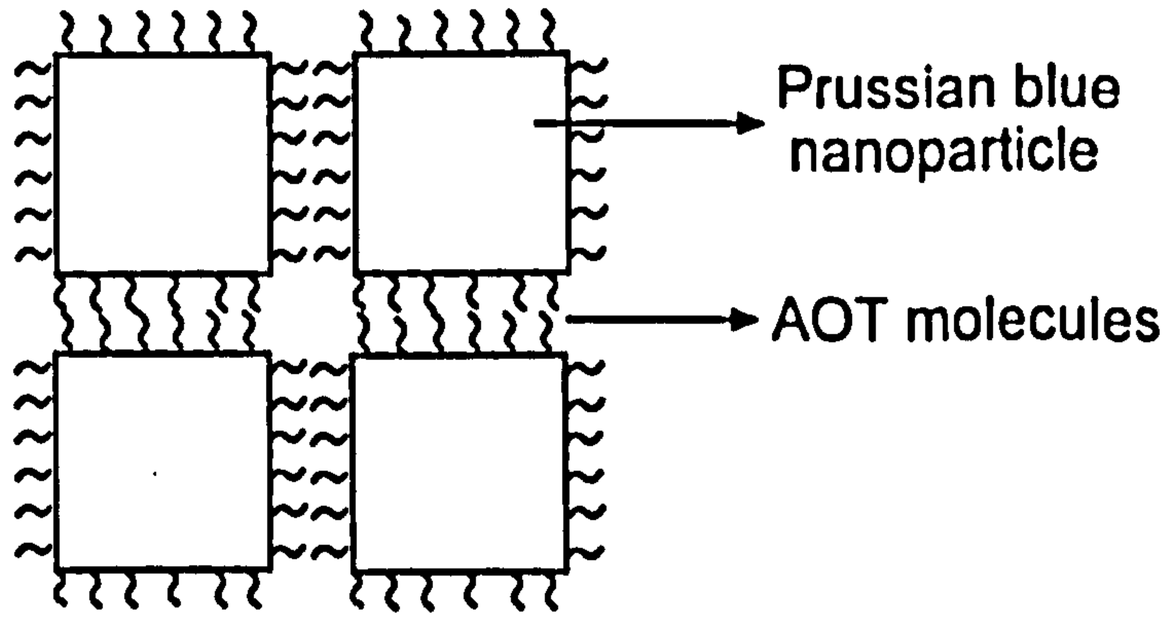

Scheme 5-1 Cubic Prussian blue nanoparticles self-assembled into a superlattice structure by hydrophobic interaction of AOT molecules.

5.2 Materials and Methods

5.2.1 Materials

All materials were of analytical grade (purity >98%) and used without further purification.

Table 5-1 Chemicals used in this chapter

Common name	Chemical name	Formula	Molecular weight	Supplier
	ammonium iron(III) oxalate	$(NH_4)_3[Fe(C_2O_4)_3]\cdot 3H_2O$	428.0	Aldrich
	potassium ferricyanide	$K_3[Fe(CN)_6]$	329.0	Aldrich
NaAOT	sodium bis(2-ethylhexyl) sulphosuccinate	$C_{20}H_{37}O_4SO_3Na$	444.6	BDH
isooctane	2,2,4-trimethyl pentane	C_8H_{18}	114.0	Aldrich

5.2.2 Methods

5.2.2.1 Preparation of the mixture of ammonium iron(III) oxalate and ammonium ferricyanide solution (the precursor solution of Prussian blue)

Prussian blue was prepared as the mixed valence ammonium cyanometallate $[(NH_4)_xFe_y\{Fe(CN)_6\}]$; $x + 3y = 4$ according to a reported method.[1] Ammonium iron(III) oxalate $\{(NH_4)_3[Fe(C_2O_4)_3]\cdot 3H_2O$, MW = 428; 2.568 g, 6 mmole$\}$ was dissolved in hot distilled water (3 ml. 50 °C) contained in a foil-covered flask. Finely powdered potassium ferricyanide $\{K_3[Fe(CN)_6$, MW = 329; 0.987 g 3 mmole$\}$ was then added to the solution while it was still hot with vigorous stirring for 20 minutes, and then sonicated for 2 minutes. The solution was left to cool in the dark for several hours. The reaction is as follows:

$$2\ (NH_4)_3[Fe(C_2O_4)_3] + K_3[Fe(CN)_6] =$$

$$K_3[Fe(C_2O_4)_3]\ (solid) + (NH_4)_3[Fe(C_2O_4)_3] + (NH_4)_3[Fe(CN)_6]$$

Green crystals of $K_3[Fe(C_2O_4)_3]$ were removed by filtration in the dark from the mixture of $(NH_4)_3[Fe(C_2O_4)_3]$ and $(NH_4)_3[Fe(CN)_6]$ solutions. We used this procedure specifically to remove potassium ions from the reaction mixture as ammonium cyanometallate is significantly more stable than the potassium salt of Prussian blue. The solution was then diluted to 10 ml with distilled water to give an equimolar mixture of $(NH_4)_3[Fe(C_2O_4)_3]$ and $(NH_4)_3[Fe(CN)_6]$ at a concentration of 0.3 M.

5.2.2.2 Preparation of Prussian blue nanoparticles in reverse microemulsions

A small amount (0.09 ~ 0.36 ml) of the mixture of ammonium iron(III) oxalate and ammonium ferricyanide aqueous solution (0.01 ~ 0.3 M in water) was added to an isooctane solution of NaAOT (10 ml, 0.1 M) at room temperature in the dark to produce an AOT water-in-oil microemulsions at the molar ratio of water to NaAOT (w) of 5 ~ 20. Yellow transparent solutions were observed in the beginning. Higher water levels (w = 15 – 20) resulted in a slight phase separation of the water in the microemulsion solutions due to the high ionic strength of the reaction solutions. This separation could be prevented by using lower concentrations of the reactants. The microemulsion was exposed to daylight for various periods to slowly photoreduce the $[Fe(C_2O_4)_3]^{3-}$ ions to $[Fe(C_2O_4)_3]^{4-}$, which serves as a source of Fe^{II} ions for treatment with aqueous $[Fe(CN)_6]^{3-}$. This latter process is analogous to the Turnbull method for producing Prussian blue, so that the solutions gradually turned into blue transparent solutions from yellow transparent solutions in two days.

$$2[Fe^{III}(C_2O_4)_3]^{3-} \xrightarrow{h\nu} 2[Fe^{II}(C_2O_4)_2]^{2-} + C_2O_4^{2-} + 2CO_2\,(g)$$

$$[Fe^{III}(CN)_6]^{3-} + [Fe^{II}(C_2O_4)_2]^{2-} \longrightarrow [Fe^{III}\{Fe^{II}(CN)_6\}]^{1-} + 2C_2O_4^{2-}$$

Control experiments used equivalent amounts of the $(NH_4)_3[Fe(C_2O_4)_3]$ and $(NH_4)_3[Fe(CN)_6]$ as an aqueous mixture (0.3 M) added to 10 ml of isooctane or water in the absence of NaAOT.

5.2.2.3 Transmission electron microscopy (TEM)

Samples for transmission electron microscopy (TEM) were collected directly from the blue transparent microemulsion solutions over two weeks, and deposited onto formvar-coated, carbon-reinforced, 3 mm diameter, copper electron microscope grids, then air-dried.

TEM analysis was performed in bright field mode using a JEOL 1200EX electron microscopy operating at 120keV (section **2.3.1**). Selected area electron diffraction (SAED) (section **2.3.2**) and energy-dispersive X-ray analysis (EDXA) (section **2.3.3**) were also used to characterize the samples imaged by TEM.

5.2.2.4 Ultraviolet and visible spectroscopy (UV-vis)

Samples for Ultraviolet and visible spectroscopy (UV-vis) were taken from blue transparent microemulsion fluids over two weeks. UV-vis measurements were carried out with a PERKIN ELMER Lambda II UV-vis spectrometer equipped with Perkin Elmer UV Winlab (Version 1.1) computer software (section **2.3.10**).

5.2.2.5 Fourier Transform Infrared spectroscopy (FTIR)

Samples for FTIR were taken from the blue fluids containing Prussian blue nanoparticles in one week following precipitation with a polar solvent (ethanol). This was consistent with the presence of hydrophobic tails of AOT on the surface of Prussian blue nanoparticles. After centrifugation, the blue precipitate was air dried. The spectra were recorded at 4000-400 cm^{-1} wavenumbers using KBr discs. Fourier Transform Infrared analysis was performed with a PERKIN ELMER Spectrum One spectrophotometer (section **2.3.9**).

5.3 Results and discussions

5.3.1 Description of Prussian blue nanoparticles

AOT reverse microemulsions containing 0.3 M ammonium iron(III) oxalate and 0.3 M ammonium ferricyanide aqueous nanodroplets at $w = 5 - 20$ were transparent yellow fluids that were stable in the dark at room temperature. Exposure of the microemulsions to daylight transformed them to a transparent blue solution in two days and no precipitate was observed for two weeks. TEM images corresponding to the samples taken from the blue microemulsions ($w = 15$) after four days showed the presence of cubic nanoparticles with a uniform shape and size (figure 5-1a). The crystals have a characteristic length of 16 nm on average, a narrow particle size distribution $\sigma = 2.7$ nm (Figure 5-1b), and a regular cubic morphology consisting of well-defined faces. The particles self-assembled into two dimensional or three dimensional highly ordered superlattices that were organized in domains up to 200 nm in length containing 60 – 100 nanoparticles. The individual nanoparticles were separated by a regular 2 or 3 nm spacing, which is consistent with a bilayer of AOT molecules[17] (Scheme 5-1).

In contrast, the results of the control experiments were remarkably different. Synthesis in water alone gave a turbid green solution and a blue bulk precipitate that consisted of large (100 ~ 250 nm) discrete cubic particles with a broad size distribution (Figure 5-2).

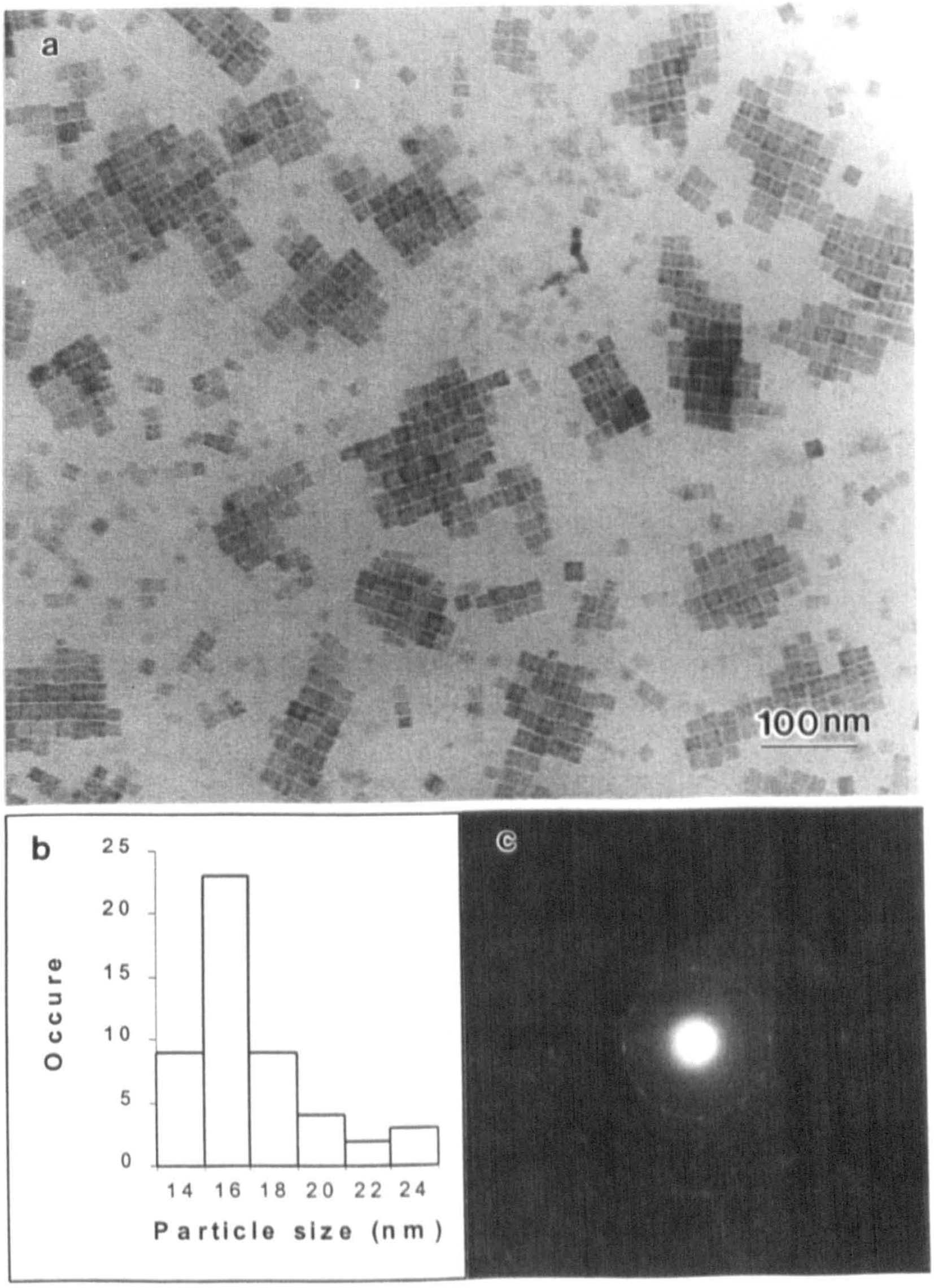

Figure 5-1 **a**) TEM image of cubic Prussian blue nanoparticles formed in AOT microemulsion at $w = 15$ showing self-assembled 2-D and 3-D superlattices, scale bar = 100 nm; **b**) Particle size distribution corresponding to a); **c**) Electron diffraction pattern from the superlattice structures showing in a).

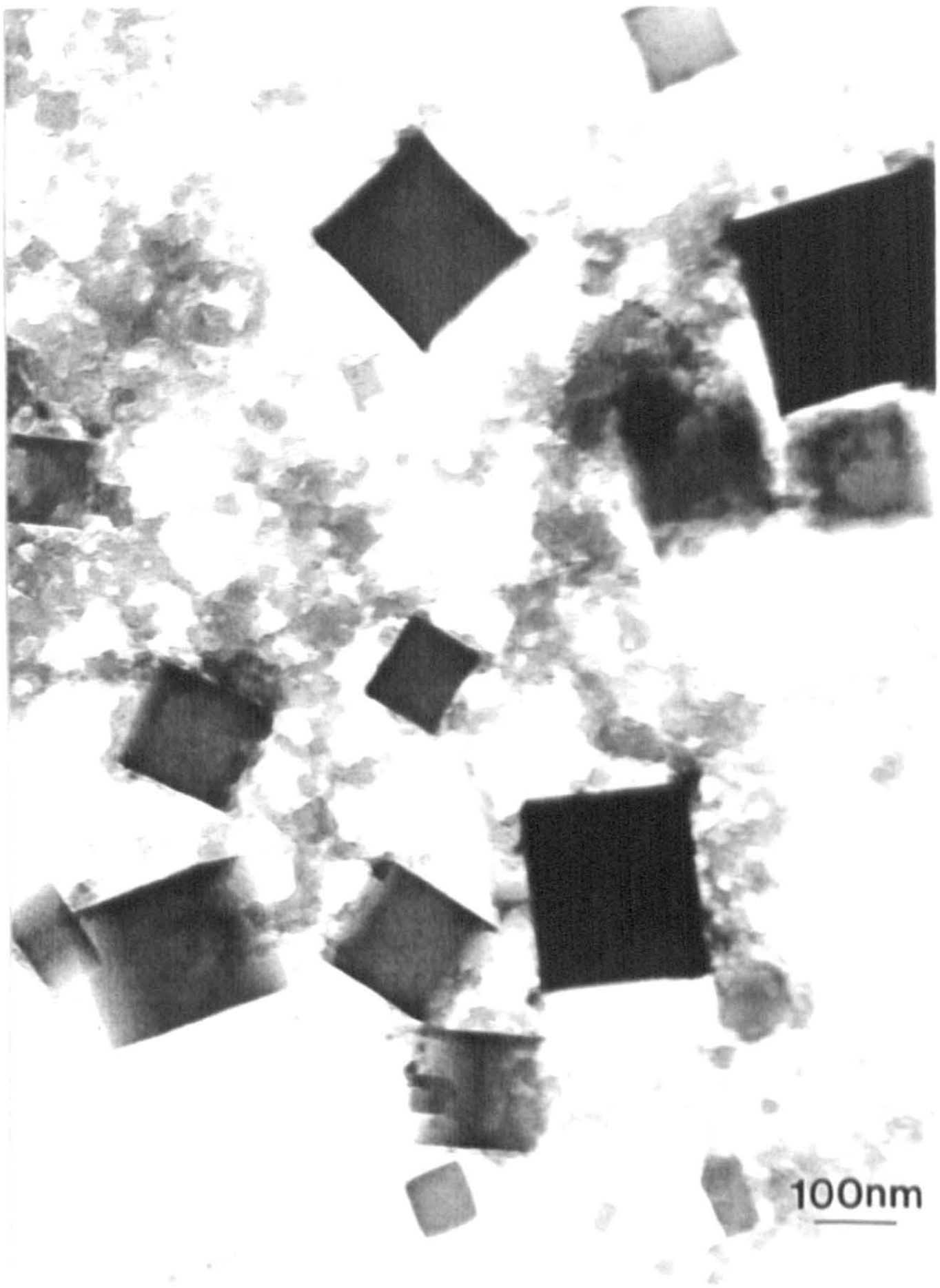

Figure 5-2 TEM image of Prussian blue particles from control experiment prepared in water without surfactant, scale bar = 100 nm.

Reaction in isooctane without AOT produced a separated aqueous blue phase containing crystals similar to those formed in pure water. No product was associated with the isooctane phase.

5.3.2 Identification of Prussian blue nanoparticles

TEM imaged Prussian blue nanoparticles were characterized by selected area electron diffraction (SAED). Although the nanoparticles were, to some extent, sensitive to the electron beam, electron diffraction patterns from the superlattice structures showed rings corresponding to d-spacings of 2.3, 2.5, 3.6 and 5.1 Å (Figure 5-1c), which is consistent with the Prussian blue cubic crystal structure; unit cell parameters a = 1.013 nm.[20] TEM imaged nanoparticles were also characterized by energy-dispersive X-ray analysis (EDXA). The EDXA spectra showed the presence of Fe (6.4 KeV) and S (2.3 KeV), respectively (Figure 5-3). This sulfur signal should be from the sulfonate headgroups of AOT molecules, this conformed the presence of AOT in the Prussian blue nanoparticles array.

Furthermore, UV/Vis absorption spectra of the blue fluids showed a broad band at 680 nm (Figure 5-4) consistent with Prussian blue

$$\{Fe^{III}[(t_{2g})^3(e_g)^2]Fe^{II}[(t_{2g})^6]\} \rightarrow \{Fe^{II}[(t_{2g})^4(e_g)^2Fe^{III}[(t_{2g})^5]\}^*$$

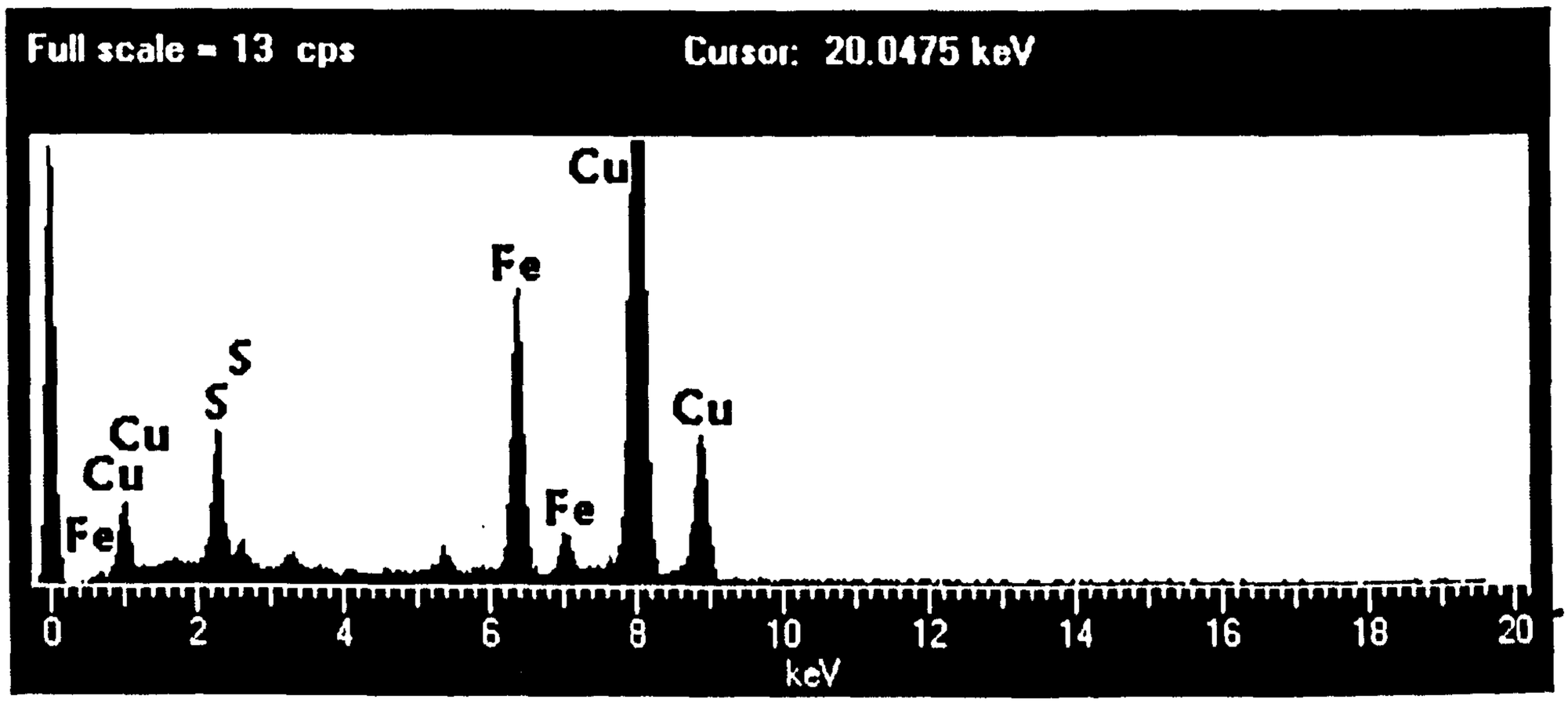

Figure 5-3 Energy-dispersive X-ray analysis (EDXA) spectrum of the superlattice structure showing the presence of iron and sulfur, corresponding to Prussian blue crystals and AOT surfactant, respectively. Copper peaks are associated with the sample grid.

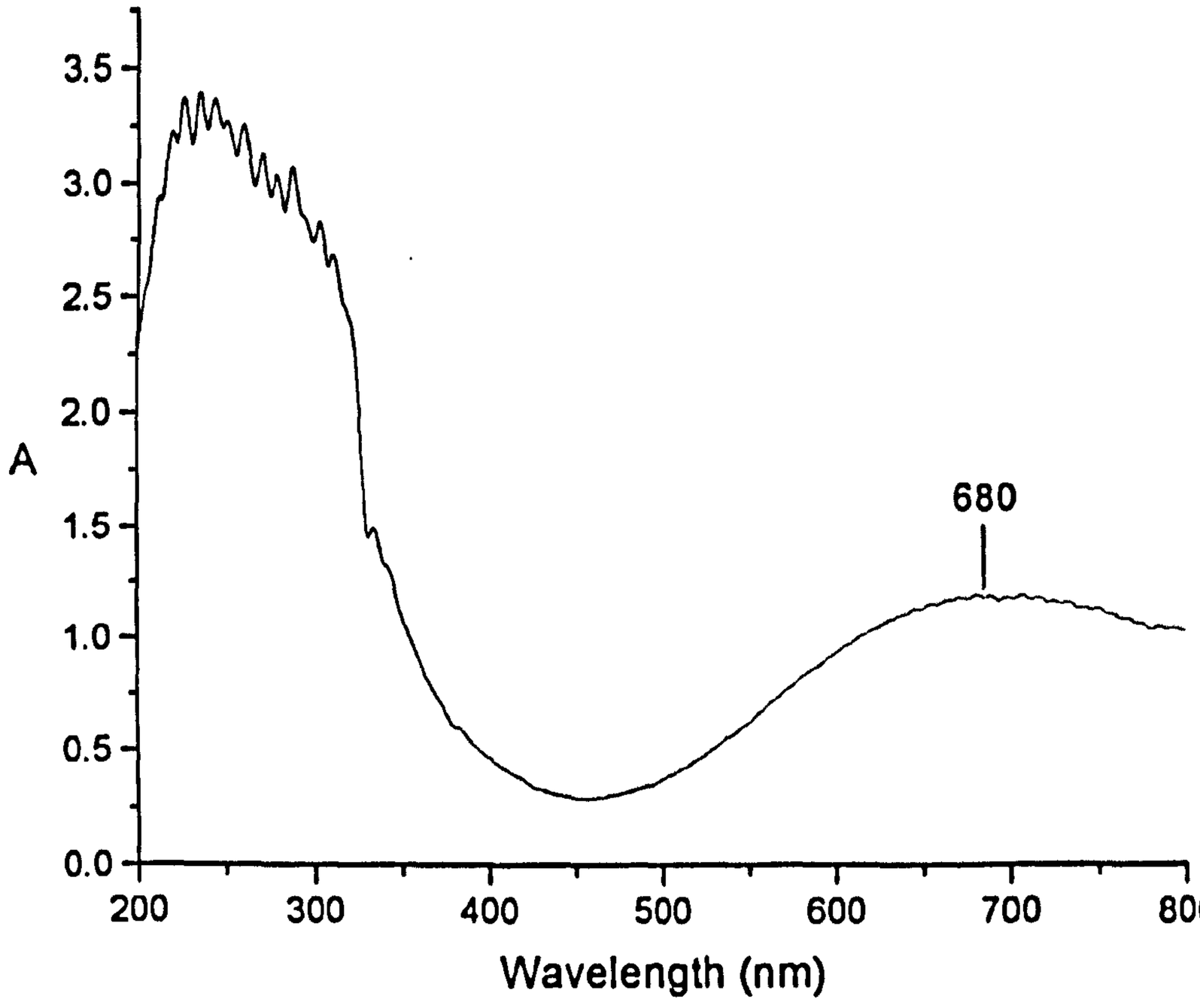

Figure 5-4 UV/Vis absorption spectrum of Prussian blue microemulsion fluids showed a broad band at 680 nm.

electron transition.[21] FTIR spectra contained a major band at 2069 cm^{-1} (Figure 5-5) that corresponds to the Fe-CN stretching mode in the cyanometallate lattice.

All the results indicated that the nanoparticles synthesised in the AOT microemulsion were typical Prussian blue crystals, but the size was remarkably different from that synthesised in the absence of surfactants.

5.3.3 The influence of water content (*w*) of the microemulsions on Prussian blue nanoparticles

The size and the superlattice domains of Prussian blue nanoparticles synthesized in AOT microemulsions were dependent on the water content (*w* value, the molar ratio of water to surfactant) of the microemulsion droplets. The size of discrete cubic nanoparticles was increased with increasing *w* value in the range of *w* = 10 – 20 under the investigated conditions. The nanoparticles synthesized at *w* = 10 were homogeneous in size (mean 12 nm, σ = 1.4 nm) and self assembled into small superlattice domains, often consisting of only four to twenty nanoparticles (Figure5-6a). At *w* =15, Prussian blue cubic nanoparticles were uniform in size (mean 16 nm, σ = 2.7 nm) and self-assembled into two dimensional or three dimensional highly ordered superlattices that were organized in domains up to 200 nm in length containing 60 – 100 nanoparticles (Figure 5-6b).

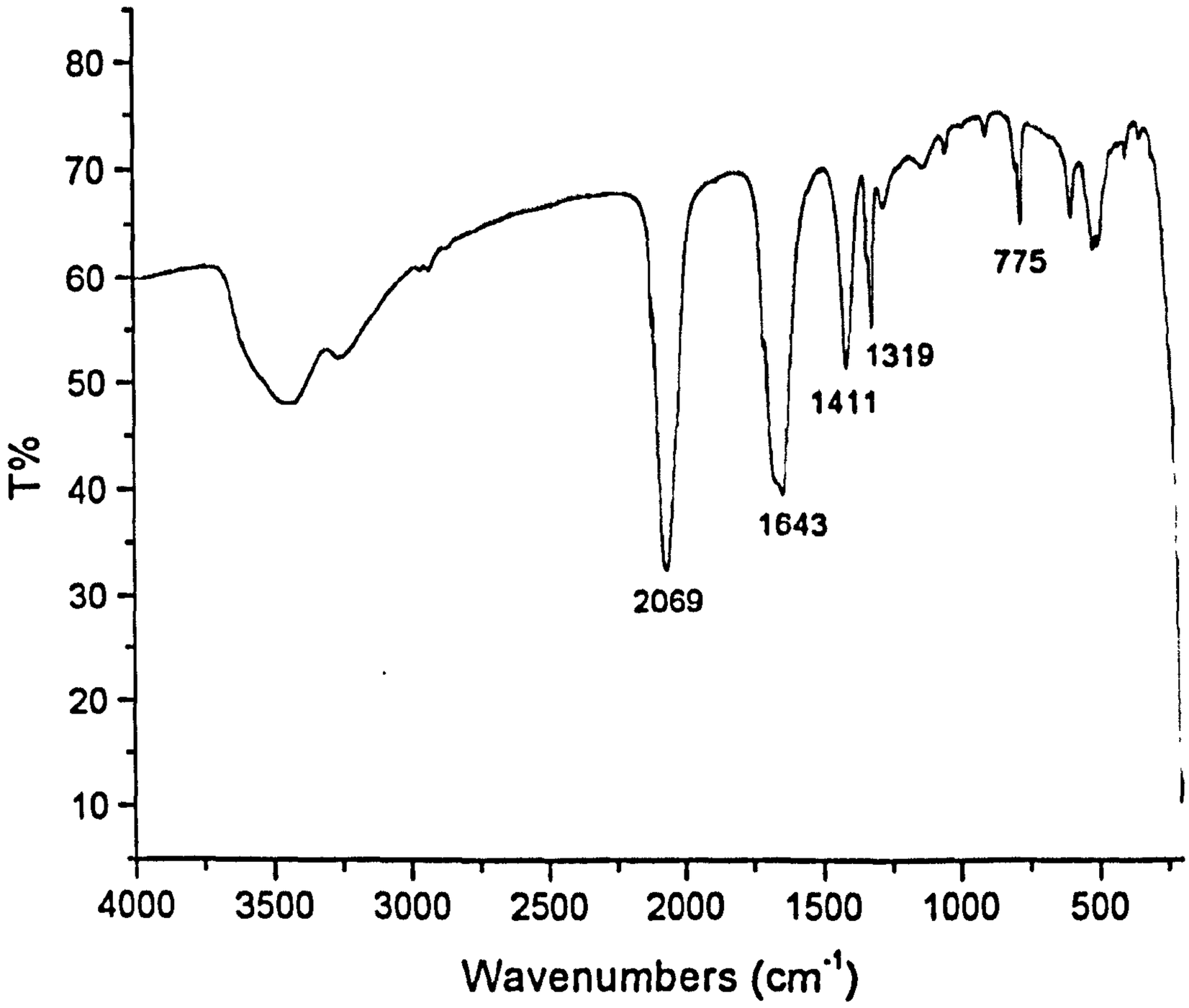

Figure 5-5 FTIR spectrum of Prussian blue nanoparticles showing a major band at 2069 cm^{-1}, that corresponds to the Fe-CN stretching mode in the cyanometallate lattice.

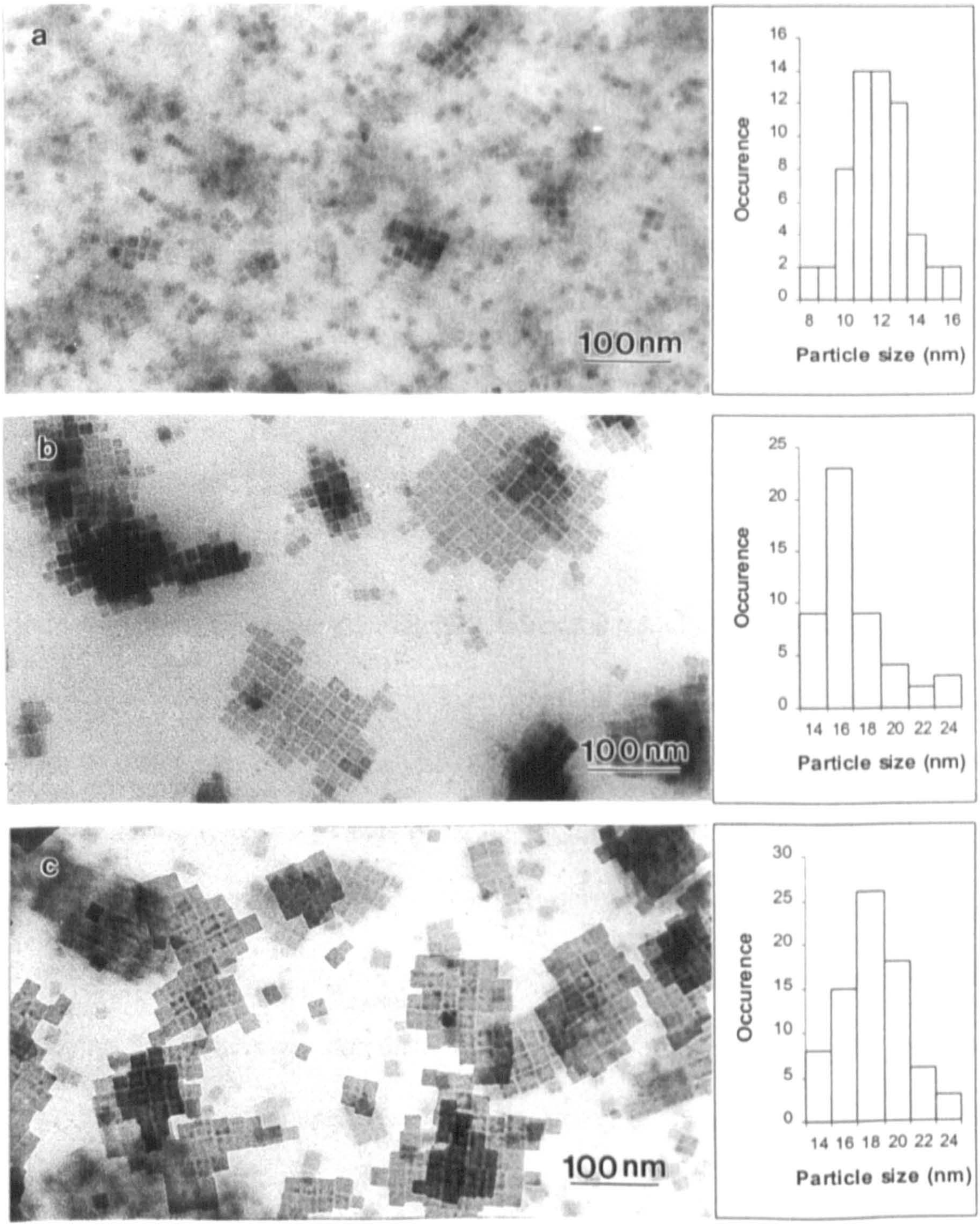

Figure 5-6 TEM images and the particle size distributions of Prussian blue nanoparticles prepared in AOT reverse microemulsion at **a**) $w = 10$; **b**) $w = 15$; **c**) $w = 20$. Scale bars = 100 nm.

Discrete particles were larger in size (mean 18 nm, σ = 2.1 nm) when synthesized at w = 20, but the superlattice domains were similar as that of w = 15 (Figure 5-6c). No nanoparticles were observed at w = 5, most probably because there is only sufficient amount of water for AOT headgroup hydration (reverse micelles) under these conditions.

5.3.4 Time dependence

Formation of the 2-D square superlattice structures from the microemulsion media was time dependent. For example, at w = 15 and from 0.3 M reaction solution, samples taken for TEM analysis after two days showed discrete cubic nanoparticles but no long-range ordering (Figure 5-7a). These particles were smaller and more heterogeneous in size distribution (mean 14 nm, σ = 4.9 nm) than those collected after four days, which showed well ordered superlattice structures and a narrower size distribution (mean 16 nm, σ = 2.7 nm) (Figure 5-7b). Prussian blue nanoparticles collected from the same microemulsion fluid after two weeks were slightly larger (mean 18 nm, σ = 2.1 nm) but the domain length of superlattices was reduced (Figure 5-7c). These results indicated that the formation of cubic Prussian blue nanoparticles was a slow process, which relates to the photoreduction and ion exchange between microemulsion droplets.

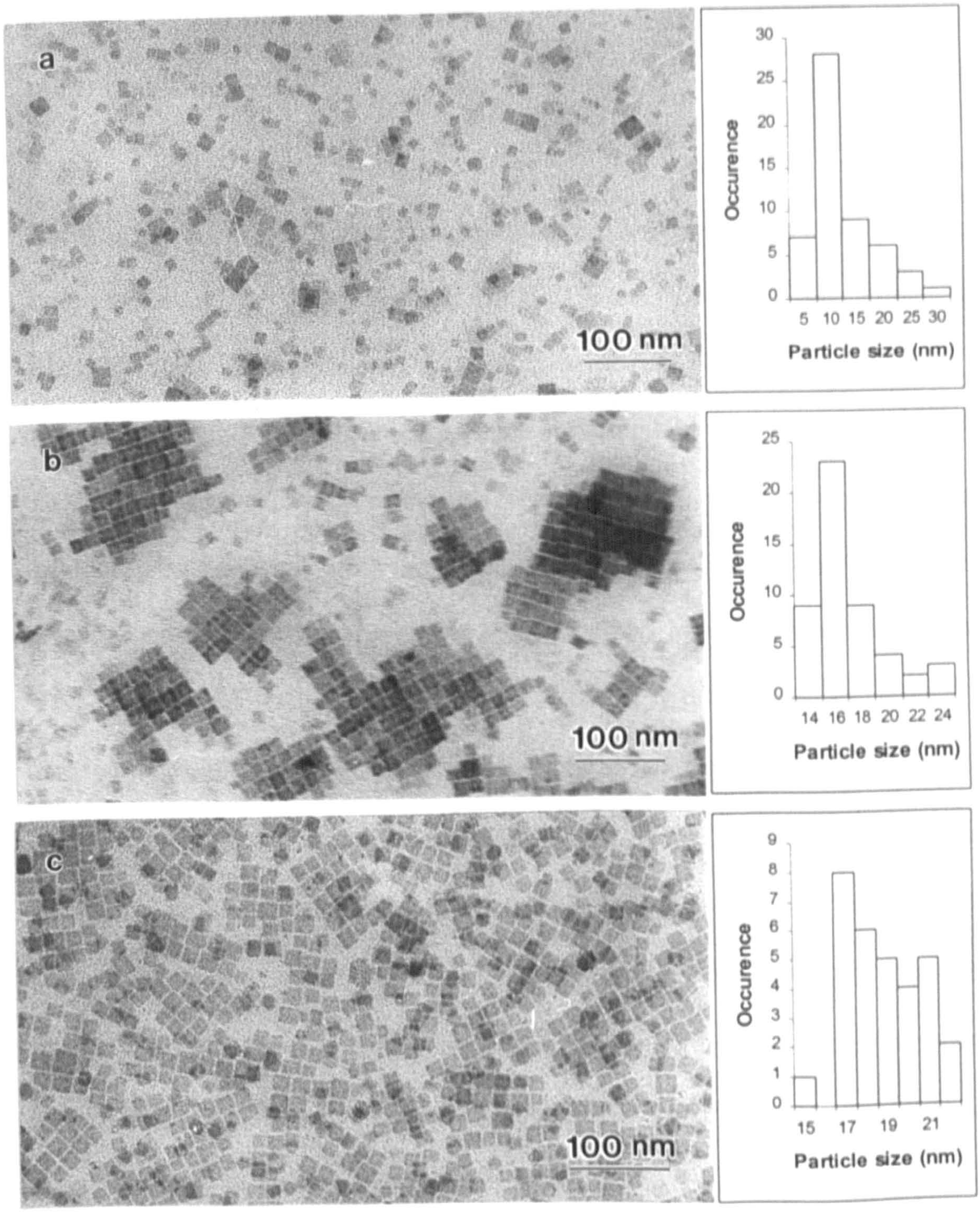

Figure 5-7 TEM images and the particle size distributions of discrete Prussian blue nanocrystals formed **a**) after two days from AOT microemulsions at $w = 15$; **b**) after four days showing superlattice structures; **c**) after two weeks showing well defined crystals but small superlattice domain sizes. Scale bars = 100 nm.

5.3.5 Investigation of the concentration of both reactants in reverse microemulsions

The size of the individual Prussian blue nanoparticles synthesized in AOT reverse microemulsions was dependent on the concentration of both the ammonium iron(III) oxalate and ammonium ferricyanide solutions. No significant changes in size (mean 16 nm) were observed between concentration values of 0.1 – 0.3 M at w = 15. However, at lower concentration (0.05 M), a pale blue transparent solution was observed after exposure to daylight for two days, which then transformed into a transparent yellow solution and blue precipitate after three days. The TEM images showed the presence of regular, cubic Prussian blue nanoparticles in the precipitate. The particles had a mean size of 39 nm (σ = 6.1 nm) and self assembled into superlattice domains (Figure 5-8a). No blue color developed in the microemulsion at reactant concentrations of 0.01 M, although a small yield of superlattice structures, consisting of cubic particles with an average size of 54 nm (σ = 4.2 nm), were observed (Figure 5-8b). This observation indicates that below a threshold value of 0.1 M, lower reactant concentrations result in fewer crystals of significantly larger dimensions. This is consistent with a nucleation-controlled process of Prussian blue deposition in the microemulsion droplets.

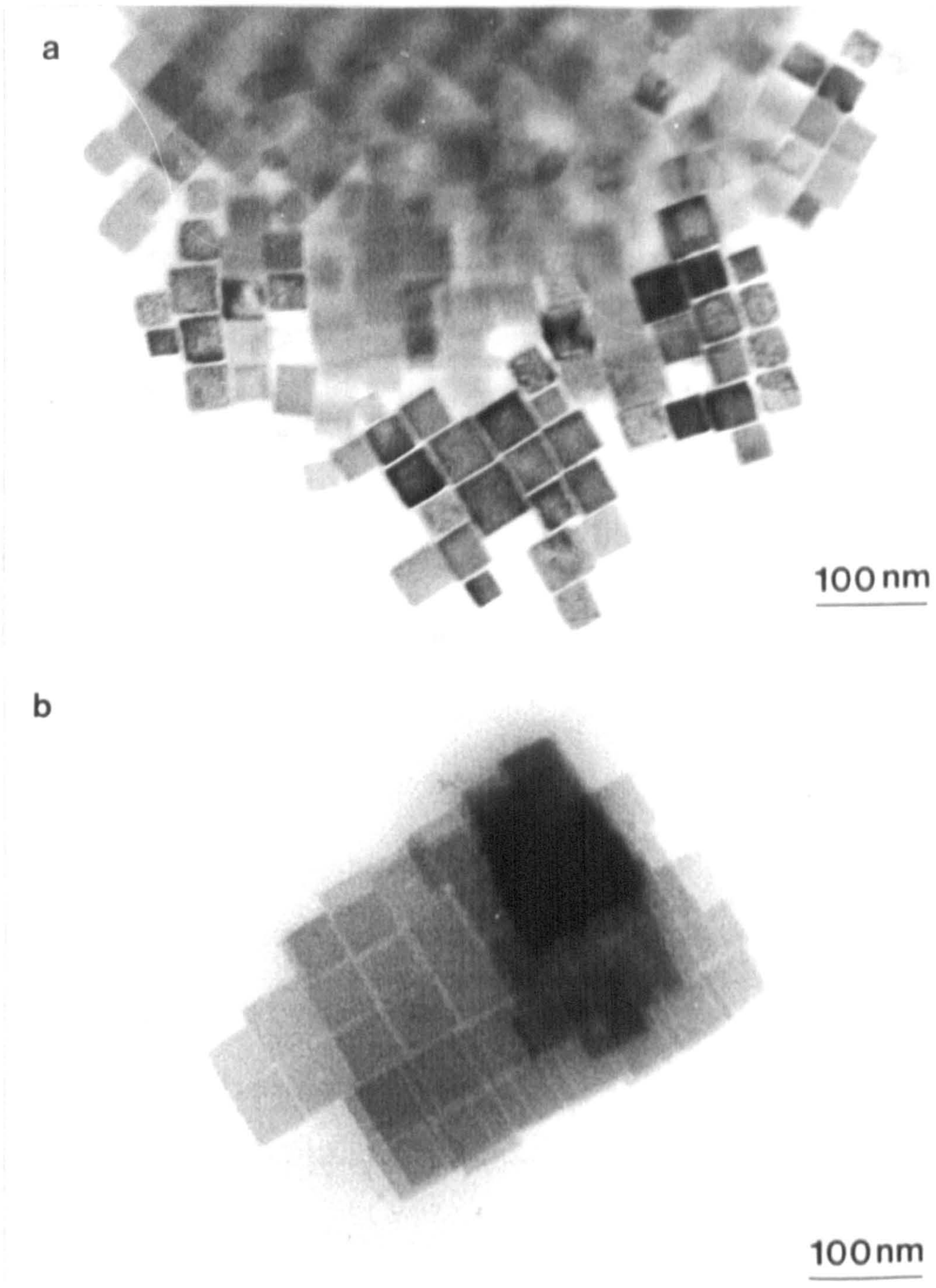

Figure 5-8 TEM images of Prussian blue nanoparticles and superlattices at w = 15 and reactant concentration of **a**) 0.05 M and **b**) 0.01 M. Scale bars = 100 nm.

5.4 Final discussion

The results clearly indicated that the formation of the cubic Prussian blue nanoparticles is dependent on various factors such as

- the rate of nucleation (photoreduction rates),
- *w* value and
- the reactant concentrations in the water droplets.

The complete formation of the cubic Prussian blue nanoparticles was a slow process (needs about four days in daylight) related to nucleation and growth. Photoreduction of $[Fe(C_2O_4)_3]^{3-}$ produces Fe^{II} ions that subsequently react with $[Fe(CN)_6]^{3-}$ ions to generate nuclei and clusters of Prussian blue encapsulated within the water droplets. Growth of the molecular magnet occurs by further exchange and fusion between microemulsion droplets to produce Prussian blue nanoparticles. The mean size of the cubic Prussian blue nanoparticles was increased from 12 nm to 18 nm on increasing the *w* value from 10 to 20; the related NaAOT microemulsion droplets were 2.2 – 3.2 nm in radius.[17] Comparing the volume of cubic nanoparticles (4096 nm^3, 16 nm in size) with that of NaAOT microemulsion droplets (82 nm^3, radius = 2.7 nm) at $w = 15$, the nanoparticles were 50 times larger than the water droplets. Moreover, at the reactant concentration of 0.3 M and $w = 15$, there are approximately 15 ions of $[Fe(C_2O_4)_3]^{3-}$ and 15 ions of $[Fe(CN)_6]^{3-}$ in each water-filled droplet cage. A 4096 nm^3 nanocrystal contains approximately 4000 unit cells, that is 16,000 $[Fe(CN)_6]^{4-}$ and 16000 Fe(III) ions. This means that at least 1000 complete transfers would

have to take place to produce crystals of the size observed. It remains unclear why the particle size is so uniform. One possibility is that, for a given concentration range, nanoparticle growth is self-limiting because of thermodynamic constraints imposed by restrictions in the membrane curvature arising from the limited numbers of water molecules that can be redistributed around the crystal surfaces.

The mature Prussian blue nanoparticles were always observed by TEM as superlattice structures rather than individual particles at $w = 15 - 20$. Such a large degree of self-assembly into superlattice domains is a direct consequence of the high concentration of Prussian blue nanoparticles with regular morphology and narrow size distributions, produced specifically by undertaking the reaction in organized media. The hydrophobic surface of the nanoparticles induced the self-assembly of the superlattice by a facile process in which the hydrophobic interactions between the surface-adsorbed AOT molecules dominate are the interparticle forces during solvent evaporation from the TEM grid. However, the developing nanoparticles (after two days, Figure 5-7a) did not produce superlattice structures, possibly because the broad size distribution of the nanoparticlesobserved at this stage.

The use of *in situ* photoreduction to prepare molecular magnet nanoparticles and superlattices from microemulsion fluids could have general applications in photo-patterning processes. For example, photo-formation of Prussian blue has been

investigated as an alternative photographic printing method,[21] and is particularly important when localized reactions and homogenous seeding are required.

5.5 Conclusions

This work shows that organic supermolecular templates and organized reaction media, which have been applied to many traditional inorganic solids for controlling particle size and shape, can also be applied to the molecular-based magnet Prussian blue.

We have developed a method to control the growth of Prussian blue and to organize the particles. Hydrophobic cubic nanoparticles with a narrow size distribution can be obtained using this method and the nanoparticles are able to self-assemble into a well-defined square superlattice. Thus, it is possible to achieve the synthesis of discrete particles of a molecular magnet material and order them into a superlattice in one step. This method has also been successfully applied to the synthesise of another molecular magnet material, Co-Fe Prussian blue.[22]

5.6 References

[1] Ware, M., *Ag+Photogr.*, **7**, 74 (1995).

[2] Ferlay, S., Mallah, T., Ouahes, R., Veillet, P.,Verdaguer, M., *Nature*, **378**, 701 (1995).

[3] Ohkoshi, S., Abe, Y., Fujishima, A., Hashimoto, K., *Phys. Rev. Lett.*, **82**, 1285 (1999)

[4] Verdager, M., Bleutzen, A., Marvaud, V., Vaissermann, J., Seuleiman, M., Desplanches, C., Scullier, A., Train, C., Garde, R., Gelly, G., Lomenech, C., Rosenman, I., Veillet, P., Cartier, C., Villain, F., *Coord. Chem. Rev.*, **190-192**, 1023 (1999).

[5] Honda, K., Hayashi, H., Chiba, K., *Chem. Lett.*, **2**,191 (1988).

[6] Avnir, D., Kagan, M. L., Ross, W., *Chem. Phys. Lett.*, **135**, 177 (1987).

[7] Ravaine, S., Lafuente, C., Mingotaud, C., *Langmuir*, **14**, 6347 (1998).

[8] Saliba, R., Agricole, B., Mingotaud, C., Ravaine, S., *J. Chem.Phys. B*, **103** 9712 (1999).

[9] Einagam, Y., Sato, O., Fujishima, A., Hashimoto, K., *J. Am. Chem. Soc.*, **121**, 3745 (1999).

[10] Moulik, S.P., De, G.C., Panda, A.K., Bhowmik, B.B., Das, A.R., *Langmuir*, **15**, 8361 (1999).

[11] Ware, M., *J. Photogr. Sci.*, **34**, 166 (1986).

[12] Kresge, C.T., Leonowicz, M.E., Roth, W.E., Vartuli, J.C., Beck, J.S., *Nature*, 379, 710 (1992).

[13] Mann, S., Burkett, S.L., Davis, S.A., Fowler, C. E., Mendelson, N.H., Sims, S.D., Walsh, D., Whilton, N.T., *Chem. Mater.*, 9, 2300 (1998).

[14] Goltner, C.G., Henke, S., Weisenberger, M.C., Antonietti, M., *Angew. Chem.*, 37, 613 (1998).

[15] Litvin, A.L., Valiyaveettil, S., Tingle, J., Kaplan, D.L., Mann, S., *Adv. Mater.*, 9, 124 (1997).

[16] Walsh, D., Lebeau, B., Mann, S., *Adv. Mater.*, 11, 324 (1999).

[17] Li, M., Schnablegger, H., Mann, S., *Nature*, 393, 402 (1999).

[18] Archibald, D.D., Mann, S., *Nature*, 364, 430 (1993).

[19] Walsh, D., Mann, S., *Adv. Mater.*, 9, 658 (1997).

[20] Herren, F., Fischer, P., Ludi, A., Haelg, W., *Inorg. Chem.*, 19, 956 (1980).

[21] M. Ware, *Cyanotype: the history, science and art of photographic printing in Prussian blue"*, the Science Museum and the National Museum of Photography, Film and Television, London, (1999). p. 142 and references there in.

[22] Fielden, J., Synthesis of Cobalt-Iron Prussian Blue Nanoparticles and Nanocrystal Superlattices in reverse microemulsions, University of Bristol, MSc thesis, 2000.

Chapter 6

Synthesis of $BaSO_4$ Nanoscale Spherical Hollow Particles (Nanoshells) Templated by Two Surfactants

6.1 Introduction

Synthesis of nanoparticles is an emerging field in material science, as small scale structures exhibit novel and useful material properties that differ from bulk properties. A large number of nanosize materials have been synthesised, such as silica,[1-2] silver,[3-5] copper,[6-10] copper sulfide,[11-12] silver sulfide,[13-15] barium chromate,[16] barium sulfate,[17] cobalt,[18] silver chloride,[19] semiconductor clusters $Cd_{1-y}Mn_yS$[20] and $Cd_yZn_{1-y}S$,[21] platinum,[22-23] and gold colloids.[24] The major approach for synthesis of nanomaterials consists of using surfactant assemblies or copolymers as growth directing agents. The actual morphology of the final materials depends on the curvature of the templating assembly. At one extreme, a synthesis taking place inside surfactant aggregates of strong negative curvature will lead to discrete nanoparticles (as exemplified by the extensive use of AOT reverse microemulsions); conversely if the growth occurs outside surfactant aggregates of positive curvature, porous solids will be formed. For example, precipitation from the mixture $Zr(SO_4)_2$/cetytrimethylammonium bromide has recently been shown to form ordered hexagonal mesophases.[25] Most nanomaterials are synthesised using either cationic or anionic surfactants as templates. Very limited work has been done in the presence of both cationic and anionic surfactants. Lisiecki *et al* (1995) have added cetytrimethylammonium chloride (CTAC) to AOT microemulsion to control the size of copper nanoparticles,[26] and Jeunieau *et al* (1999) have added

hexadecyltrimethyl-ammonium bromide (CTAB) to AOT microemulsion to increase the stability of silver halide nanoparticles.[27]

Under appropriate conditions a mixture of an anionic and a cationic surfactant is known to produce a salt – a so-called catanionic surfactant. Supramolecular behaviour of catanionic surfactants has been reviewed[28] but no attention has been paid to the synthesis of inorganic salts evolved during mixing of the two surfactants.

The growing scientific and technological interest in nanosize particles is fuelling a quest for new synthesis methods. In this work, we report for the first time a new method that produces $BaSO_4$ spherical nanoscale hollow particles (nanoshells) formed by reaction of aqueous hexadecyltrimethylammonium sulfate $[(CTA)_2SO_4]$ micelles with barium bis(2-ethylhexyl) sulfosuccinate $[Ba(AOT)_2]$ reverse micelles in isooctane. Surfactant $(CTA)_2SO_4$ forms micelles in water with SO_4^{2-} anions associated to some extent with the surface of the micelles (scheme 6-1). In contrast, $Ba(AOT)_2$ forms reverse micelles in isooctane (scheme 6-1). If these two functionalised surfactants are mixed, $BaSO_4$ crystals could form between the two surfactants. Furthermore, because of the positive curvature of CTA aggregates and negative curvature of AOT aggregates, hollow spherical crystals might be produced (Scheme 6-1).

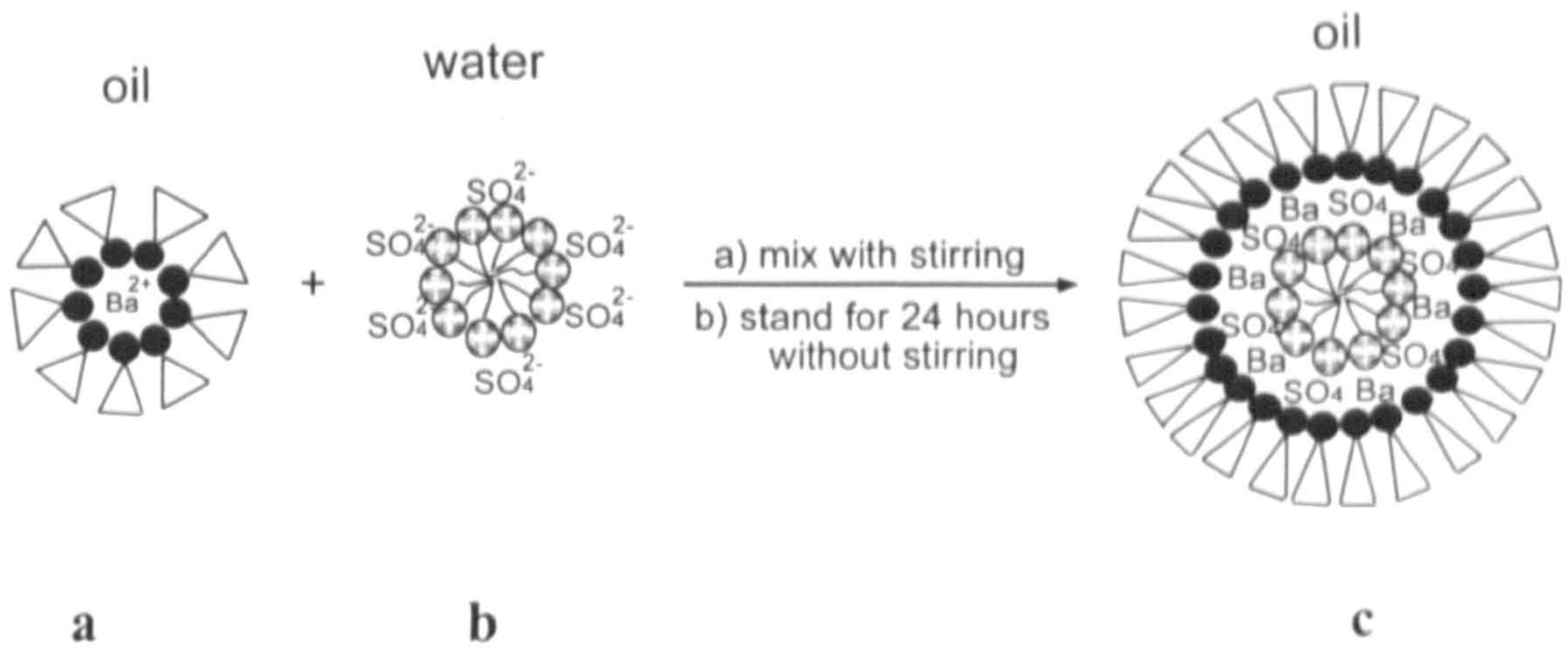

Scheme 6-1. Sketch of the synthesis process for $BaSO_4$ spherical hollow nanoparticles. **a**, $Ba(AOT)_2$ reverse micelle in isooctane. **b**, $(CTA)_2SO_4$ micelle in water. **c**, $BaSO_4$ hollow particles template by two surfactants.

Traditional methods of synthesis of hollow spheres involve spherical templates such as colloidal particles. A thin coating of inorganic material is formed on beads to create a core-shell composite, and subsequent removal of the template by calcination or selective etching in an appropriate solution generates hollow spheres whose inner diameter is determined by the size of the template, typically a few hundred nanometres to few micrometres in size. The colloidal particles that have been used include nanoscale gold, silver, CdS and microscale silica or polymer beads.[30-34] Compared with these existing methods, the work described in this chapter aims to develop a direct one-step synthesis route to nanoscale hollow

inorganic spheres. Such materials could be useful in many areas especially in delivery of drugs (150-200 nm in external diameter),[35-36] development of artificial cells, and protection of biologically active agents such as proteins, enzymes or DNA.[37] They might also be useful as carriers of perfumes (2-15 μm in external diameter)[38]

6.2 Materials and Methods

6.2.1 Materials

All materials were of analytical grade and used without further purification.

Table 6-1 Chemicals used in this chapter

Common name	Chemical name	Formula	Molecular weight	Supplier
CTAB	hexadecyltrimethyl ammonium bromide	$C_{19}H_{42}N\,Br$	364.0	Aldrich
	silver sulphate	Ag_2SO_4	311.8	Aldrich
NaAOT	sodium bis(2-ethylhexyl) sulphosuccinate	$C_{20}H_{37}O_4SO_3Na$	444.6	BDH
	barium chloride	$BaCl_2$	208.2	Aldrich
	silver nitrate	$AgNO_3$	169.9	Aldrich
isooctane	2,2,4-trimethyl pentane	C_8H_{18}	114.0	Aldrich

6.2.2 Methods

6.2.2.1 Preparation of surfactants

A Hexadecyltrimethylammonium sulphate [$(CTA)_2SO_4$]

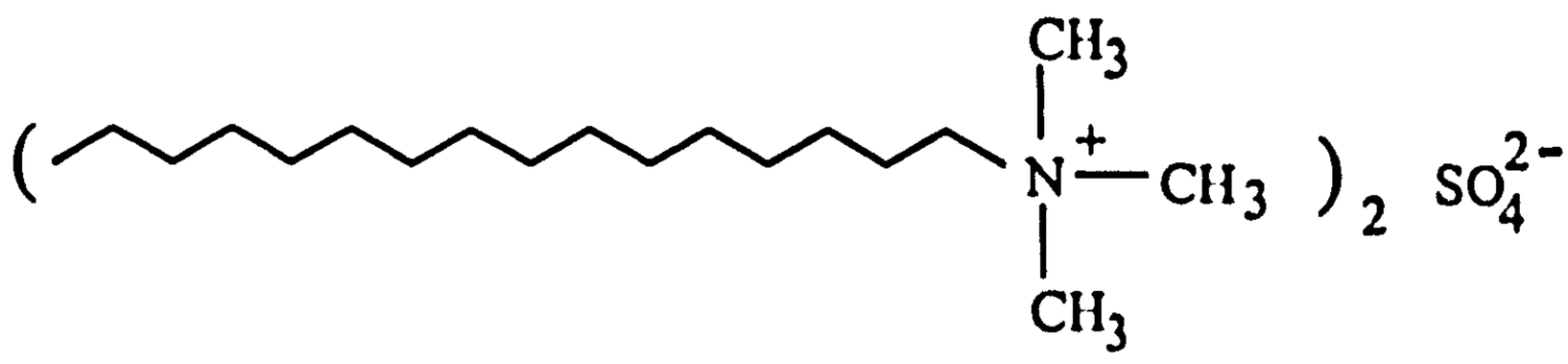

$(CTA)_2SO_4$ (MW = 665) was prepared from hexadecyltrimethylammonium bromide (CTAB) by metathesis using solid silver sulphate in methanol followed by recrystallization from acetone-methanol.[39-40] In a light-protected flask, 3.12g of white powdered Ag_2SO_4 was added to 100 ml of a 0.2 M CTAB methanolic solution under stirring, which leads to immediate precipitation of yellow AgBr. The reaction mixture was sonicated for 5 minutes and then kept under stirring for a further two hours. After centrifugation, acetone was added to the supernatant until a white precipitate appeared. The product was filtered and the white $(CTA)_2SO_4$ powder was dried under vacuum for 2 days. The product was dissolved in water and titrated with $AgNO_3$ aqueous solution, no yellow AgBr precipitate was observed. The product was titrated with $BaCl_2$ aqueous solution, and a white $BaSO_4$ precipitate appeared immediately, implying that ion exchange SO_4^{2-} against Br^- was complete. The FTIR spectrum (cm^{-1}) showed: 2945(sh), $\nu_{as(CH_3)}$; 2919(vs), $\nu_{as(CH_3)}$; 2849(vs), $\nu_{as(CH_2)}$; 1467(m), $\delta_{s(CH_2)}$; 1221(m) $\nu_{terminal(S=O)}$ 1190(sh), $\nu_{3a(S=O)}$; 1054(m), $\nu_{3b(S=O)}$; 960-870(w), $\nu_{1(S=O)}$ and $\nu_{(N-CH_3)}$; 589(m), $\nu_{4(S=O)}$[41-42] (Figure 6-14h). Mass spectrometry showed that the molecular weight of the exchange product was 665. M.S., Fast Atom Bombardment result; (FAB) (+) m/z: 666, 20% $[CTA_2SO_4H]^+$; 284, 100% $[CTA]^+$. The protonated molecular peak present when CTA is associated to SO_4^{2-} anion has no equivalent in FAB spectrum of CTABr.

B Barium bis(2-ethylhexyl) sulfosuccinate [$Ba(AOT)_2$]

$Ba(AOT)_2$ (MW = 980) was prepared by direct reaction of sodium AOT and barium chloride in water[17] (section **3.2.1.2**).

6.2.2.2 Preparation of barium sulphate nanoshells

Typically, 5 ml of $Ba(AOT)_2$ transparent isooctane solution (4 mM) was added to 10ml of $(CTA)_2SO_4$ transparent aqueous solution (4 mM) with gentle stirring to give a very milky liquid. After standing on the bench at room temperature for 24 hours without stirring, three layers were observed in the solution. The top layer was a clear organic solution, the middle layer was a white milky liquid and the bottom layer was a turbid aqueous solution. Characterization was performed on each layer. The nanoshells were contained in the top and middle layers.

6.2.2.3 Characterization

A. Transmission Electron Microscopy (TEM): samples for TEM were collected separately from each layer of the solution and deposited onto Formvar-coated, carbon-reinforced, 3 mm diameter, copper electron microscope grids. For the samples from the top and second layers, the grids were washed with pure isooctane after being air-dried. For the samples from the bottom layer, the grids were washed with water. TEM analysis was performed in bright field mode using either a JEOL 2000 FX high-resolution electron microscope operating at 200 keV or a JEOL 1200 EX electron microscope operating at 120 keV (section **2.3.1**). The imaged crystals were characterized by selected area electron diffraction (SAED) (section **2.3.2**) and energy-dispersive X-ray analysis (EDXA) (section **2.3.3**). The former were indexed with reference to the unit cell of barium sulphate

a, b, c, = 8.909, 5.467, 7.188 Å (Table 4-2). Particle size distributions were calculated by TEM image analysis.

B. Fourier Transform Infrared (FTIR) analysis was performed with a BRUKER IFS25 spectrophotometer. Samples for FTIR were taken from the top and the middle layers that were precipitated with a polar solvent (ethanol). After centrifugation, the precipitate was washed gently with ethanol to remove free AOT molecules, and air-dried. FTIR measurements were performed using KBr discs.

C. Dynamic Light Scattering (DLS) was performed with a Malvern Autosizer 4700 at 532 nm and 90° detector angle. Samples for DLS were $(CTA)_2SO_4$ micelles in aqueous solution. Prior to measurement all samples has been filtrated through a 0.2 μm membrane.

6.3 Results and Discussion

6.3.1 Description of hollow particles

5 ml of $Ba(AOT)_2$ transparent solution (4mM in isooctane) was added to 10ml of $(CTA)_2SO_4$ aqueous transparent solution (4 mM) with gentle stirring to give a very milky solution with final molar ratio $Ba(AOT)_2/(CTA)_2SO_4$ = 1 : 2. After standing at room temperature for 24 hours without stirring, three layers were observed in the solution. The top layer was a transparent organic solution and the bottom layer was a turbid aqueous solution. The middle layer between the organic and inorganic phases was a white milky liquid. TEM images corresponding to samples removed from the top layer showed individual spherical hollow nanoparticles (Figure 6-1a and 6-2) with 9.6 ± 1.5 nm external diameter (Figure 6-1b) and 3.4 ± 0.3 nm internal diameter (Figure 6-1c). The shell thickness is 3.1 nm (Scheme 6-2).

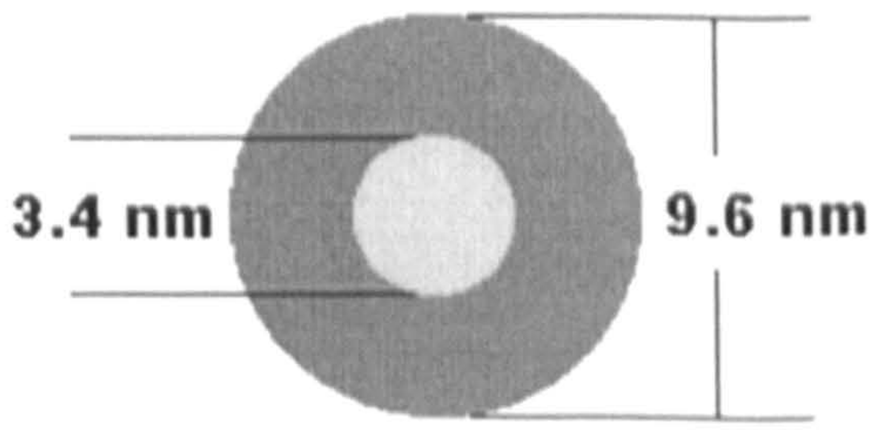

Scheme 6-2. Sketch of $BaSO_4$ spherical hollow particle.

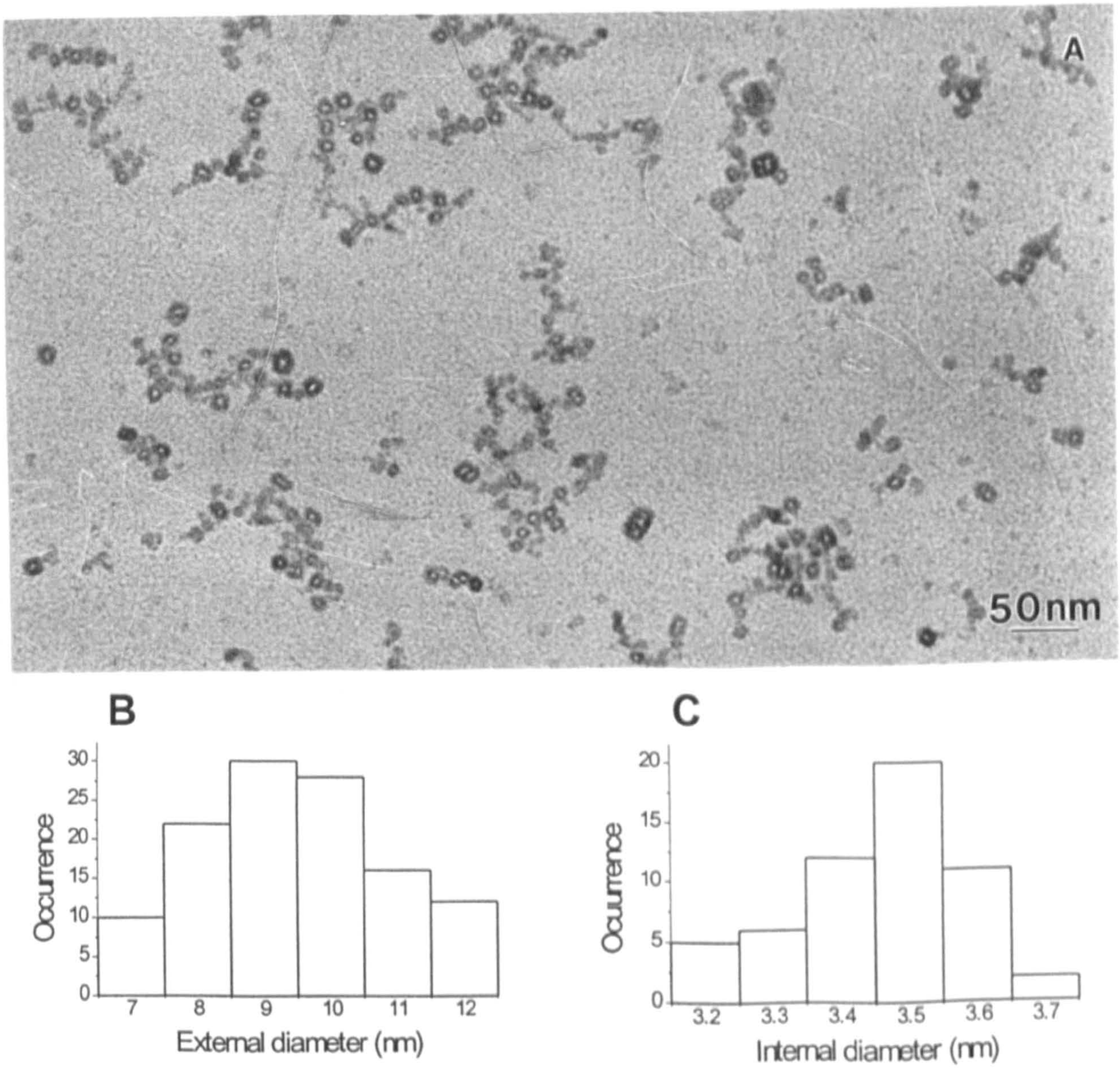

Figure 6-1. **(a)** TEM image of $BaSO_4$ nanoshells prepared in the presence of two functionalized surfactants $(CTA)_2SO_4$ (4 mM in H_2O) and $Ba(AOT)_2$ (4 mM in isooctane). Sample was taken from top layer. Scale bar = 50 nm. **(b)** histogram of external diameter and **(c)** internal diameter of $BaSO_4$ nanoshells.

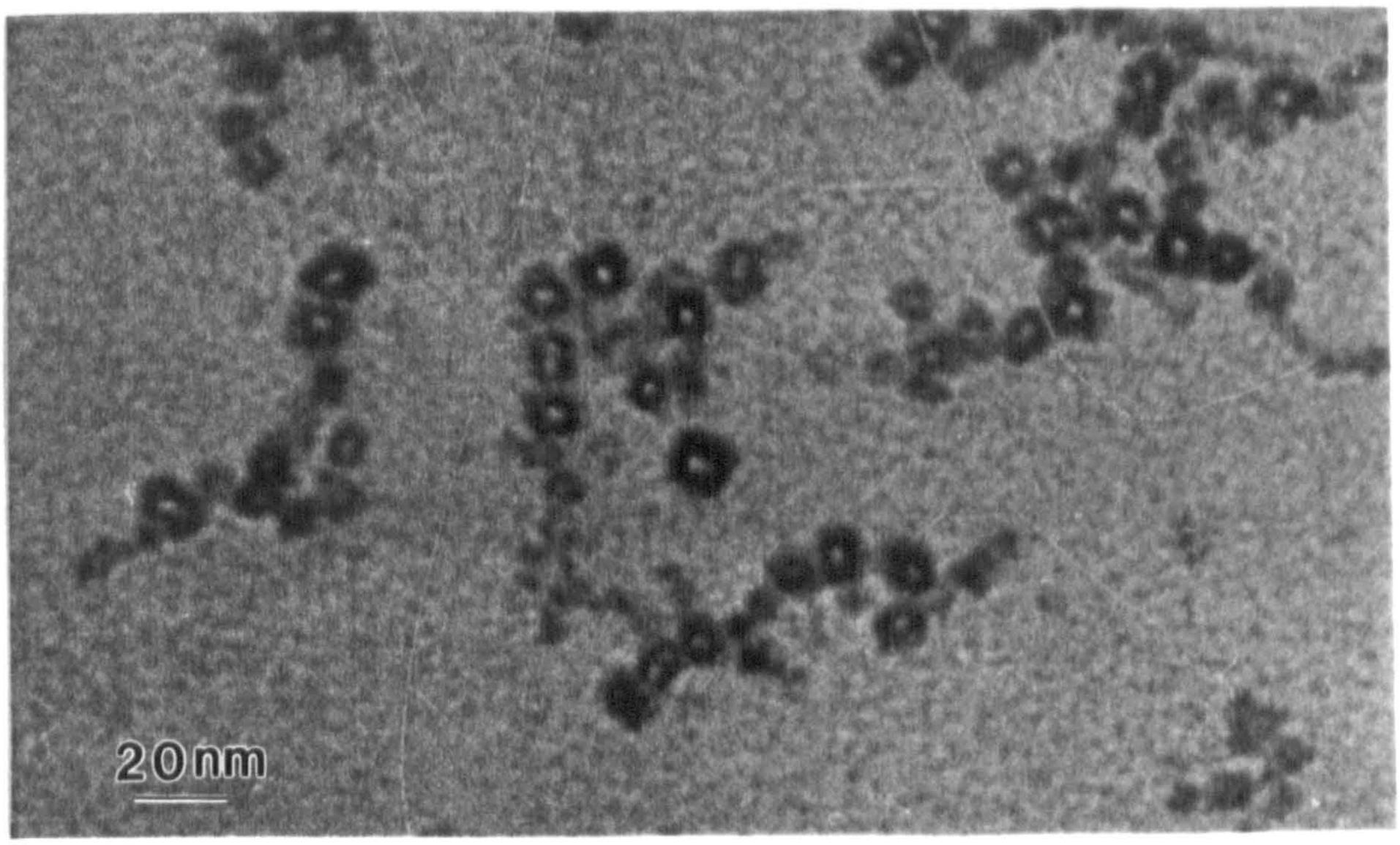

Figure 6-2. Enlarged TEM image of figure 6-1a. Scale bar = 20 nm.

Corresponding samples from the middle layer showed spherical hollow nanoparticles with the same external and internal diameters as the top layer but the particles were more aggregated (Figure 6-3a). Samples from the bottom layer showed $BaSO_4$ particles with irregular shape and size (50-350 nm) (Figure 6-4).

6.3.2 Identification of hollow particles

TEM imaged hollow particles were characterized by energy-dispersive X-ray analysis (EDXA). The EDXA spectrum indicated the presence of Ba (4.4, 4.8, 5.1 KeV) and S (2.3, 2.6 KeV) (Figure 6-3b). Imaged hollow particles were also characterized by selected area electron diffraction (SAED). Typical barium sulphate d-spacings 4.35Å {011}, 3.91Å {111}, 3.45Å {210}, 3.34Å {102}, 3.12Å {211} and 2.74Å {301} indexed according to Barite reference data (Cambridge database) (Table 4-2) were obtained by measuring the diffraction pattern (Figure 6-3c). High resolution TEM images (Figure 6-3d) showed lattice fringes corresponding to the (210) d-spacings (3.5 Å). From figure 6-3d we can see that the lattice fringes traverse over the whole image, implying that the central hollow area was covered by the $BaSO_4$ crystal lattice. This indicates that the image corresponds to a spherical hollow particle and not a toroidal structure.

Thus, the results indicate that the particles (ca. 10 nm) synthesized by using two functionalised surfactants—$Ba(AOT)_2$ and $(CTA)_2SO_4$—were hollow crystalline shells (ca. 3 nm in thickness) of barium sulphate.

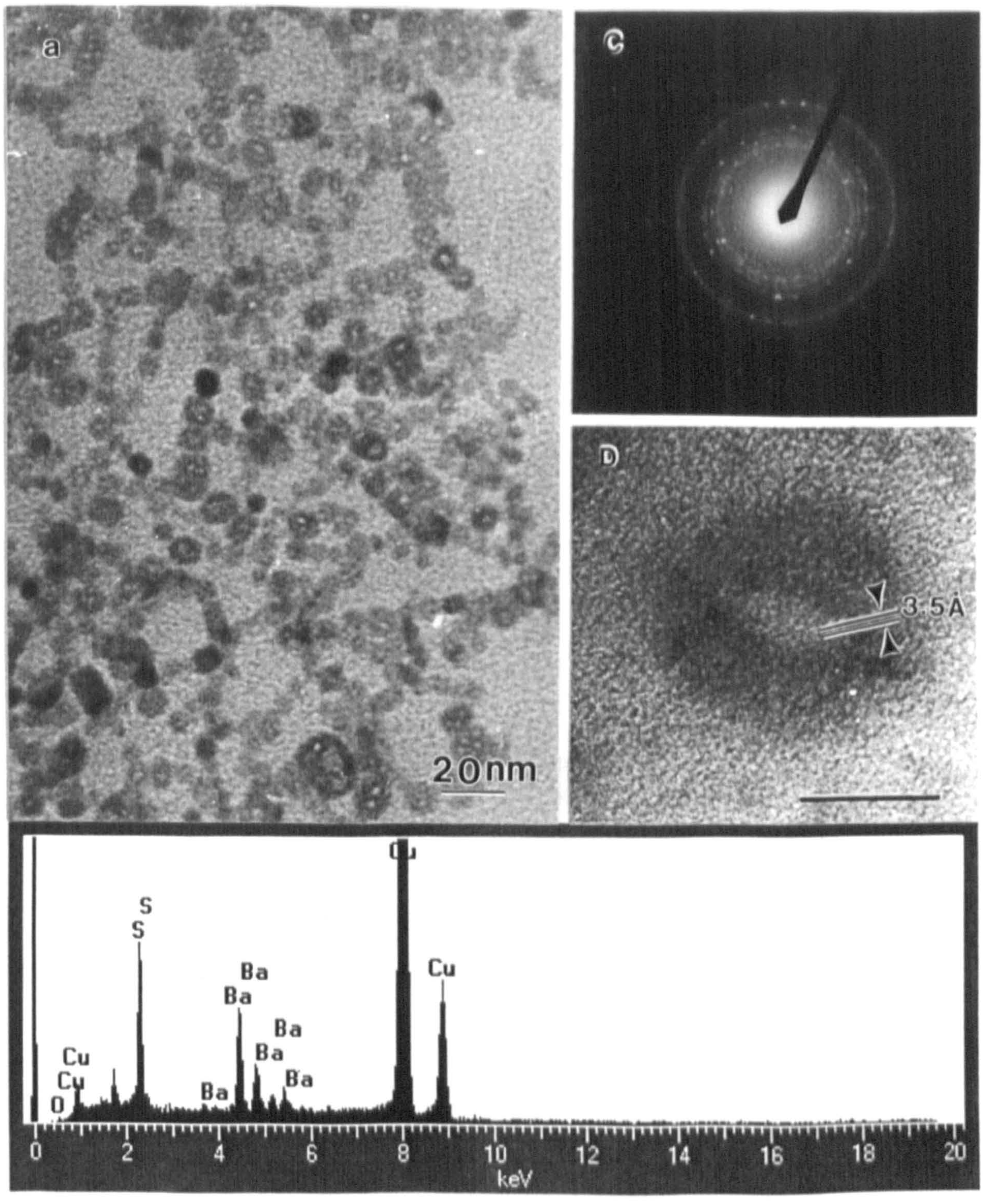

Figure 6-3. **(a)** TEM image of aggregated $BaSO_4$ nanoshells prepared in the presence of two functionalized surfactants $(CTA)_2SO_4$ (4 mM in H_2O) and $Ba(AOT)_2$ (4 mM in isooctane). The sample was taken from middle layer. Scale bar = 50 nm. **(b)** energy-dispersive X-ray analysis (EDXA) spectrum recorded from (a) area, **(c)** selected (a) area electron diffraction (SAED) pattern and **(d)** high resolution TEM image of single $BaSO_4$ nanoshell, Scale bar = 5 nm.

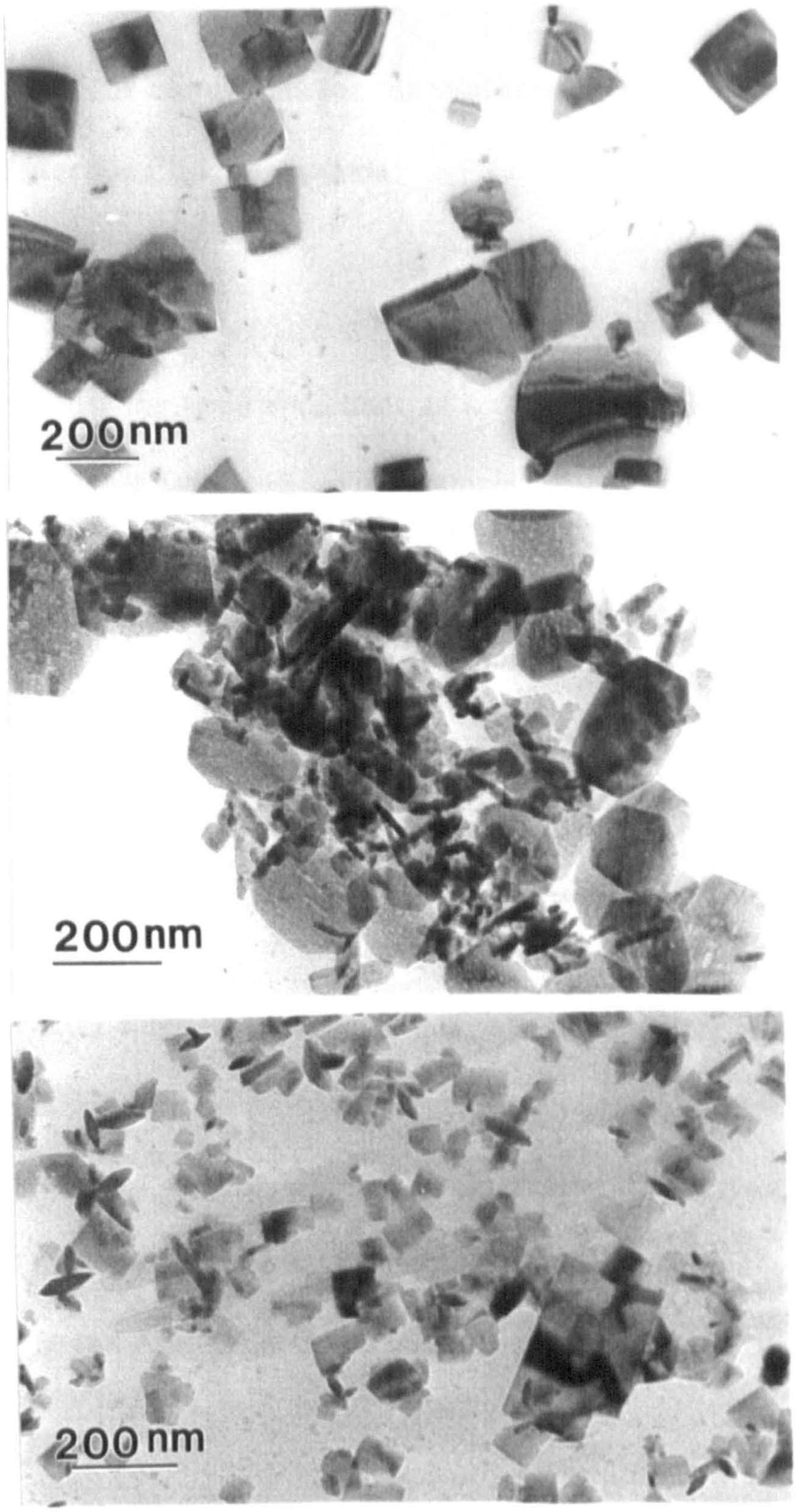

Figure 6-4. TEM images of $BaSO_4$ particles. Samples were taken from bottom layer of solution prepared in the presence of two functionalized surfactants $(CTA)_2SO_4$ (4 mM in H_2O) and $Ba(AOT)_2$ (4 mM in isooctane). Scale bars = 200 nm.

6.3.3 Investigation of the conditions for the synthesis of nanoshells

6.3.3.1 Influence of functionalised surfactants

If only one functionalised surfactant was used to synthesize barium sulphate nanoparticles under the same conditions as section 6.3.1, particles of different shape and size were produced. For example, if 5 ml of unfunctionalized surfactant NaAOT isooctane solution (20 mM) was added to 10 ml of functionalised surfactant $(CTA)_2SO_4$ aqueous solution (10 mM) (AOT/CTA = 1 : 2) with stirring, and then 0.1 ml of $BaCl_2$ (500 mM) aqueous solution was added to the mixture of surfactants (Ba^{2+}/SO_4^{2-} = 1 : 2), $BaSO_4$ nanoscale spherical hollow particles could not be found in any of the three layers. Instead, spherical nanoparticles with 3.7 ± 0.4 nm in diameter were produced (Figure 6-5a) in the middle milky layer between organic and inorganic phases. Energy-dispersive X-ray analysis (EDXA) (Figure 6-5b) and selected area electron diffraction (SAED) pattern (Figure 6-5c) showed that the nanoparticles were crystalline barium sulphate. No particles could be observed by TEM in the top turbid layer in which catanionic surfactant AOT-CTA should be contained.

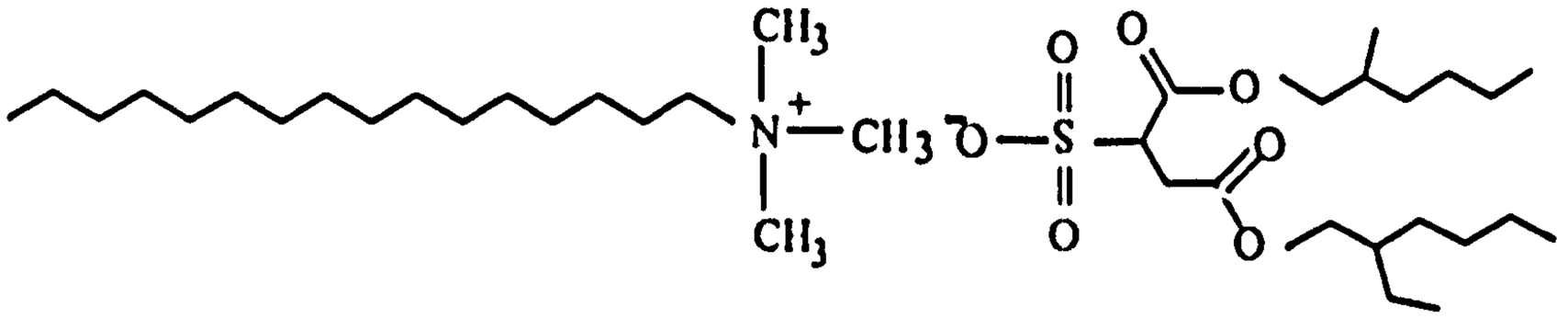

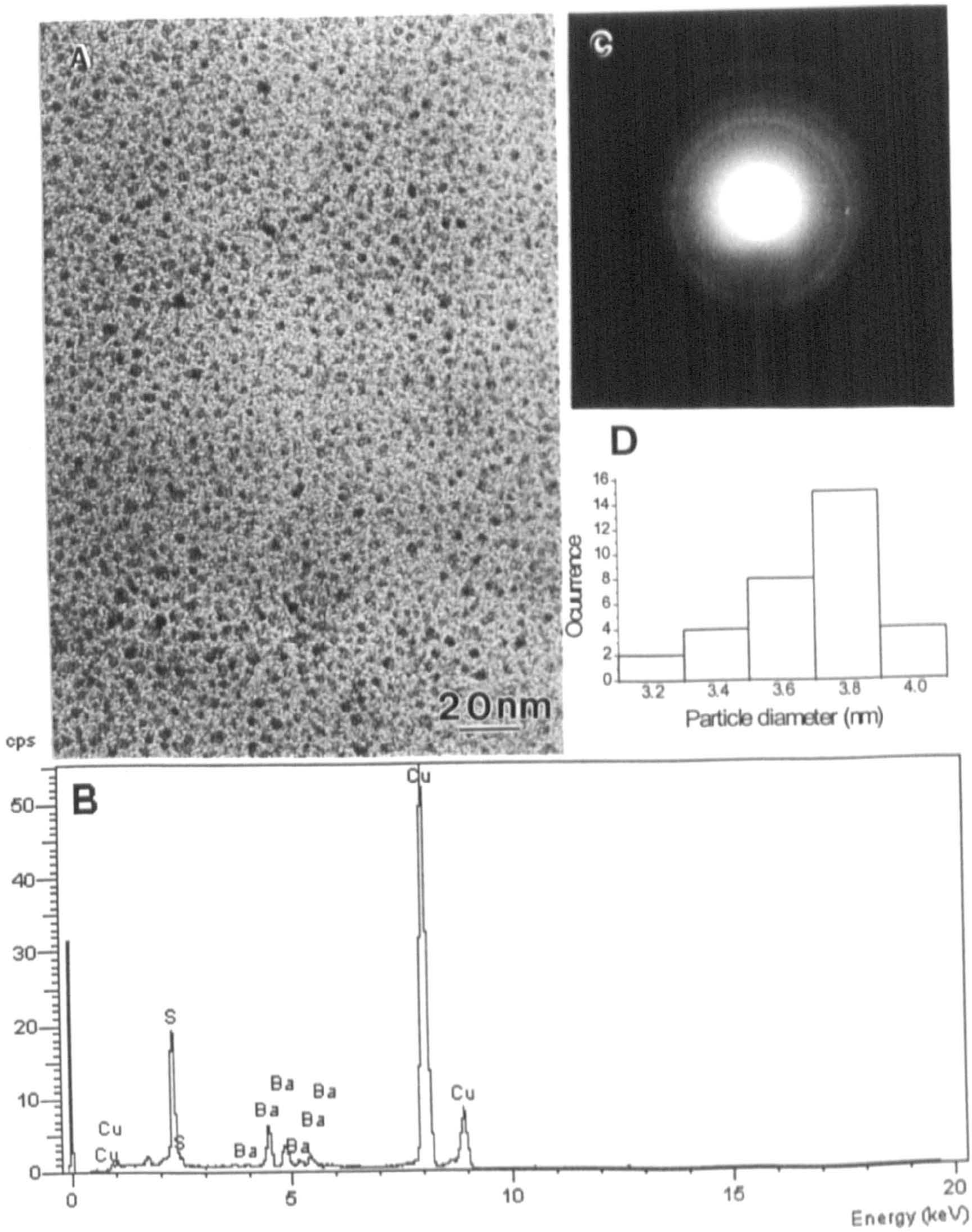

Figure 6-5. **(a)** TEM image of $BaSO_4$ spherical nanoparticles prepared in the presence of unfunctionalized surfactant NaAOT (20 mM in isooctane) and functionalised surfactant $(CTA)_2SO_4$ (10 mM in H_2O), scale bar = 20 nm; **(b)** energy-dispersive X-ray analysis (EDXA) spectrum recorded from (a) area; **(c)** selected (a) area electron diffraction (SAED) pattern and **(d)** distribution of the diameter of nanoparticles.

Rectangular $BaSO_4$ particles with irregular size (80 – 200 nm) were observed in the white precipitate extracted from inorganic bottom layer (Figure 6-6).

However, if 5 ml of functionalised surfactant $Ba(AOT)_2$ isooctane solution (10 mM) was mixed with 10 ml of unfunctionalized surfactant CTABr aqueous solution (20 mM) containing 0.2 ml of Na_2SO_4 aqueous solution (500 mM) with stirring (AOT/CTA = 1 : 2, and Ba^{2+}/SO_4^{2-} = 1 : 2), after standing at room temperature without stirring for 24 hours, three layers were observed. TEM images corresponding to the top organic layer of milky solution and the middle layer of thick milky liquid showed cubic nanoparticles (Figure 6-7a and 6-8) with very narrow size distribution (7.5 ± 0.6 nm in size) (Figure 6-7b) packed into small domain superlattices with ~2 nm spaces between the particles, that is typical for an interdigitated bilayer of surfactant AOT molecules.[16] Interestingly, there was a 2.4 ± 0.2 nm (Figure 6-7c) diameter hole in the middle of some of the nanoparticles (about 20%) (Figure 6-7a). Selected area electron diffraction (SAED) patterns showed d-spacing of 3.45 Å, 2.86 Å 2.63 Å and 2.09 Å (Figure 6-7a insert) and EDXA showed the presence of Ba (4.4, 4.8, 5.1 keV) and S (2.3, 2.6 keV) (Figure 6-7d), implying that the nanocubes consisted of crystalline $BaSO_4$. TEM images corresponding to the bottom layer of turbid aqueous solutions showed 50 – 500 nm particles of irregular shape, as well as many ring shaped particles, 50 – 200 nm in internal diameter and 200 – 500 nm in external diameter (Figure 6-9a,b). Energy-dispersive X-ray analysis (EDXA) indicated the presence of Ba (4.4, 4.8, 5.1 KeV), S (2.3, 2.6 KeV) and Br (1.5, 11.9, 12.2 KeV). However, electron diffraction result showed single crystal pattern of $BaSO_4$

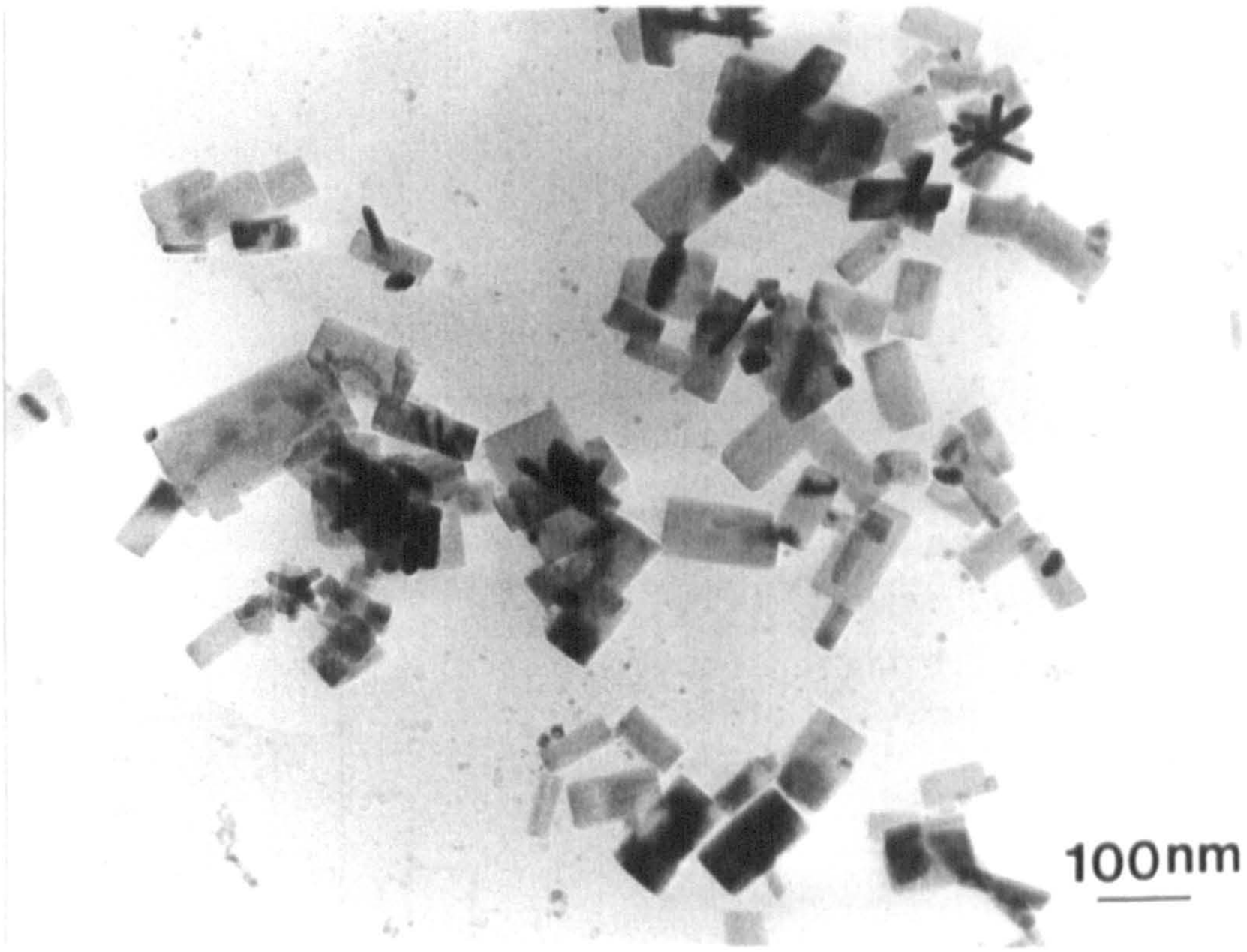

Figure 6-6. TEM image of $BaSO_4$ particles prepared in the presence of functionalised surfactant $(CTA)_2SO_4$ (10 mM in H_2O) and unfunctionalised surfactant NaAOT (20 mM in isooctane). Sample was taken from precipitate. Scale bar = 100 nm.

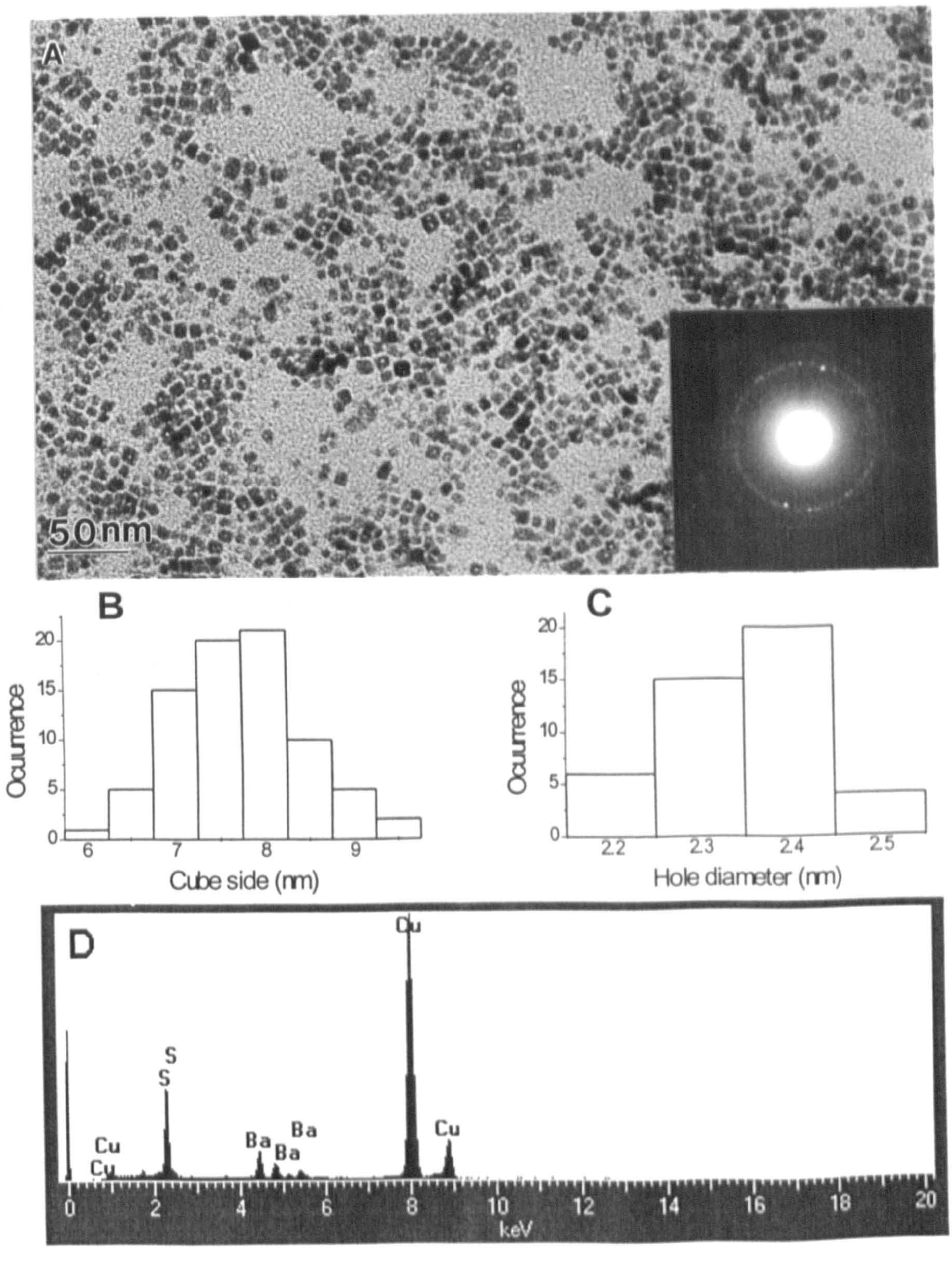

Figure 6-7. **(a)** TEM of $BaSO_4$ cubic hollow nanoparticles prepared in the presence of functionalised surfactant $Ba(AOT)_2$ (10 mM in isooctane) and unfunctionalized surfactant CTAB (20 mM in H_2O) and selected area electron diffraction (SAED) pattern (insert), scale bar = 50 nm; **(b)** distribution of cube side and **(c)** the hole diameter; **(d)** energy-dispersive X-ray analysis (EDXA) spectrum recorded from (a) area.

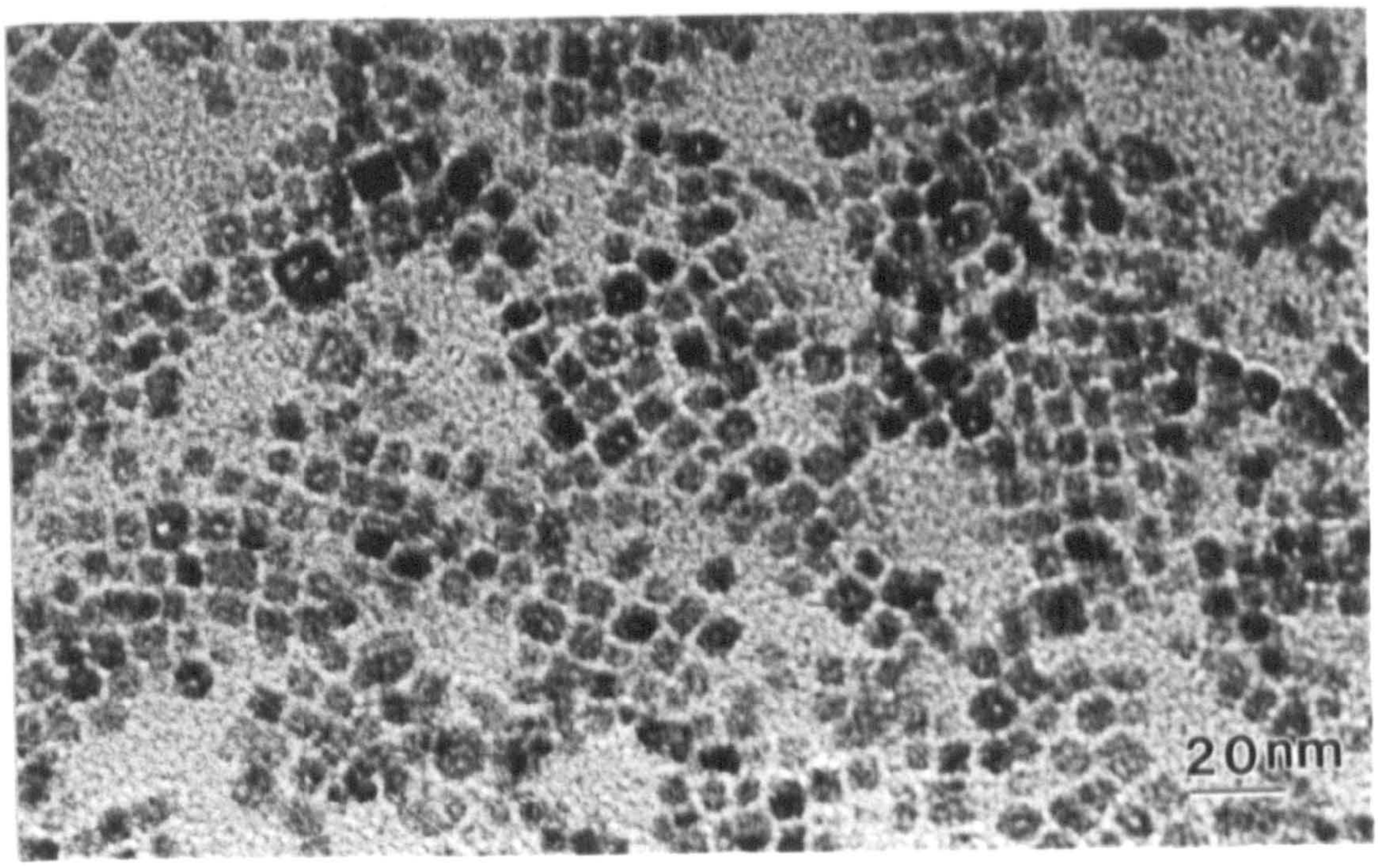

Figure 6-8. Enlarged TEM image of figure 6-7a. Scale bar = 20 nm.

(Figure 6-9d), indicating that the large ring structure particles were crystalline barite. The Br signal observed by EDXA was from CTABr.

Finally, if 10 ml of unfunctionalized surfactant CTABr aqueous solution (10 mM) containing 0.2 ml of 500 mM Na_2SO_4 was mixed with 5 ml of unfunctionalized surfactant NaAOT isooctane solution (10 mM) and then 0.1 ml of 500 mM $BaCl_2$ was added to the mixture, only rectangular $BaSO_4$ particles with irregular size can be observed (Figure 6-10).

6.3.3.2 Concentration of two surfactants in the synthesis of nanoshells

Three groups of 20 experiments have been performed to investigate the influence of the concentrations of two surfactants on the synthesis of $BaSO_4$ spherical hollow nanoparticles (nanoshells). For all three groups of experiments, the molar ratio of two surfactants was constant at $Ba(AOT)_2/(CTA)_2SO_4 = 1 : 2$. In the first group, the concentrations of two surfactants were equal in each single experiment and were varied in a range of 0.2 to 100 mM (see Table 6-2).

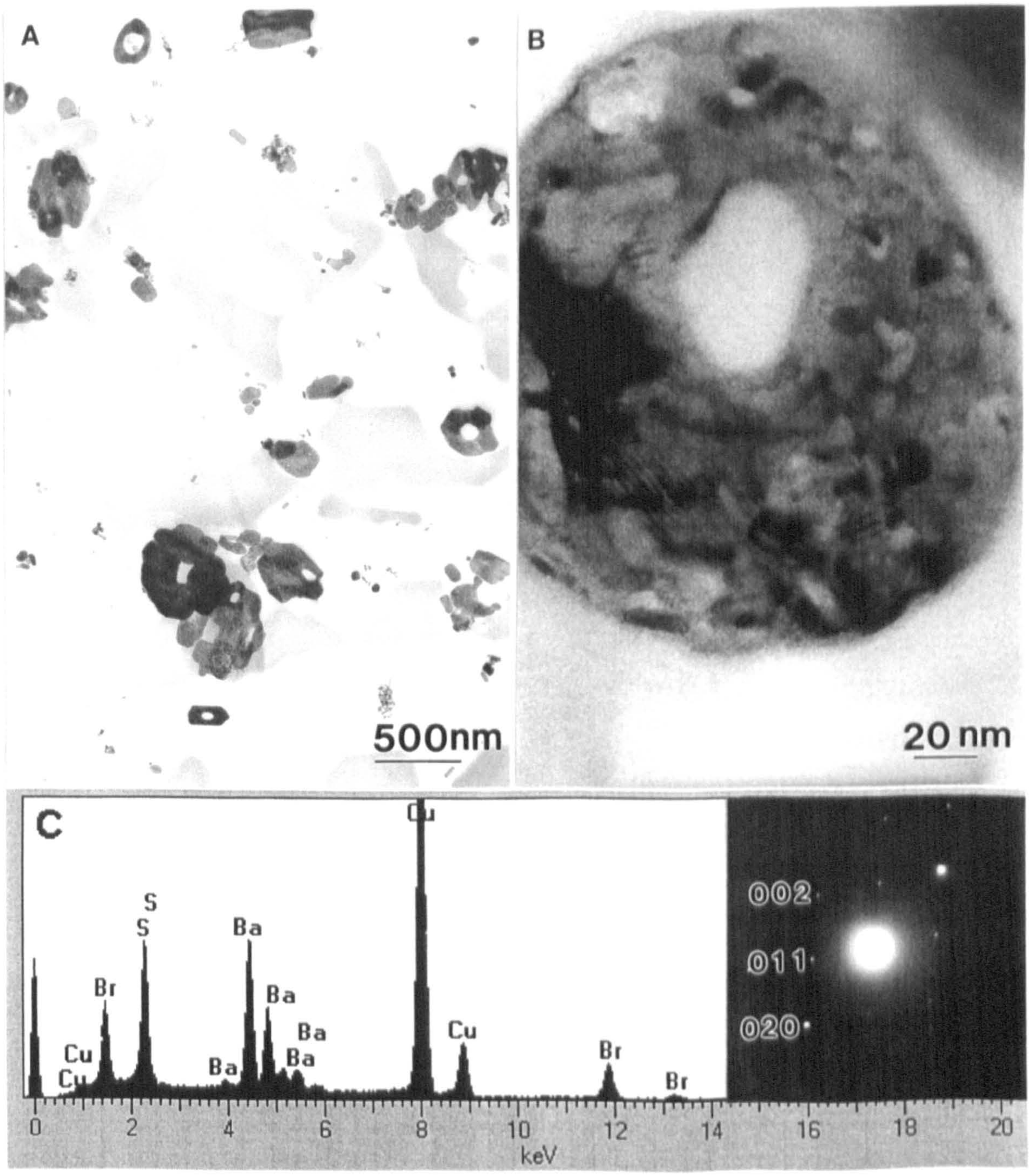

Figure 6-9. **(a)** TEM image of ring-like particles obtained in the water phase in the presence of functionalised surfactant $Ba(AOT)_2$ (10 mM in isooctane) and unfunctionalized surfactant CTAB (20 mM in H_2O) scale bar = 500 nm, and **(b)** high resolution image, scale bar = 20 nm; **(c)** energy-dispersive X-ray analysis (EDXA) spectrum recorded from (a) area.

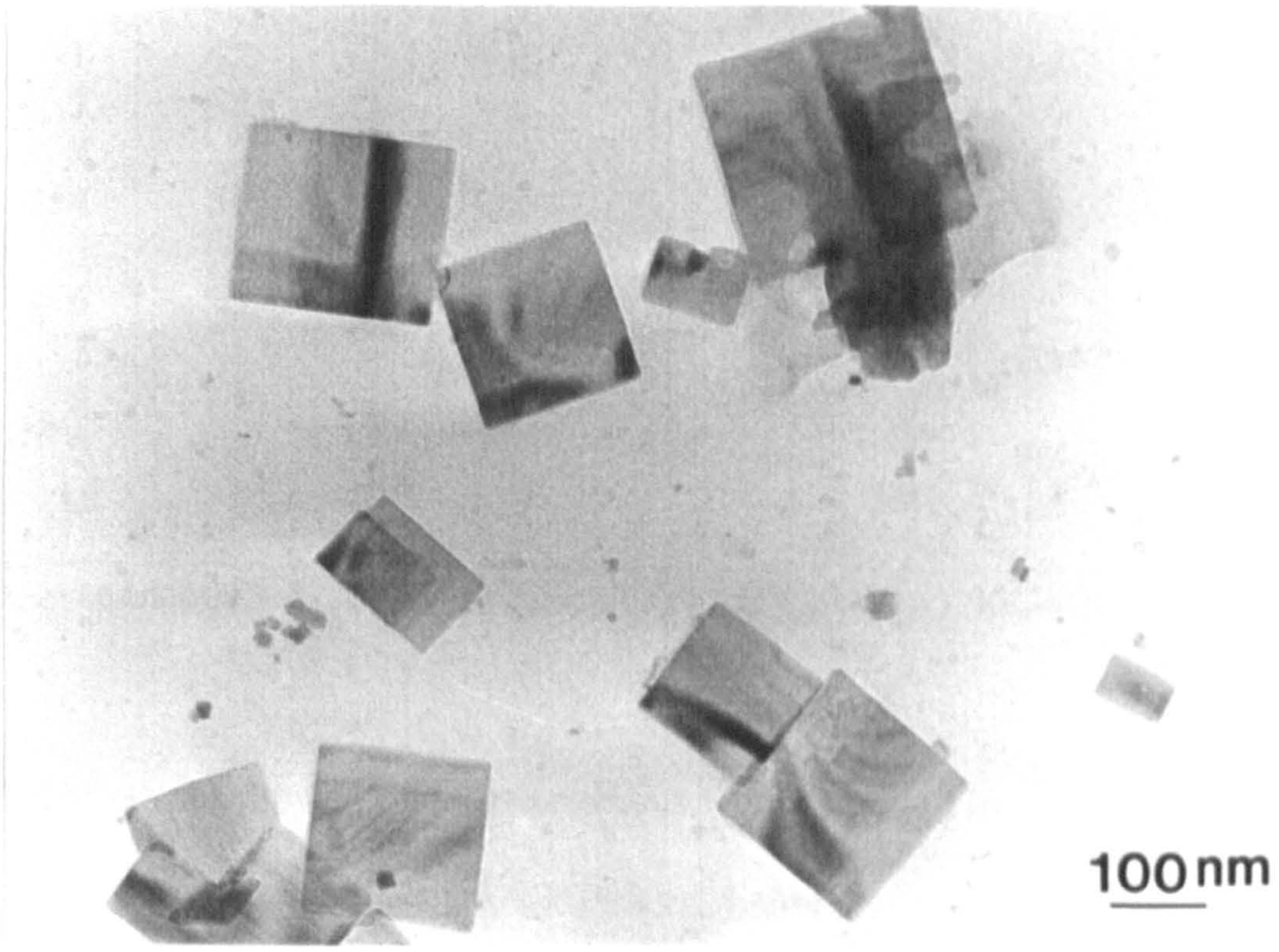

Figure 6-10. TEM image of $BaSO_4$ particles prepared in the presence of two unfunctionalised surfactants CTAB (10 mM in H_2O) and NaAOT (10 mM in isooctane). Scale bar = 100 nm.

Table 6-2 Group 1 experiments

No.	$Ba(AOT)_2$		$(CTA)_2SO_4$	
	Volume (ml)	C (in isooctane) (mM)	Volume (ml)	C (in H_2O) (mM)
1	5	0.2	10	0.2
2	5	0.6	10	0.6
3	5	1	10	1
4	5	2	10	2
5	5	4	10	4
6	5	10	10	10
7	5	20	10	20
8	5	50	10	50
9	5	80	10	80
10	5	100	10	100

C = concentration, the molar ratio of $Ba(AOT)_2/(CTA)_2SO_4$ = 1 : 2.

TEM results showed that no nanoshells were observed in experiments numbers 1 and 2 (C = 0.2 and 0.6 mM, which were below the critical micelle concentration of $(CTA)_2SO_4$). $BaSO_4$ nanoshells were obtained in the experiments number 3 – 6 (C = 1 – 10 mM) (Figure 6-1a); the same $BaSO_4$ nanoshells were still obtained in the experiments 7 – 8 (C = 20 – 50 mM) but the size of the nanoshells was not as regular as that from the experiments 3 – 6; and quite a lot of bigger particles with multiholes appeared (Figure 6-11). When the concentration was over 50 mM, nanoshells could not be observed (experiments 9 – 10); only big particles with multiholes were obtained in the top milky layer (Figure 6-12). The results of this group of experiments indicated that the ideal concentration of both surfactants for synthesis of $BaSO_4$ nanoshells was 1 – 10 mM at the molar ratio of $Ba(AOT)_2/(CTA)_2SO_4$ = 1 : 2.

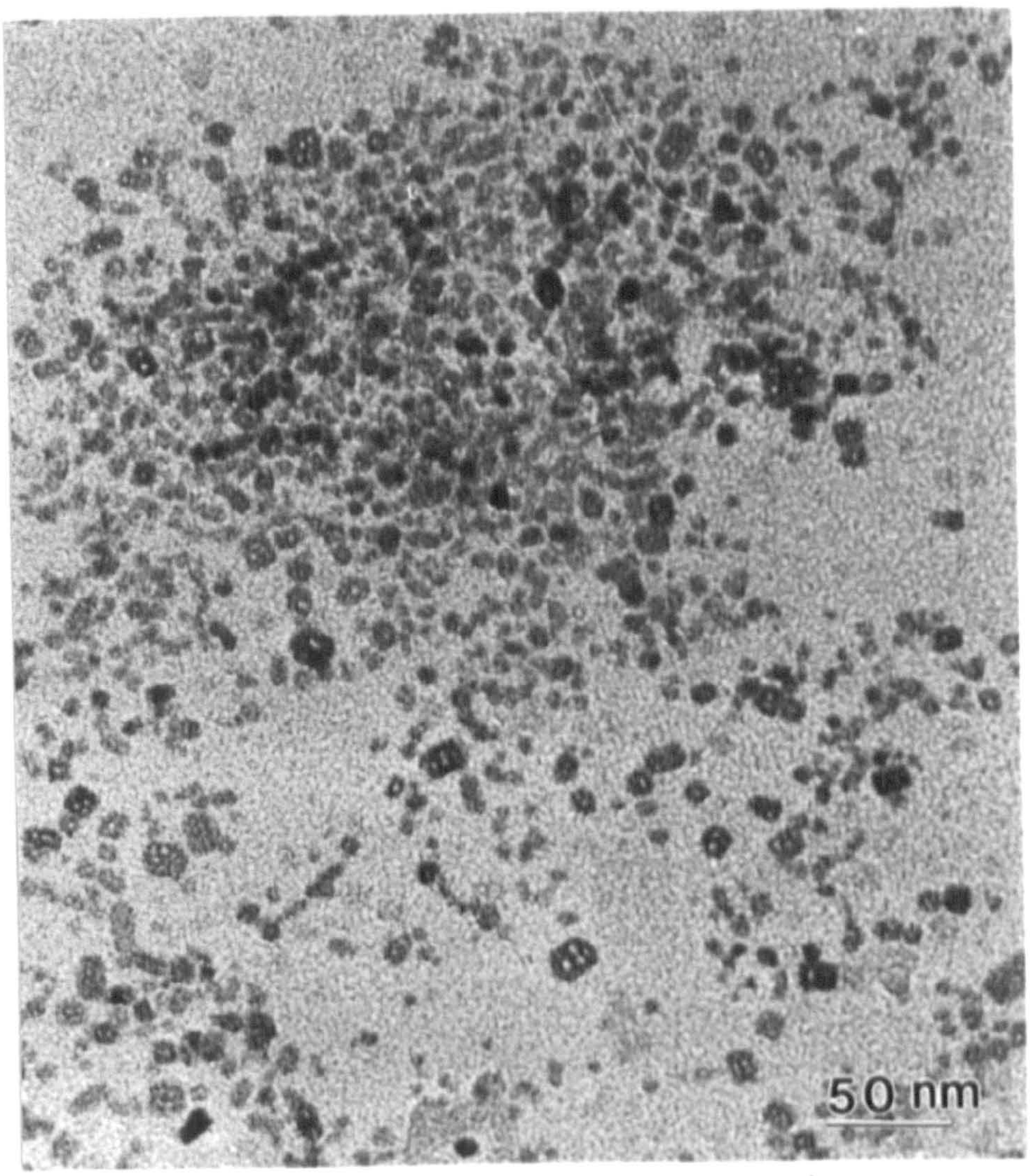

Figure 6-11. TEM image of irregular hollow particles obtained by using high concentration of surfactants $Ba(AOT)_2$ and $(CTA)_2SO_4$ (20 – 50 mM), scale bar = 50 nm.

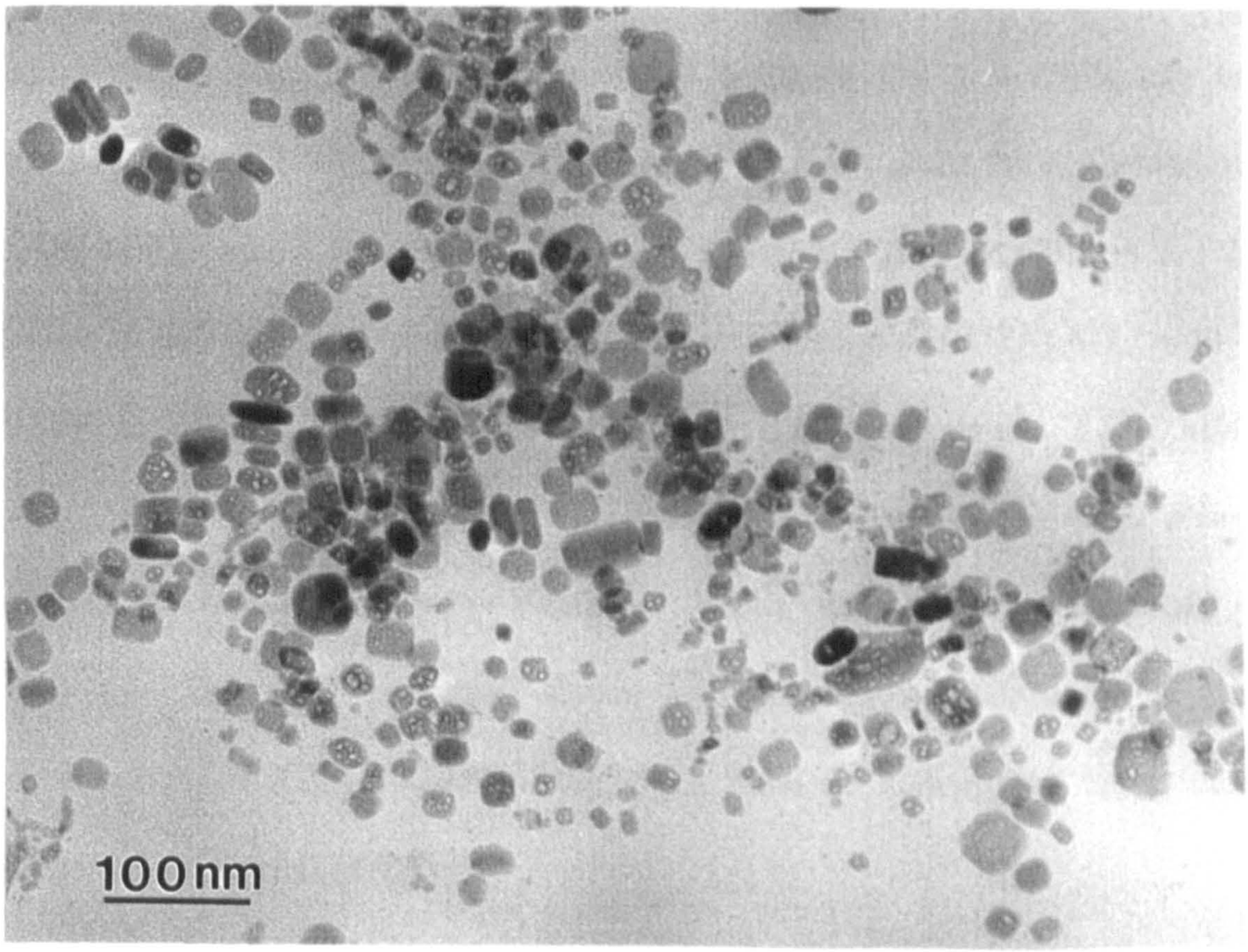

Figure 6-12. TEM image of $BaSO_4$ particles prepared in the presence of a high concentration of functionalised surfactants $(CTA)_2SO_4$ (100 mM in H_2O) and $Ba(AOT)_2$ (100 mM in isooctane). Sample was taken from the top layer. Scale bar = 100 nm.

In the second group of experiments, the concentration of one surfactant $Ba(AOT)_2$ was kept at 4 mM in isooctane and the other one $(CTA)_2SO_4$ was varied in a range of 1 – 100 mM in water (Table 6-3). The volume ratios of oil to water were greater than 1 (except No.1). The results indicated that nanoshells can be obtained at concentrations of $[(CTA)_2SO_4]$ = 1 – 50 mM when the concentration of $Ba(AOT)_2$ was a constant (4 mM) and at $Ba(AOT)_2/(CTA)_2SO_4$ = 1 : 2. Similar to the first group experiments, at the concentration of $[(CTA)_2SO_4]$ = 20 – 50 mM, the nanoshells were not as regular as that at concentrations of 1 – 10 mM, indicating that the concentration of $(CTA)_2SO_4$ and the volume of water phase have not affected the synthesis of $BaSO_4$ nanoshells very much in the range of 1 – 50 mM. The most important factor for synthesis of nanoshells is the concentration of $(CTA)_2SO_4$ in water which must be higher than the critical micelle concentration of 0.6 mM.[29]

Table 6-3 Group 2 experiments

No.	$Ba(AOT)_2$		$(CTA)_2SO_4$		Volume ratio of oil to water
	Volume (ml)	C (in isooctane) (mM)	Volume (ml)	C (in H_2O) (mM)	
1	5	4	40	1	1 : 8
2	5	4	4	10	1.25 : 1
3	5	4	2	20	2.5 : 1
4	10	4	1.6	50	6.25 : 1
5	10	4	0.8	100	12.5 : 1

C = concentration, the molar ratio of $Ba(AOT)_2/(CTA)_2SO_4$ = 1 : 2.

The third group of experiments were designed to be similar to the second group, but in this case the concentration of $(CTA)_2SO_4$ was kept at 4 mM in water and the concentration of $Ba(AOT)_2$ was varied in a range of 1 – 100 mM in isooctane (Table 6-4), and the volume ratio of oil to water was less than 1 (except No. 1).

The results differed from that of the second group. TEM images showed that a very low yield of $BaSO_4$ nanoshells were observed in the top and middle layers at low concentrations of $Ba(AOT)_2$ (experiment number 1, C = 1 mM) due to the large volume of solvent was used to keep the molar ratio of $Ba(AOT)_2/(CTA)_2SO_4$ = 1 : 2. Only two layers (milky organic layer and turbid inorganic layer) were observed for the experiments 2 to 5. A high yield, and aggregated rather than individual $BaSO_4$ nanoshells, was obtained from the organic phase of experiment 2; a very high yield and irregular hollow nanoparticles were observed in the organic phase of experiment 3 (Figure 6-13); and no nanoshells or hollow particles were observed in experiments 4 – 5 at all. The results of this group indicated that the volume of organic phase was an important factor. In experiments 1 and 2, we used ideal concentration of 1 and 10 mM of $Ba(AOT)_2$ but different volumes, and the results were totally different from that of the first group, suggesting that the nanoshells were extracted into the organic phase after formation and a small volume of the organic phase did not have sufficient capacity for a stable dispersion of nanoshells so that the shells aggregated.

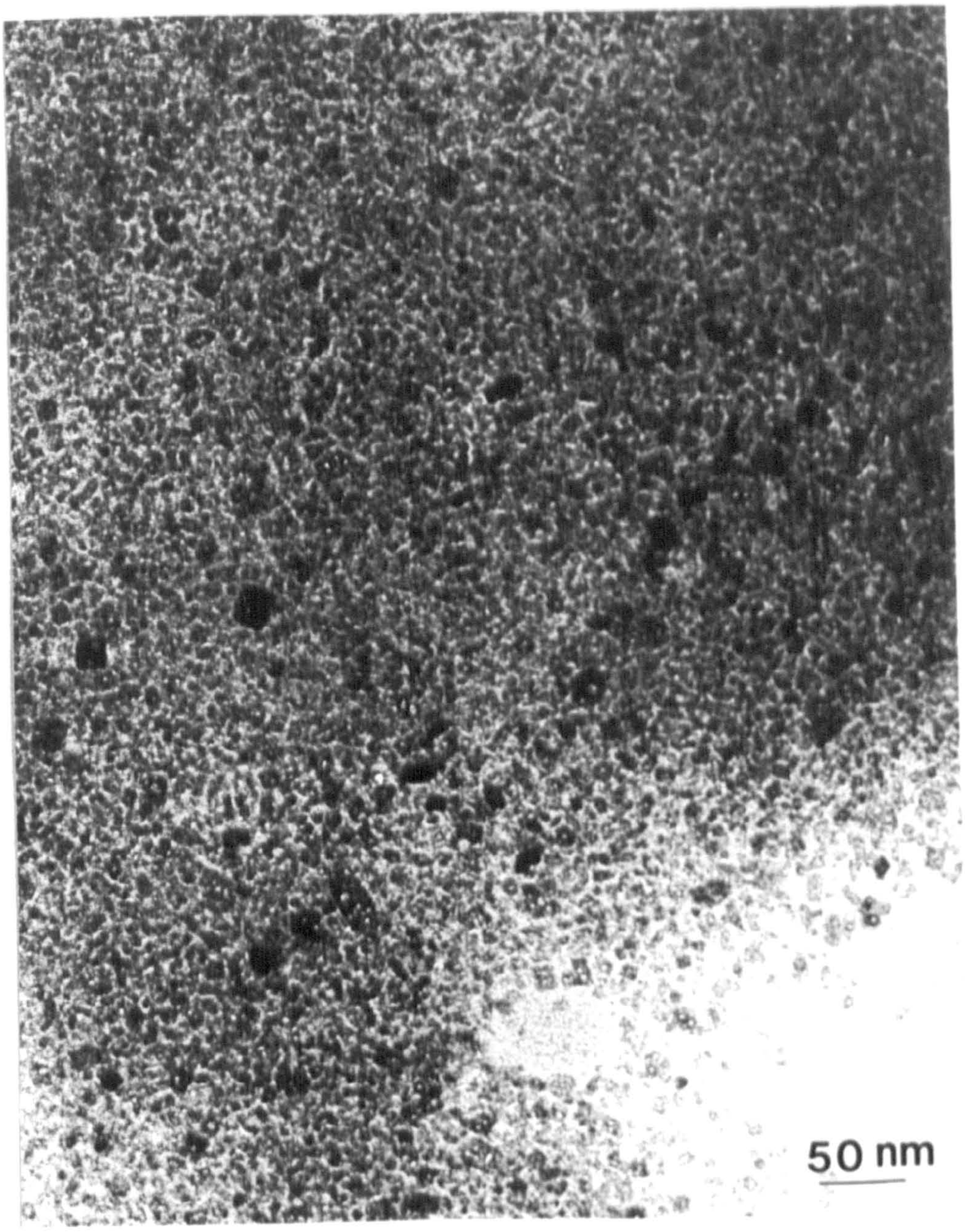

Figure 6-13. TEM image of $BaSO_4$ hollow particles obtained by using small volume of organic phase.

Table 6-4 Group 3 experiments

No.	$Ba(AOT)_2$		$(CTA)_2SO_4$		Volume ratio of oil to water
	Volume (ml)	C (in isooctane) (mM)	Volume (ml)	C (in H_2O) (mM)	
1	10	1	5	4	2 : 1
2	1	10	5	4	1 : 5
3	1	20	10	4	1 : 10
4	0.8	50	20	4	1 : 25
5	0.4	100	20	4	1 : 50

C = concentration, the molar ratio of $Ba(AOT)_2/(CTA)_2SO_4$ = 1 : 2.

All the results from the above three groups of experiments implied that both the concentration of $Ba(AOT)_2$ and the volume of the organic phase were very important factors for synthesis of $BaSO_4$ nanoshells. Small volumes of organic phase and high concentration of $Ba(AOT)_2$ induce aggregation. The ideal concentrations of both surfactants for the synthesis of barium sulphate nanoshells were 1 – 10 mM.

6.3.3.3 Molar ratio of two surfactants $Ba(AOT)_2/(CTA)_2SO_4$

Four experiments were performed at molar ratios of $Ba(AOT)_2/(CTA)_2SO_4$ from 1:1 to 1:4, with concentrations of 10 mM for both surfactants. The results showed that same nanoshells (as 1:2) could be synthesized from the molar ratios of 1:1 to 1:4. However, when the molar ratio of $Ba(AOT)_2/(CTA)_2SO_4 \geq 2$ (= 2 – 6), only irregular shaped particles could be observed. According to the above investigations, the nanoshells could be obtained when the molar ratio of two

surfactants $Ba(AOT)_2/(CTA)_2SO_4 \leq 1$. Because the nanoshells were extracted into the organic phase, they are likely to be coated by surfactants (AOT) adsorbed with their polar heads on the $BaSO_4$ surface. Therefore, the concentration of $Ba(AOT)_2$ and the volume of the organic phase were the key control factors and $(CTA)_2SO_4$ was less important so long as the concentration was over 0.6 mM. Presumably, provided the concentration of two surfactants is between 1 – 10 mM, the quantity of the $(CTA)_2SO_4$ seems to be not very important. The excess $(CTA)_2SO_4$ can stay in the water phase after reaction ($(CTA)_2SO_4$ is not soluble in isooctane) and so will not affect the formation of barium sulphate nanoshells. However, the mechanism is not clear yet.

6.3.4 Study of formative mechanism of nanoshells

The results indicated that all the $BaSO_4$ nanoshells synthesised were solubilised preferentially in the isooctane organic phase (top and middle layers) rather than remain in the underlying aqueous phase, implying that $BaSO_4$ nanoshells behaved as hydrophobic particles. Bare barium sulphate surface itself is not expected to be hydrophobic on its own indicating that the nanoshells are likely to be coated by surfactants adsorbed with their polar headgroups on the $BaSO_4$ surface. According to the mechanism proposed in scheme 1 we assume that AOT molecules mainly form the hydrophobic coating of the nanoshells (in a similar way as a long chain carboxylate adsorbs onto barium sulphate).[44] To confirm this hypothesis we proceeded to selectively remove the external coating. The evolution of the system was followed by FTIR and TEM.

A polar solvent ethanol was added to the top layer of clear oil containing the nanoshells to give a white precipitate. This is consistent with the presence of hydrophobic tails of AOT on the surface of $BaSO_4$ nanoshells that will aggregate in the polar solvents. After centrifugation, the precipitate was washed gently with ethanol to remove free AOT molecules, air-dried and analysed by FTIR and TEM (Figure 6-14a, b). The FTIR spectrum showed the existence of $BaSO_4$ with the two bands associated to the low symmetry sulphate degenerated in two doublets: 608, 639 and 1080, 1108 cm^{-1} [42] in good agreement with the pure $BaSO_4$ spectrum, (Figure 6-14i). Furthermore, the ester group carbonyl ($\nu_{(C=O)}$, 1734 cm^{-1}) of AOT (compare with the pure $Ba(AOT)_2$ spectrum Figure 6-14g) and the alkyl bands (2848, 2918, 2958 cm^{-1}), from the alkyl chains of both AOT and CTA were observed. The strongest band in the spectrum was at 1208 cm^{-1} which is an overlap of the $\nu_{(C(O)OC)}$ from AOT and $\nu_{(S=O)}$ bands from both sulphate and sulphonate moieties.

The nanoshells precipitated by ethanol as above were gently treated with 1% H_2SO_4 aqueous solution, to displace adsorbed AOT from the $BaSO_4$ external surface by protonation of the sulphonate headgroup. TEM images still showed nanoshells but the surface shape was not as regular as before (Figure 6-14d). The corresponding FTIR spectrum still indicated the existence of $BaSO_4$ and alkyl bands but the $\nu_{(C=O)}$ band was absent (Figure 6-14c), and a net intensity decrease of the band near 1200 cm^{-1} was observed, suggesting that AOT had been removed from the surface (Scheme 6-3).

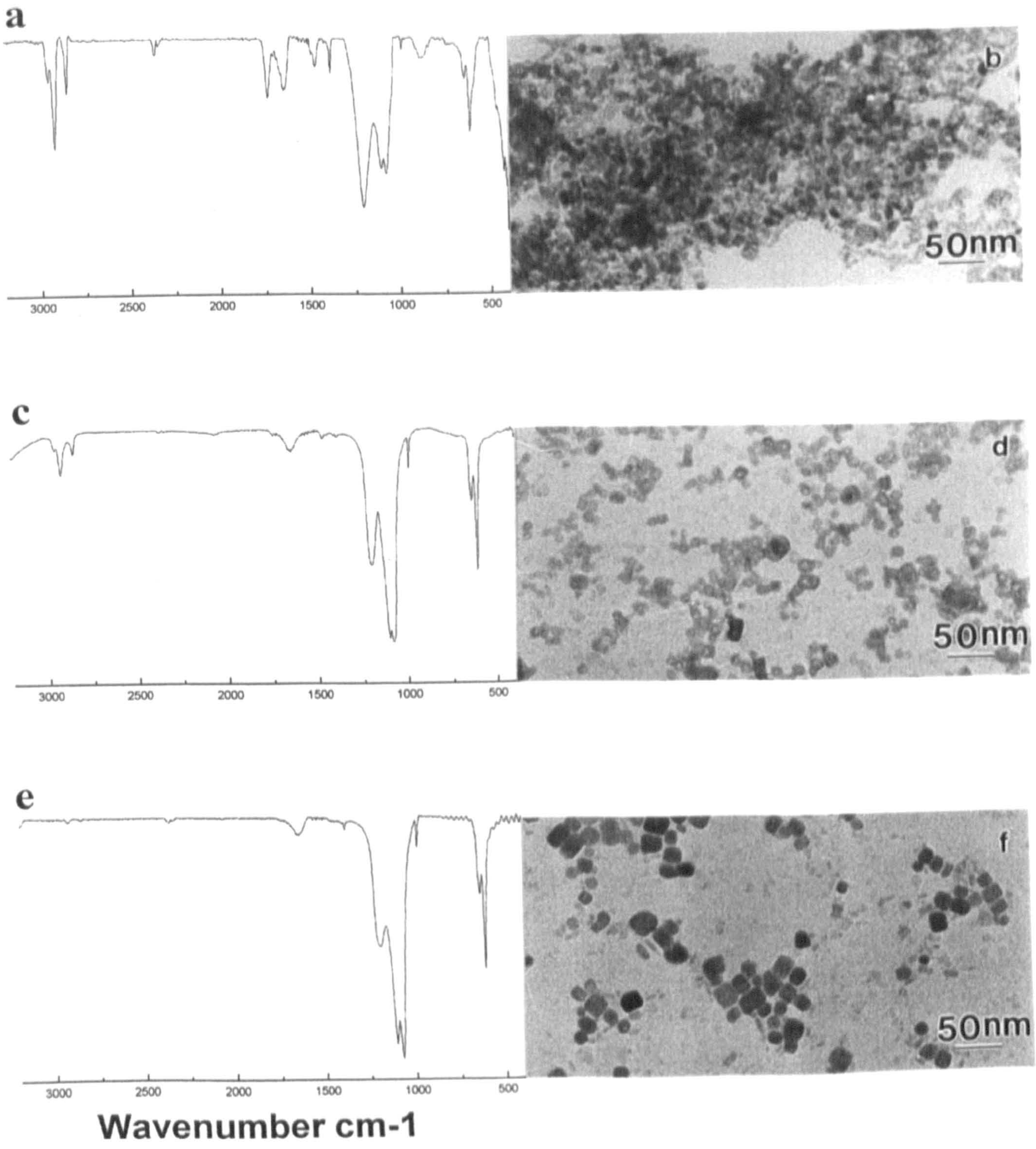

Figure 6-14: **(a)** and **(b)** FTIR spectrum and TEM image of $BaSO_4$ nanoshells precipitated by ethanol. **(c)** and **(d)** FTIR spectrum and TEM image of $BaSO_4$ nanoshells after washing with 1% H_2SO_4 aqueous solution. **(e)** and **(f)** FTIR spectrum and TEM image of $BaSO_4$ nanoshells after washing with 1% H_2SO_4 aqueous solution and then washing by ethanol and water with sonication. **(g)** FTIR spectrum of $Ba(AOT)_2$. **(h)** FTIR spectrum of $(CTA)_2SO_4$. **(i)** FTIR spectrum of $BaSO_4$. Scale bars = 50 nm.

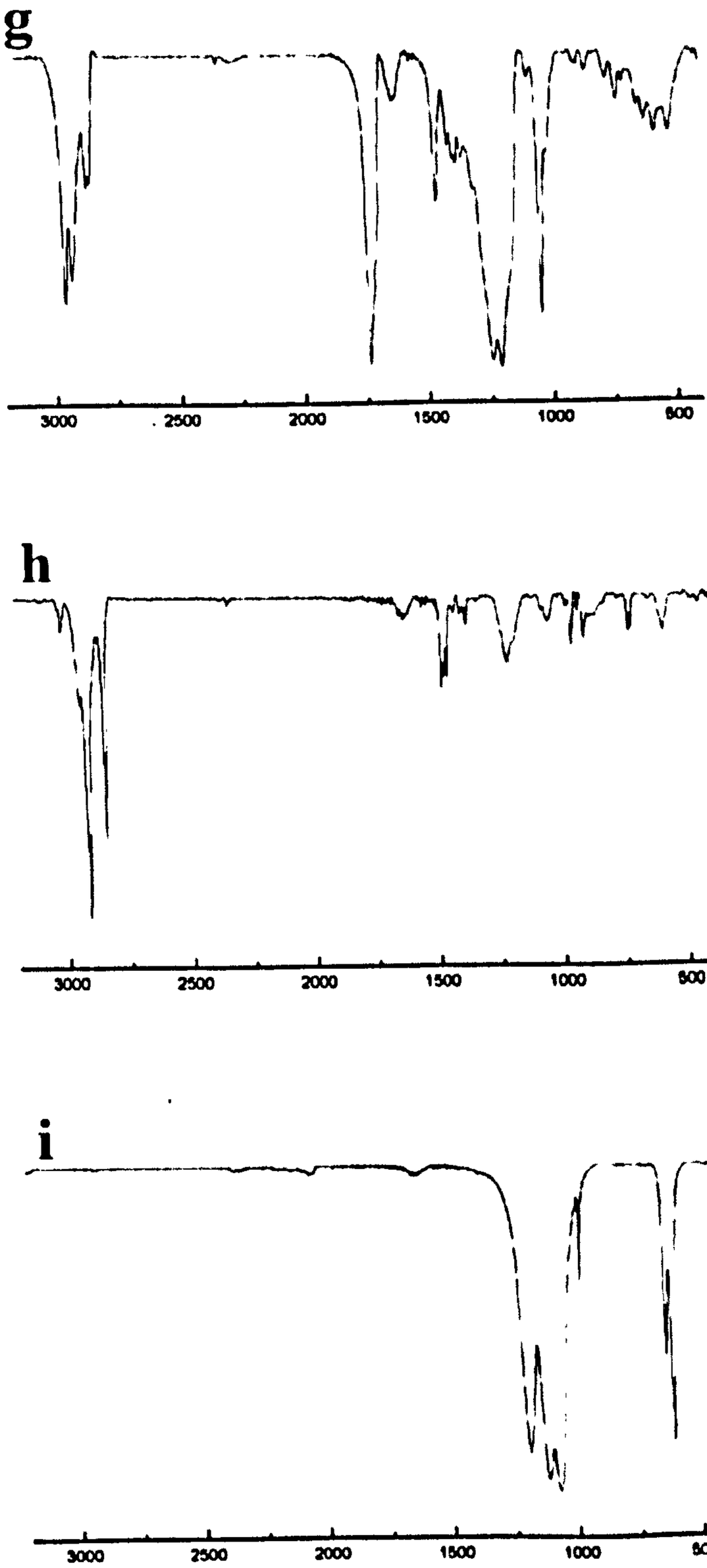

Figure 6-14 g,h,i

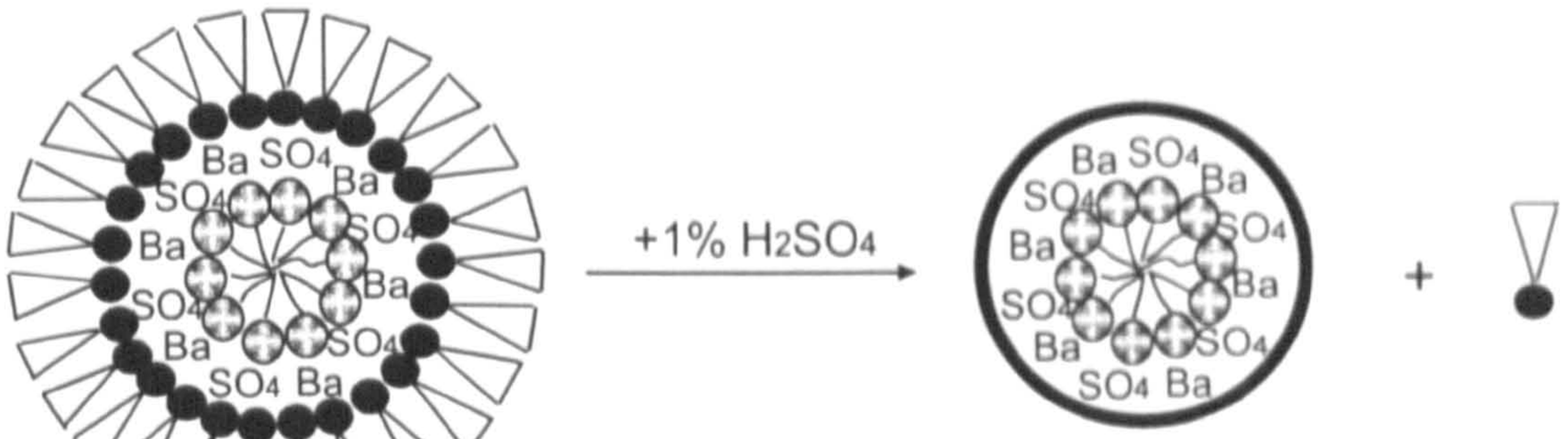

hydrophobic nanoshell

naked nanoshell

AOT

Scheme 6-3. Sketch of the process of removal of AOT molecules from the surface of $BaSO_4$ nanoshells.

The sample after removal of AOT from the surface was thoroughly washed with ethanol and then sonicated in water for two minutes using an ultrasonic disintegrator. TEM images showed that the morphology of nanoshells had been drastically altered into rectangular $BaSO_4$ particles with occasional holes inside the particles. The size of the rectangular particles (15 – 30 nm) was much bigger then that of the initial nanoshells (Figure 6-14f). The corresponding FTIR spectrum indicated the existence of $BaSO_4$ (Figure 6-14e) with only trace amounts of the CTA alkyl chains (Scheme 6-4).

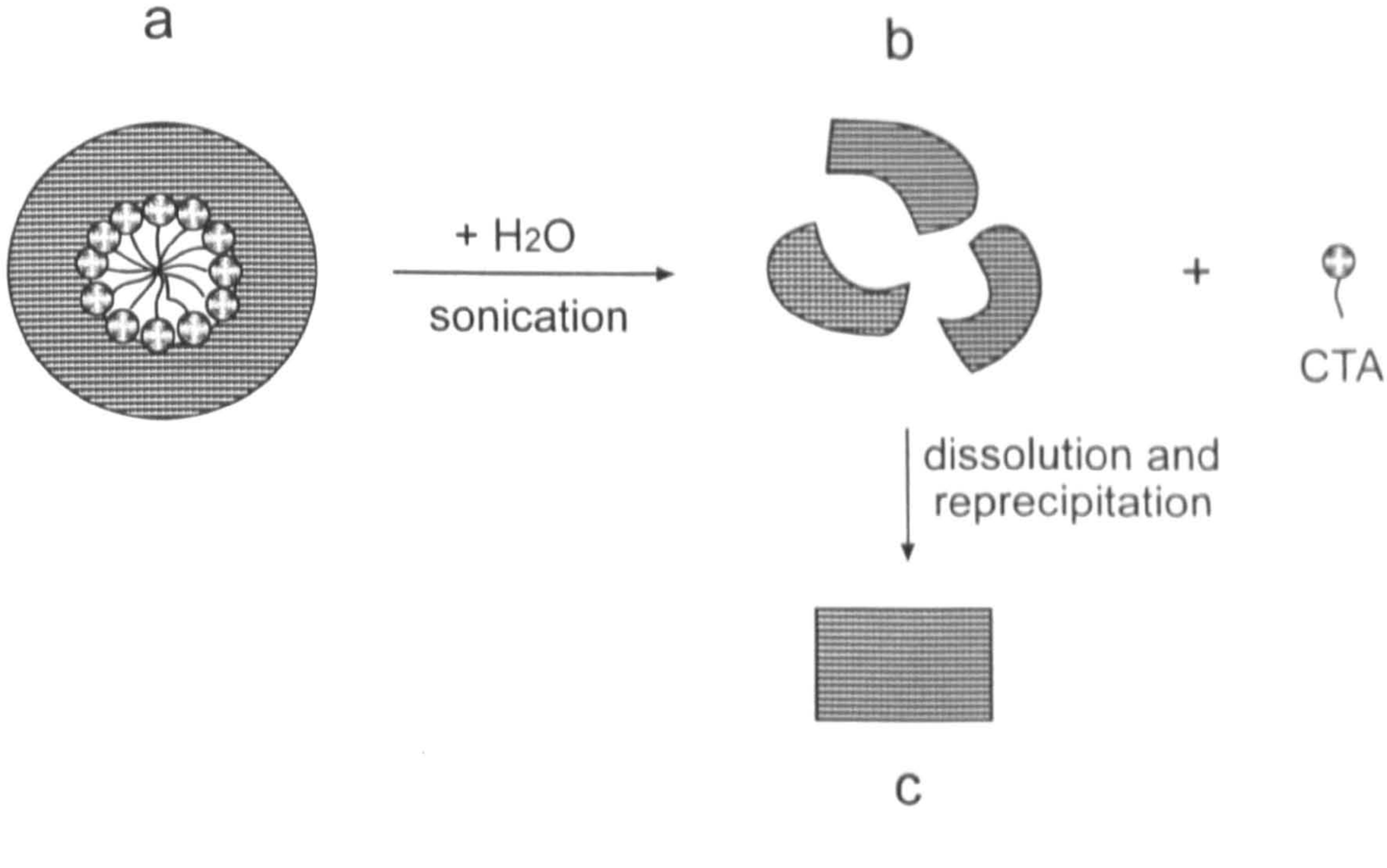

Scheme 6-4. Sketch of the transformation process of $BaSO_4$ nanoshells to rectangular particles. **a)** naked $BaSO_4$ nanoshell. **b)** fragments of nanoshells. **c)** rectangular $BaSO_4$ nanoparticles (the scale should be larger than that of **a)** and **b)**).

6.4 General discussion and conclusion

6.4.1 Formation model

The experiments describe a model for the formation of $BaSO_4$ nanoshells by using two discrete assemblies of functionalised surfactants. $(CTA)_2SO_4$ formed normal micelles in water (Scheme 6-5), and the average diameter was 3.3 nm measured by dynamic light scattering (DLS) for the concentrations of 4 mM to 20 mM (Figure 6-15). $Ba(AOT)_2$ formed reverse micelles in isooctane (Scheme 6-5). When two phases were mixed under stirring, the sulphate anions surrounding the spherical $(CTA)_2SO_4$ micelles were brought in close contact with the barium cations located on the inside of $Ba(AOT)_2$ reverse micelles resulting in the formation of $BaSO_4$ crystals surround the CTA micelles. AOT head groups adsorbed on the surface of $BaSO_4$ crystals and restricted the development of the crystals (Scheme 6-5). Therefore spherical hollow nanoparticles were generated. Due to AOT hydrophobic tails coating the surface of the nanoshells, they behaved as hydrophobic particles, and the internal diameter of the nanoshells was just same as the size of $(CTA)_2SO_4$ micelles, which should support the model proposed.

MALVERN

AUTOSIZER

Size Report

$(CTA)SO_4$ 20mM

Sample

Record Number:	data
Filename:	
File Path:	.
Sample RI:	1.60, Abs:0.00
Dispersant RI:	1.33
Disp. Viscosity (cP):	0.851
Date (DMY):	13/08/99
Time:	13:13:42

System

Instrument Type:	Autosizer 4700
Temperature (°C):	27.0
Count rate (kCps):	129.1
Cell Type:	Unknown (-1)
Detector Angle (deg.):	90.00
Wavelength (nm):	532.0

Result

Quality Factor:	Fail
Z Average Mean(nm):	3.3
Polydispersity:	0.03
Intensity Mean (nm):	3.3
Analysis Mode:	Monomodal

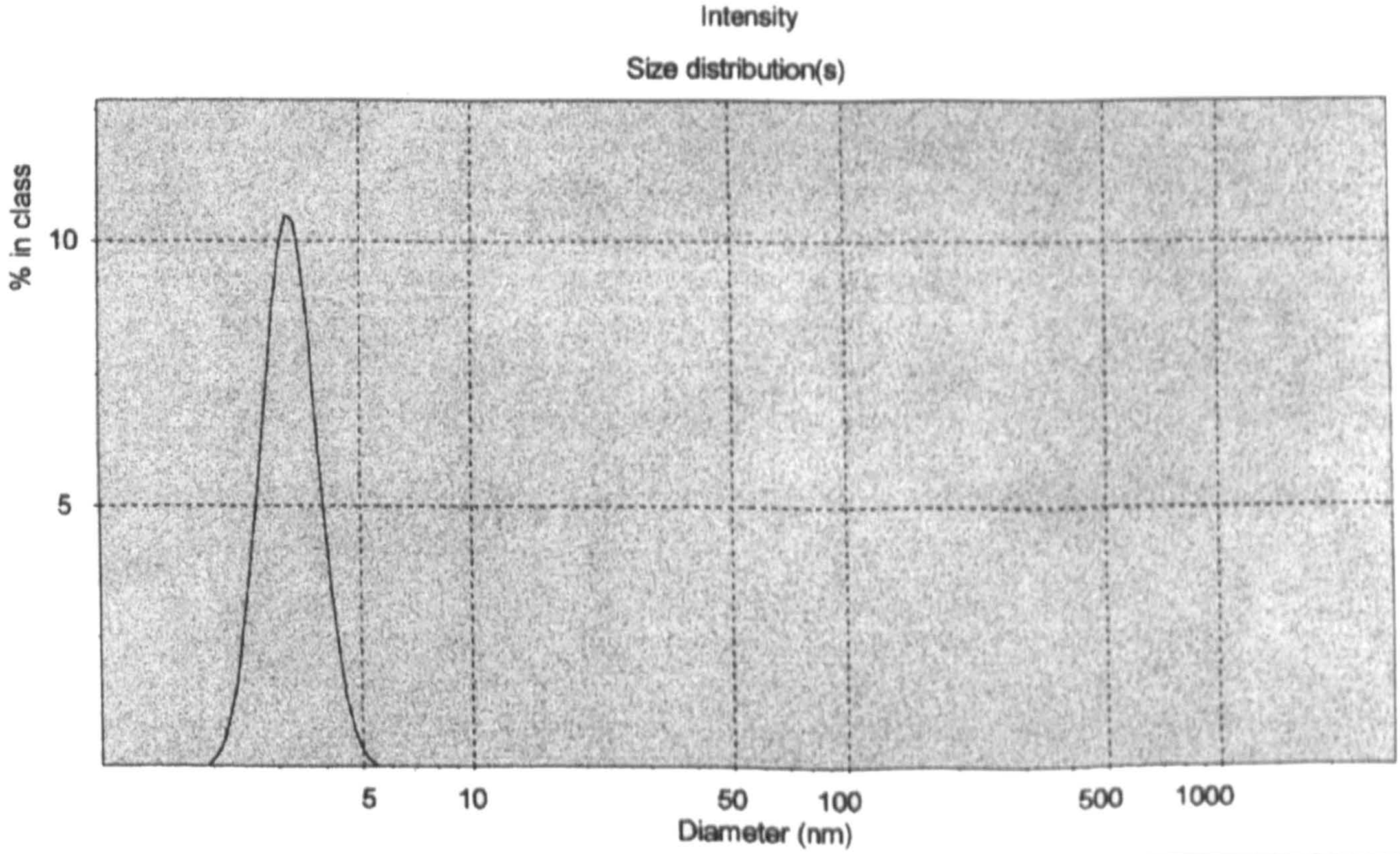

Figure 6-15. Size distribution of $(CTA)_2SO_4$ micelles reported by Dynamic Light Scattering

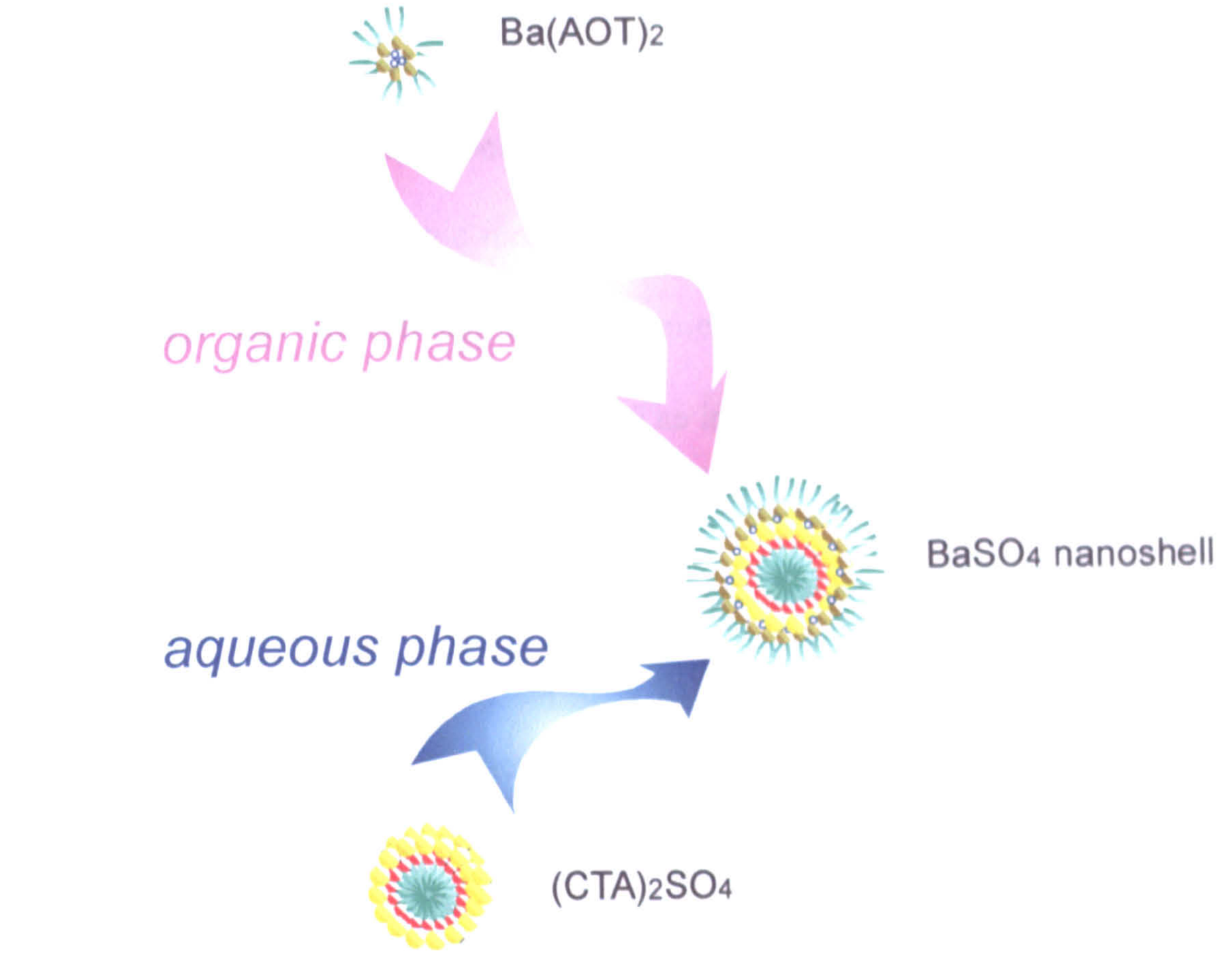
Ba(AOT)2
organic phase
BaSO4 nanoshell
aqueous phase
(CTA)2SO4
organic phase
aqueous phase

Scheme 6-5

This work shows that the inorganic salt formed by mixing two functionalised micellar surfactants of opposite charge and curvature allows control of the growth of an onion-like (organic-inorganic-organic) material via asymmetric interfacial delivery. The external and internal diameters of $BaSO_4$ nanoshells were 9.6 ± 1.5 nm and 3.4 ± 0.3 nm, respectively. The internal diameter of the nanoshells could be determined by the size of CTA micelles, which is easy to understand. However, what is the driving force controlling the external size? One possibility might relate to the water content of AOT reverse microemulsions. When $(CTA)_2SO_4$ micelles in the water phase were mixed with $Ba(AOT)_2$ reverse micelles in isooctane phase under stirring (Scheme 6a and b), two kinds of micelles were brought in close proximity at the interface (Scheme 6-6c). In this case, Ba^{2+} and SO_4^{2-} ions might contact as shown in scheme 6d and result in a rearrangement of AOT aggregates. This will generate a new AOT microemulsion containing the CTA micelles, nuclei seeds of $BaSO_4$ and water inside with the maximum *w* value (Scheme 6-6e). The new AOT microemulsion will be extracted into the organic phase and behave like a normal AOT reverse microemulsion undergoing collision and ion exchange to generate $BaSO_4$ hollow particles (Scheme 6-6f).

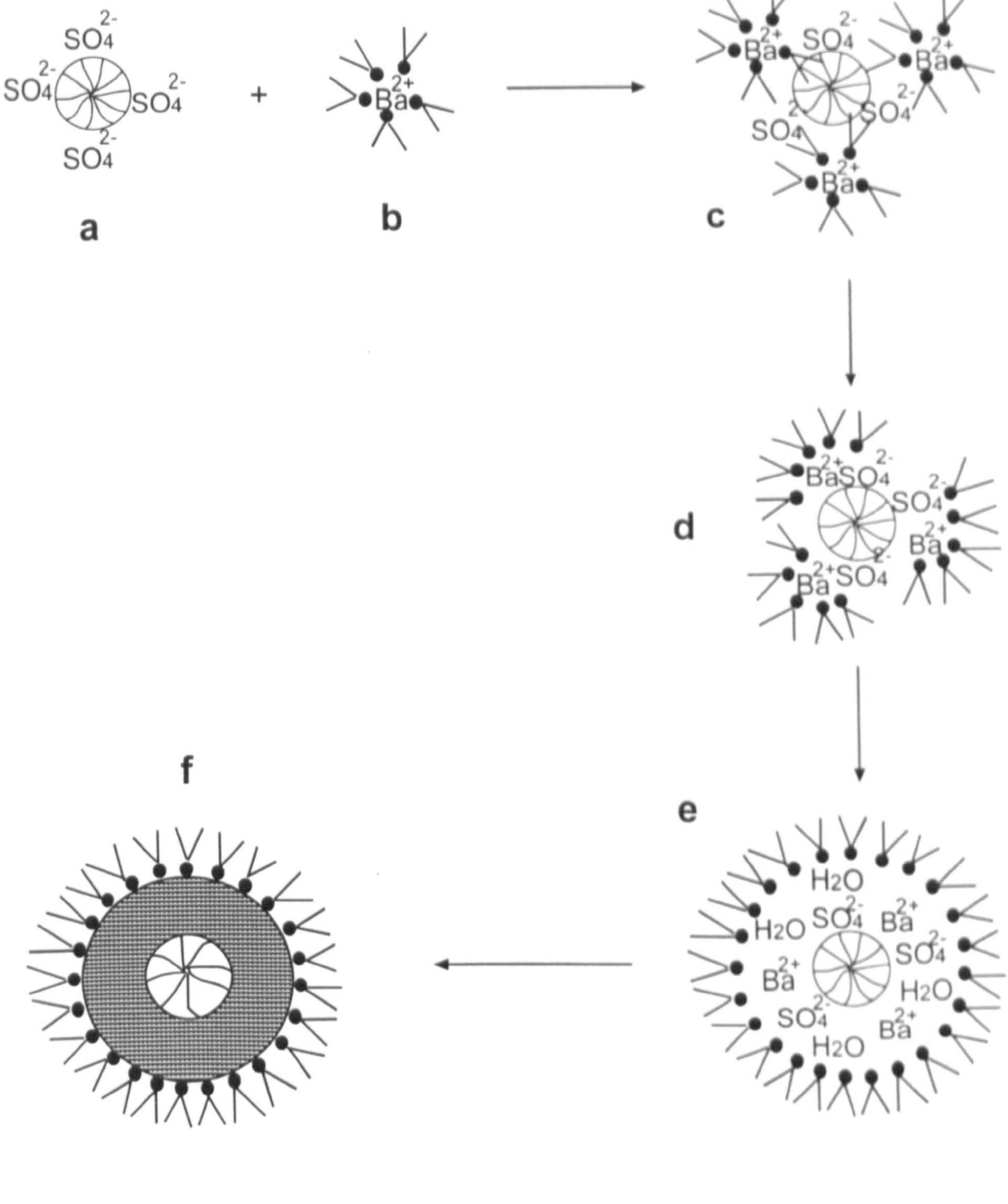

Scheme 6-6. Sketch of the process of formation of $BaSO_4$ hollow particles.

6.4.2 Functionalization of surfactants

All the results in this chapter implied that $BaSO_4$ nanoscale spherical hollow particles could be only achieved by using two functionalised surfactants $(CAT)_2SO_4$ and $Ba(AOT)_2$. The nanoshells will not form either by using one functionalised surfactant and one unfunctionalised surfactant, or by using two unfunctionalised surfactants. When $Ba(AOT)_2$ is mixed with $(CTA)_2SO_4$, however, the formation of $BaSO_4$ crystals inhibits the contact between the AOT and CTA headgroups, so a catanionic surfactant AOT-CTA cannot form. The $BaSO_4$ crystals can then form between these two surfactants to generate the hollow particles.

However, if one functionalised surfactant $Ba(AOT)_2$ and one unfunctionalized surfactant CTABr were employed, cubic nanoparticles were obtained and about 20% of nanocubes were hollow. In this case, the SO_4^{2-} anions did not associate with the CTA micelles; the process of the formation of particles should then be different from that using two functionalised surfactants. Basically, the cubic particles should not be associated with CTA micelles, but the micelles might occasionally be buried inside the particles to form a hollow cube.

6.4.3 Concentrations and volume ratios of oil to water

The formation of nanoshells was dependent on the concentration of both surfactants and the volume ratio of oil to water. When the concentration of

$(CTA)_2SO_4$ was lower than 1 mM (close to the reported value critical micelle concentration of 0.6 mM[29]), the nanoshells could not be synthesised. The ideal concentrations of both surfactants were between 1 to 10 mM at a volume ratio of oil to water ≥ 1:1.

The volume of organic phase is very important for synthesis of nanoshells, because the nanoshells were extracted into the organic phase after formation, and a small volume of the organic phase did not have sufficient capacity for a stable dispersion of nanoshells so that the shells aggregated.

6.5 References

[1] Arriagada, F.J., Osseo-Asare, K., *J. Colloid Interface Sci.*, **211**, 210 (1999).

[2] Arriagada, F.J., Osseo-Asare, K., *J. Colloid Interface Sci.*, **170**, 8 (1995).

[3] Taleb, A., Petit, C., Pileni, M.P., *Chem. Mater.*, **9**, 950 (1997).

[4] Petit, C., Lixon, P., Pileni, M.P., *J. Phys. Chem.*, **97**, 12974 (1993).

[5] Taleb, A., Petit, C., Pileni, M.P., *J. Phys. Chem. B,* **102**, 2214 (1998).

[6] Lisiecki, I., Pileni, M.P., *J. Phys. Chem.*, **99**, 5077 (1995).

[7] Tanori, J., Pileni, M.P., *Adv. Mater.*, **7**, 862 (1995).

[8] Pileni, M.P., Gulik-Krzywicki, T., Tanori, J., Filankembo, A., Dedieu, J.C., *Langmuir*, **14**, 7359 (1998).

[9] Tanori, J., Pileni, M.P., *Langmuir*, **13**, 639 (1997).

[10] Pileni, M.P., Tanori, J., Filankembo, A., *Colloid and Surfaces A*, **123-124**, 561 (1997).

[11] Haram, S.K., Mahadeshwar, A.R., Dixit, S. G., *J. Phys. Chem.*, **100**, 5868 (1996).

[12] Petit,C., Pileni, M.P., *J. Phys. Chem.*, **92**, 2282 (1988).

[13] Motte, L., Billoudet, F., Lacaze, E., Pileni, M.P., *Adv. Mater.*, **8**, 1018 (1996).

[14] Motte, L., Billoudet, F., Pileni, M.P., *J. Phys. Chem.*, **99**, 16425 (1995).

[15] Motte, L., Billoudet, F., Lacaze, E., Douin, J., Pileni, M.P., *J. Phys. Chem. B*, **101**, 138 (1997).

[16] Li, M., Schnablegger, H., Mann, S., *Nature*, **402**, 393 (1999).

[17] Hopwood, J., Mann, S., *Chem. Mater.*, **9**, 1819 (1997).

[18] Petit, C., Taleb, A., Pileni, M.P., *Adv. Mater.*, **10**, 259 (1998).

[19] Bagwe, R.P., Khilar, K.C., *Langmuir*, **13**, 6432 (1997).

[20] Levy, L., Hochepied, J.F., Pileni, M.P., *J. Phys. Chem.*, **100**, 18322 (1996).

[21] Cizeron, J., Pileni, M.P., *J. Phys. Chem.*, **99**, 17410 (1995).

[22] Ahmadi, T.S., Wang, Z.L., Henglein, A., Ei-Sayed, M.A., *Chem. Mater.*, **8**, 1161 (1996).

[23] Ahmadi, T.S., Wang, Z.L., Green, T.C., Henglein, A., Ei-Sayed, M.A., *Science*, **272**, 1924, (1996).

[24] Badia, A., Gao, W., Singh, S., Demers, L., Cuccia, L., Reven, L., *Langmuir*, **12**, 1262 (1996).

[25] Linden M., Blanchard J., Schacht S., Schunk S.A., Schueth F., *Chem. Mater.*, **11**, 3002 (1999).

[26] Lisiecki, I., Björling, M., Motte, L. Ninham, B., Pileni, M. P., *Langmuir*, **11**, 2385 (1995).

[27] Jeunieau, L., Nagy, J.B., *Colloids and Surfaces A*, **151**, 419 (1999).

[28] Khan K., Marques E., In *Specialist Surfactants* Edited by Robb ID, Blackie Academic and Professional, London, 1997.

[29] Sepulveda, L., Cortes, J. *J. Phys. Chem.*, **89**, 5322 (1985)

[30] Kawahasji, N., Matijevic, E., *J.Colloid Interface Sci.*, **143**, 103 (1991).

[31] Chang, S.Y., Lui, L., Asher, S.A., *J. Am. Chem. Soc.*, **116**, 6745 (1994).

[32] Walsh, D., Mann, S., *Nature*, **377**, 320 (1995).

[33] Giersig, M., Liz-Marzan, L.M., Ung, T., Su, D., Mulvaney, P., *Ber. Bunsenges. Phys. Chem.*, **101**, 1617 (1997).

[34] Correa-Duarte, M.A., Giersig, M., Liz-Marzan, L.M., *Chem. Phys. Lett.*, **286**, 497 (1998).)

[35] Calvo, P., Vilajato, J.L., Alonso, M.J., *J. Pharma. Sci.*, **85**, 530 (1996).

[36] Fritz, H., Maier, M., Bayer, E., *J. Colloid Interface Sci.*, **195**, 272-288, (1997).

[37] Zhong, Z., Yin, Y., Gates, B., Xia, Y., *Adv. Mater.*, **12**, 206 (2000).

[38] Hongu T., Phillips G.O., In *New Fibres*, Ellis Horwood ltd, Chichester (1990)

[39] Lissi, E.A., Abuin, E.B., Sepulveda, L., Quina, F. H., *J. Phys. Chem.*, **88**, 81 (1984).

[40] Broxton, T.J., Sango, X., Wright, S., *Can. J. Chem.*, **66**, 1566 (1988).

[41] Hori T., Sugiyama M., Himeno S., *Chem. Lett.*, 1017 (1987).

[42] Nakamoto, K. *Infrared and Raman Spectra of Inorganic and Coordination Compounds*, 3rd Ed, John Wiley and Sons, Inc. Chichester (1978).

[43] Veith, H. J., *Organic Mass Spectrometry*, **11**, 629 (1976)

[44] Neagle W., Rochester C. H., *J. Chem. Soc.,Faraday Trans. 1*, **85**, 429 (1989).

Chapter 7

Organic-inorganic thin films formed by self-assembly of surfactant AOT on the solid surface

7.1 Introduction

The supermolecular assembly of surfactant and polymer molecules at a solid-liquid interface can produce hierarchical structures[1], inorganic thin films[2] and tubular structures [3,4]. These nanostructured films hold much promise for applications such as their use as orientated nanotubules[5], sensor/actuator arrays[6,7], and optoelectronic devices[8]. The driving forces of molecular self-assembly in the supermolecular chemistry of the nanoscopic world include various weak physicochemical intermolecular interactions, e.g. van der Waals forces, hydrogen bonding, hydrophobic interactions, electrostatic forces, etc. Recent research has focused on the use of functionalized organic surfaces to form continuous inorganic thin films, based on a two-step mechanism. Firstly, surfactant micellar structures are self-assembled at the solid-liquid interface, and secondly, inorganic precursors condense to form an inorganic-organic nanocomposite. The structures of thin films formed at the solid-liquid interface depend on the properties of surfactants and substrates, and the interactions between surfactants and substrates. The use of a hydrophilic surface of mica, hydrophobic surface of graphite and amorphous silica substrates result in different self-assembly patterns with cetyltrimethylammonium chloride (CTAC) surfactant[2].

This work showed, as the very first stage, inorganic-organic thin films formed at a substrate surface by self-assembly of the surfactant molecule (AOT) in

combination with the inorganic compound uranyl acetate [$UO_2(CH_3COO)_2$]. Typically, AOT isooctane solutions were deposited on the surface of carbon films based on Formvar-coated copper TEM grids. After rapid solvent evaporation, dissipative structures formed as regular patterns on the substrate surface. Uranyl acetate was then deposited on the surface of the AOT thin film to generate a UO_2-AOT inorganic-organic thin film on the carbon substrate.

Application of a univalent compound surfactant (NaAOT) and a divalent compound surfactant ($Ba(AOT)_2$) to generate the thin films on the carbon substrates resulted in different patterns. Addition of divalent anions (SO_4^{2-} or CrO_4^{2-}) or trivalent anions (PO_4^{3-}) to the solution of surfactants produced different patterns of thin films. However, the molecular organization and self-assembly of surfactants at interfaces is a widely researched area. Our work is just beginning to involve this area and further studies need to be carried out. For example, the interaction between surfactants and substrates, how to control the pattern and the thickness of the thin film, need to be investigated.

7.2 Materials and Methods

7.2.1 Materials

All materials were of analytical grade (purity >98%) and used without further purification.

Table 7-1 Chemicals used in this chapter

Common name	Chemical name	Formula	Molecular weight	Supplier
NaAOT	sodium bis(2-ethylhexyl) sulphosuccinate	$C_{20}H_{37}O_4SO_3Na$	444.6	BDH
isooctane	2,2,4-trimethyl pentane	C_8H_{18}	114.0	Aldrich
	uranyl acetate	$UO_2(C_2H_3O_2)_2$,	388.15	AGAR
$Ba(AOT)_2$	Barium bis(2-ethylhexyl) sulfosuccinate .	$(C_{20}H_{37}O_4SO_3)_2Ba$	980.0	synthesised (section 3.2.1.2)
	sodium sulphate	Na_2SO_4	142.0	Aldrich
	sodium phosphate	Na_3PO_4	164.0	Aldrich
	phosphotungstic acid	$H_3PW_{12}O_{40}$	2880.2	AGAR

7.2.2 Experimental methods

7.2.2.1 Preparation of microscopic patterns

A drop (5 μl) of surfactant solution (0.1 M NaAOT in isooctane, or 0.05 M $Ba(AOT)_2$ in isooctane, or the mixture of both) was deposited onto the surface of carbon films which was based on the Formvar-coated copper electron microscope grid, and exposed in air until evaporation of solvent was complete and a thin film of AOT was obtained. The grid was then placed on a filter paper and a very small amount (2 μl) of 1% (w/v) uranyl acetate ($UO_2(C_2H_3O_2)_2$) aqueous solution was dropped on the grid. Due to the presence of the filter paper, water was quickly removed.

7.2.2.2 Transmission Electron Microscopy (TEM)

Samples for Transmission Electron Microscopy (TEM) were prepared as in section 7.2.2.1, and TEM analysis was performed in bright field mode using either a JEOL 2000FX high – resolution electron microscopy operating at 200keV or a JEOL 1200EX electron microscopy operating at 120keV (section **2.3.1**).

7.3 Results

7.3.1 The patterns of NaAOT-UO_2^{2+} thin film

TEM images corresponding to NaAOT (0.1 M in isooctane) and $UO_2(CH_3COO)_2$ thin films fixed on a substrate (carbon) surface after solvent evaporation (section **7.2.2.1)** showed stripe patterns with discontinuous lines and a regular interline distance of 60 – 150 nm (Figure 7-1). Interestingly, an enlarged image showed that the stripe patterns consist of small lines (30 – 40 nm in length, ~2 nm in width) perpendicular to the stripe direction, and the small lines were separated by a regular space of ~2 nm. Furthermore, there were indistinct wave patterns between the stripe lines, and the small electron dense lines were positioned just on the wave crest and trough (Figure 7-2).

7.3.2 The patterns of $Ba(AOT)_2$-UO_2^{2+} thin film

TEM images corresponding to $Ba(AOT)_2$ (0.05 M in isooctane) and $UO_2(CH_3COO)_2$ thin films prepared as in section **7.2.2.1** showed tyre-shaped patterns 2 – 8 μm in external diameter and containing emanative lines in the middle (Figure 7-3,4). The enlarged images corresponding to the middle part of the tyre-shaped pattern showed similar patterns to that of NaAOT-$UO_2(CH_3COO)_2$ but the lines were not parallel (Figure 7-5a).

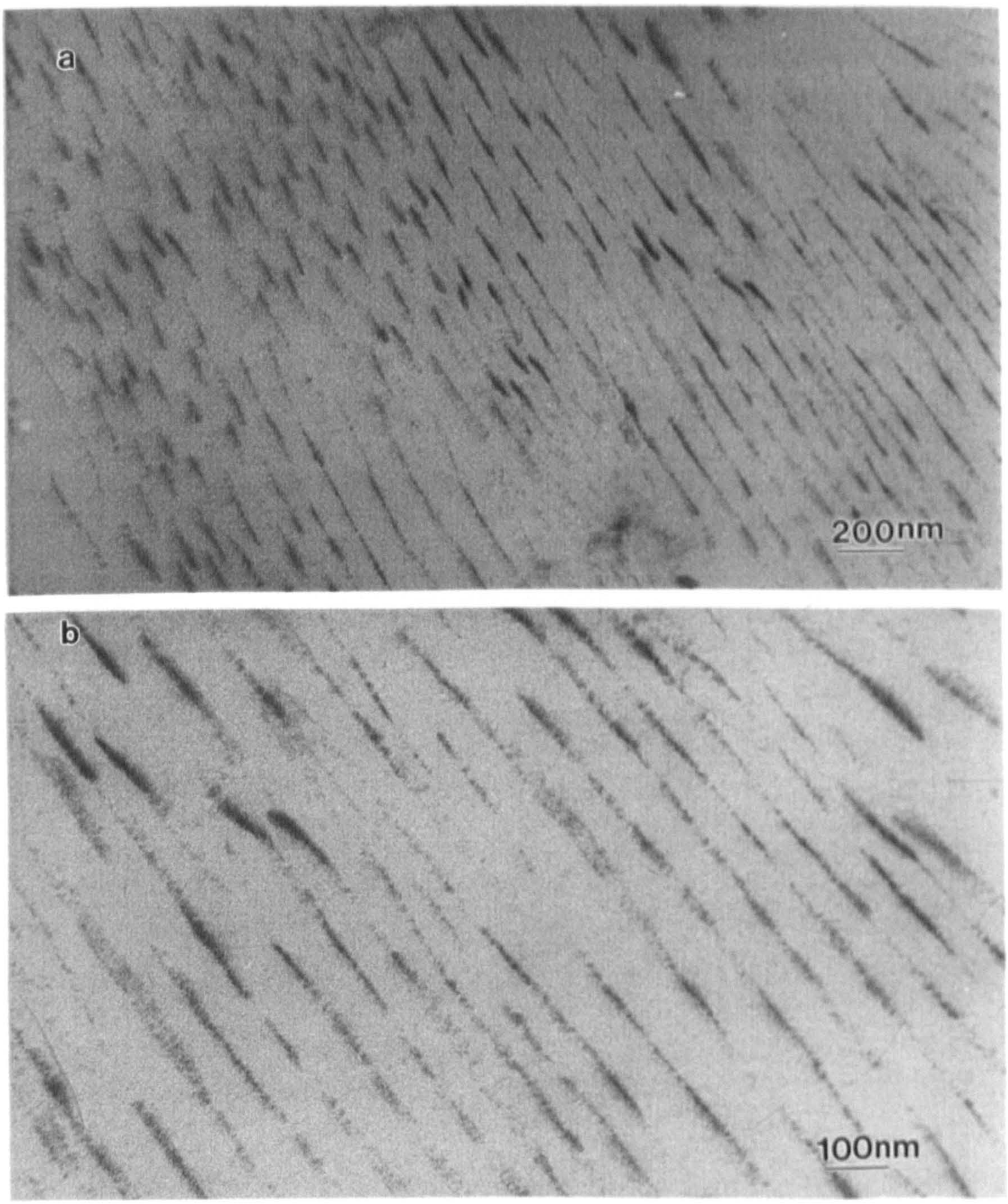

Figure 7-1: TEM images of NaAOT-UO_2^{2+} organic-inorganic thin films formed on the surface of solid by self-assembly of surfactant showing the stripe patterns. Scale bars **a** = 200 nm, **b** = 100 nm.

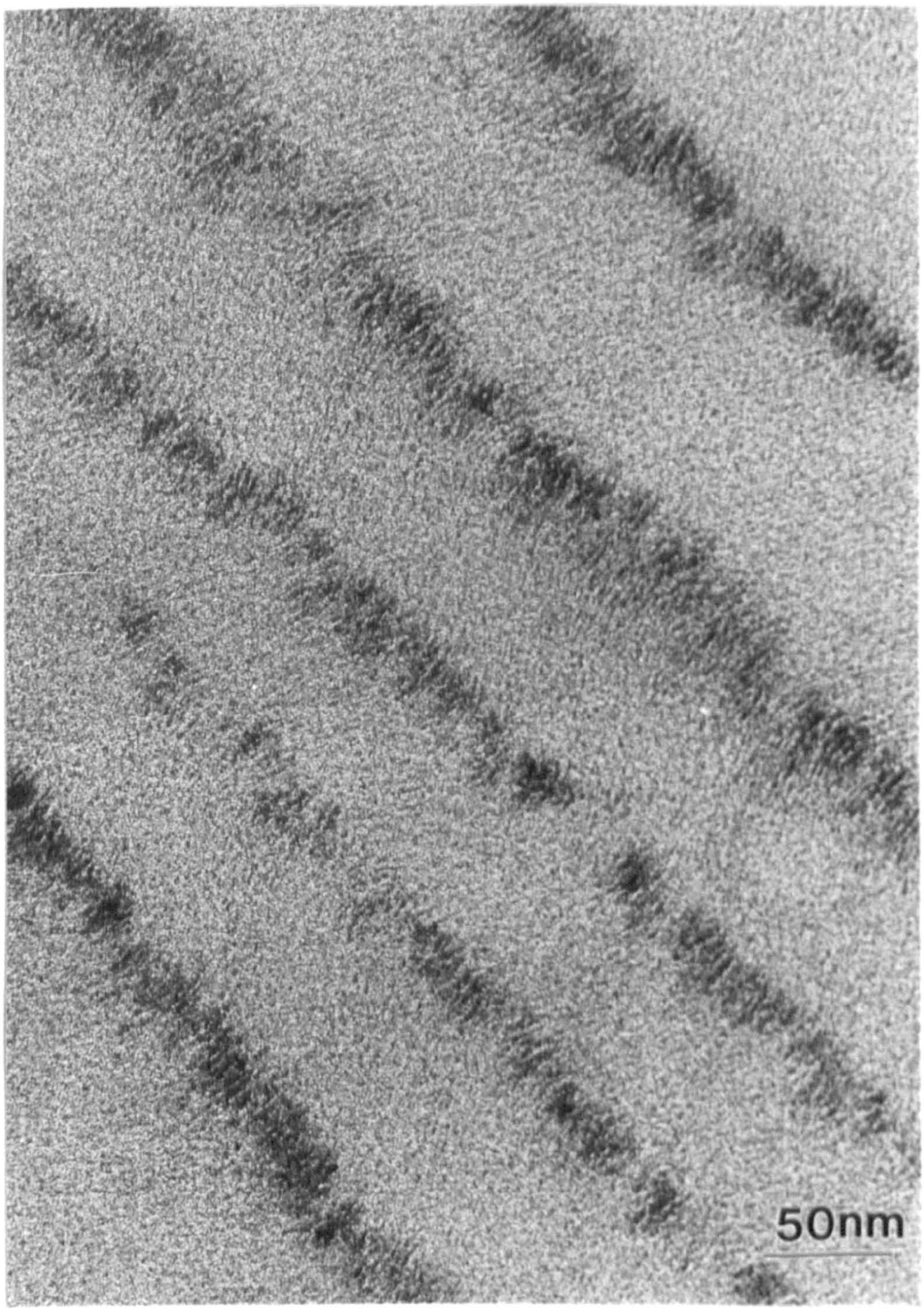

Figure 7-2: Enlarged TEM image of NaAOT-UO_2^{2+} organic-inorganic thin film shows the stripe patterns and indistinct wave patterns between the stripe lines. Scale bar = 50 nm.

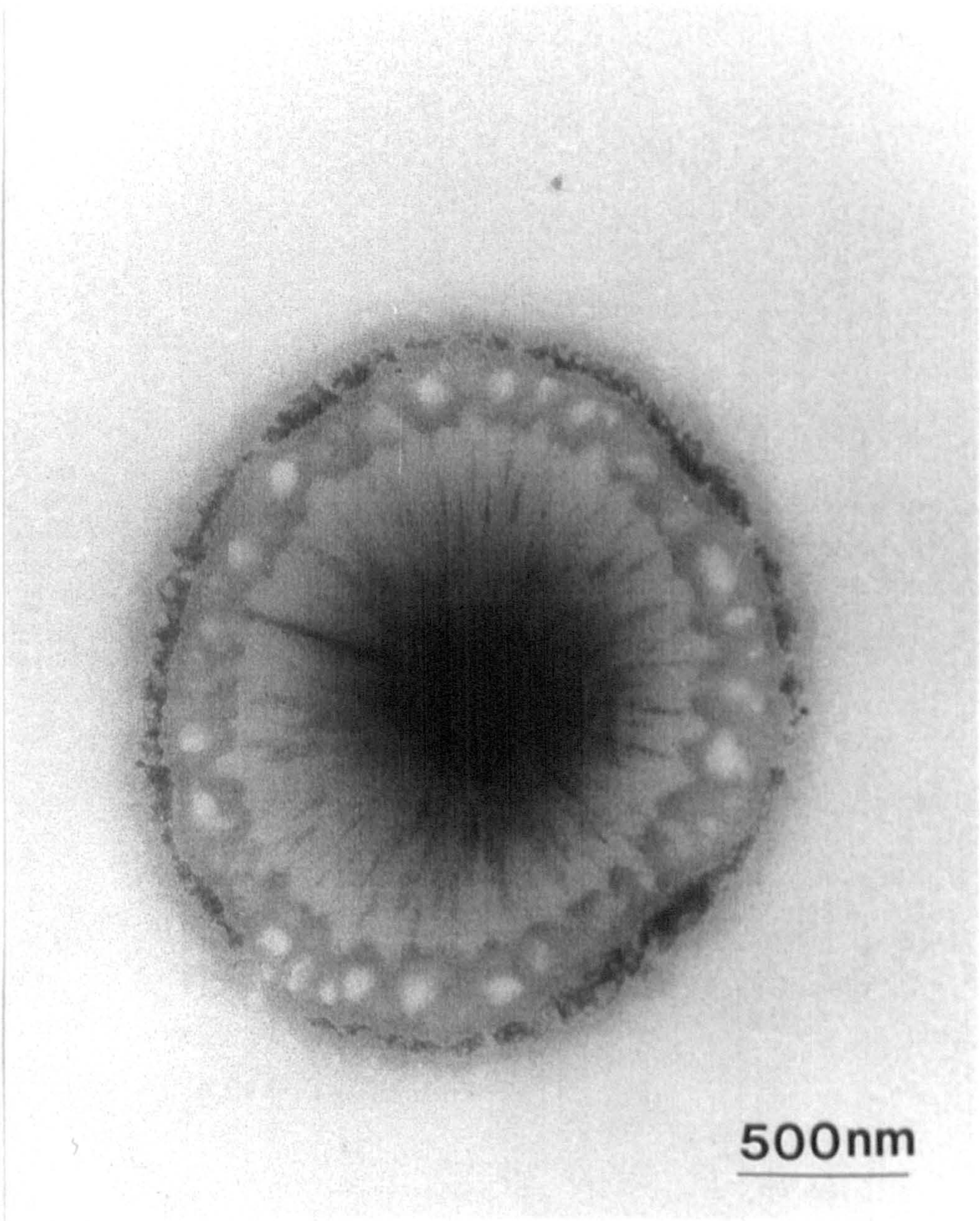

Figure 7-3: TEM image of $Ba(AOT)_2$-UO_2^{2+} shows tyre-shaped pattern containing emanative lines in the middle formed on the surface of the solid by self-assembly of surfactant. Scale bar = 500 nm.

Figure 7-4: TEM image of $Ba(AOT)_2$-UO_2^{2+} shows tyre-shaped patterns with emanative lines in the middle formed on the surface of solid by self-assembly of surfactant. Scale bar = 1 µm.

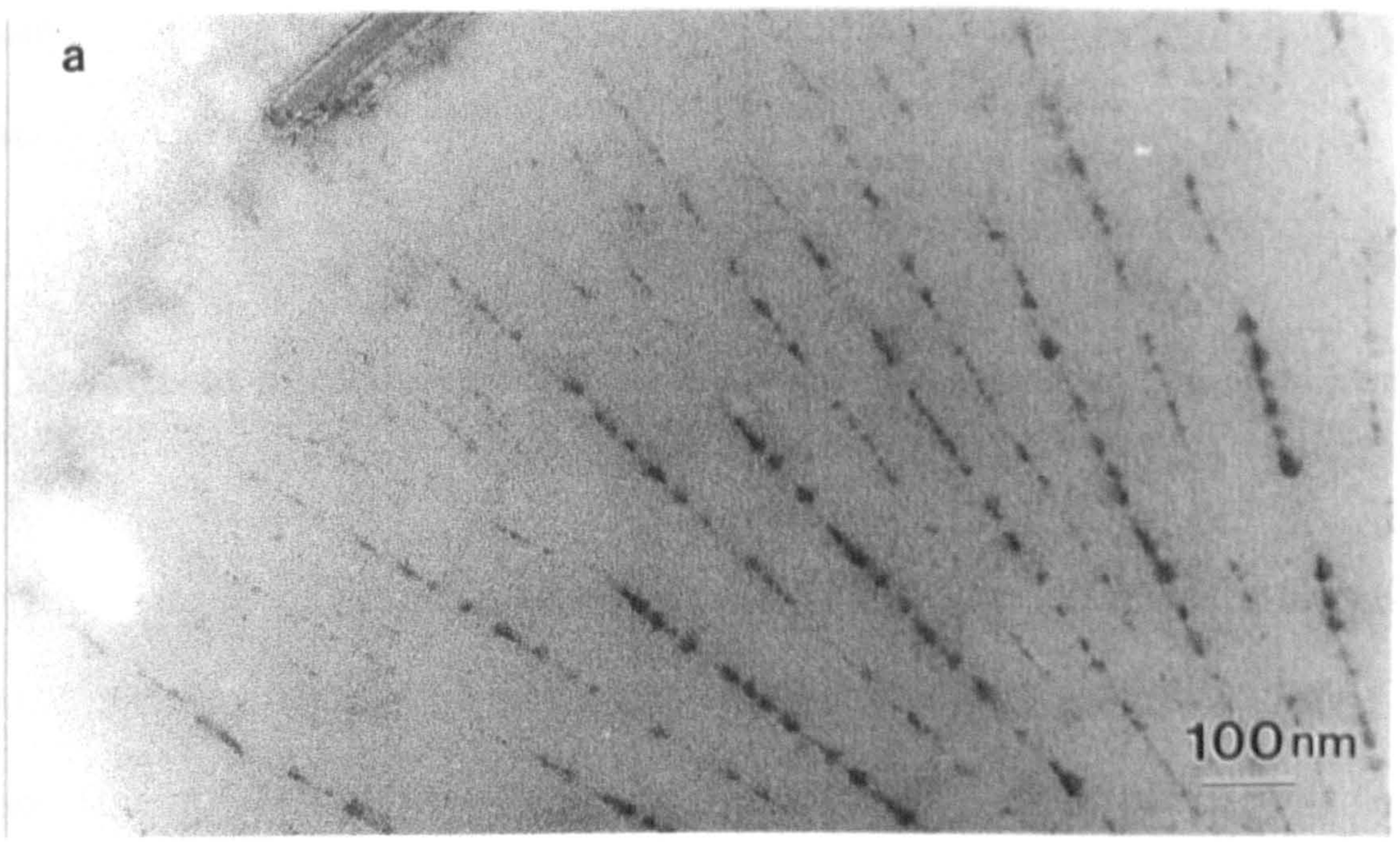

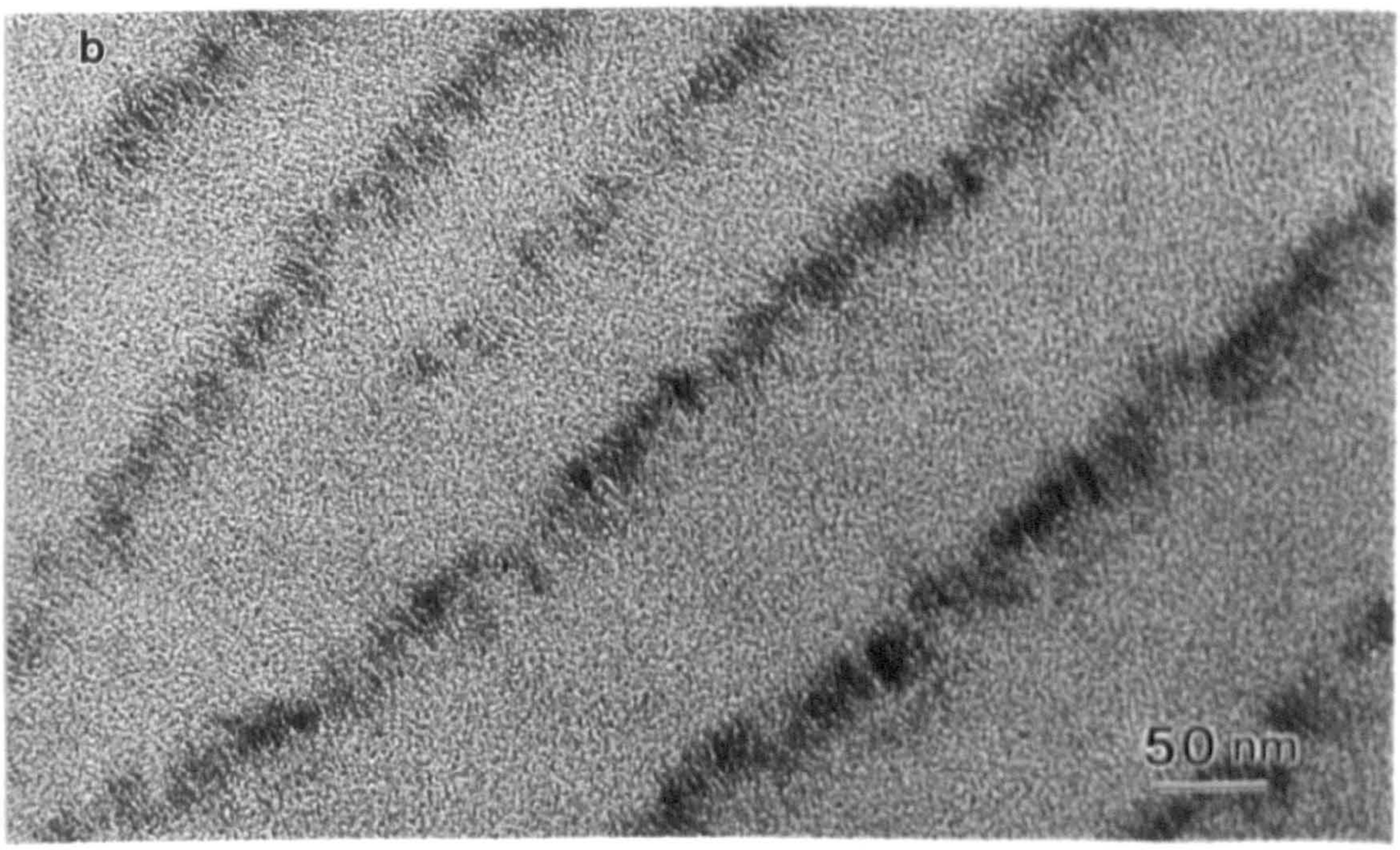

Figure 7-5: Enlarged TEM images of middle part of $Ba(AOT)_2$-UO_2^{2+} tyre-shaped patterns **(a)** shows emanative lines, scale bar = 100 nm. **(b)** stripe patterns and indistinct wave patterns cross the stripe lines. Scale bar = 50 nm.

On further increase of the magnification, the images showed indistinct wave patterns and the small lines were the same as that of NaAOT- $UO_2(CH_3COO)_2$ (section **7.3.1**) (Figure 7-5b).

7.3.3. The patterns of the mixture of NaAOT and $Ba(AOT)_2$ in the presence of water

A small amount of water was added to 0.1 M NaAOT isooctane solution to obtain AOT microemulsion at w = 10 (H_2O/AOT). $Ba(AOT)_2$ solution (0.05 M in isooctane, w < 1) was then added to the microemulsion to give NaAOT/$Ba(AOT)_2$ = 50:1. Thin films of the above mixture were prepared as in section **7.2.2.1** and the TEM images showed stripe patterns within many small domains and the directions of the stripe patterns were different in each domain (Figure 7-6). Enlarged, a single domain image showed the same stripe pattern as that of the pure NaAOT- $UO_2(CH_3COO)_2$ thin film (Figure 7-7). The tyre-shaped patterns of $Ba(AOT)_2$ were not observed.

7.3.4 Patterns of the mixture of NaAOT and $Ba(AOT)_2$ in the presence of salts

7.3.4.1 Addition of divalent salt Na_2SO_4

Addition of small amounts of Na_2SO_4 aqueous solution (0.02 M) to NaAOT isooctane solution (0.1 M) produced Na_2SO_4-containing AOT microemulsions

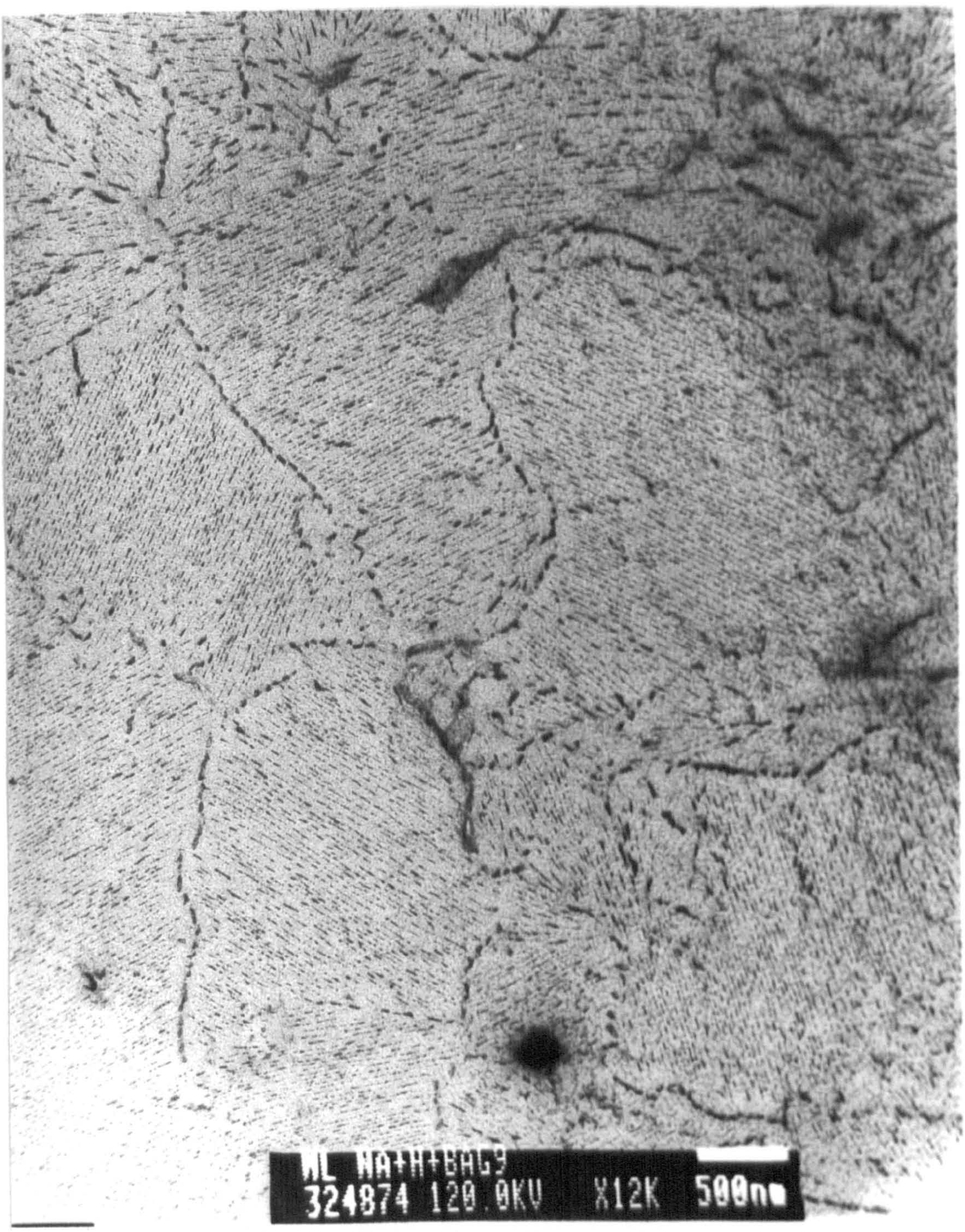

Figure 7-6: TEM image of NaAOT-$Ba(AOT)_2$-UO_2^{2+} organic-inorganic thin films formed on the surface of substrate by self-assembly of surfactant in the presence of a small amount of water. The result shows the stripe patterns within small domains. Scale bar = 500 nm.

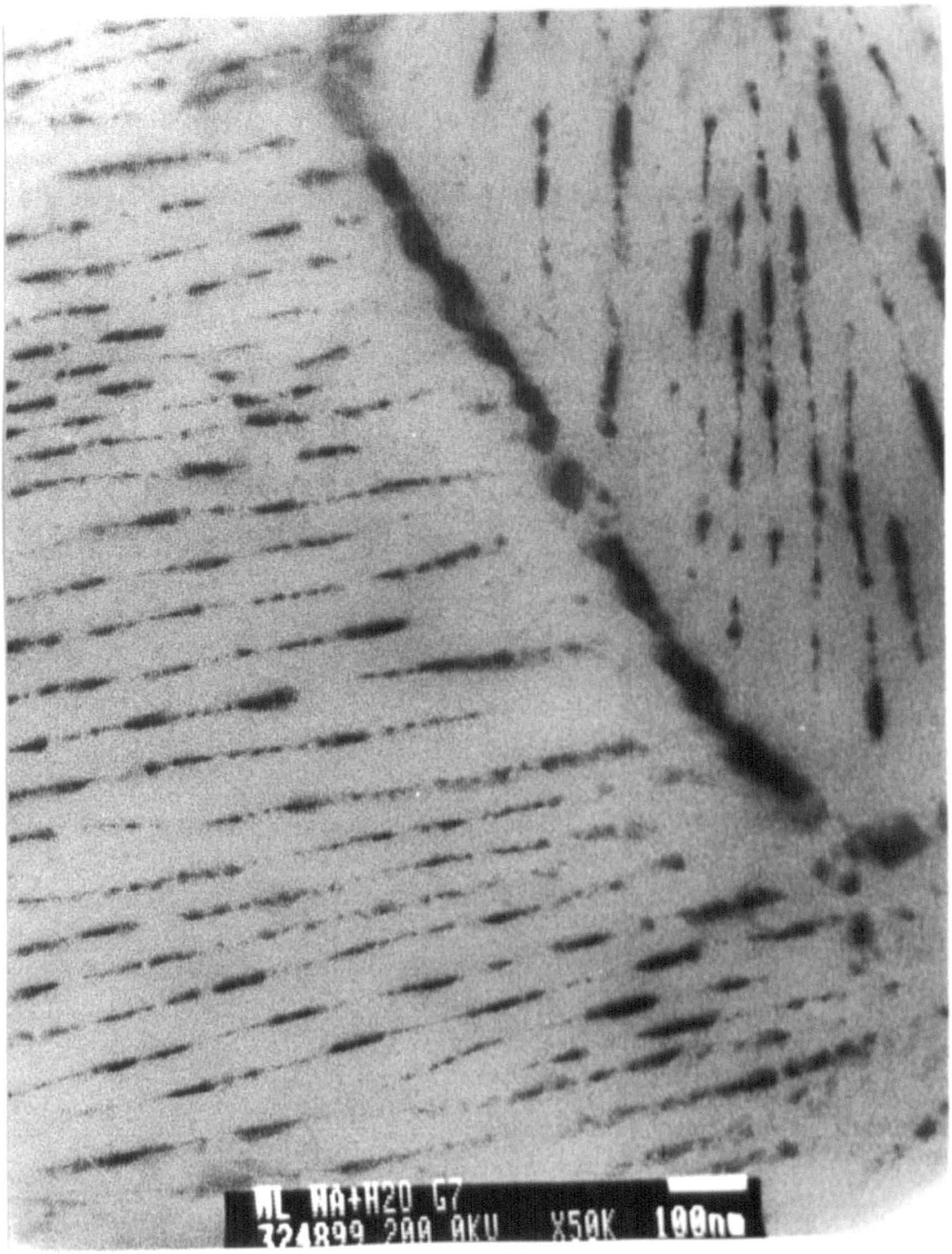

Figure 7-7: Enlarged TEM image of NaAOT-$Ba(AOT)_2$-UO_2^{2+} organic-inorganic thin films formed on the surface of substrate by self-assembly of surfactant in the presence of a small amount of water. Scale bar = 100 nm.

at w = 10. $Ba(AOT)_2$ isooctane solution (0.05 M) was then added to the microemulsion to give a molar ratio of $NaAOT/Ba(AOT)_2$ = 50:1. The thin films of this mixture were prepared immediately as in section 7.2.2.1 after mixing all the solutions. TEM images showed several kinds of patterns (Figure 7-8).

7.3.4.2 Addition of divalent salt Na_2CrO_4

Similar to section 7.3.4.1, a small amount of Na_2CrO_4 aqueous solution (0.02 M) was added to NaAOT isooctane solution (0.1 M) to produce a Na_2CrO_4-containing AOT microemulsion at w = 10. $Ba(AOT)_2$ isooctane solution (0.05 M) was then added to the microemulsion to give the molar ratio of $NaAOT/Ba(AOT)_2$ = 50:1. Thin films of this mixture were prepared immediately as in section 7.2.2.1 after mixing all the solutions. TEM images showed patterns similar to liquid crystals achieved by adding small quantities of azobenzene compounds to the chiral smectic C phase[9] (Figure 7-9).

7.3.4.3 Addition of trivalent salt Na_3PO_4

Similar experiments as in section 7.3.4.1 were undertaken with mixture of $Ba(AOT)_2$ (0.05 M in isooctane, w < 1) and NaAOT microemulsion containing aqueous Na_3PO_4 (0.02 M) at w = 10 to give final molar ratios NaAOT : $Ba(AOT)_2$ = 50:1. TEM images corresponding to the thin films of the above mixture showed different patterns when compared with those prepared with Na_2SO_4 and Na_2CrO_4 (Figure 7-10).

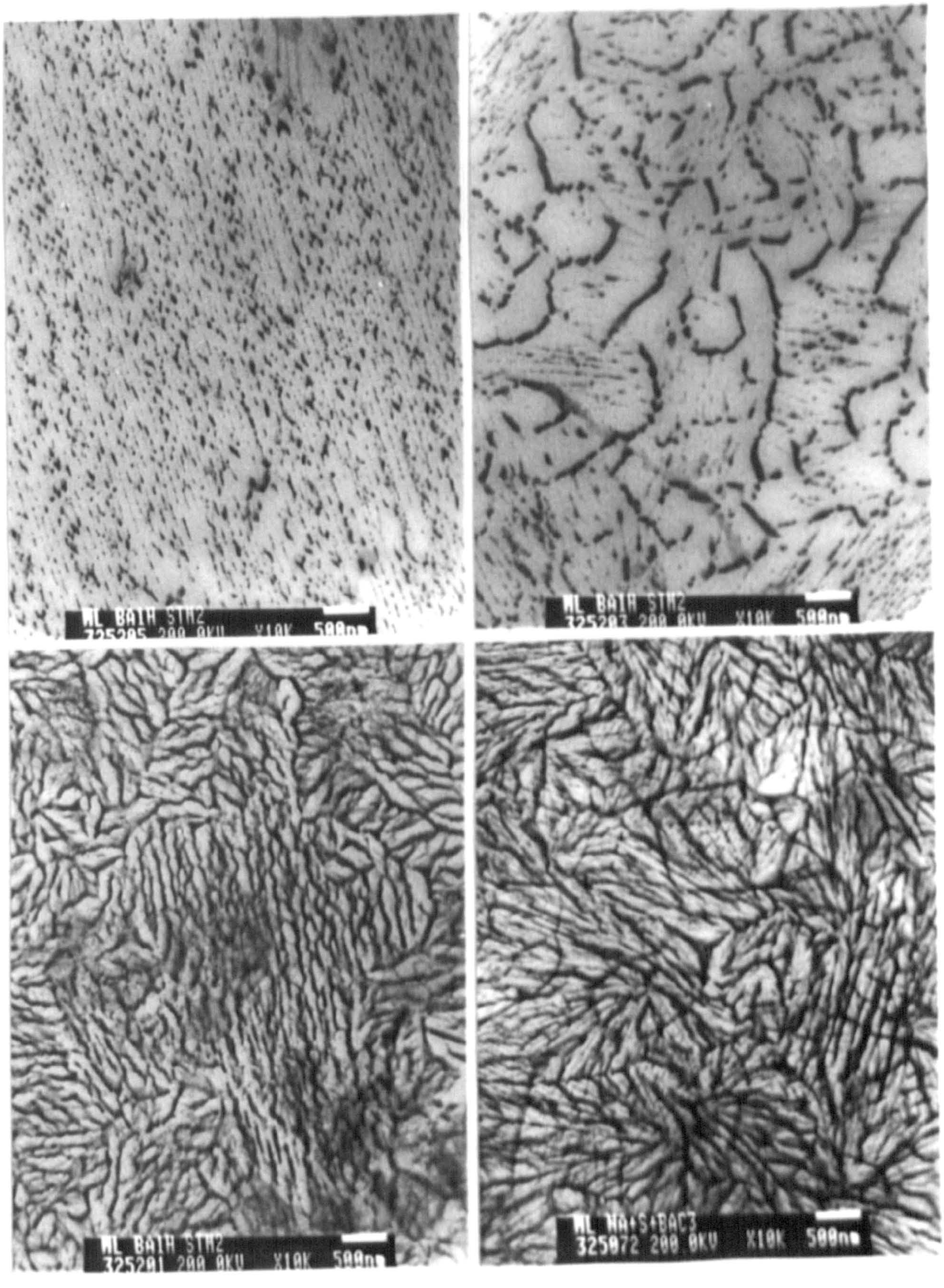

Figure 7-8: TEM images of NaAOT-$Ba(AOT)_2$-UO_2^{2+} organic-inorganic thin films formed on the carbon substrate by self-assembly of surfactant in the presence of a small amount of Na_2SO_4. Scale bars = 500 nm.

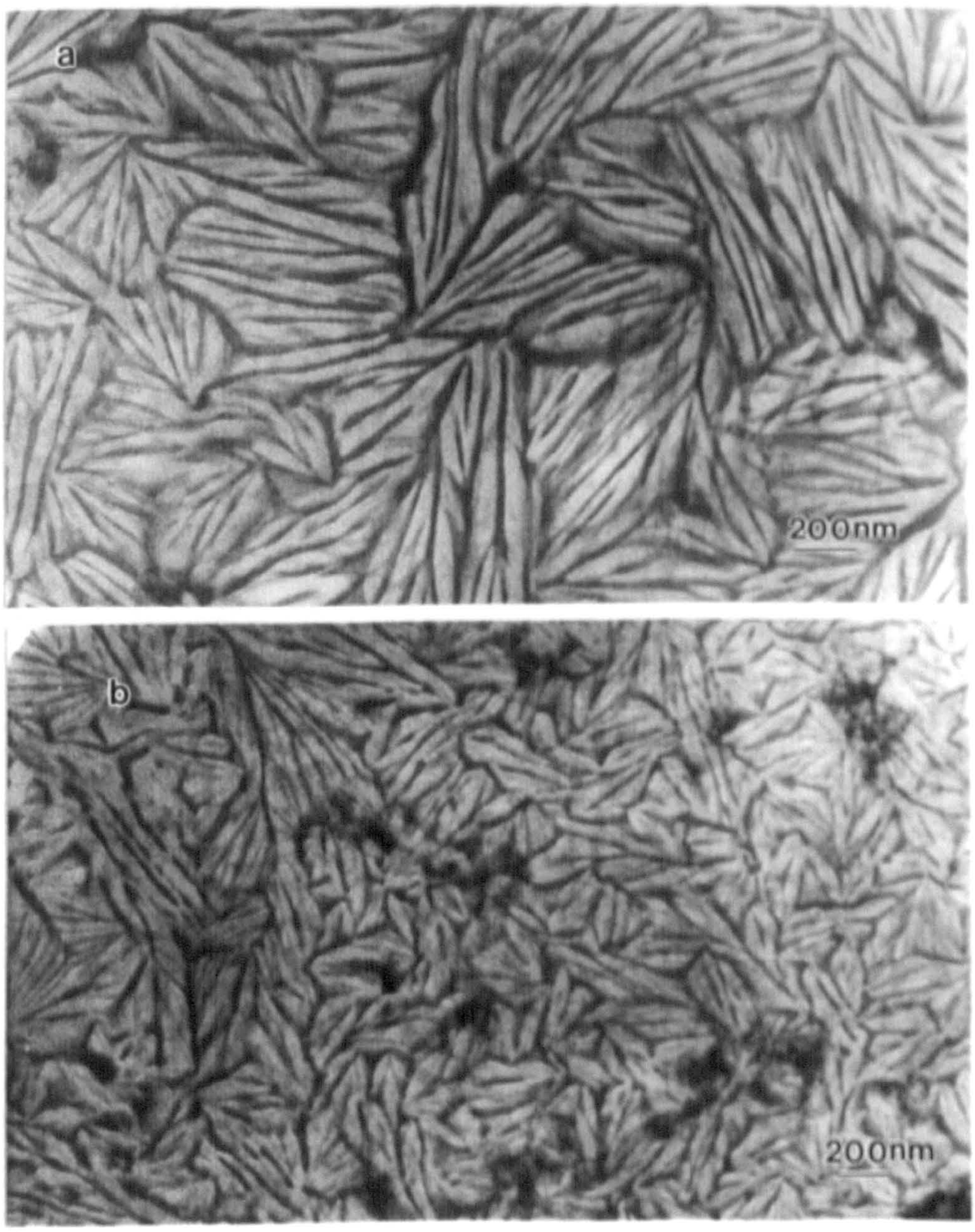

Figure 7-9: TEM images of NaAOT-$Ba(AOT)_2$-UO_2^{2+} organic-inorganic thin films formed on the surface of substrate by self-assembly of surfactant in the presence of a small amount of Na_2CrO_4. Scale bars = 200 nm.

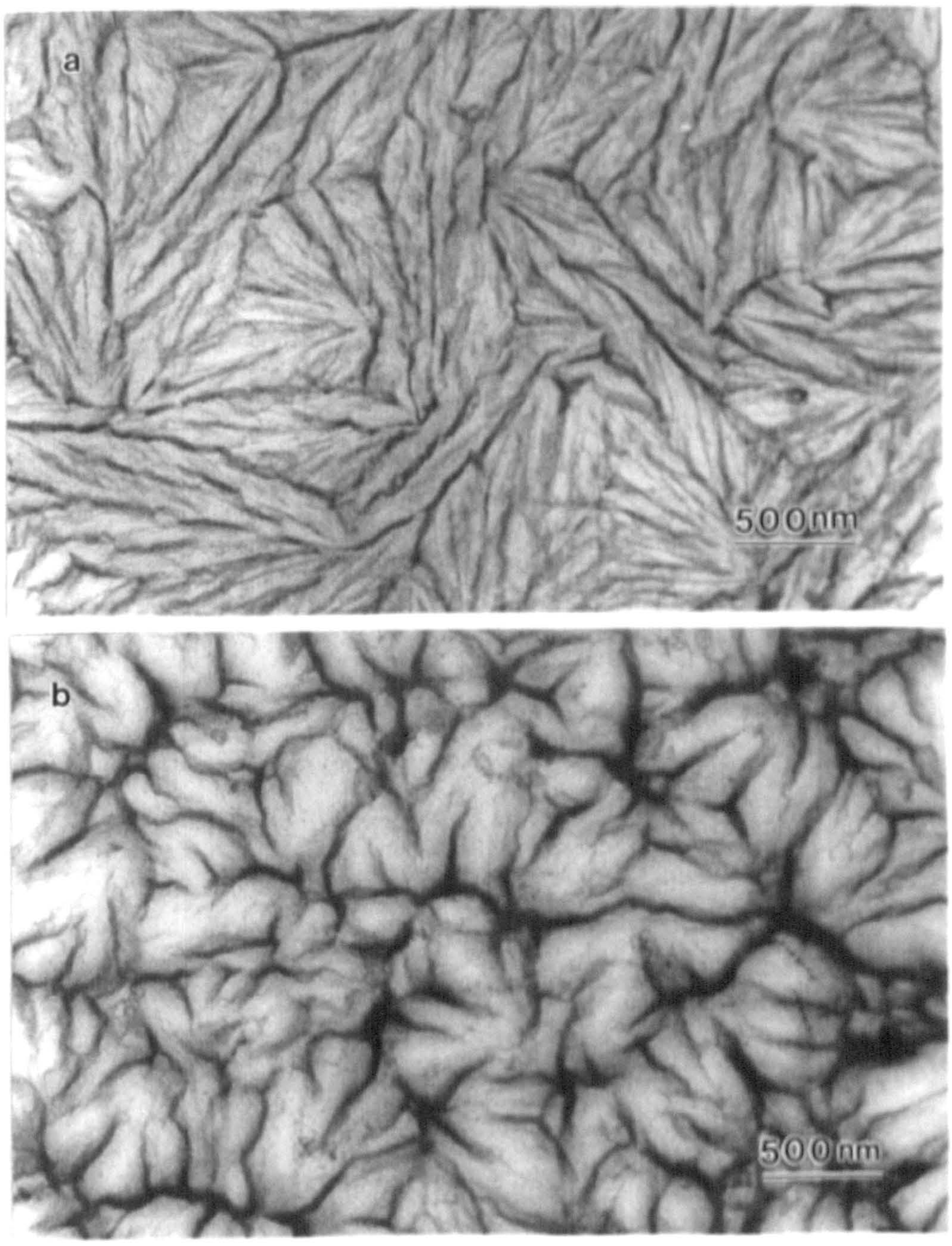

Figure 7-10: TEM images of NaAOT-$Ba(AOT)_2$-UO_2^{2+} organic-inorganic thin films formed on the carbon substrate by self-assembly of surfactant in the presence of a small amount of Na_3PO_4. Scale bars = 500 nm.

7.3.5 Control experiments

Thin films were prepared in control experiments as in section 7.2.2.1 but without the uranyl acetate stain. TEM images showed no objects on the grid. Moreover, deposition of isooctane (without any surfactants and salts) on the grid followed by staining with uranyl acetate gave no patterned objects when examined by TEM.

7.4 Discussions

AOT-UO_2 organic-inorganic thin films formed by self-assembly of surfactants on the solid substrate surface involves two steps. Firstly, the organic solution of AOT (0.1 M in isooctane) was deposited onto the surface of carbon film. After evaporation of solvent, the phase behavior of the surfactant transferred from a reverse micelle phase to a liquid crystal phase and interacted with the surface of solid substrate to form a dissipative structured organic thin film with regular patterns. The interline distances of the small lines and the wave lines in Figure 7-2 were consistent with that of the AOT bilayer lamella, indicating that the wave patterns were formed by self-assembly of AOT molecules (Scheme 7-1). However, why did the patterns form in a wave shape? This concerned the interaction of surfactants and the substrates. Further investigation needs to be carried out, for example, on whether the patterns will change or not by using alternative substrates.

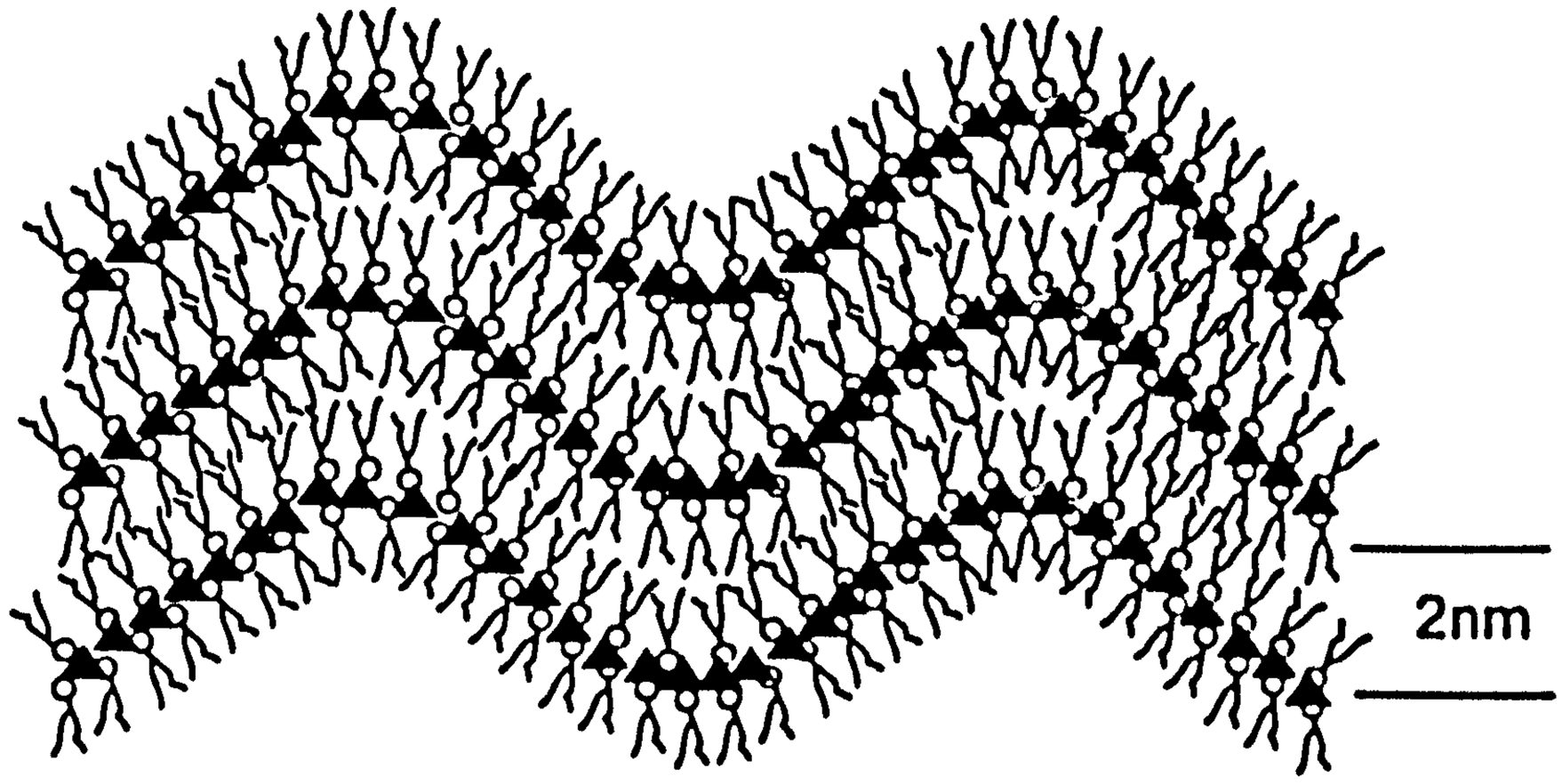

Scheme 7-1 The sketch of the structure of AOT-UO_2^{2+} thin film.

The formation of organic thin films was affected by the properties of substrates and surfactants, and the self-assembly structures of surfactants. Different patterns were observed between NaAOT and $Ba(AOT)_2$, implying that the influences were not just from the surfactant itself; the counterions were also important.

Secondly, the inorganic compound $UO_2(CH_3COO)_2$ was deposited onto the AOT film after drying to form organic–inorganic thin films on the substrate surface. UO_2^{2+} cations bonded to negatively charged AOT headgroup to give electron dense AOT-UO_2 thin films with regular patterns. The formation of the stripe patterns was related to the drying process. One possibility is that the organic thin film already formed on the substrate surface with the patterns, and the inorganic compound $UO_2(CH_3COO)_2$ just stained the organic thin film without changing the patterns. In this case, the organic film acted as a substrate for the inorganic compound, the evaporation of inorganic solution underwent a stick and slip movement of the receding front, which might be ascribable to the local gelation effect at the three-phase line (liquid-substrate-air boundary) where the concentration is assumed to be higher than in the bulk solution.[1] Another possibility is that when the inorganic solution was dropped on the organic thin film, the surfactant was redissolved and reacted with the inorganic compound. The product (AOT-UO_2) then interacted with the carbon substrate and underwent the same drying process to form the regular patterns by surfactant self-assembly.

The patterns of the organic-inorganic thin films were affected by adding small amounts of inorganic salts to the surfactants. The mechanism needs to be further investigated.

This subject needs to be further developed. The understanding of the formation process could lead to innovative materials synthesis by using AOT as a template.

7.5 References

[1]. Maruyama, N., Karthaus, O., Ijiro, K., Chimomura, M., Koito, T., Nishimura, S., Sawadaishi, T., Nishi, N., Tokura, S., *Supermolecular Science*, 5, 331 (1998).

[2]. Aksay, I.A., Trau, M., Manne, S., Honma, I., Yao, N., Zhou, L., Fenter, P., Eisenberger, P.M., Gruner, S.M., *Science*, 273, 892 (1996).

[3]. Trau, M., Yao, N., Kim, E., Xia, Y., Whitesides, G.M., Aksay, I.A., *Nature*, 390, 674 (1997).

[4]. Yang, H., Kuperman, A., Coombs, N., Mamiche-Afara, S., Ozin, G.A., *Nature*, 379, 703 (1996).

[5]. Li, W.Z., Xie, S.S., Qian, L.X., Chang, B.H., Zou, B.S., Zhou, W.Y., Zhao, R.A., Wang, G., *Science*, 274, 1701 (1996).

[6]. Sakai, H., Baba, R., Hashimoto, K., Fujishima, A., Heller, A., *J. Phys. Chem.*, 99, 11896 (1996).

[7]. Tamagawa, C.Y., Schiller, P., Polla, D.L., *Sensoers Actuators A.* 35, 77 (1992).

[8]. Fendler, J.H., *Chem. Mater.*, 8, 1616 (1996).

[9]. Xu, Z.S., Lemieux, R.P., Natansohn, A., Rochon, P., Shashidhar, R., *Chem. Mater.*, 10. 3269 (1998).

Chapter 8

Organization Of Inorganic Nanoparticles Using Biotin-Streptavidin Connectors

(Published in *Chem. Mater.*, 11, 23-26, 1999)

8.1 Introduction

There is increasing interest in the synthesis and organization of inorganic nanoparticle materials by using biological and organic molecules. Initial studies have shown that complementary strands of DNA molecules can be used to self-assemble inorganic nanoparticles;[1,2] the highly specific recognition properties of antibodies and antigens were also used to organize inorganic nanoparticles;[3,4] self-assembled bacterial S-layers were used for the synthesis of cadmium sulphide superlattices;[5] and self-organized organic molecules were used for linking inorganic nanoparticles.[6-12] Attention has been paid to the synthesis and assembly of new forms of inorganic matter organized at the nanometre and mesoscopic length scales by using biological and organic molecules. Because these nanoparticles have unusual structures and properties in chemistry and physics they may find application in catalysis, electro-optical devices, semiconductors, and the synthesis of strong ceramics. On the other hand, the connection of DNA and biological or organic molecules with inorganic nanoparticles may create excellent organized structures with surprizing new properties. In this chapter, we describe an alternative biomimetic approach in which we use the high affinity binding of streptavidin to biotinylated amino acid residues on the surface of the protein, ferritin, to generate reversible networks of superparamagnetic iron oxide nanoparticles. The use of the streptavidin/biotin recognition motif in gold nanocrystal aggregation was also reported by Connelly and Fitzmaurice.[13]

Ferritin is a spherical hollow protein shell, 7-8 nm in internal diameter (12-13 nm in external diameter), which is composed of a quaternary structure of 24 polypeptide subunits (Mr about 500 000). The central cavity usually contains a ferric oxide core of structure similar to that of the mineral ferrihydrite ($5Fe_2O_3.9H_2O$).[14] Hydrophilic and hydrophobic channels penetrate the shell and as a result, iron atoms can be removed from the cage by reductive dissolution. Moreover, the mineral phase can be reconstituted with other inorganic material. This provides an attractive means by which inorganic nanoparticles can be synthesized with controllable sizes, as well as exhibiting potential biocompatible properties. Indeed, inorganic nanoparticles, such as a ferrimagnetic iron oxide magnetite (Fe_3O_4)[15], iron(III) sulfide[16], manganese oxide[17] and cadmium sulfide[18] have been synthesized within the ferritin cages *in vitro* by reconstitution of apoferritin (ferritin without ferric oxide core). The nanoscale of these particles endows them with unusual structures and properties in chemistry and physics that may find applications in many research areas of current interest.

The connection of inorganic nanoparticles into two or three dimensional arrays has recently received much attention. Organic molecules have an unparalleled ability for chemical specificity onto particular partners *via* molecular recognition. In contrast, it is more difficult to link condensed inorganic materials. Integration of these two chemical families could create organized structures with surprising new properties. Over the past few years, chemists have begun initial studies in

this area, where DNA, proteins, antibodies and other biological or organic molecules are used to help connect small inorganic particles to create exquisitely organized structures with marvelous properties.[19]

Here, we describe a route to organizing inorganic nanoparticles, in which biotinylated functionalized ferritin is linked into network structures by auxiliary protein molecules (streptavidin). In recent years the biotin/streptavidin system has become a very commonly used affinity labeling system. It was also used for organization of 'soft' composite material as a ligand-receptor.[20] Streptavidin is a tetrameric protein (molecular weight = 4×15,000), and remarkable for its ability to bind up to four molecules of biotin with unusually high affinity of the non-covalent interaction [dissociation constant $K_d = 10^{-15}$ M].[21] Comparison of the refined crystal structures of apo- and a streptavidin/biotin complex shows that the high affinity results from several factors, for example, the high affinity of multiple hydrogen bonds and *van der Waals* interactions between biotin and streptavidin, together with the ordering of surface polypeptide loops that bury the biotin in the streptavidin interior.

Native horse spleen ferritin was modified with biotin (N-hydroxysuccinimide ester, water soluble) *via* nucleophilic reaction (S_N2). Biotin can react with amino groups of proteins under mild basic conditions. The reaction route is illustrated in Scheme 8-1. The reaction took place spontaneously under basic conditions at room temperature. The product was biotinylated ferritin.

After modification with biotin, the biological and physicochemical properties of ferritin were not changed significantly. Biotinylated ferritin still has the property of storing an iron core inside the hollow shell. Likewise, the biotin moiety of the derivatized molecule was still available for interaction with streptavidin. Because the interaction is so strong, that even biotin coupled to large protein molecules is available for binding streptavidin[22] and the association of streptavidin and biotin is remarkably rapid and stable.[23] The general interaction reaction between biotinylated ferrtin and streptavidin is shown in Scheme 8-2. The cross-linking reaction took place spontaneously under mild basic condition at room temperature. However, the rate of cross-linking reaction and the degree of organization were affected by the ratio of biotinylated ferritin to streptavidin as well as the concentration of both reactants.

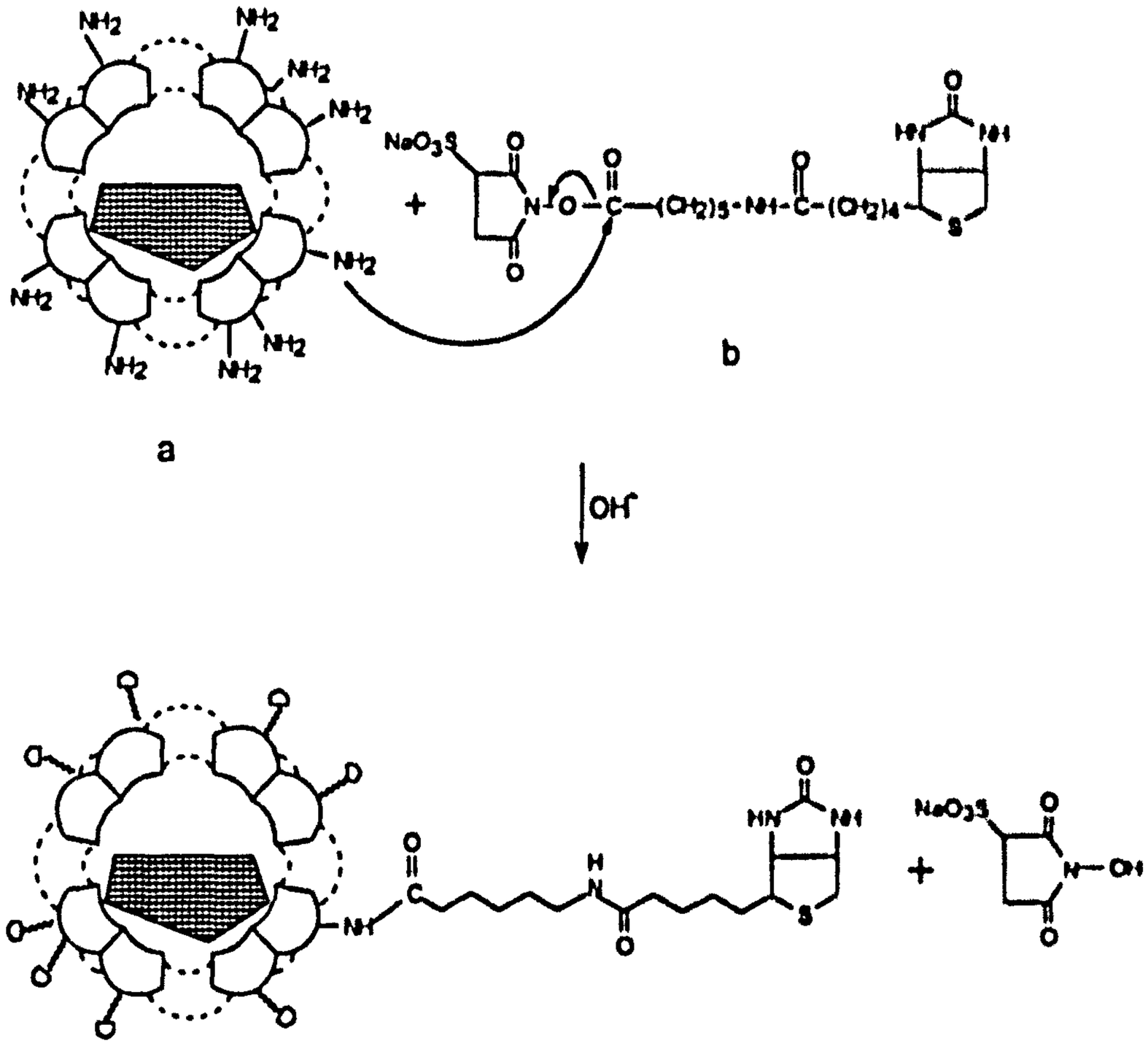

a b c

Scheme 8-1: reaction scheme for biotinylated ferritin. **(a)** native horse spleen ferritin; **(b)** sulfosuccinimidyl-6-(biotinmaido)hexanoate; **(c)** biotinylation of surface lysine residues.

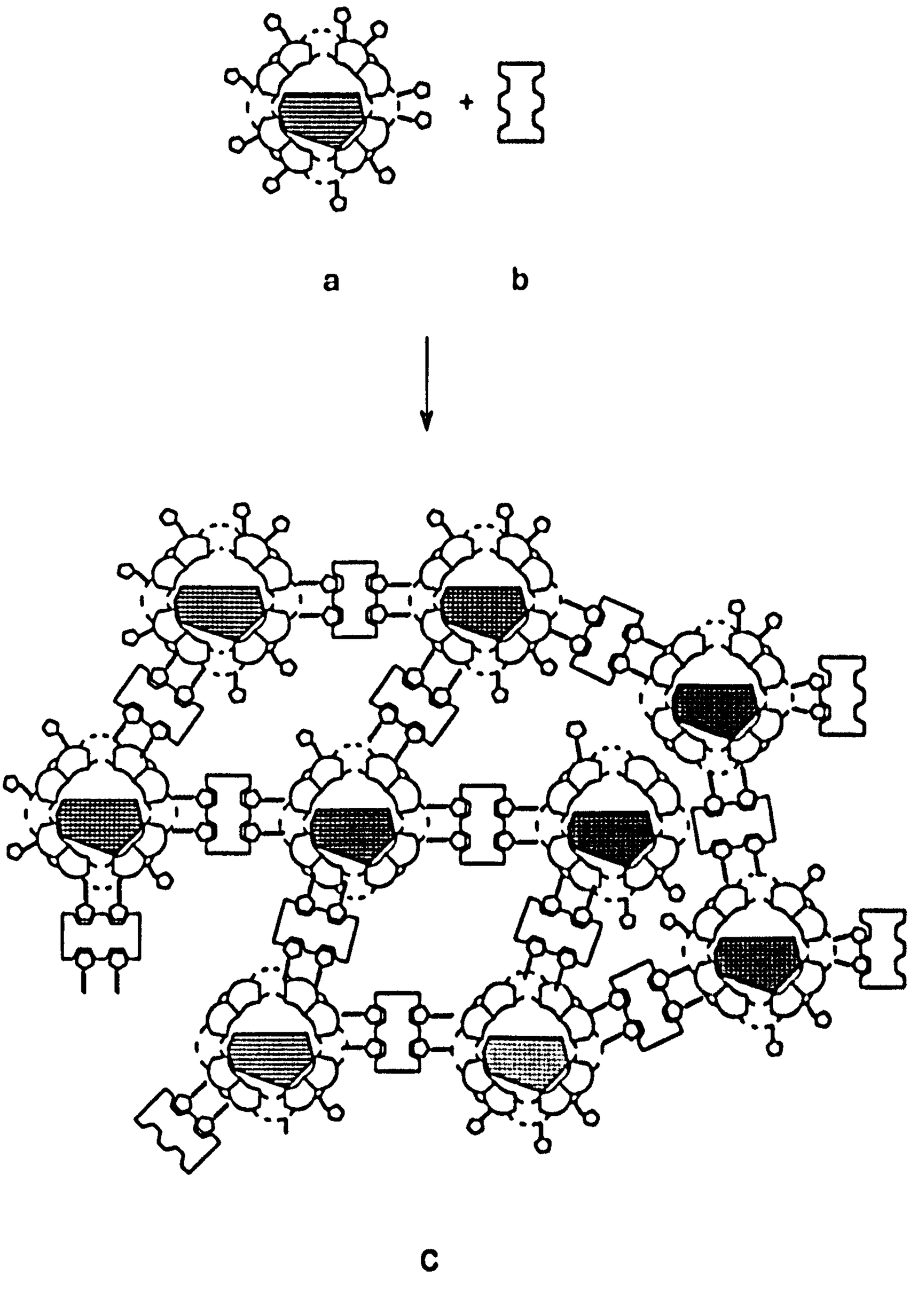

Scheme 8-2: Controlled aggregation of iron oxide nanoparticles in biotinylated ferritin by streptavidin connectors. (a) biotinylated ferritin; (b) streptavidin; (c) organized product.

8.2 Materials and Methods

8.2.1 Materials

All materials were of analytical grade (purity >98%) and used without further purification.

Table 8-1 Chemical and biological materials used in this chapter

Ferritin:	Highly purified Equine spleen Ferritin, M.W. 500,000, Iron 11.4% (by weight protein). (CALBIOCHEM)
Biotin:	Biotin (Long Arm) NHS-water soluble (NHSws) Sulfosuccinimidyl-6-(Biotinamido) Hexanoate Sodium Salt Empirical formula $C_{20}H_{29}N_4NaO_9S_2$, FW: 556.57. (Vector Laboratories)
Streptavidin:	Purity, homogeneous by SDS-PAGE; Percent activity, 98% bound to immobilized biotin. M.W 60,000 (Vector Laboratories)
HEPES:	*N*-[2-Hydroxyethyl]piperazine-*N*'-[2-ethanesulfonic acid] FW: 238.3, pKa=7.5 at 25 °C, useful pH range 6.8-8.2 (SIGMA)
HABA	4-hydroxyazobenzene-2'-carboxylic acid, FW: 242.2 (SIGMA)
KH_2PO_4	FW: 136.1 (SIGMA)
Na_2HPO_4	FW: 142.0 (SIGMA)
SDS	sodium dodecylsulphate, $C_{12}H_{25}O_4SNa$, FW: 288.4 (Aldrich)
Tris	tris(hydroxymethyl)aminomethane, FW: 157.6 (SIGMA)
Glycerol	$C_3H_8O_3$, FW: 92.09 (SIGMA)

TEMED	N,N,N',N'-tetramethylethylenediamine, C6H16N2, FW: 116.2 (SIGMA)
APS	ammonium persulphate, $(NH_4)_2S_2O_8$, FW: 228.2 (SIGMA)
Methanol	CH_3OH, FW: 32 (SIGMA)
Mercaptoethanol	$HSCH_2CH_2OH$, FW: 78.13 (Aldrich)
bromophenol blue	3′, 3″, 5′, 5″-Tetrabromophenolsulfonephthalein, sodium salt, $C_{19}H_9Br_4O_5SNa$, FW: 691.9 (SIGMA)
Brilliant blue R	Coomassie brilliant blue R250, FW: 826.0 (SIGMA)
glacial acetic acid	CH_3COOH, FW: 60.0 (SIGMA)
uranyl acetate	$UO_2(C_2H_3O_2)_2$, FW: 388.15 (AGAR)
Bicinchoninic Acid	4,4′-Dicarboxy-2,2′-biquindine Disodium salt, $C_{20}H_{10}N_2O_4Na_2$, FW: 388.3 (SIGMA)
Protein Assay Kit:	SIGMA procedure No. TPRO-562
Acrylamide/bisacrylamide	30% solution, 37.5:1 ratio (SIGMA)

8.2.2 Methods

8.2.2.1 Biotinylation of the ferritin

In a typical reaction, 40 µl of aqueous biotin (sodium sulfosuccinimidyl-6-biotinamido hexanoate, 25 mg/ml, $C_{20}H_{29}N_4NaO_9S_2$, 44.9 mM,) was added at room temperature to 5 ml of a horse spleen ferritin solution (4 µM, 2 mg/ml), buffered at pH 8.5 (100 mM HEPES [*N*-(2-hydroxyethyl)piperazine-*N'*-(2-ethanesulfonic acid)]). The reaction solution was occasionally stirred over a period of 4 hours at room temperature, and then dialyzed against 2L of HEPES

buffer (100 mM, pH 8.5) at 4 °C for 24 hours to remove the unreacted reagent and small molecule reaction products. The concentration of yellow transparent biotinylated ferritin solutions was determined by use of a Bicinchoninic Acid Protein Assay Kit (section 8.2.2.2). Approximately 60 to 70 lysine residues were accessible to surface biotinylation (section 8.2.2.3) (arginine residues were not coupled under the reaction conditions used).

8.2.2.2 Protein assay

After biotinylation, the concentration of biotinylated ferritin was determined by use of a Bicinchoninic Acid Protein Assay Kit (SIGMA procedure No. TPRO-562).

The protein reduces alkaline Cu(II) to Cu (I) in a concentration dependent manner. Bicinchoninic acid is a highly specific chromogenic reagent for Cu(I) forming a purple complex with an absorbance maximum at 562 nm. Because of this property, bicinchoninic acid can be substituted for the Folin-Ciocalteu reagent for the determination of protein, as the resultant absorbance at 562 nm is directly proportional to the protein concentration.

The assay procedure was as follows:

1 Freshly prepare the required amount of protein determination reagent by adding 1 part Cu(II) sulfate pentahydrate 4% (w/v) solution to 50 parts bicinchoninic acid solution (containing bicinchoninic acid, sodium carbonate, sodium tartrate and sodium bicarbonate in 0.1 N NaOH, pH = 11.25).

2 Prepare assay solution as in table 8.2

3 Incubate the assay solutions at 37 °C for 30 minutes.

4 Cool to room temperature and determine the absorbance at 562 nm by using a PERKIN ELMER Lambda II UV-vis spectrometer.

5 Make a standard curve with number 1 – 6 in table 8.2 and calculate the concentration of biotinylated ferritin with number 7 – 10 in table 8.2.

Table 8.2 Assay set-up table (All in ml)

No	water	protein standard	biotinylated ferritin	protein reagent
1	0.10	0	–	2.0
2	0.08	0.02	–	2.0
3	0.06	0.04	–	2.0
4	0.04	0.06	–	2.0
5	0.02	0.08	–	2.0
6	0	0.10	–	2.0
7	0.10	–	0	2.0
8	0.08	–	0.02	2.0
9	0.08	–	0.02	2.0
10	0.08	–	0.02	2.0

Protein standard solution was 1.0 mg/ml bovine serum albumin in 0.15 M NaCl with 0.05% sodium azide as a preservative and was supplied in the kit.

8.2.2.3 Spectrophotometric determination of biotin on the surface of ferritin[24]

Since avidin combines stoichiometrically with biotin, it is possible to use any physicochemical difference between avidin and the avidin-biotin complex as the basis of an assay method for either component. This method is based on the use of the dye 4-hydroxyazobenzene-2′-carboxylic acid (HABA), which binds only to

avidin and can therefore be used as an indicator for unoccupied binding sites. HABA is not bound by the avidin-biotin complex, and since the dissociation of the latter is so low (10^{-15} M) the dye is stoichiometrically displaced by biotin.

0.2 ml of streptavidin (1 mg/ml) was mixed with 0.025 ml of HABA (10 mM) in phosphate buffer at pH = 6.9, measured by UV/vis at 500 nm to give an absorbance A_1. 10 µl of unknown biotinylated ferritin (v, ml) was then added to the mixture above and the absorbance was again measured to give A_2. The concentration of the total biotin in the added volume of biotinylated ferritin was calculated as follows:

$$[\text{Biotin}] = \frac{A_1 - A_2(v+1)}{24}\,\text{mM}$$

The number of biotin molecules on the surface of each ferritin can be obtained by calculating the moles of biotin to ferritin.

8.2.2.4 Organization of the biotinylated ferritin using streptavidin

Molecular cross-linking of the biotinylated ferritin was carried out at room temperature by addition of streptavidin (167 µM, 1.0 mg in 0.1 ml of 10 mM phosphate/0.15 M NaCl buffer, pH 7.5) to solutions of biotinylated ferritin. The mole ratio of biotinylated ferritin : streptavidin was varied between values of 1 : 2 and 1 : 12.

8.2.2.5 SDS-polyacrylamide gel electrophoresis (SDS-PAGE)

The reagents were prepared as follows:

Table 8-3 Separating gel (7.5% Acrylamide)

Chemicals	Volume	Final concentration
acrylamide (30%, w/v)/ bisacrylamide (0.8%, w/v)	7.50 ml	7.5 %
3 M Tris (pH 8.8)	3.75 ml	0.375 M
deionized water	18.45 ml	
degassed for 10 mins----------		
SDS (10%, w/v)	0.30 ml	0.1 %
TEMED	15 µl	0.1 %
APS (10%, w/v)	150 µl	0.05 %

Table 8-4 Stacking gel (3% acrylamide)

Chemicals	Volume	Final concentration
Acrylamide (30%, w/v)/ bisacrylamide(0.8%, w/v)	2.0 ml	3 %
3 M Tris (pH 6.8)	5.0 ml	0.125 M
10% (w/v) SDS	0.2 ml	0.1 %
deionized water	12.8 ml	
TEMED	20 µl	0.1 %
APS (10%, w/v)	100 µl	0.05 %

Table 8.5 2×Sample buffer

Chemicals	Quantity	Final Concentration
Mercaptoethanol	2.5 ml	10%
SDS	1g	4%
Tris (pH 6.8)	6.25 ml (0.5M)	0.125 M
Glycerol	5 ml	20%
bromophenol blue	1 mg	0.004%

Make up to final volume of 25 ml with distilled water.

Table 8.6 Running buffer

Chemicals	Amount
Tris	6 g
Glycine	29 g
SDS	1 g

Make up to final volume of 1000 ml with distilled water.

Table 8-7 Coomassie blue stain solution

Chemicals	Amount
Coomassie blue	0.5g
Water	530 ml
Methanol	400 ml
Acetic acid	70 ml

Table 8-8 Destain solution

Chemicals	volume
water	800 ml
methanol	100 ml
Acetic acid	100 ml

7.5 % separating gel and 3% stacking gel were used for analysis of the proteins (ferritin, biotinylated ferritin streptavidin and the aggregation products) according to the method of Laemmli (1970)[25]. The gels were poured between two clean grease-free glass plates separated by a plastic slate to give a gel width of

approximately 0.75 mm. After pouring the separating gel, water was layered on top of the separating gel to give it a flat face on which to cast the stacking gel. Formation of an interface between the separating gel and the water indicated that the gel had set. The water was removed. The stacking gel was poured on top of resolving gel and the comb was inserted. After the gel had set, the comb was removed.

The gel was placed in an electrophoresis chamber filled with 1 × running buffer. Unheated samples (1-10 μg protein in 20μl sample buffer) were loaded and ran at 120V for about 4 hours, with conventional cathode to anode polarity, until the tracking near the bottom of the resolving gel. The gel was then removed and stained with staining solution for 30 min followed by a destaining reagent until the backgroud was clear. The gel was dried with Biometra gel drier at 50 °C for 1 hour.

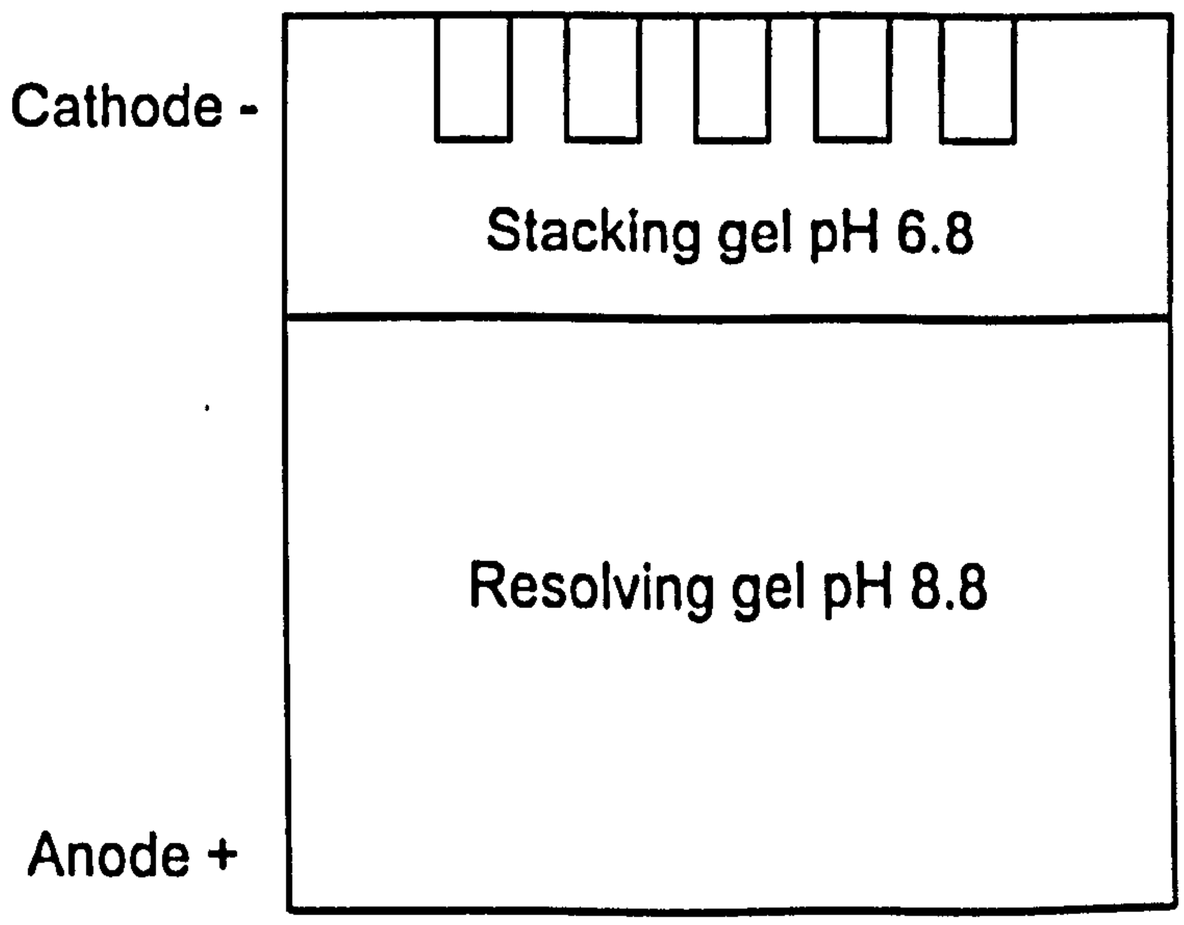

Scheme 8-3: Sketch of the gel.

8.2.2.6 Turbidity measurement

The change in turbidity (τ) of solutions containing various mole ratios of biotinylated ferritin and streptavidin was determined by monitoring the optical transmission ($T=\frac{I}{I_0}$) at 600 nm with time, using a Perkin Elmer Lambda II UV-vis spectrometer equipped with Perkin Elmer UV Winlab (Version 1.1) computer software (section **2.3.10**). The turbidity was calculated from:

$$\tau = -\frac{\ln(T)}{l}$$

where l is the cell length equal to 1.0 cm.

8.2.2.7 Electron microscopy

Samples for transmission electron microscopy (TEM) were taken directly from the solutions of native horse spleen ferritin, biotinylated ferritin or organized ferritin, and air dried onto Formvar-Coated, carbon-reinforced, copper electron microscope grids. The grids were then washed with water to remove salt crystals. TEM analysis was performed in bright-field mode using either a JEOL 1200EX electron microscope operating at 120 keV or a JEOL 2000FX high-resolution electron microscope operating at 200 keV (section **2.3.1**). Some samples were negatively stained with a 1% (w/w) solution of uranyl acetate.

8.3 Results and discussions

8.3.1 Description of organized nanoparticles within the ferritin

Biotinylated derivatives of horse spleen ferritin synthesized according to standard procedures (section **8.2.2.1**) gave transparent yellow solutions similar to native horse spleen ferritin. TEM images corresponding to biotinylated ferritin (Figure 8-1) were also similar to those recorded for native ferritin solutions prepared with the same protein at a similar concentration (Figure 8-2), which showed discrete electron dense iron oxide cores within the intact polypeptide shells (Figre8-1b) with occasional small aggregates due to the air drying procedure. Additions of streptavidin to the solution of biotinylated ferritin to give biotinylated ferritin : streptavidin mole ratios of 1 : 6 produced turbid suspensions, and yellow-brown macroscopic precipitates with clear colorless supernatants within a few hours. TEM images corresponding to the precipitate showed that the streptavidin-biotinylated-ferritin conjugates were extensively aggregated across the TEM grid (Figure 8-3a). The supramolecular aggregates were highly disordered and superlattice arrays with periodic order were not observed. Negative staining of the extended structures showed that the constituent iron oxide cores were surrounded by an intact polypeptide shell (Figure 8-3b), implying that the nanoparticle networks originate from specific intermolecular interactions between streptavidin and the surface biotinylated ligands of the modified shell of ferritin. TEM images corresponding to the supernatant showed no objects on the grid.

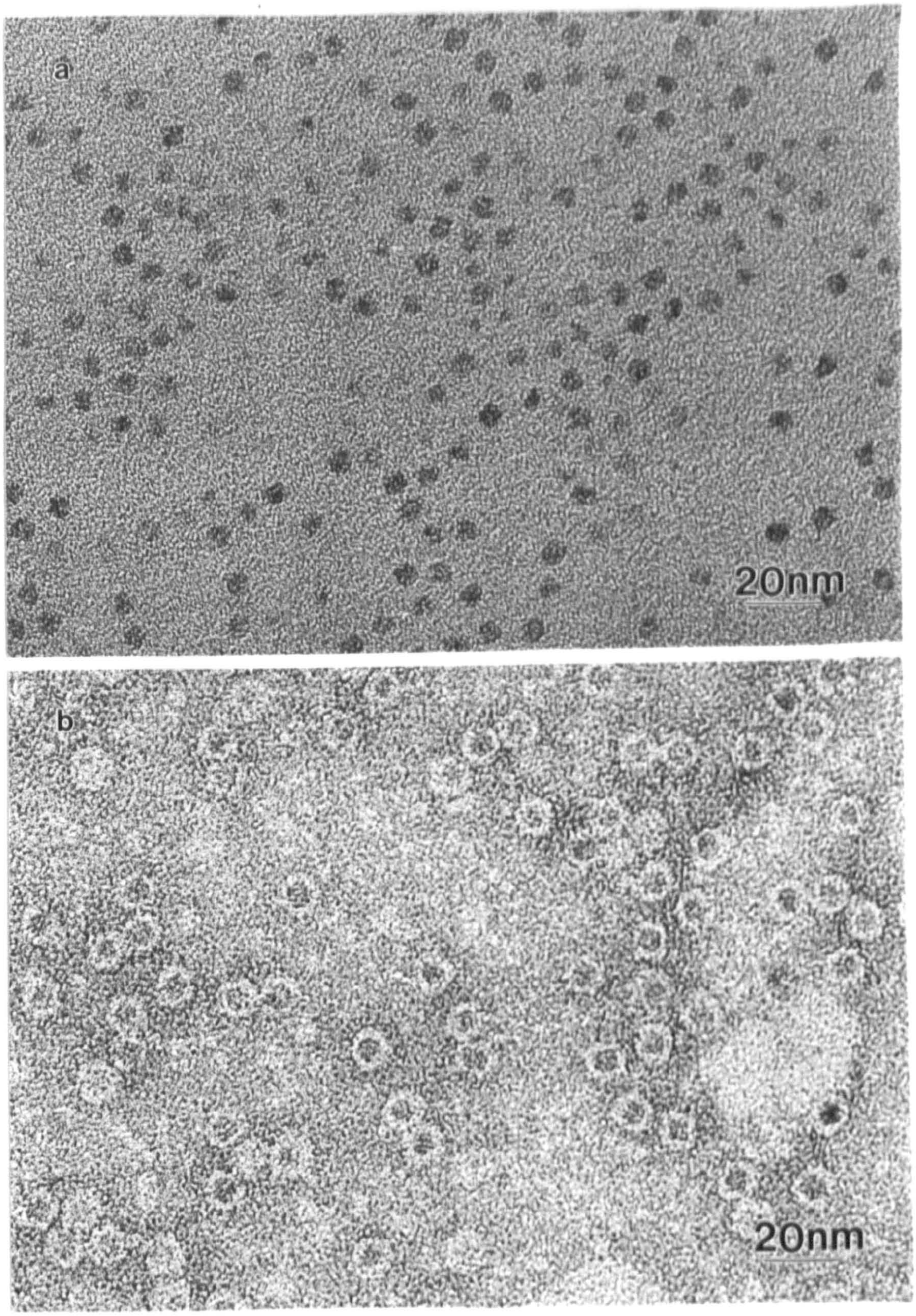

Figure 8-1: **(a)** TEM image of biotinylated ferritin showing discrete electron dense iron oxide cores, scale bar = 20 nm. **(b)** uranyl acetate negative stained TEM image of biotinylated ferritin showing individual protein shells with the iron oxide cores inside, scale bar = 20 nm.

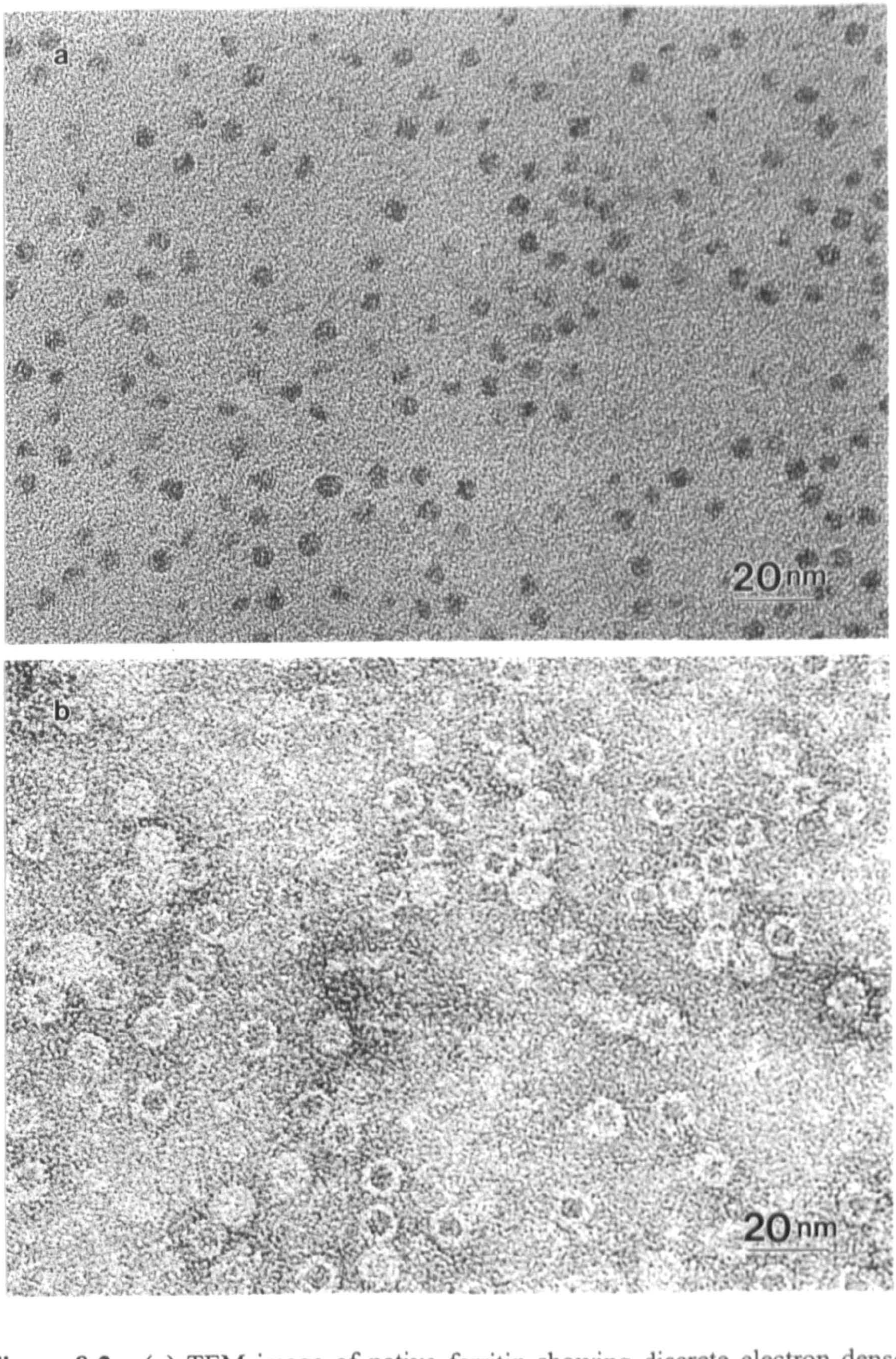

Figure 8-2: **(a)** TEM image of native ferritin showing discrete electron dense iron oxide cores, scale bar = 20 nm. **(b)** uranyl acetate negative stained TEM image of native ferritin showing individual protein shells with the iron oxide cores inside, scale bar = 20 nm.

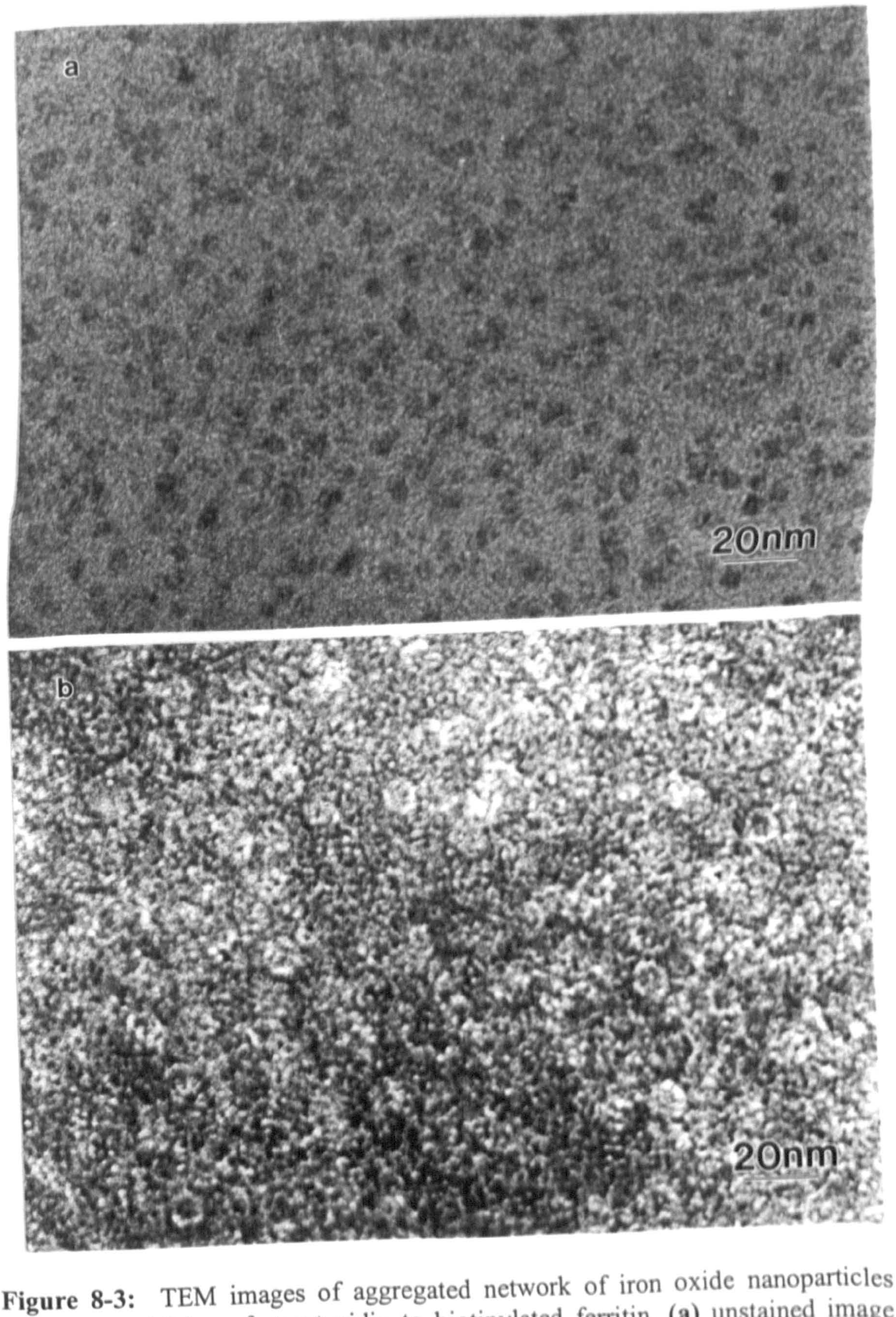

Figure 8-3: TEM images of aggregated network of iron oxide nanoparticles formed by addition of streptavidin to biotinylated ferritin. **(a)** unstained image showed disordered aggregation of nanoparticles without physical touching, **(b)** uranyl acetate negative stained TEM image of aggregated network showing that the aggregation occurs between the protein shells, not the cores. Biotinylated ferritin : streptavidin molar ratio = 1:6 in both cases. Scale bars = 20 nm.

In contrast, a biotin-free control reaction, in which native ferritin was mixed with streptavidin in a mole ratio of 1 : 6, remained clear and gave no suspension and bulk precipitate in several days. TEM images of the control sample (native ferritin + streptavidin) were similar to those recorded for native ferritin or biotinylated ferritin solutions prepared with the same protein similar concentrations.

The strength and specificity of the interactions between streptavidin and biotinylated ferritin was confirmed by SDS-polyacrylamide gel electrophoresis (SDS-PAGE). The control sample lane showed well-separated discrete bands of streptavidin and native ferritin (Figure 8-4, lane 4), consistent with a non-interacting system, the precipitated biotinylated ferritin/streptavidin material showed no bands for the constituent proteins (Figure 8-4, lane 5). Instead, a broad band was present in the stacking gel at the top of the lane, which corresponded to a conjugated material with significantly increased molecular weight. Although the intermolecular cross-linking was sufficiently strong to withstand deaggregation under the relatively harsh conditions used for SDS-PAGE, the intermolecular cross-liking could be deaggregated by adding excess free biotin. The reversibility of the aggregation process was demonstrated by adding a 20-fold excess (with respect to strepavidin) of free biotin to the turbid suspensions of the conjugated materials. The solutions turned clear yellow immediately and no suspension or precipitate were observed after several days. TEM images showed that protein-encapsulated iron oxide nanoparticles were dispersed back to their original non-associated state as shown in Figure 8-5.

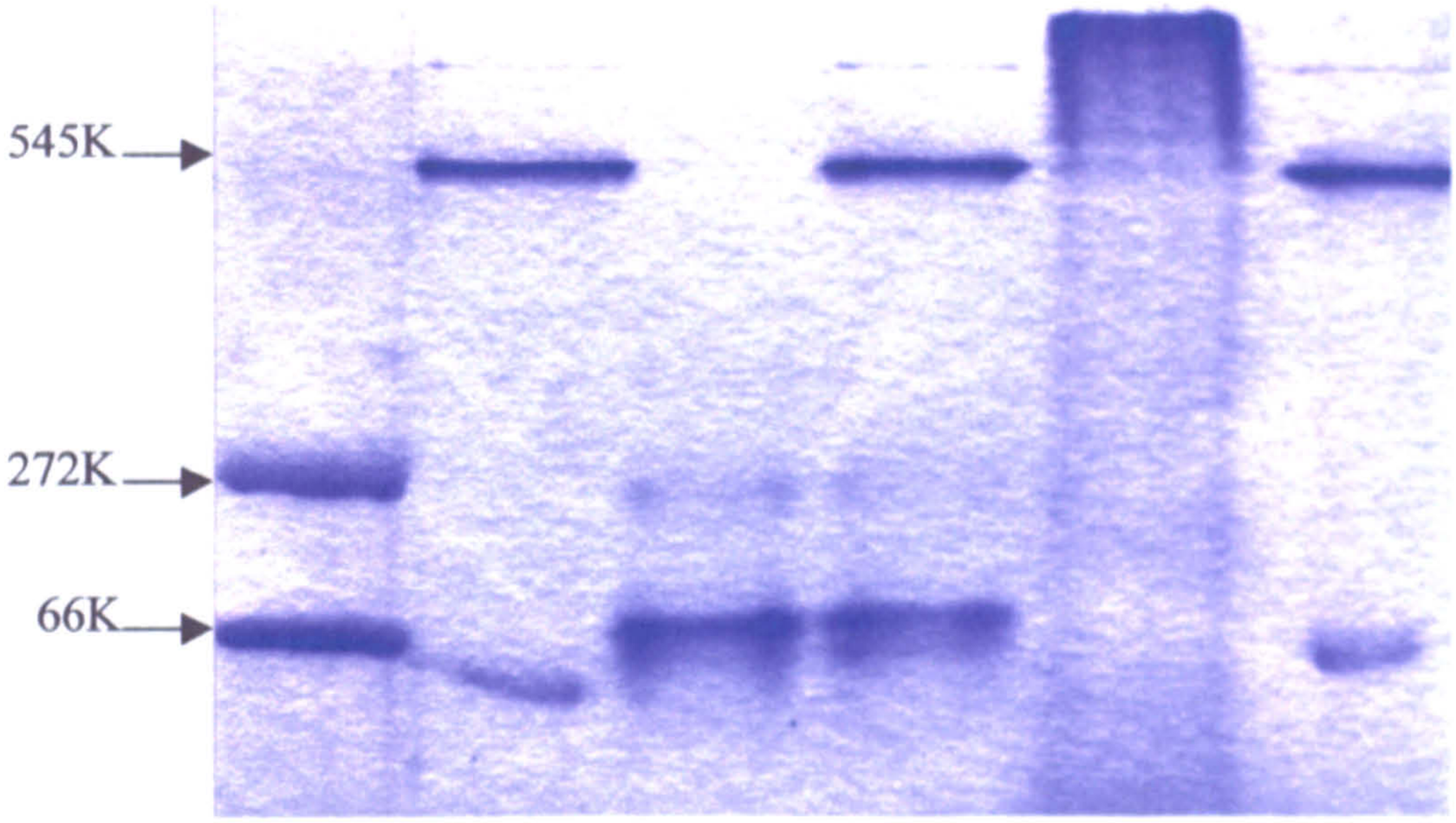

Figure 8-4: Coomassie blue stained SDS-PAGE profiles: Lanes **(1)** protein markers, **(2)** native ferritin, **(3)** streptavidin, **(4)** control (native ferritin + streptavidin), **(5)** biotinylated ferritin + streptavidin [1 : 6], **(6)** biotinylated ferritin.

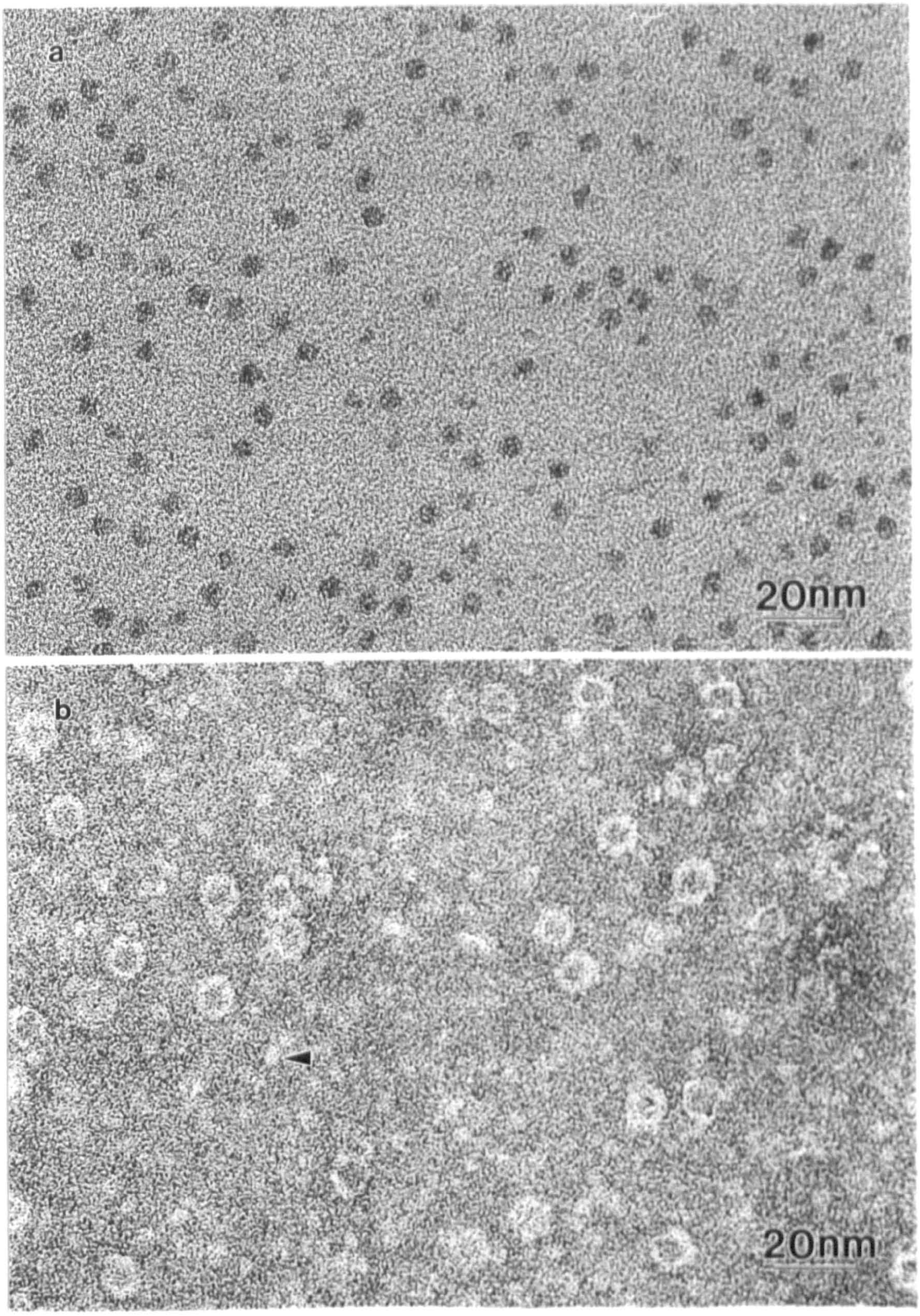

Figure 8-5: **(a)** TEM image of control experiment (addition of streptavidin to native ferritin) showing discrete electron dense iron oxide cores of nonaggregated protein molecules. Scale bar = 20 nm. **(b)** uranyl acetate negative stained TEM image of control experiment showing individual protein shells with the iron oxide cores inside and the streptavidin molecules (arrow), scale bar = 20 nm.

8.3.2 The effect of the concentration and the molar ratio of biotinylated ferritin to streptavidin on the aggregation

The formation of the supermolecular aggregates was studied by changes in turbidity. In general, the curves were characterized by an increase in turbidity to a threshold value within the first 10 to 15 minutes after mixing, followed by a discontinuous decrease due to macroscopic precipitation over periods of several hours. The first stage in this process represents the formation of supramolecular aggregates of colloidal dimensions whereas the second stage is associated with larger extended structures that sediment under gravity. Measurements for a series of samples at a constant molar ratio of 1 : 6, showed that the rate of formation and degree of colloidal aggregation increased with higher concentrations of biotinylated ferritin and streptavidin present in the solutions (Figure 8-6). Similar turbidity measurements at different ratios (1:2 – 1:12) of biotinylated ferritin to streptavidin at a constant ferritin concentration of 0.8 μM indicated that the rate of the formation of the cross-linking reaction and extent of aggregation of the organized conjugate were dependent on the ratio of biotinylated ferritin to streptavidin. The greatest reaction rate was observed at a mole ratio of 1:6 (figure 8-7c), and the turbidity curve reached the threshold value within 10 minutes. Meanwhile, a cloudy suspension of the conjugate appeared in the reaction mixture, and a yellow-brown bulk precipitate was observed after a few hours. Simultaneously, the supernatant turned colorless and transparent, indicating that there was almost no residual iron(III) in the supernatant.

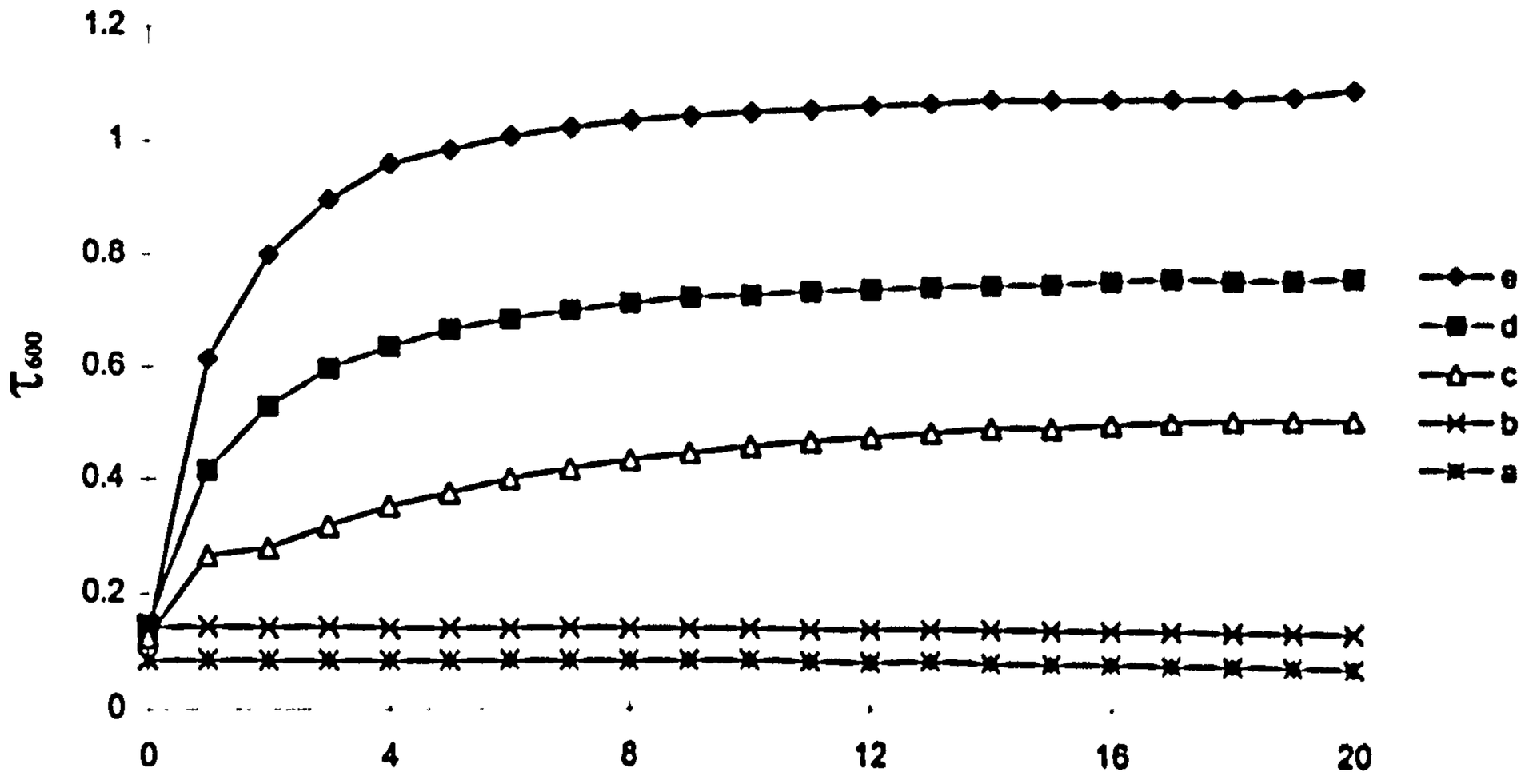

Figure 8-6: Change in turbidity at 600 nm (τ_{600}) with time after addition of streptavidin (SA) to biotinylated ferritin (BFn) at a constant mole ratio of 6 : 1 respectively. (a) control, 4.8 μM SA + 0.8 μM native ferritin; (b) control, 0.8 μM BFn; (c) 2.4μM SA + 0.4 μM BFn; (d) 3.6 μM SA + 0.6 μM BFn; (e) 4.8 μM SA + 0.8 μM BFn.

Thus the biotinylated ferritin molecules were almost completely organized by streptavidin cross-linking into the extended network of the bulk precipitate, which was conformed by TEM (section **8.3.1**). However, at the molar ratio of 1:4 the turbidity was remarkably lower than that of 1:6 (Figures 8-7c), the precipitate was dramatically less and the supernatant remained pale yellow and transparent after a few hours, indicating that the biotinylated ferritins were not completely interconnected. Increasing the concentration of streptavidin to a molar ratio of biotinylated ferritin to streptavidin of 1:8 resulted in a turbidity curve that was below that at 1:6 and which took 60 minutes to reach the threshold value (Figure 8-7d). Although the amount of precipitate was similar to that of 1:6 after a few hours a slight pale yellow supernatant was observed, indicating that the rate of cross-linking reaction was lower than that of 1:6 but the degree of organization was similar to that of 1:6. Further increasing the strepavidin concentration to a molar ratio of 1:12, resulted in no turbidity change (Figure 8-7b) and no precipitate as for 1:2 (Figure 8-7a). In contrast, the control experiments, which was the mixture of native ferritin and streptavidin or pure biotinylated ferritin, showed no changes in turbidity over periods of several days (Figure 8-6a,b). In summary, the rates of formation of ligand-induced cross-linking and the degree of associated aggregation were increased with the molar ratio of biotinylated ferritin to streptavidin from 1:2 to 1:6, and decreased from 1:6 to 1:12 at a constant ferritin concentration of 0.8 μM.

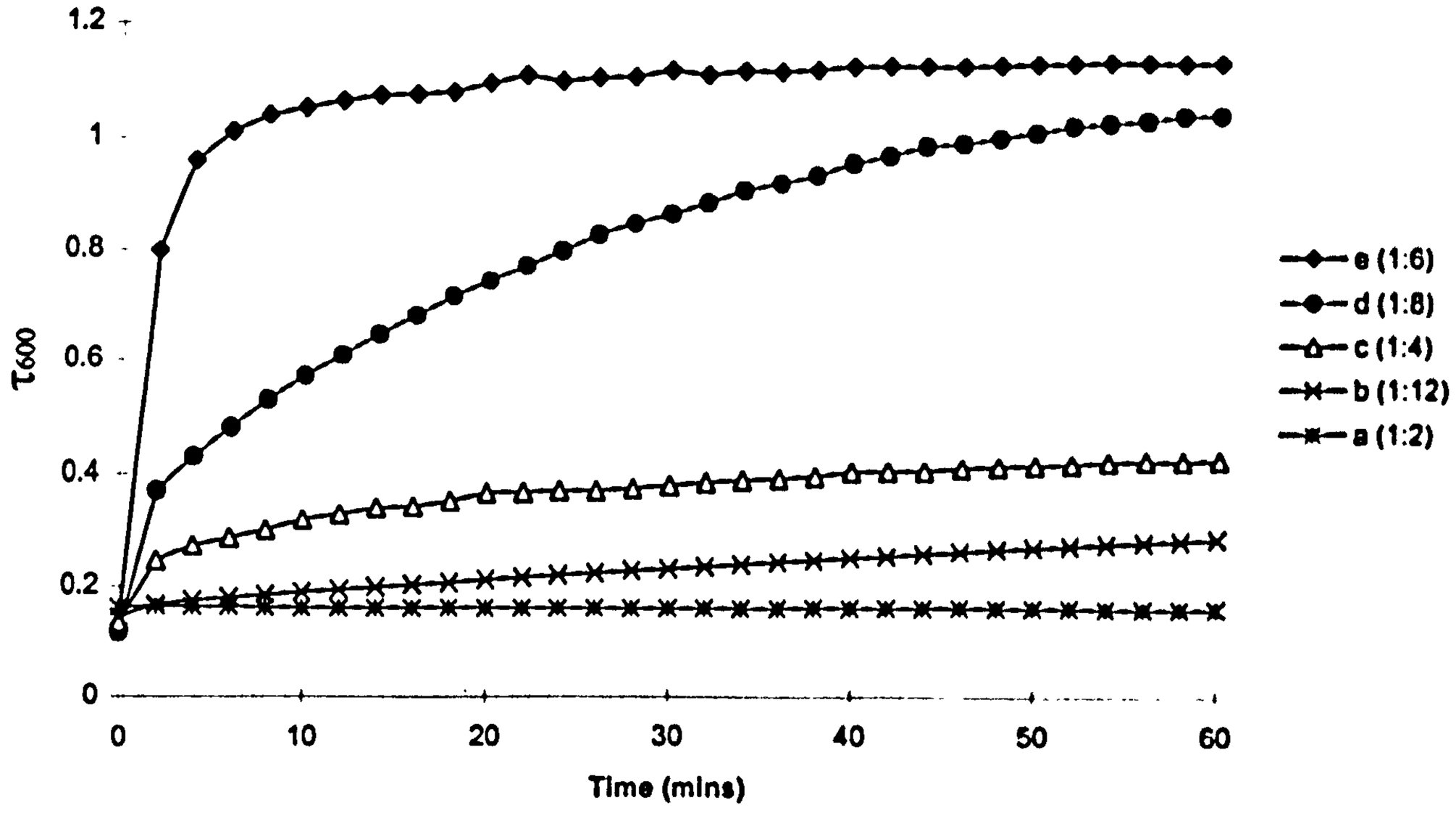

Figure 8-7. Change in turbidity at 600 nm (τ_{600}) with time after the addition of different amounts of streptavidin (SA) to 0.8 μM solutions of biotinylated ferritin (BFn; ca. 72 biotin ligands per molecule) to give ferritin to streptavidin mole ratios of (a) 1 : 2, (b) 1 : 12 , (c) 1 : 4 (d) 1 : 8, (e) 1 : 6.

8.4 General discussion

The results indicate that the rates and extent of formation of biotin-induced streptavidin cross-linking of ferritin molecules were dependent on the concentrations and stoichiometry of the components of the aggregated system. The turbidity curve for a 1 : 6 mixture of the biotinylated ferritin and streptavidin clearly indicates the formation of supramolecular aggregates and extended structures. However, at ferritin to streptavidin mole ratios less than 1 : 4, the turbidity curve showed a very low concentration of aggregation products, since there is insufficient streptavidin in the system to induce the formation of extended networks of protein-encapsulated inorganic nanoparticles. The rate of aggregation was particularly enhanced for a six-fold molar excess of streptavidin. Interestingly, further increases in the streptavidin concentration resulted in progressive decreases in aggregation. Thus, although the degree of bulk precipitation observed after several hours for mixtures with a mole ratio of 1 : 8 was similar to that at a ratio 1 : 6, the rate of aggregation within the first 30 minutes was significantly reduced at the higher ratio. Increasing the biotinylated ferritin to streptavidin mole ratio to 1 : 12 gave changes in turbidity that were less pronounced than those recorded for samples prepared with the much lower ratio of 1 : 4. In general, the propagation of such arrays will depend not only on the concentration of streptavidin, but the distribution and number of both free and streptavidin-bound biotinylated ligands on the surface of individual ferritin molecules in solution. As the number of biotinylated groups (72 per ferritin

molecule) was significantly larger than the number of added streptavidin molecules, an excess of unbound ligands was always present in the experiments studied. Thus the effective factor for cross-linking interactions should relate to the number of ferrtin and streptavidin molecules, not the number of biotin molecules. However, relatively large amounts of surface-bound streptavidin could sterically block the remaining (uncoupled) ligands from participating in bridging interactions with other streptavidin-ferritin complexes. This appears to be the case at a mole ratio of 1 : 12, where streptavidin-coated ferritin molecules remain dispersed in solution. Moreover, the results suggest that there is an optimum stoichiometry (1 : 6) at which the biotinylated ferritin molecules bind sufficient numbers of streptavidin molecules without seriously compromising the cross-linking interactions. This must represent a balance between primary and secondary coupling of the biotinylated moieties to the binding sites of streptavidin and streptavidin-ferritin complexes, respectively. It seems possible that these interactions could become cooperative rather than competitive under certain conditions. Whether this process is structurally determined, for example by the high (cubic) symmetry of the ferritin 24-mer, or arises from the minimization of steric and electrostatic forces between streptavidin molecules attached to the ferritin surface, is not currently known.

8.5 Conclusions

We have shown that the well-known specific binding of streptavidin to biotin can be exploited in the reversible assembly of disordered networks of inorganic nanoparticles. Ferritin is an attractive candidate for this approach because the polypeptide shell can be readily derivatized with approximately 70 biotinylated ligands that are available to interact with streptavidin to form a network of intermolecular crosslinks. In addition, the 8 nm internal cavity of apoferritin can be reconstituted with a variety of non-native inorganic cores, such as magnetite,[15] iron sulfide,[16] manganese oxides[17] and cadmium sulfide,[18] which have particle sizes determined by the metal-ion loadings used in the synthesis procedure. Thus, it should be possible to generate nanoparticle networks consisting of other inorganic components with controllable size and composition by development of this ligand-induced cross-linking approach. Because encapsulation of the inorganic phase within the protein cage restricts the scale of particle-particle interactions, and prevents direct physical contact and particle fusion and growth within the organized phase, ferritin-based arrays could have important applications in magnetic storage and nano-electronic devices.

8.6 References

[1] Alivisatos, A.P., Johnsson, K.P., Peng, X., Wilson, T.E., Loweth, C.J., Bruchez, M.P., Schultz, P.G., *Nature*, **382**, 609 (1996).

[2] Mirkin, C.A., Letsinger, R.L., Mucic, R.C., Storhoff, J.J., *Nature*, **382**, 607 (1996).

[3] Shenton, W., Davis, S.A., Mann, S., *Adv. Mater.*, **11**, 449 (1999).

[4] Mann, S., Shenton, W., Li, M., Connolly, S., Fitzmaurice, D., *Adv. Mater.*, **12**, 147 (2000).

[5] Shenton, W., Pun, D., Sleytr, U.B., Mann S., *Nature*, **389**, 585 (1997).

[6] Li, M., Schnablegger, H., Mann, S., *Nature*, **402**, 393 (1999).

[7] Kimizuka N., Kunitake T., *Adv. Mater.*, **8**, 89 (1996).

[8] Motte, L., Billoudrt, F., Lacaze, E., Pileni, M. P., *Adv. Mater.*, **8**, 1018 (1996).

[9] Colvin, V.L., Goldstein, A.N., Alivisatos, P., *J. Am. Chem Soc.*, **114**, 5221 (1992).

[10] Andres, R.P., Bielefeld, J.D., Henderson, J.I., Janes, D.B., Kolagunta, V.R., Kubiak, C.P., Mahoney, W.J., Osifchin, R.G., *Science*, **273**, 1690 (1996).

[11] Petit, C., Taleb, A., Pileni, M.P., *Avd. Mater.*, **10**, 259 (1998).

[12] Burkett, S.L., Mann, S., *Chem. Commun.*, **3**, 321 (1996).

[13] Connolly, S., Fitzmaurice, D., *Adv. Mater.*, **11**, 1202 (1999).

[14] Harrison, P.M., Paolo, A., *Biochemica et Biophysica Acta*, **1275**, 161 (1996).

[15] Meldrum, F.C., Heywood, B.R., Mann, S., *Science*, **257**, 522 (1992).

[16] Douglas, T., Dickson, D.P.E., Betteridge, S., Charnock, J., Garner, C.D., Mann, S., *Science*, **269**, 54 (1995).

[17] Meldrum, F.C., Douglas, T., Levi, S., Arosio, P., Mann, S., *J. Inorganic Biochem.*, **8**, 59 (1995).

[18] Wong, K.K.W., Mann, S., *Adv. Mater.*, **8**, 928 (1996).

[19] Service, R.F., *Science*, **277**, 1036 (1997).

[20] Chiruvolu S., Walker S., Israelachvili J., Schmitt F.J., Leckband D., Zasadzinski, J.A., *Science*, **264**, 1753 (1994).

[21] Weber, P.C., Ohlendorf, D.H., Wendoloski, J.J., Salemme, F. R., *Science*, **243**, 85 (1989).

[22] Wilchek, M., Bayer, E.A., *Methods in Enzymology*, Volume **184**, 5 (1990).

[23] Heitzmann, H., Richards, F.M., *Proc. Nat. Acad. Sci. USA*, **71**, 3537 (1974).

[24] Green, N.M., in *Methods in Enzymology*, (McCormick, D.B. and Wright, L.D., eds.), Vol. **18A**, p.418 (1970).

[25] Laemmli, U.K., *Nature*, **227**, 680 (1970).

Chapter 9

Conclusions

The work in this thesis shows that the morphology of nanoparticles ($BaCrO_4$, $BaSO_4$) prepared in AOT reverse microemulsions (w = 10) can be controlled by chemical stoichiometry. At the chemical equivalence of two reactants located inside different AOT micelles or microemulsions (the molar ratio of $[Ba^{2+}]$:$[CrO_4^{2-}]$ or $[Ba^{2+}]$:$[SO_4^{2-}]$ ≈ 1), prismatic nanocrystals (~16 nm in length) were produced. For an excess of anionic reactants (1 : 4.6 ≤ $[Ba^{2+}]$: $[CrO_4^{2-}]$ ≤ 1 : 2.7 or $[Ba^{2+}]$:$[SO_4^{2-}]$ ≈ 1 : 5) spherical nanoparticles (~ 10-11 nm in diameter) were formed, whereas for an excess of cationic reactants (the molar ratio of 2.7 : 1 ≤ $[Ba^{2+}]$: $[CrO_4^{2-}]$ ≤ 5.5 : 1 or 1.4 : 1 ≤ $[Ba^{2+}]$:$[SO_4^{2-}]$ ≤ 5.5 : 1) nanofilaments (20 μm in length) were obtained. The filamentous structures were specifically formed when the $[Ba^{2+}]$: $[SO_4^{2-}]$ molar ratio was greater than 1. Under these conditions, there is an excess of barium in the reaction system and the primary $BaSO_4$ nanoparticles are positively charged. This results in a strong electrostatic interaction with the anionic AOT surfactant headgroups to produce the surfactant-nanoparticle aggregates that are the key intermediates for filament formation. A morphological evolution from nucleation, reconstruction and hydrophobic aggregation of interfilaments was followed.

The different nanoparticle morphologies were obtained from the same microemulsion system, which contains a mixture of sodium sulfate (or sodium chromate) containing NaAOT (0.1 M in isooctane, w = 10) microemulsion droplets and $Ba(AOT)_2$ (0.05 M in isooctane, w < 1) micelles. The NaAOT

microemulsion droplets are spheres with ~2.2 nm radius and the $Ba(AOT)_2$ micelles are also spheres with ~0.9 nm radius. The morphology of the nanoparticles is related to the molar ratio of the two reactants inside the micelles and microemulsion droplets with all other parameters constant. Clearly, there is no relationship between nanoparticle morphology and microemulsion shape under the conditions investigated.

Comparing the final size of the particles shows there is no direct link with the size of the microemulsion droplets in which they formed. Under certain conditions the crystalline particles that form are significantly larger than the microemulsion droplets. However, the sizes of the nanoparticles (barium chromate, barium sulfate and Prussian blue) increased with increasing of microemulsion droplet size, implying that the size of the nanoparticles synthesized in the microemulsion was associated with the number of reactant ions per droplet, local concentration and the exchange rate *etc.*

Self-assembly of nanoparticles into superlattices may spontaneously occur in solution when the particles are in specific shapes and are coated with surfactant hydrophobic tails. The particle shape is a very important factor in the self-assembly of nanoparticles into superlattices. In the same AOT microemulsion system, prismatic $BaSO_4$ and $BaCrO_4$ nanoparticles can spontaneously self-assemble into linear array structures in solution and subsequently into two-dimensional superlattice structures. Since there is a large surface area between the

particles, AOT lamellar structures form by hydrophobic interactions. In contract, spherical nanoparticles cannot self-assemble in the solution. Moreover, the cubic shaped Prussian blue nanoparticles transform readily into long-range square superlattices on drying on the TEM grids.

The well-known specific binding of streptavidin to biotin can also be used to organize inorganic nanoparticles into disordered networks. Cross-linking the iron storage protein ferritin, which has been functionalized with biotin, with streptavidin produces aggregates of iron nanoparticles. It should be possible to generate nanoparticle networks consisting of other inorganic components (such as magnetite, iron sulfide, manganese oxides and cadmium sulfide) with controllable size and composition by development of our ligand-induced cross-linking approach.